Thermodynamic and heat transfer analysis of a Activated carbon – R723 adsorption system

by

MohammadHasan Khaliji Oskouei

A thesis submitted in partial fulfilment of the requirements for the Degree of Doctor of Philosophy

University of Warwick, School of Engineering

November 2016

Contents

List of figures

List of tables

Acknowledgements

I would like to express my gratitude for all those who have helped me in completing my PhD thesis. Special thanks go to my supportive PhD supervisor Dr Zacharie Tamainot-Telto. I also need to thank many staff members and colleagues at the Department of Engineering of the University of Warwick, particularly Professor Critoph, Dr Metcalf, Dr Thorpe and Dr Rivero Pacho, for their helpful comments.

I am also indebted to D. Ali Abdi and Patricia Abdi, as well as Saeideh Abdi and Dr Mohammad Reza Asghari for being friends over the last four years. I would like to thank Dr Morteza Hashemi and Dr Soroush Abolfathi for advice regarding this thesis. My final and special acknowledgement goes to my beloved parents, Professor Mohsen Khaliji and Simin Abdi, and my beloved wife, Mahdiyeh Dabaghzadeh, for their encouragement and for being such great inspirations in my life. This dissertation is dedicated to them.

Declaration

The work presented in this thesis has been produced solely by the author under the supervision of his thesis supervisors. The material in this thesis is submitted for a degree of Doctor of Philosophy to the University of Warwick only and has not been submitted to another university.

MohammadHasan Khaliji Oskouei

28/11/2016

Publication

Published conference paper

M. Khaliji Oskouei, Z. Tamainot-Telto, Effect of packing density on thermal properties of granular activated carbon packed bed by using of inverse heat conduction method, 2014; 10th International conference on heat Transfer, fluid mechanics and Thermodynamics, HEFAT 2014, USA, Orlando, Florida.

Abstract

The main challenge of adsorption systems today is to improve the performance of the thermal generator in order to make adsorption systems economically viable. The key novelty of this doctoral thesis is its evaluation of the potential use of a new refrigerant, R723, in an adsorption system using activated carbon as adsorbent. Granular activated carbon is a well-known and effective adsorbent in adsorption systems. The R723 refrigerant was introduced into the market in early 2004; this new refrigerant is an azeotropic mixture of *40%* ammonia and *60%* dimethyl ether by mass. The new refrigerant is compatible with copper alloy (Cu-Ni 90/10), in comparison with ammonia, which is only compatible with stainless steel. The high thermal conductivity of Cu-Ni 90/10 causes an improvement in heat exchange in the thermal generator.

This work investigates the effect of granular activated carbon packed bed density on gas permeability. A correlation was found between granular activated carbon packing density and refrigerant pressure drop over the thermal generator.

The porosity of granular activated carbon in terms of adsorbing the R723 was determined. The porosity was evaluated using the gas mixture adsorption theory and using the porosity experimental data for granular activated carbon / ammonia and granular activated carbon / dimethyl ether pairs.

The performance of the adsorption system for different applications was determined with the activated carbon / R723 pair. The effects of concentration of R723 and granular activated carbon packing density on the thermal parameters of activated carbon packing, including the thermal conductivity and heat transfer coefficients of the contact wall/packed carbon, were studied simultaneously. A correlation was established showing the connection between the thermal parameters of the packed bed, and the concentration of R723 and the density of the granular activated carbon packed bed.

Finally, this thesis demonstrates modelling procedures for a tubular generator with the granular activated carbon (208-C) / R723 pair, with regard to different applications such as air conditioning, ice making and a heat pump. The model under consideration included the ideal desorption effect without heat and mass recovery, while imposing the

ideal temperature jump into the boundary of the tubular generator. During the modelling, information such as driving temperature (Tg), coefficient of performance (COP), and specific cooling and heating powers (SCP & SHP), was collected. The collected information was used to established a correlation in order to estimate the optimum driving temperature, COP, SHP and SCP, based on different governing parameters, such as granular activated carbon packing density, outside diameter (OD) and the length of the thermal generator. This information is useful in choosing the correct typical standard tube size of the thermal generator with the granular activated carbon (208-C) / R723 pair for specific applications, based on optimum governing parameters, such as the range of heat source availability and the power requirement. The other key point which was examined was the effect of tubular generator body material on COP and SCP (SHP) for different applications. The model used stainless steel and Cu-Ni 90/10 with standard wall thickness.

Nomenclature

***Chapter 3*……....**

B	Forchheimer or Ergun coefficient	m^{-1}
C_E	Ergun coefficient	
F	Flow rate correction factor	
β_r	Radial Forchheimer or Ergune coefficient	m^{-1}
β_a	Axial Forchheimer or Ergune coefficient	m^{-1}
K_p	Specific permeability	m^2
$K_{p\text{-}r}$	Radial permeability	m^2
$K_{p\text{-}a}$	Axial permeability	m^2
LPM	Liter per minute	
m_r	Radial mass flow rate	$Kg\ .sec^{-1}$
m_a	Axial mass flow rate	$Kg\ .sec^{-1}$
P	Fluid density	$kg.m^{-3}$
Q	Volumetric flow rate	LPM
R	Gas constant	$J.kg^{-1}.K^{-1}$
R	Sample radius	m
Re	Reynolds number	
S	Cross section area, perpendicular to the flow direction	m^2
T	Sample temperature	K
V_D	Darcy velocity	$m.sec^{-1}$
∇P	Pressure gradient	$Pa.m^{-1}$
μ	Viscosity of the flowing fluid	$Pa.sec$
β_r	Radial Forchheimer or Ergune coefficient	m^{-1}
β_a	Axial Forchheimer or Ergune coefficient	m^{-1}

***Chapter 4*……....**

A	Corresponding to the slop of the saturation curve on a plot of ln(P) vs. -1/ Tsat	
CP	Overall specific heat	$J.kg^{-1}.K^{-1}$
$C_{p\text{-}Carbon}$	Carbon specific heat	$J.kg^{-1}.K^{-1}$
$C_{p\text{-}R723Liquid}$	Liquid R723 specific heat	$J.kg^{-1}.K^{-1}$

d	Sample thickness	m
dT	Temperature changes over the representing cell	K
d_p	Particle diameter	mm
dr	Length increment	m
D	Sample holder outside diameter	m
Dt	Time increment	S
D_o	Inside thermocouple tube – outside diameter	m
F	Reference thermal resistance	$m^{2}.K.W^{-1}$
h	Heat transfer coefficients of the contact wall/packed carbon	$W.m^{-2}.K^{-1}$
H	Heat of sorption	$J.kg^{-1}$
I	Node representing	
ID	Inner diameter	m
k_{carbon}	Carbon thermal conductivity	$W.m^{-1}.K^{-1}$
k_{steel}	Steel thermal conductivity	$W.m^{-1}.K^{-1}$
k	D-A parameter	
L_C	Carbon sample length	m
M_{Carbon}	Mass of carbon for each representing cell	kg
m_{R723}	Mass of adsorbed R723	kg
n	D-A parameter	
OD	Outer diameter	m
P_{carbon}	Carbon density	$kg.m^{-3}$
P	Pressure	bar
Q	Heat transfer rate	W
$\dot{q}$	Heat flux	$W.m^{-2}$
$R_{Total\ Conduction}$	Total thermal resistance	$m^{2}.K.W^{-1}$
R_{Sample}	Thermal resistance of sample	$m^{2}.K.W^{-1}$
$R_{internal}$	Interfacial thermal resistance	$m^{2}.K.W^{-1}$
R	gas constant	$J.kg^{-1}$
S	Area	m^{2}
t	Time step representing	
T	Temperature	K

T_b	Bulk temperature	K
T_u	Temperatures of upper plate	K
T_1	Temperatures of lower plate	K
Th	Temperatures of heat sink	K
T_{sat}	Saturation temperature corresponding to the gas pressure	K
UA	Overall heat transfer coefficient	$W.K^{-1}$
x_o	R723 concentration under saturation condition corresponding to the maximum concentration	$kg.kg^{-1}$
x	R723 concentration at desire pressure and temperatures	$kg.kg^{-1}$
Λ	Thermal conductivity	$W.m^{-1}.K^{-1}$
δx	Conduction length in the direction of heat flow	m

***Chapter 5*……....**

A	Slope of fitted curve at Clapeyron diagram	
B	Intercept of fitted curve at Clapeyron diagram	
DME	Dimethyl ether	
E	Adsorption energy of adsorbate	$kJ.mol^{-1}$
E_0	Adsorption energy for the reference adsorbate (benzene)	$kJ.mol^{-1}$
$\bar{E}_0$	Average adsorption energy for the reference adsorbate (benzene) from experiment	$kJ.mol^{-1}$
k	D-A equation parameter for mass concentration uptake theory	
k_1	D-A equation parameter for volumetric uptake theory	
K_1	Parameter for linear fitting of D-A equation	$K^{1/n}$
m_h	Sample holder basket weight	g
m_f	Sample holder basket and dried adsorbent weight	g
m_c	Dried adsorbent weight	g
m_t	Aperient mass of sample holder basket, dried adsorbent and adsorbed adsorbate	g
m_b	Correction mass because of bouncy effect	g
M_w	Adsorbate molecular weight	$g.mol^{-1}$
$m_{correctet}$	Real mass of the adsorbent, adsorbate, holding basket and bouncy correction	g

NH3	Ammonia	
n	D-A equation parameter for mass concentration uptake theory	
n_1	D-A equation parameter for volumetric uptake theory	
n_i	Molar capacity of the component in the adsorbed mixture	*mol*
n_i^o	Reference adsorbed molar capacity of the pure components	*mol*
P	System pressure	*bar*
P_{sat}	Saturation pressure	*bar*
P_c	Adsorbate critical pressure	*bar*
P_i	Partial pressure of the component *i* in the mixture	
P_i^*	Vapor pressure of the pure component *i*	
RE170	Dimethyl ether (DME)	
R717	Ammonia (NH3)	
R723	Azeotropic blend of R717 and RE170 with 60% and 40% mass fraction	
R	Gas constant	$J.K^{-1}.mol^{-1}$
SSE	Error sum of squares	
T	Temperature	K
T_b	Adsorbate normal boiling point	K
T_c	Adsorbate critical temperature	K
V	Volume filled at an equipotential surface per kilogram of adsorbent	$m^3.kg^{-1}$
V_0	Micropore limiting volume per kilogram of adsorbent	$m^3.kg^{-1}$
V_s	Micro-pores specific volume of activated carbon	$cm^3.g^{-1}$
V_T	Theoretical volumetric adsorption uptake for refrigerant mixture	$m^3.kg^{-1}$
V_1	Theoretical volumetric adsorption uptake for first pure component refrigerant	$m^3.kg^{-1}$
V_2	Theoretical volumetric adsorption uptake for second pure component refrigerant	$m^3.kg^{-1}$
x	Adsorbate mass concentration	$g.g^{-1}$
x_o	Limiting adsorbate mass concentration.	$g.g^{-1}$
X_i	Mole fraction of the component *i* in the mixture.	

ε_i	Polanyi potential field	
β	Affinity coefficients	
ρ_h	Sample holder basket density	$kg.m^{-3}$
ρ_c	Activated carbon packed density	$kg.m^{-3}$
ρ_{gas}	Adsorbate density at certain temperature and pressure	$kg.m^{-3}$
ρ_L	Liquid density at normal pressure condition or atmospheric pressure	$kg.m^{-3}$
v	Specific volume of adsorbed phase	$m^3.kg^{-1}$
v_a	Van der Waals volume	$m^3.kg^{-1}$
v_b	Specific volume of adsorbate at normal boiling point	$m^3.kg^{-1}$
Ω	Adsorbate thermal expansion coefficient	K^{-1}

***Chapter 6*……....**

COP	Coefficient of performance	
Cp	Specific heat	$J.kg^{-1}.K^{-1}$
CP	Adsorbent and liquid adsrobate specific heat	$J.kg^{-1}.K^{-1}$
Cu	Copper	
GAC	Granular activated carbon	
h	Heat transfer coefficients of the contact wall/packed carbon	$W.m^{-2}.K^{-1}$
ID	Inner diameter	*m*
L_C	Carbon sample length	*m*
LH	Evaporation heat	$J.kg^{-1}$
Ni	Nickel	
OD	Outer diameter	*m*
Pe	Evaporation pressure	*bar*
Pc	Condensation pressure	*bar*
SCP	specific cooling power	$W.kg^{-1}$
SHP	specific heating power	$W.kg^{-1}$
t_w	Wall thickness	*m*
T	Temperature	*K*
T_e	Evaporation temperature	^oC
T_C	Condensation temperature	^oC

T_g	Driving temperature	^oC
x	Adsorbate mass concentration	$g.g^{-1}$
ρ	Density	$kg.m^{-3}$
λ	Thermal conductivity	$W.m^{-1}.K^{-1}$

Chapter 1

Introduction

1.1. Background

During the last two decades, global warming and CO_2 emissions have been brought to the attention of the public because of health issues. Burning fossil fuels for the purposes of domestic heating and electricity production for general usage has a huge impact on the environment. Many researchers have as a result tried to improve cooling and heating systems, in order to reduce the use of electricity as a primary source, by proposing systems that could use heat sources such as solar energy, agricultural waste or biomass. Adsorption machines are examples of such alternative machines, which could use renewable energy sources or waste heat from industrial activities. Moreover, adsorption machines are helping to improve anti-global warming activities by using non-CFC or HCFC refrigerants.

Machines based on vapour compression, absorption and adsorption can be used in refrigeration and heat pump applications. In order to improve the performance of refrigeration and heat pump systems, a hybrid mechanism was suggested and developed. A hybrid system is a combination of vapour compression and adsorption cycles. The key element in a hybrid system is the working refrigerant. In a hybrid system, the refrigerant should be compatible with both vapour compression and adsorption.

1.2. Aims and objective

Activated carbon / ammonia (R717) is one of the common pairs used in adsorption refrigeration and heat pump applications. High latent heat, and small and polar molecules, which improve its adsorption by the adsorbent, makes ammonia a good refrigerant. Ammonia has zero ozone depletion potential ($ODP_{R717} = 0$), which

makes it environmentally friendly, and means that it has no effect on global warming ($GWP_{R717} = 0$). The disadvantage of ammonia is that it is corrosive to copper and its alloys. In *2004* a new refrigerant was introduced to the market, called R723.

R723 is an azeotropic blend of R717 and RE170 (dimethyl ether) with *60%* and *40%* mass fractions, respectively. A vast study has been carried out in order to evaluate the use of R723 in vapour compression systems. In this thesis, I evaluate the new refrigerant in terms of its use in an adsorption system. This evaluation will help improve the hybrid system in future, by allowing use of R723 as a shared refrigerant between vapour compression and adsorption cycles. The new refrigerant guarantees the advantageous substitution of pure R717, but unlike R717 is compatible with copper alloys (*CuNi90/10*). The thermal conductivity of copper alloy ($\lambda_{CuNi\ 90/10} = 42\ W.m^{-1}.K^{-1}$) is *2.6* time higher than stainless steel ($\lambda_{Steel} = 16.3\ W.m^{-1}.K^{-1}$), therefore the thermal generator's size and the desorption cycle time will both decrease. The compatibility of R723 with copper alloy causes a fabrication cost reduction for adsorption systems and makes the thermal generator economically viable.

The aim of this project is to develop and design a tool for a new adsorption pair, granular activated carbon / R723, for use in a thermal generator for adsorption refrigeration, ice making and heat pump applications. The objectives of the project are as follows:

- To study the interaction of R723 and granular activated carbon in adsorption and desorption phases. The interaction will be studied in terms of establishing the concentration of R723 within the activated carbon.
- To study the permeability of air and argon in granular activated carbon packed beds.
- To investigate the heat transfer properties of granular activated carbon packed beds in the presence of R723.
- To carry out computational modelling and optimization of a tubular thermal generator for air conditioning, ice making and heat pump applications.

1.3. Scope

Chapter 2 provides a review of previous studies of solid sorption machines and their application, including the coefficient of performance (COP), and specific heating and cooling powers.

In Chapter 3 the effect of granular activated carbon packing density on the pressure drop of the flow of air and argon is investigated. The data collected and the Darcy-Forchheimer model were used to establish permeability and shape factor as characteristics of packed beds.

Chapter 4 deals with the heat transfer properties of granular activated carbon in the presence of the refrigerant. This chapter establishes a correlation connecting the thermal properties of granular activated carbon / R723 to packing density and adsorbate concentration.

Chapter 5 is about understanding the basics of the adsorption mechanism and finding the porosity characteristics, based on the Dubinin-Astakhov equation, for 208-C / R717, 208-C / DME (RE170) and 208-C / R723. In the remainder of this chapter, mixture theory was used to predict the porosity parameters of 208-C / R723 from pure component porosity characteristics.

Chapter 6 covers how, once all adsorbent and adsorbate properties were established (208-C / R723), a simulation was conducted for air conditioning, ice making and heat pump applications, for a tubular thermal generator. A copper alloy, which contain *10%* nickel (*CuNi 90/10*) and stainless steel, was used as a tubular generator body material, while the outside diameter was set to 1/4″, 1/2″, 3/4″, 1″and 1.1/8″. The *CuNi 90/10* tubular generator wall thickness for different outside diameters was kept constant at *1 mm* throughout the whole analysis, while the stainless-steel wall thickness was *0.15 mm*, *0.25 mm*, *0.56 mm*, *0.71 mm* and *0.91 mm*, according toouter diameter. The coefficient of performance (COP), and specific cooling and heating powers (SCP and SHP) were collected for each type of tubular generator, with specific physical appearances, for air conditioning, ice making and heat pump applications. Finally, all performance indicators were compared for each type of application, between two types of tubular generator. Correlations were established for evaluation of the driving temperature and COP, using the generator's physical

appearance, including outside diameter, body material and granular activated carbon packing density.

Chapter 7 provides a conclusion and offers suggestions for further research.

Chapter 2

Literature review

2.1. Introduction

The objective of this chapter is to discuss the adsorption system, which stands among the other heating and cooling systems, to provide a fundamental understanding of adsorption systems and to review other researchers' work in order to show current developments in this area.

The effects of human activity, such as transport, industrial work and domestic usage, are revealed in the environment by measurement of greenhouse gas (GHG) emissions. CO_2, CFCs and HCFC are three gases which have a huge impact on the environment, with an average ozone depletion potential (ODP) of zero, *1* and *0.3*, and global warming potential (GWP) of *1*, *10900* and *1810*, respectively. To control GHG emissions, so as to reduce the effect of human activity on the environment, the Kyoto protocol was established in *1997* [1] by the United Nations Framework Convention on Climate Change (UNFCCC), which entered into force in *2005*.

The Kyoto protocol specified a reduction in greenhouse gas emissions of *80%* by *2050* from the baseline of *1990* levels. The UK government, in order to satisfy the Kyoto protocol, set four interim carbon budgets up to *2027* [2], of which the first measure was completed by *2012*, a *12.5%* reduction [2] in GHG emissions, and involving a *34%* reduction by *2020*, in comparison to the *1990* emissions baseline. Table 2.1 shows the carbon emissions budget level set by the UK government in order to satisfy the Kyoto protocol. Figure 2.1 illustrates the UK government's achievements in controlling GHG emissions compared to their targets.

	Budget 1	Budget 2	Budget 3	Budget 4
	2008-12	2013-17	2018-22	2023-27
Budget level ($MtCO_2e$)	3,018	2,782	2,544	1,950
Equivalent average annual emissions	603.6	556.4	508.8	390.0

Table 2.1. Summary of UK Carbon Budgets from *2008* to *2027* (millions of tons of CO_2 emission: $MtCO_2e$) [2].

A report released in *2015* by the Department of Energy and Climate Change [4] showed that *38.5%*, *16.1%* and *16%* of carbon dioxide emissions are caused by the fuel consumption of energy suppliers, businesses and residential housing, respectively. The Department of Business, Energy and Industrial Strategy published a report on energy consumption in the UK in July *2016* [5]. This report showed that in *2015* the usage of natural gas in heat generation and other domestic areas is *40%*, while electricity generation makes up *27%* of total usage. Looking into the figures provided, an amount of natural gas equivalent to *4317 thousand tonnes of oil* [5] was used in heat generation and domestic areas in the second quarter of *2016*. Therefore, a great deal of effort and a number of changes, such as improvements to building construction and insulation, better industrial processes, and increases in air conditioning efficiency through new and improved technology, need to be provided in order to hit the carbon dioxide emissions target by *2050*.

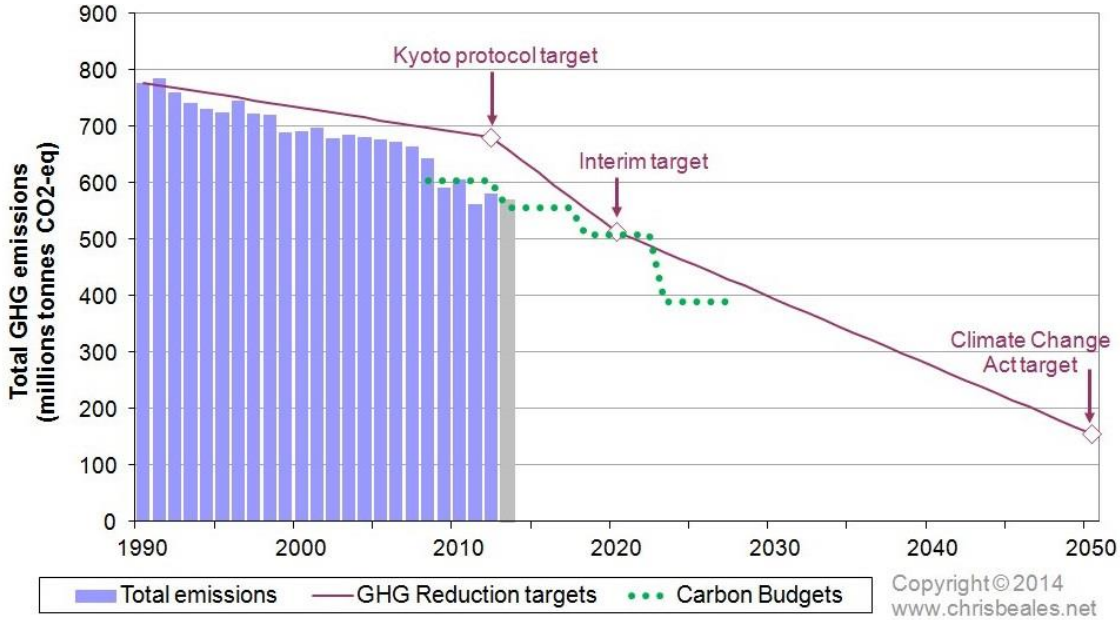

Figure 2.1. UK greenhouse emissions compare to targets [3].

Using the proposed adsorption air conditioning system for heating and cooling will increase performance by combining the primary energy source (natural gas) with

low-grade energy sources. The other advantage of using primary energy sources is a reduction in usage of secondary energy sources (electricity) by air conditioning applications, and therefore losses from the conversion of fuel to electricity, electricity grid transmission and electricity to mechanical movement are going to be less significant, causing a reduction in fuel usage and total carbon dioxide emission.

2.2. Adsorption basics

The history of adsorption refrigeration system based on an AgCl / ammonia pair thermal generator dates back to 1848 by Faraday [7, 32]. Later the adsorption system for air conditioning application in the rail industry was developed by Hulse [8] and Miller [9]. In 1960 Plank et al. [6] reports the construction of NH3 / CaCl and activated carbon / methanol to make an adsorption refrigeration system for rail industry.

Tamainot-Telto et al. [10] explain the basic operation of an adsorption system, illustrated in Figure 2.2. In principle, the adsorption refrigeration system consists of two linked vessels, one of them named the thermal generator, which contains the adsorbent / adsorbate pair, and the other vessel named the evaporator – condenser, which only contains the adsorbate (refrigerant).

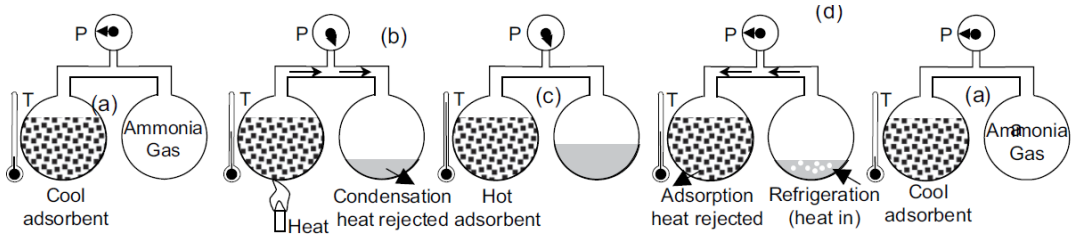

Figure 2.2. Principle of adsorption refrigeration technology [10].

At the starting point, the thermal generator is fully charged and saturated (Figure 2.2-a), while the evaporator and condenser are filled with just the refrigerant gas. The second step starts with the isosteric heating process (Figure 2.3-right: 1 to 2; Figure 2.2-b): the thermal generator is heated by an external heating source and system pressure is increased until it reaches the condensing pressure. When the system reaches the condensing pressure, the adsorbate condensation process starts, while at the same time the desorption process ocurs in the thermal generator. The desorption process continues until the concentration of adsorbate reaches its minimum (Figure

2.3-right: 2 to 3; Figure 2.2-c). At the third step, the liquid refrigerant moves into the evaporator and the thermal generator starts to adsorb the adsorbate at low pressure (Figure 2.2-d; Figure 2.3-right: 3 to 4 – 4 to 1).

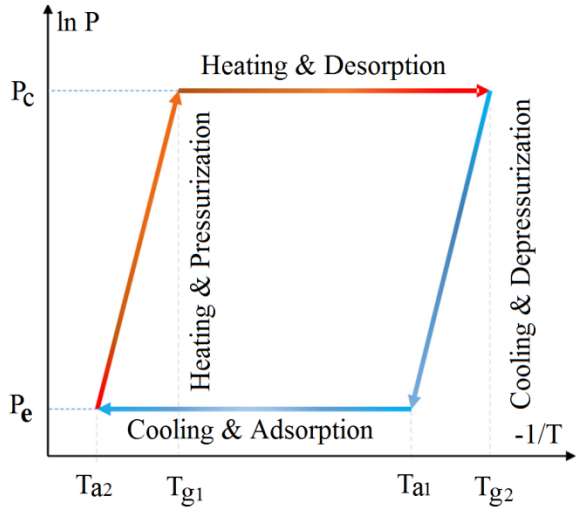

Figure 2.3. P-T diagram for basic adsorption cycle: (a-b) heating and pressurization; (c) eating and desorption and condensation; (c) cooling and depressurization; (d) cooling, adsorption and evaporation [11, 12].

Each system has its own benefits and difficulties; the following is a quick summary of the advantages and disadvantages that the solid sorption system provides:

a) Adsorption refrigeration systems can be employed in situations in which there is a high level of vibration, such as transportation and cargo cars [13, 14].
b) The number of moving parts in an adsorption system is less than in vapour compression systems.
c) Solid sorption systems can be powered by low temperature heat sources or sustainable sources. Temperatures as low as 50^{oC} can be used as a heat source for solid sorption machines [15, 16].
d) Adsorption systems have poor heat transfer properties, due to high porosity of the material, which causes discontinuity in the solid structure.

The multi-bed adsorption system is named the continuous cycles system [17]. Several different technologies have been suggested by researchers for continuous adsorption cycles, including mass recovery adsorption refrigeration [13] and heat

recovery adsorption refrigeration [13, 18]. Figure 2.4 shows a summary of different technology used for a continuous adsorption cycle [19].

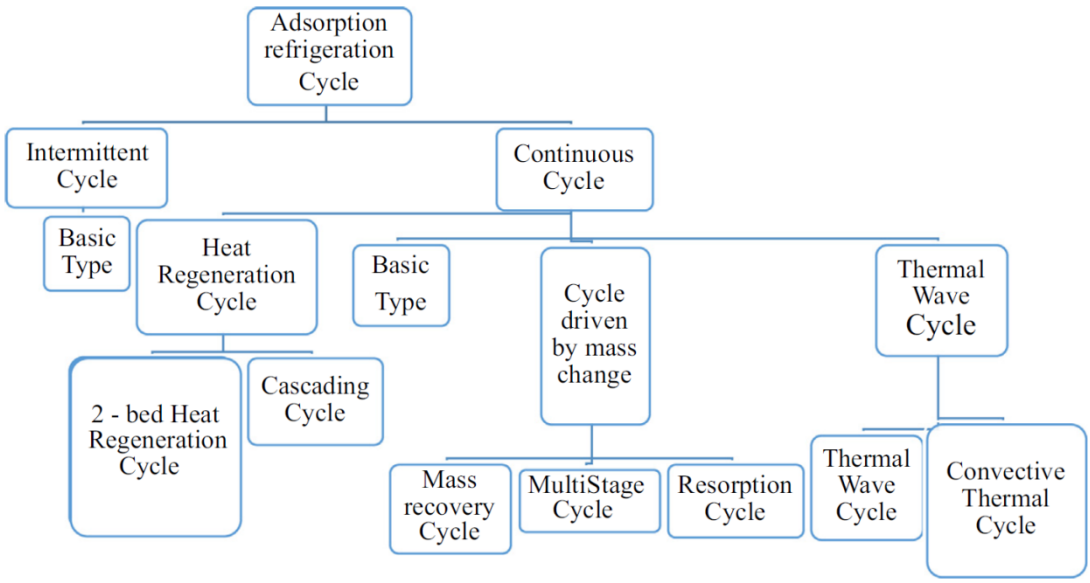

Figure 2.4. Different technologies suggested for the adsorption refrigeration cycle [19].

The heat recovery cycle usually works with two adsorption beds in order to improve the system's coefficient of refrigeration performance (COP). In the arrangement of the heat recovery cycle, while one bed is in adsorption mode, the other one is in desorption mode, therefore the heat which is extracted from the adsorption cycle will be used in the desorption cycle in order to improve overall COP and reduce external heat input. Figure 2.8 shows the heat recovery lines between two adsorption beds. Wang et al. [20] show that by implementing passive heat recovery on the silica gel / water adsorption beds, COP was improved by *38%* and *25%*, respectively, without having a significant effect on specific cooling capacity (SCP). Another way to improve the adsorption system's performance is mass recovery. Adsorption configuration with a mass recovery cycle has two adsorption beds, the same as the heat recovery adsorption system. Akahira et al. [18] aimed to improve SCP through the mass recovery process, but kept COP constant because they were using waste heat and low-grade energy. L.W. Wang et al.'s [21] study of the mass recovery effect on adsorption systems with an ctivated carbon / Aammonia pair showed that by increasing system adsorption capacity by *47.6%* via mass recovery at *-15^{o}C* of evaporating temperature, SCP and COP were improved by *48.6%* and *54.5%*, respectively. They also showed that by decreasing evaporating temperature to *-30^{o}C*, mass recovery causes a *78%* improvement in adsorption capacity. Normally the heat

and mass recovery methods are used simultaneously in order to increase the COP and SCP of the adsorption system [13]. Wang [22] showed that the heat and mass recovery in a double-bed adsorption system, compared to a single adsorption bed system, increased COP by *25%* and *10%*, respectively. In a subsequent study, Wang showed that the COP for a basic double-bed adsorption system with 100^oC driving temperature and 6^oC evaporating temperature is *0.39*, and that by adding the effect of heat and mass recovery into the system, the COP was improved by *30%*, reaching *0.51*.

As mentioned previously, the porous nature of the adsorbent results in weak heat and mass transfer through the adsorption bed, therefore another way to improve the performance of the adsorption machine is to enhance the speed of the heat and mass transfer through the bed during the adsorption / desorption processes. Improving the thermo-physical properties of the adsorbent in the presence of the adsorbate, and optimization of the adsorption bed design, are key elements in enhancing heat and mass transfer through the adsorption machine.

2.3. Solid sorption application

Over the years, many researchers have designed and developed various adsorption machines for heat pump, air conditioning and ice-making applications, by employing different heat sources such as solar energy, waste heat or direct gas fires. This section will review some of the suggested adsorption machines for different applications.

- For ice making applications in remote areas or off-grid places, used for vaccine or food preservation. Solar ice making machines are categorised based on using a solar collector, flat plate collector [23, 24] or compound parabolic collector [25]. Figure 2.5 shows a solid sorption machine for ice making and vaccine preservation with a flat solar collector [23]. The pair used was activated carbon / methanol.
- Figure 2.6 shows an engine waste heat-driven solid sorption machine designed by Wanget al. [26] for the purpose of food preservation in a fishing boat.

- Figure 2.7 shows the solid sorption machine designed at Shanghai Jiao Tong University [27] to produce chilled water for air conditioning purposes. A silica-gel / water pair, with adopted mass recovery, was used to accommodate low-range driving temperatures, in the range of 75^oC to 80^oC. Driven heat was provided from hot water stored from a solar collector, which was categorised as a low-grade energy source. As a result, they achieved a *9kW* cooling capacity with a COP of *0.5*, while the driving and evaporating temperatures were set at 80^oC and 13^oC, respectively.
- Figure 2.8 shows the engine waste heat-driven solid sorption machine developed at the University of Warwick [13] for the purposes of mobile air conditioning. The target COP and cooling capacity were *0.24* and *1.2 kW*, respectively, with a driving temperature of 90^oC. The COP and cooling capacity achieved, with mass recovery, were *1.6 kW* and *0.22*, respectively. The results show that the archived cooling performance was *33%* more than the targeted value, while because of a lack of cycle time optimization for each condition, the archived COP was *8%* less than the targeted value.
- Figure 2.9 shows the domestic adsorption gas-fired heat pump which is under development at the University of Warwick by Critoph [28].

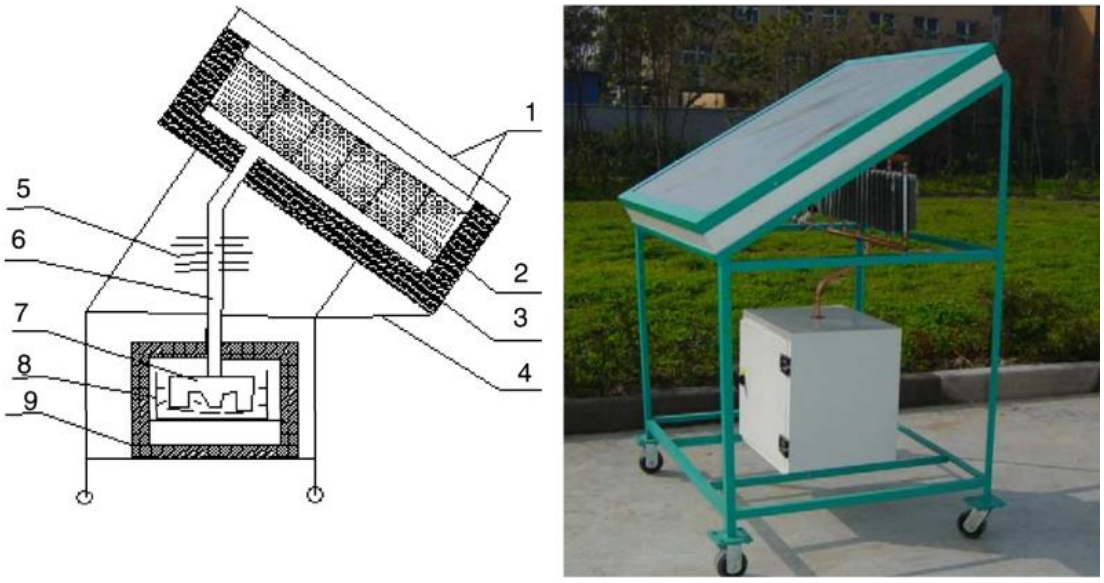

Figure 2.5. Solar ice maker without valves: (1) cover plate, (2) adsorbent bed, (3) insulation materials, (4) ice frame, (5) condenser, (6) connecting pipe, (7) evaporator, (8) water tank, (9) insulation box [23].

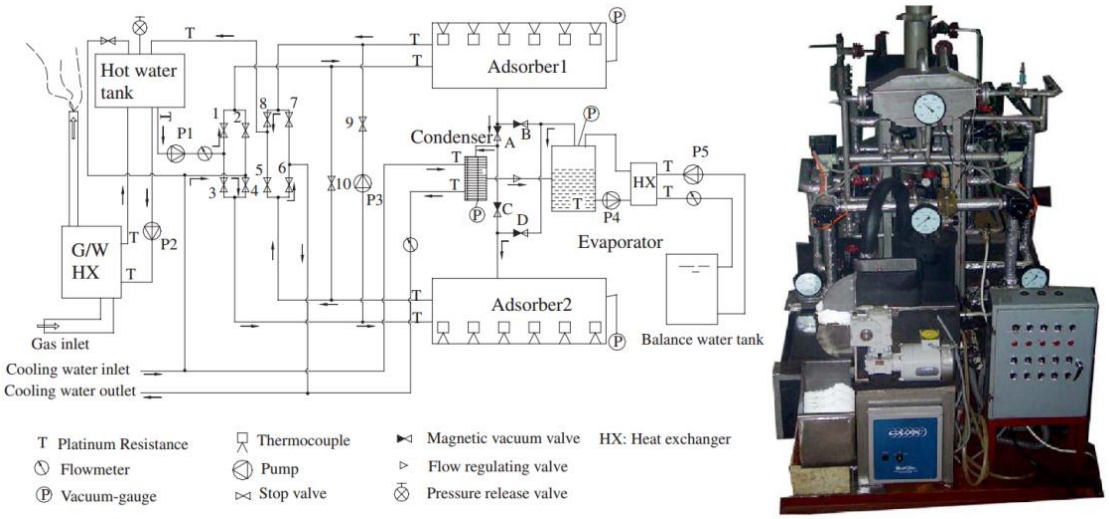

Figure 2.6. Ice making adsorption machine for a fishing boat using engine waste heat, with activated carbon / methanol pair [26].

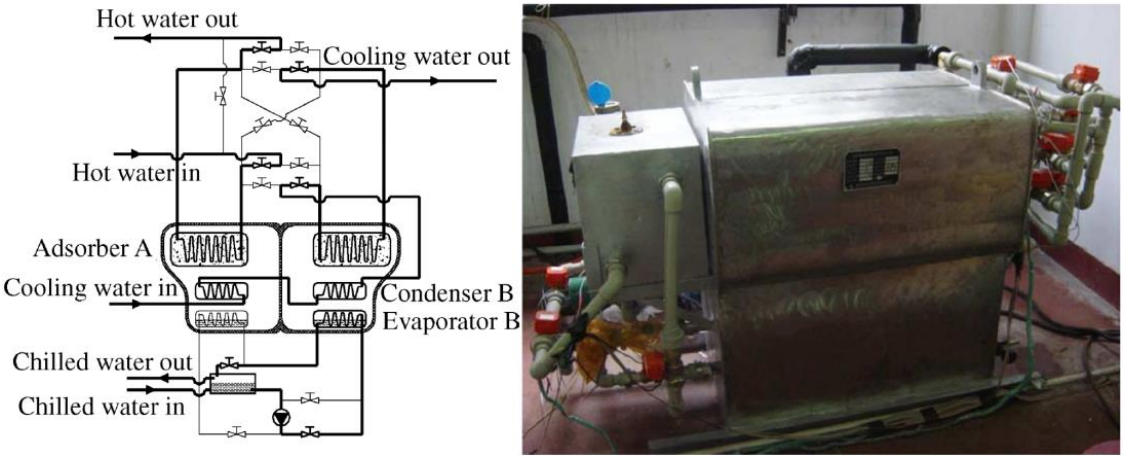

Figure 2.7. Adsorption machine for an air conditioning application with a silica gel / water pair [27].

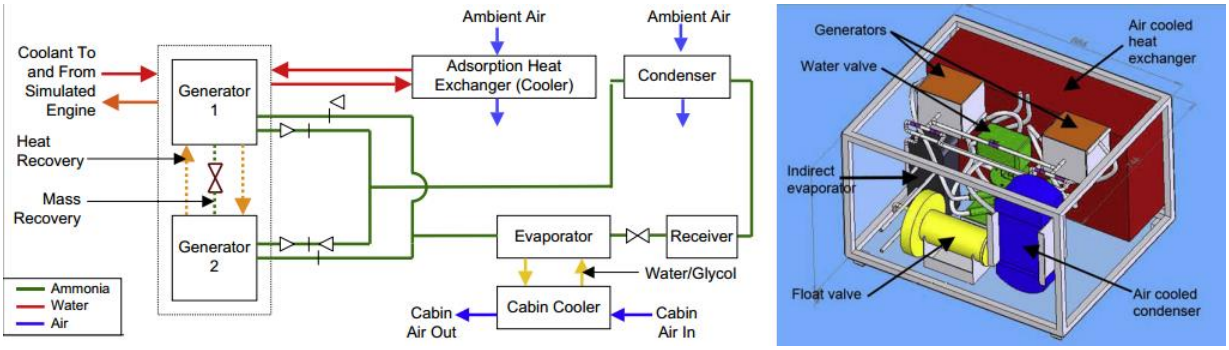

Figure 2.8. Mobile air conditioning system with combustion engine waste heat source, with an activated carbon / ammonia pair [13].

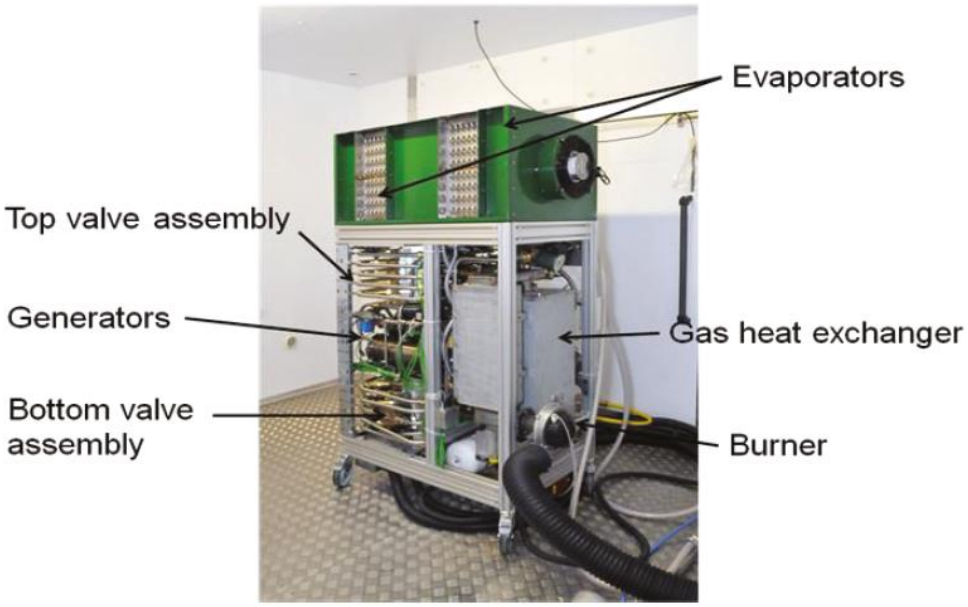

Figure 2.9. Prototype of a domestic adsorption gas-fired heat pump at the University of Warwick, with an activated carbon / ammonia pair [28].

2.4. Thermal generator

The heart of an adsorption system is a thermal generator. The thermal generator is a heat exchanger which transfers heat between the adsorbent and the heat transfer fluid. Therefore, the performance of the adsorption system will increase by increasing the heat transfer rate between the adsorbent and the heat transfer fluid, and by decreasing the generator's structural mass.

The key parameters of the thermal generator are the adsorbent, the physical appearance of the generator and the materials which are used in the body.

2.4.1. Adsorption pairs

Over the years many researchers have examined different adsorbent / adsorbate pairs for use in a solid sorption machine. Some examples of such pairs are activated carbon / ammonia, activated carbon / methanol, activated carbon / butane, activated carbon / CO_2, zeolite / water and silica gel / water.

The key parameters of adsorbate evaluation are enthalpy of vaporisation per unit volume of liquid, molecular polarity and molecular weight. Low molecular weight and high polarity increase the adsorption of the refrigerant over the adsorbent. The amount of heat extraction from the heat source during desorption depends on the

level of enthalpy of vaporisation; the higher the enthalpy of vaporisation, the more heat extraction from the heat source and the greater the reduction in waste of the sensible heating of the adsorbent [29].

Its small molecular weight, non-toxicity and high latent heat make water a good adsorbate. Therefore water is often used as an adsorbate in adsorption machines, in conjunction with zeolite [30] or silica gel [27]. The adsorption heat of a zeolite / water pair is about *3300–4200 kJ.kg^{-1}*, in comparison to *2500 kJ.kg^{-1}* for a silica gel / water pair. The desorption process needs a higher temperature. The silica gel / water pair normally uses low-grade heat sources in the range of *50^{o}C* to *150^{o}C*. A silica gel / water pair does not perform well with low- and middle-range heat sources; evaporation temperatures and the performance of the pair will increase by increasing the heat source temperature above *200^{o}C* [31]. On the other hand, water has certain disadvantages, such as that it is difficult to reach to its freezing temperature in the ice making application, as well as thermal generator sub-atmospheric working pressure and low vapour pressure. To compensate, the COP the cycle time should be increased; longer cycle time leads to system SCP reduction [31]. Compared to water, ammonia has a lower molecular weight and half the latent heat, but it has a higher vapour pressure, which prevents mass transfer limitations and could be used for cooling the system to *-40^{o}C*. As well as these advantages of ammonia, it has some disadvantages, such as toxicity, and non-compatibility with copper and copper alloys [32].

R723 is an azeotropic mixture made of *60%* ammonia (R717) and *40%* dimethyl ether (RE170). The molecular polarity of R723 is higher than that of ammonia molecules, while it has less latent heat. Therefore, the amount of heat energy required for the desorption process of an activated carbon / R723 pair will increase. Another consequence of this is a decrease in system performance.

2.4.2. Physical appearance

In a thermal generator, the adsorbent is located inside the heat exchanger, around the tube where the heating and cooling fluids pass through, or packed between the fins which are attached to those tubes. The heat exchanger can be either of the shell and tubes type, where the adsorbent either has direct contact with the heat transfer tubes or has contact with the fins which are attached to the tubes. Figure 2.10 shows the

shell and tube heat exchanger which Wang [22] used to pack the activated carbon inside while the heat transfer fluid passed through the tubes. In order to increase the heat transfer rate during the adsorption and desorption courses, aluminium fins were attached to the heat transfer fluid tubes. The adsorbent is in direct contact with the tubes and fins. The heat exchanger was later improved by Gui [33], with thinner tubes and shell walls, in order to decrease the generator body's thermal mass.

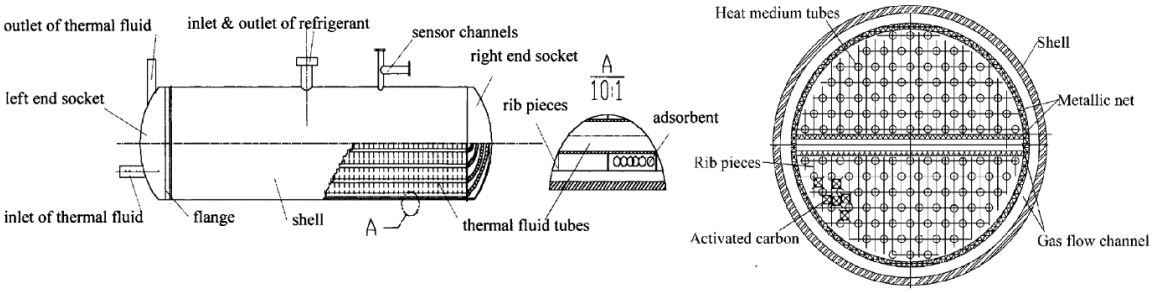

Figure 2.10. Thin wall shell and tube heat exchanger designed by Gui [33] and Wang [22].

The other type of heat exchanger is the plate heat exchanger designed by Tamainot-Telto [13]. Figure 2.11 shows that, in this design, the activated carbon was allocated in a *4 mm* gap, which was limited from top and bottom with stainless steel plates constructed from chemically etched shims, with *0.5 mm* square water flow channels on a *1 mm* pitch.

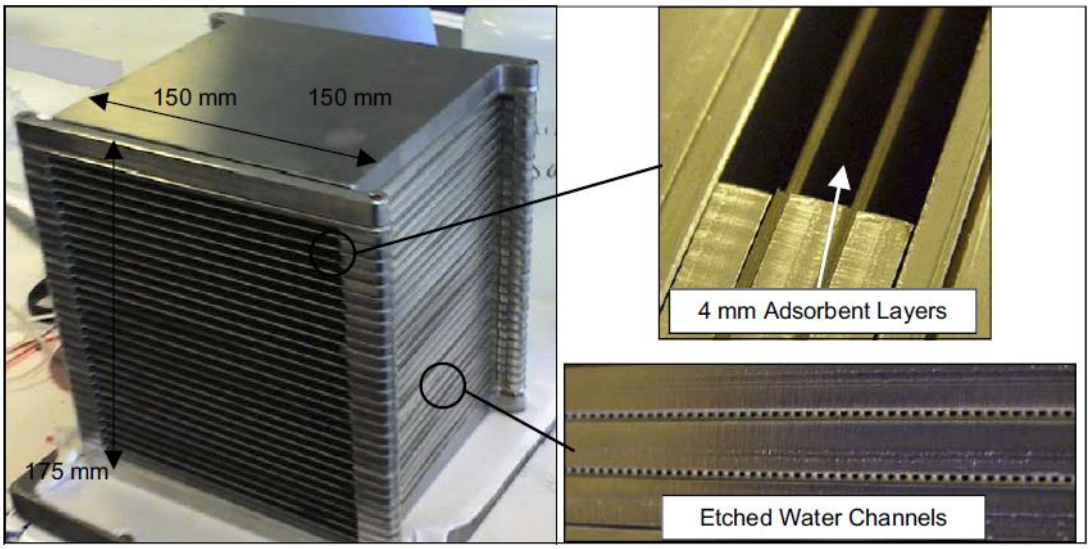

Figure 2.11, Plate heat exchanger designed by Tamainot-Telto [13].

For water and methanol as an adsorbent, it is possible to use material based on copper, which has higher thermal conductivity than stainless steel, but ammonia does not have this compatibility. Therefore, the compatibility of R723 with copper alloy

could bring new advantages, such as having an adsorbate similar to ammonia, with high vapour pressure, while also having copper's higher heat transfer rate advantages. Currently R723 is used in the market for refrigeration only via a vapour compression mechanism. Therefore, the new refrigerant could help improve existing systems and increase their efficiency, by coupling those systems with adsorption refrigeration.

References

[1]. http://unfccc.int/resource/docs/convkp/kpeng.html

[2]. UK progress towards GHG emissions reduction targets, Statistical release: Official Statistics Report Table 2, (19th March 2015) by Department of Energy & Climate Change,. https://www.gov.uk/government/publications/2010-to-2015-government-policy-greenhouse-gas-emissions/2010-to-2015-government-policy-greenhouse-gas-emissions#appendix-4-carbon-budgets

[3]. http://www.chrisbeales.net/environment/emissions_UK%20targets.html#p0

[4]. 2013 UK Greenhouse Gas Emissions, Final Figures and Statistical Release Table 2 (3th February 2015) by Department of Energy & Climate Change. https://www.gov.uk/government/publications/2010-to-2015-government-policy-greenhouse-gas-emissions/2010-to-2015-government-policy-greenhouse-gas-emissions#appendix-1-reducing-greenhouse-gas-emissions-from-agriculture

[5]. Energy Consumption in the UK (July 2016) by Department of Business, Energy & Industrial Strategy. https://www.gov.uk/government/statistics/energy-consumption-in-the-uk

[6]. R. Plank, J. Kuprianoff, Die Kleinkältemaschine. 2. Aufl., Springer-Verlag; 1960, Berlin, Göttingen, Heidelberg, Germany.

[7]. A.O. Dieng, R.Z. Wang, Literature review on solar adsorption technologies for ice-making and air-conditioning purposes and recent developments in solar technology. 2001, 5 (4): 313-342.

[8]. G. E. Hulse, Freight car refrigeration by an adsorption system employing silica gel. Refrigeration Engineering, 1929; 17.

[9]. E. B. Miller, The Development of SilicaGel, Refrigerating Engineering—The American Society of Refrigerating Engineers, 1929.

[10]. Z. Tamainot-Telto, S.J. Metcalf, R.E. Critoph, Y. Zhong, R. Thorpe, Carbon–ammonia pairs for adsorption refrigeration applications: ice making, air conditioning and heat pumping, In: International Journal of Refrigeration, 2009; 32(6):1212–1229.

[11]. P. Goyal, , P. Baredar , A. Mittal, A. R. Siddiqui, Adsorption refrigeration technology – An overview of theory and its solar energy applications. Renewable and Sustainable Energy Reviews, 2016; 53: 1389-1410.

[12]. M.A. Hadj Ammara, B. Benhaoua, M. Balghouthi, Simulation of tubular adsorber for adsorption refrigeration system powered by solar energy in sub-Sahara region of Algeria. Energy Conversion and Management, 2015; 106: 31-40.

[13]. Z. Tamainot-Telto, S.J. Metcalf, R.E .Critoph., Novel compact sorption generators for car air conditioning. In: Int J Refrig 2009; 32(4): 727–733.

[14]. Suzuki M., Application of adsorption cooling system to automobile. In: Proc. Of the symposium: solid sorption refrigeration; 1992.p. 1541–59.

[15]. Z. Tamainot-Telto, S.J. Metcalf, R.E. Critoph, Y. Zhong, R. Thorpe, Carbon–ammonia pairs for adsorption refrigeration applications: ice making, air conditioning and heat pumping, In: Int J Refrig, 2009; 32(6):1212–1229

[16]. R. E. Critoph, Carbon–ammonia systems-revious experience, current projects and challenges for the future. In: Proceedings of the international sorption and heat pump conference (ISHPC 2002), China, 2002.

[17]. H. Demir, M. Mobedi, and S. Ülkü, A review on adsorption heat pump: problems and solutions, In: Renewable and Sustainable Energy Reviews, 2008; 12(9): 2381-2403.

[18]. A. Akahira, , K.C. A. Alam, Y. Hamamoto, A. Akisawa, T. Kashiwagi, Experimental investigation of mass recovery adsorption refrigeration cycle, In: Int J Refrig, 2005; 28(4): 565–572.

[19]. R. Wang, L. Wang, J. Wu, Adsorption Refrigeration Technology: Theory and Application (1st Ed), Wiley (2014), ISBN: 978-1-118-19743-1.

[20]. X. Wang, H. T. Chua, K. C. Ng, Experimental investigation of silica gel–water adsorption chillers with and without a passive heat recovery scheme. In: Int. J. Refrig, 2005; 28(5): 756–765.

[21]. L.W. Wang, , R.Z. Wang, Z.S. Lu, C.J. Chen, J.Y. Wu, Comparison of the adsorption performance of compound adsorbent in a refrigeration cycle with and without mass recovery. In: Chemical Engineering Science, 2006; 61(11): 3761–3770.

[22]. R.Z. Wang, Performance improvement of adsorption cooling by heat and mass recovery operation. In: Int. J. Refrig, 2001; 24(7): 602–611.

[23]. M. Li,C.J. Sun, R.Z. Wang, W.D. Cai, Development of no valve solar ice maker, In: Applied Thermal Engineering, 2004; 24 (5-6): 865-872.

[24]. Z. Tamainot-Telto, R.E. Critoph, Adsorption refrigerator using monolithic carbon-ammonia pair, In: Int. J. Refrig, 1997; 20(2): 146–155.

[25]. Z. Tamainot-Telto, R.E. Critoph, Solar sorption refrigerator using a CPC collector, In: Renewable Energy, 1999; 16(1-4): 735-738.

[26]. D.C. Wang, J.Y. Wu, Influence of intermittent heat source on adsorption ice maker using waste heat, In: Energy Conversion and Management, 2005; 46 (6): 985-998.

[27]. Y. L. Liu, R. Z. Wang, Z. Z. Xia, Experimental study on a continuous adsorption water chiller with novel design. In: Int J Refrig, 2005;28(2):218–30.

[28]. Annett Kühn, Thermally driven heat pumps for heating and cooling. Chapter 3: Thermally driven heat pump for heating. Technical University of Berlin, 2013. ISBN 978-3-7983-2686-6 (print) and ISBN 978-3-7983-2596-8 (online).

[29]. R.E. Critoph, Evaluation of alternative refrigerant-adsorbent pairs for refrigeration cycles. In: Applied Thermal Engineering, 1996; 16(11): 891-900.

[30]. D.C. Wang, Z.Z. Xia, J.Y. Wu, Design and performance prediction of a novel zeolite–water adsorption air conditioner. In: Energy Conversion and Management, 2006; 47(5): 590–610.

[31]. L.W. Wang, R.Z. Wang, R.G. Oliveira, A review on adsorption working pairs for refrigeration. In: Renewable and Sustainable Energy Reviews, 2009; 13(3): 518–534.

[32]. R.E. Critoph, Y Zhong, Review of trends in solid sorption refrigeration and heat pumping technology. In: Proceedings of the Institution of Mechanical Engineers, Part E: Journal of Process Mechanical Engineering, 2005; 219: 285-300.

[33]. Y.B. Gui, R.Z. Wang, W. Wang, J.Y. Wu, Y.X. Xu, Performance modeling and testing on a heat-regenerative adsorptive reversible heat pump. In: Applied Thermal Engineering, 2002; 22(3): 309–320.

Chapter 3

Permeability of granular activated carbon packed bed

3.1. Introduction

One of the physical properties that has an effect on the design criteria of the thermal compressor in the adsorption refrigeration system is permeability. The granular activated carbon (GAC) which is packed in the thermal generator behaves like a porous material, as illustrated in Figure 3.1. For flow through porous material, it is important to be able to predict the flow rate obtainable from a given energy input, or to be able to predict the pressure drop necessary to achieve a specific flow rate [1].

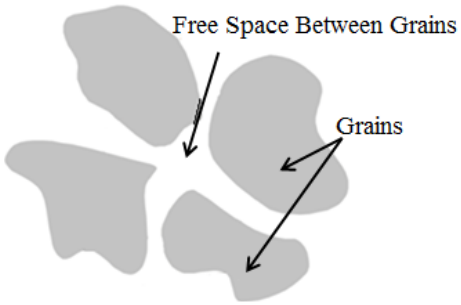

Figure 3.1. The carbon grains and the free space between them.

This chapter presents the correlation between the density of the GAC packed bed and the pressure drop, based on inert gas permeability tests. These correlations will show the effect of packing density on pressure drop, and the subsequent performance of the thermal generator.

3.2. Fluid flow in porous media

3.2.1. Permeability and Darcy's law

The French engineer Henry Darcy introduced permeability for the first time in 1856 [2], when he was working on the water supply of a city (Dijon, France). During his experiment with the set-up shown in Figure 3.2, he found that the volumetric flow rate *Q (LPM)* is directly proportional to head loss (pressure gradient) through the

medium cross section, and inversely proportional to the depth of the sand bed in the cylinder. This could be written as:

$$Q \propto \frac{S}{Z} \Delta P \tag{3.1}$$

This constant proportional term is named permeability, 'K_p'. From experiments with various fluids, Darcy's law was established:

$$Q = S \,.\, \frac{\Delta p}{\Delta z} \,.\, \frac{K_p}{\mu} \tag{3.2}$$

where Q is the water flow rate (*LPM*), S is the cross-section of the porous medium perpendicular to the flow direction *(m^2)*, K_p is the specific permeability or intrinsic permeability as a material property *(m^2)*, Z is the length of the porous media in the direction of flow *(m)*, Δp is the pressure difference along the porous medium *(Pa)*, and μ is the viscosity of the flowing fluid *(Pa.sec)*.

By rearranging Equation 3.2, we can find the unit of permeability, which is known in geophysics as *Darcy*. The permeability of the porous media is *1 Darcy*, if a fluid with *1 cP* viscosity flowing with a rate of *1 $cm^3.s^{-1}$* in a *1 cm^2* cross-section causes a pressure drop of *1 $atm.cm^{-1}$*:

$$K_p = \frac{\frac{\mu q}{S}}{\frac{\Delta P}{Z}} = \frac{[(cP)(cm^3/s)/cm^2]}{[atm/cm]} = 1Darcy \tag{3.3}$$

In SI-Units this could be written as:

$$\frac{[[Nsm^{-2}][m^3 s^{-1}]/m^2]}{[Nm^{-2}/m]} = [m^2] \qquad \text{and} \qquad 1\text{Darcy} = 0.987 \times 10^{-12}[m^2]$$

If we express the V_D as a Darcy velocity or superficial velocity $V_D = {}^{q}/_{S}$, the pressure gradiant in an isotropic medium would be:

$$-\nabla P = \frac{\mu}{K_p} v_D \tag{3.4}$$

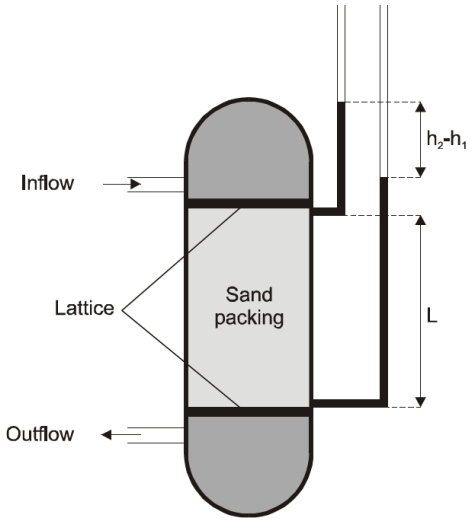

Figure 3.2. Schematic diagram of Darcy's experimental set-up.

In Darcy's flow model, the following assumptions were made [2], [3]:

- The flow velocity is very low. By this assumption, the *Reynold's* number is between *1* to*10* and the regime of this flow is called a creeping flow. Regarding the definition of the Darcy Reynold's number, which is illustrated in Equation 3.5, the inertia forces in the fluid are neglected in comparison to the viscous terms.

$$Re_D = \frac{\rho d v_D}{\mu} = \frac{Inertial\ Force}{Viscous\ Froce} \tag{3.5}$$

- A large surface area of the porous medium is exposed to the fluid flow; hence the viscous force is more than the inertia force in the fluid.

3.2.2. Darcy's law improvements

Based on the Reynold's number, it is possible to define four regimes for fluid flow in a porous medium [3]. Figure 3.3 illustrates the Ergun model and the different flow regimes by means of a plot of velocity verses pressure:

- The first region is creeping or Darcy flow, where $1 < Re < 10$. The viscosity of the fluid has more effect on the fluid flow through the porous media and the pressure gradient varies linearly with flow velocity.
- The second region is viscous-inertial flow,, where the Reynold's number range varies between *10* and *300*. The inertial force has a dominant effect on fluid flow. By increasing the Reynold's number toward the end of the range,

vortices and wake oscillations will develop in the flow profile renders Darcy's Law invalid.

- The third and final regime is called unsteady and chaotic flow, where the *Re* number is more than 300.

Figure 3.3 shows that Darcy's law successfully represents the linear behaviours between fluid velocity and pressure drop because of viscous flow, whilst, by entering into the transient region, it shows that a linear behaviour between pressure drop and fluid velocity is no longer valid.

Forchheimer [4] observed that local inertia forces such as direction changes and drag forces become notable in fluid through the porous medium, when flow velocity is increased. He added the inertia effect term to Darcy's equation, which leads to the Darcy-Forchheimer equation.

$$-\nabla P = \begin{Bmatrix} \frac{\mu}{K_p} v_D \\ ViscousEffect \end{Bmatrix} + \begin{Bmatrix} \beta \rho v_D^2 \\ Inercial\ Force\ Effect \end{Bmatrix} \qquad (3.6)$$

where ∇P is pressure gradient (Pa.m^{-1}), μ is viscosity of the flowing fluid *(Pa.s)*, K_p is specific permeability or intrinsic permeability as a material property *(m^2)*, V_D is Darcy velocity *($m.s^{-1}$)*, β is the Forchheimer coefficient *(m^{-1})*, and ρ is fluid density *($kg.m^{-3}$)*.

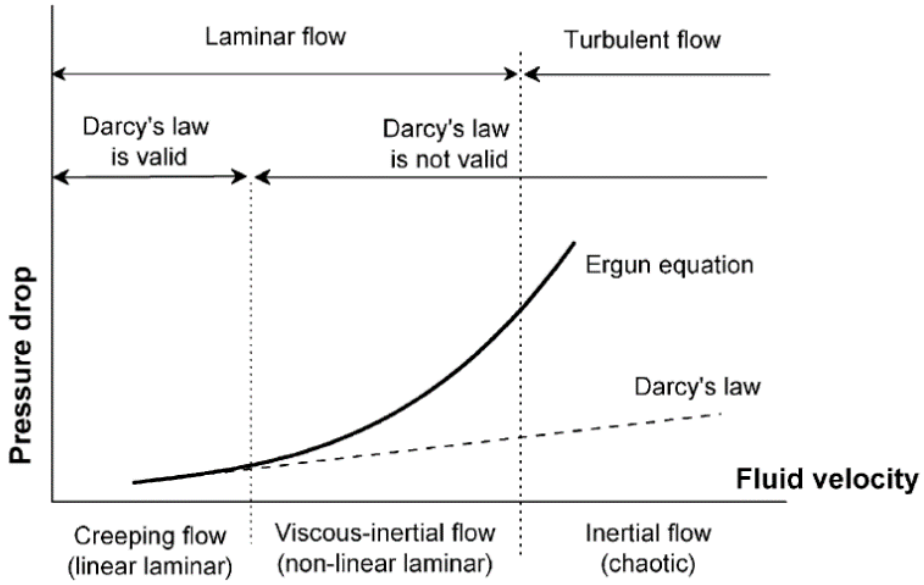

Figure 3.3. Characterization of different hydrodynamic regimes in fixed beds by means of pressure drop – flow rate behaviour [4].

The Forchheimer coefficient β is obtained from the best fit to the experimental data. Ergun [3], based on previous work with Orning [3] on fluid flow through packed columns and fluidized beds, suggested a new expression for the Forchheimer coefficient and named it the Ergun coefficient C_E, which depends on the flow regime.

$$\beta = \frac{C_E}{\sqrt{K_p}} \tag{3.7}$$

where K is intrinsic permeability.

$$-\nabla P = \frac{\mu}{K_p} v_D + \frac{C_E}{\sqrt{K_p}} \rho v_D^2 \tag{3.8}$$

For finding the value of the coefficients, the viscous effect section shows that we could rewrite the Ergun-Forchheimer equation into a linear form for both radial and axial flow [5,6].

$$-\frac{dP}{dz} = \frac{\mu}{K_{p-a}} v_a + \beta_a \rho v_a^2 \quad (axial\ flow) \tag{3.9}$$

$$-\frac{dP}{dr} = \frac{\mu}{K_{p-r}} v_r + \beta_r \rho v_r^2 \quad (radial\ flow) \tag{3.10}$$

where Z is sample length *(m)*, r is sample radius *(m)*, K_{p-a} and K_{p-r} are axial and radial permeability, respectively, *(m^2)*, V_a and V_r are axial and radial velocities *($m.s^{-1}$)*, and β_a and β_r are axial and radial Ergun coefficients, respectively *(m^{-1})*.

The gas which was used in the test was assumed as ideal, using the ideal gas theory:

$$P = \rho R T \tag{3.11}$$

where P is gas pressure *(Pa)*, ρ is gas density *($kg.m^{-3}$)*, T is the sample temperature *(K)* and R is the gas constant *($J.kg^{-1}.K^{-1}$)*.

If we assume the entire porous sample is a control volume and there is no mass accumulation, then the gas mass flow rates for axial and radial flows are:

$$m_a = \rho S v_a (\ axial) \quad and \quad m_r = 2\pi r \Delta z \rho v_r \ \ (radial) \tag{3.12}$$

where S is sample cross section *(m^2)*, r is sample radius *(m)*, and Δz is the total sample thickness m.

In the following assumptions, Equations 3.13 and 3.14 are derived from the Ergun-Forchheimer Equations 3.9 and 3.10 for axial and radial flow.

$$-PdP = \left(\frac{\mu RT}{K_{p-a}S} m_a + \beta_a \frac{RT}{S^2} m_a^2\right) dz \quad (aixial\ flow) \tag{3.13}$$

$$-PdP = \left(\frac{\mu RT}{2\pi r\, \Delta z K_{p-r}} m_r + \beta_r \frac{RT}{4\pi^2 r^2 \Delta z^2} m_r^2\right) dr \quad (radial\ flow) \tag{3.14}$$

The mathematical integration of Equations 3.13 and 3.14 leads to the following expressions:

$$\frac{(P_1^2 - P_2^2)S}{2RT\mu\, m_a \Delta z} = \frac{1}{K_{p-a}} + \beta_a \left(\frac{m_a}{\mu S}\right) \quad (axial\ flow) \tag{3.15}$$

$$\frac{(P_2^2 - P_1^2)\pi\Delta z}{2RT\mu\, m_{rc} \ln\left(\frac{R_2}{R_1}\right)} = \frac{1}{K_{p-rc}} + \beta_{rc} \left(\frac{\left(\frac{1}{R_1} - \frac{1}{R_2}\right) m_{rc}}{2\pi\Delta z \mu \ln\left(\frac{R_2}{R_1}\right)}\right) (radial - converging\ flow) \tag{3.16}$$

$$\frac{(P_1^2 - P_2^2)\pi\Delta z}{2RT\mu\, m_{rd} \ln\left(\frac{R_2}{R_1}\right)} = \frac{1}{K_{p-rd}} + \beta_{rd} \left(\frac{\left(\frac{1}{R_1} - \frac{1}{R_2}\right) m_{rd}}{2\pi\Delta z \mu \ln\left(\frac{R_2}{R_1}\right)}\right) (radial - diverging\ flow) \tag{3.17}$$

For the former expressions, we could use linear regression to find the given parameters in Equation 3.18. The expression of each of the terms in the linear equation is shown in Table 3.1.

$$W = \frac{1}{K} + \beta X \tag{3.18}$$

Flow configuration	Axial	Radial converging	Radial diverging
B	β_a	β_{rc}	β_{rd}
K	K_{p-a}	K_{p-rc}	K_{p-rd}
W	$\frac{(P_1^2 - P_2^2)S}{2RT\mu m_a \Delta z}$	$\frac{(P_2^2 - P_1^2)\pi\Delta z}{RT\mu m_{rc} \ln\left(\frac{R_2}{R_1}\right)}$	$\frac{(P_1^2 - P_2^2)\pi\Delta z}{RT\mu m_{rd} \ln\left(\frac{R_2}{R_1}\right)}$
X	$\left(\frac{m_a}{\mu S}\right)$	$\left(\frac{\left(\frac{1}{R_1} - \frac{1}{R_2}\right) m_{rc}}{2\pi\Delta z \mu \ln\left(\frac{R_2}{R_1}\right)}\right)$	$\left(\frac{\left(\frac{1}{R_1} - \frac{1}{R_2}\right) m_{rd}}{2\pi\Delta z \mu \ln\left(\frac{R_2}{R_1}\right)}\right)$

Table.3.1. Expression of β, K, W and X functions of gas flow configurations for linear fitting in linear regression [5].

Equation 3.19 shows the accuracy of estimated shape factor as a linear regression slope for Equation 3.18.

$$\beta_{accuracy} = \frac{Linear\ Regression\ Error}{\sqrt{\left(X - X_{average}\right)^2}} \tag{3.19}$$

Equation 3.20 shows the accuracy of estimated permeability as a reverse linear regression intercept for Equation 3.18.

$$K_{p-accuracy} = \sqrt{\left(\frac{Intercept_{estimated\ error}}{Intercept^2}\right)^2} \tag{3.20}$$

where,

$$Intercept_{estimated\ error} = \frac{Linear\ Regression\ Error}{\sqrt{\text{Fitting population}}} \times \sqrt{\frac{1 + Mean\ (X^2)}{Variance(X)}} \tag{3.21}$$

3.3. Permeability measurement set-up

The typical generator is a cylindrical tube that is filled with suitable GAC material. Therefore, the cylindrical test rigs were designed in order to determine the permeability of the GAC packed bed based on gas flow patterns, as shown in Figure 3.4. The test rig was designed to measure the pressure drop through the test sample, while measuring the inlet and outlet temperatures, when the gas flow rate varies from *1 LPM* to a maximum *4 LPM* in increments of *0.25 LPM*. Test rig details will be presented in sections 3.3.3, 3.3.4 and 3.3.6.

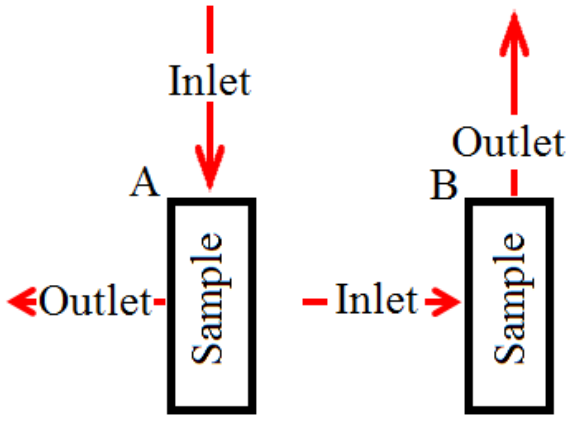

Figure 3.4. Basic concept for radial permeability test rig. A: Radial-Diverging. B: Radial-Converging.

3.3.1. Granular packed bed

The packed carbon samples were made from *208-C* (coconut shell base) granular activated carbon from the Chemviron Carbon Company, with a mesh size of *12 × 30* (1.5 mm × 0.6 mm, Appendix E). The same carbon grain size was used in making five different packing densities: *508 kg.m^{-3}*, *575.8 kg.m^{-3}*, *589.5 kg.m^{-3}*, *625.7 kg.m^{-3}* and *655.8 kg.m^{-3}*. For minimum density, the sample holder was filled with carbon particles, while it was vibrated at a constant rate without any external force on the particles. To achieve the higher densities, external force was applied to the carbon particles, after the sample holder vibrating process.

3.3.2. Sample holder fabrication

A first step in measuring the permeability of packed GAC is finding a way to hold the granular particles and pack them at the different densities. To force the flow to pass through the packed bed in a radial configuration, the granular particles were allocated in an annular configuration (Figure 3.5 A). The annular configuration has the advantage of passing the flow perpendicular to the packed bed.

Stainless-steel wire cloth mesh (Figure 3.5 B) was made into a circular profile in order to make an annular shape for holding the granular particles in two circular meshes. The inside mesh was made with a *19.05 mm ± 0.01 mm* outside diameter (Figure 3.5 C) and the outside mesh was made with a *50.8 mm ± 0.01 mm* inside diameter (Figure 3.5 D). The stainless-steel wire cloth mesh was provided by the G. BOPP Company. This particular mesh has a *0.425 mm* aperture size, *0.112 mm* wire diameter and *63%* open area.

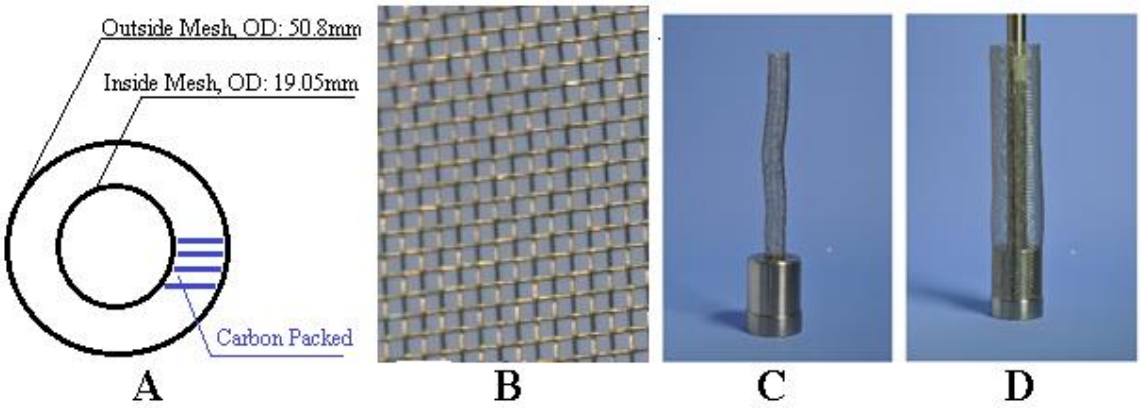

Figure 3.5. GAC radial sample holder. (A) top view of meshes arrangement with OD, (B) wire mesh general view with 63% open area, (C) side view of inner mesh with bottom extender, (D) side views of inner and outer stainless steel meshes; bottom extender and *¾"* steel tube support the inside mesh during the packing process, prevent any rupture and maintain sample rigidity.

3.3.3. Packed bed preparation

Two mechanisms were used to pack the granular carbon between the meshes. As a first step, a vibrator desk (Figures 3.6 A and 3.6 C) was used to achieve the minimum thickness at a constant surface area for a given amount of carbon, then a plunger was used to transfer the packing force from the press machine (Figure 3.6 B) to the packed surface. The pressing process was continued until the given packed thickness was reached, regarding the proposed bed density.

It is part of the nature of granular carbon particles to stick to the surface when the press machine applies the load on the plunger. The applied load varies between *3 kN* to *54 kN* for different densities. The attachment of particles causes non-uniform densities within the bed, especially at the top section of the packed bed, because of the unloading processes. To prevent non-uniform packing during the unloading process, a top extender (Figures 3.6 C and 3.7) was used. One side of the top extender was attached to the plunger while the other side was attached to the carbon surface; at the end of the packing processes the top extender will be locked in with a crocodile hose clip to the outer mesh.

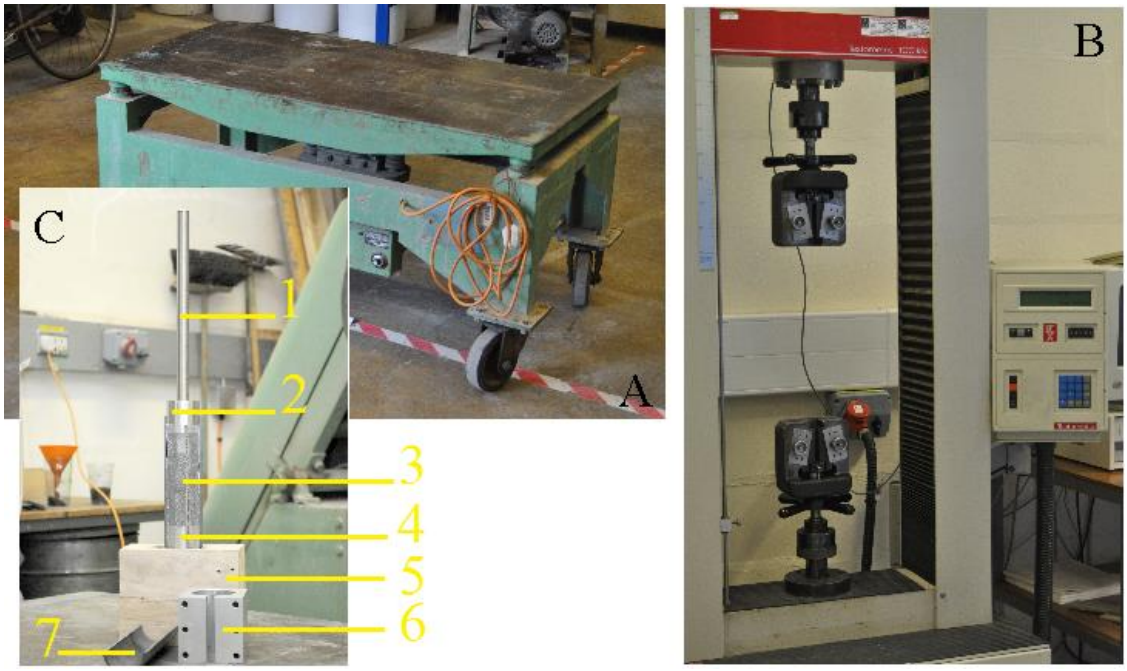

Figure 3.6. (A) vibrator desk, (B) press machine, (C) configuration of sample holder on vibrator desk, (C-1) *¾"* steel tube support for inner mesh, (C-2) top extender, (C-3) outer stainless steel mesh with 63% open area, (C-4) bottom extender, (C-5) wooden support block, (C-6) aluminium block to support the PVC pipe during the packing process, (C-6) PVC tube to support the outer mesh to prevent the mesh rupturing and to keep the rigidity of sample; the tube was bisected from the middle

for easy separation from the sample after the packing process to prevent any deformation and so as not to disturb the sample's rigidity.

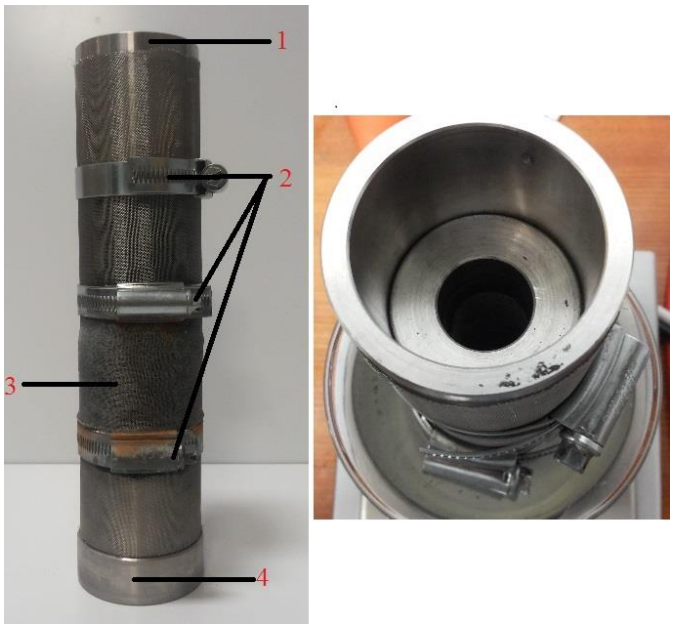

Figure 3.7. Left – (1) top extender, (2) crocodile hose clips, (3) carbon sample (4), bottom extender. Right – top extender with section for inner mesh and ¾" flow passage.

A special plunger and support was designed to apply the desired force to the granular carbon packing from the press machine, to generate different densities without any damage to the holder meshes. Damage to the mesh structure could cause measurement error:

- Mesh bending causes blockage in the flow and decreases the general open area. The reduction of the open area leads to higher pressure drop in the packed bed in comparison with an intact mesh;
- Mesh rupture causes a non-uniform air profile through the packed bed and changes the packing density by loss of carbon particles.

To prevent bending, rupture or the diameter changing of the inside and outside meshes, two supports were used. A steel tube with an *18.8 mm* outside diameter (Figure 3.8 A) was located inside the inner mesh. Two split PVC pipes with *50.8 mm* internal diameter (Figure 3.8 B) and four aluminium blocks (Figure 3.8 C) were located outside the outer mesh. The aluminium blocks have the same bore diameter size as the PVC outside diameter, to prevent deformation of the PVC pipe during packing.

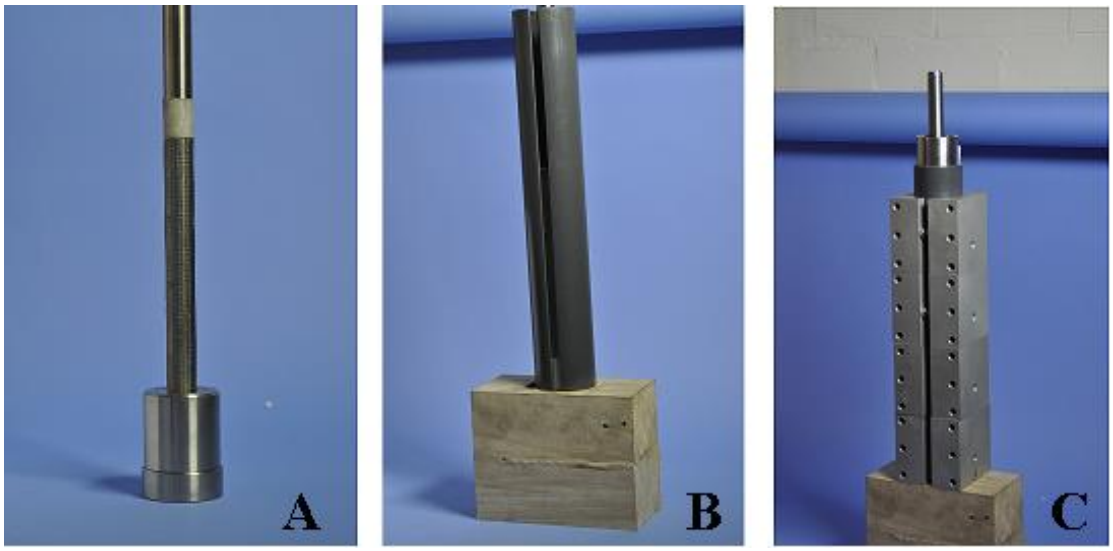

Figure 3.8. (A) Inside ¾" stainless steel tube support for inner mesh with inner mesh and bottom extender, (B) split PVC pipe to support outer mesh during the packing process and wooden support, (C) aluminium blocks to support the PVC pipe and location of top extender before packing process.

3.3.4. Packing location and rig overview

Based on the basic concept shown in Figure 3.4, Figure 3.9A shows that the packing sample was fixed between two flanges, and that it delivers the inert gas to the inner section of the annular mesh via a ¾" stainless-steel line (this tube will act as a collector in the converging flow pattern); the 3" stainless steel tube is used as an outside shell (Figure 3.9 B), and used as a collector in the diverging flow pattern. The details of assembly are mentioned in Appendix A-2.

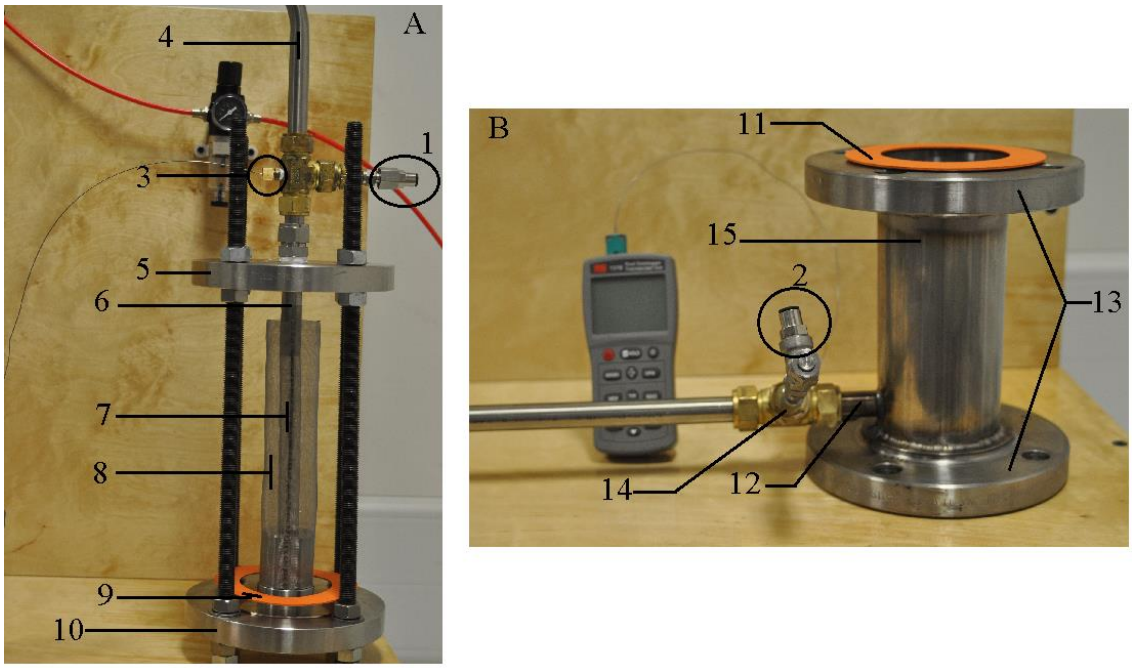

Figure 3.9. (A) GAC packed holder and how to install it in a radial test rig with connection to a ¾" line. (B) Outside shell or collector general view with ¾" connection line. (1) Pressure *8 mm* push fit

connection, (2) pressure *8 mm* push fit connection, (3) thermocouple *1/8"* stainless-steel compression fitting, (4) *¾"* stainless-steel tube line, (5) top raised faced modified ANSI B 16.5 Class 150 blank flange, (6) supplier and collector *¾"* stainless-steel line for inner mesh, (7) inner stainless-steel mesh, (8) outer stainless-steel mesh, (9) bottom sealing gasket, (10) bottom raised faced modified ANSI B 16.5 Class 150 blank flange, (11) top sealing gasket, (12) *¾"* stainless steel tube line, (13) outside shell raised faced flanges ANSI B 16.5 Class 150 lap joint flanges, (14) thermocouple *1/8"* stainless-steel compression fitting, (15) *3"* stainless-steel seam welded pipe with schedule10 for outside shell.

3.3.5. Measuring instrument

Three major parameters were measured: flow rate, pressure drop and temperature. The flow rate was adjusted by a rotameter at the rig entrance (Figure 3.9-A-4). Pressure drop across the packed bed was measured using a differential manometer which was connected to the pressure sockets (Figure 3.9-A-1 and 3.9-B-2). Inert gas temperature was measured at the inlet and outlet of the packed sample (Figure 3.9-A-3 and 3.9-B-14).

3.3.5.1. Pressure drop

For measuring the pressure drop between the inlet and outlet of the packed bed, a handhold deferential manometer from Digitron Instrumentation Ltd was used. The differential manometer model was a *2020P* and its operating range is *0.00* to *25.00 mbar*. Table 3.2 illustrates the instrument's accuracy for the two temperature ranges .

Temperature Range	Measuring Accuracy
$+20^oC$ to $+30^oC$	± *0.10%* reading digit
-10^oC to $+50^oC$	± *0.15%* reading digit

Table 3.2. Handhold digital deferential manometer measuring accuracy for each temperature range.

3.3.5.2. Temperature

K type thermocouples from the TC Direct Company were used to measure the temperature in the test rig. The thermocouple body material is a *310* stainless-steel sheath with a *1 mm* diameter, mineral insulation and miniature flat pin plug. The thermocouples were provided by the TC Direct Company.

A digital thermometer, provided by the RS Company, was used for temperature reading purposes. The measurement accuracy of the instrument was $\pm 0.5^oC$ and its display resolution was 0.1^oC.

3.3.5.3. Flow rate

The flow rate was measured at the inlet of the test rig with a rotameter provided by Key Instruments Ltd. The instrument's measuring range is *0.1 LPM* to *10 LPM* in increments of *0.25 LPM* and an accuracy of *±4%* of Full Scale.

The rotameter was calibrated for air at standard pressure (*1 bar*) and standard temperature (20^oC). Equation 3.19 shows that by measuring the temperature and pressure for air and argon during the test, the flow rate correction factor was derived by dividing the air density at standard situation to the air or any other gas densities at measuring point.

$$F = \sqrt{\frac{\rho_{Calibrated\ point}}{\rho_{Measured\ point}}} \tag{3.22}$$

3.3.6. Flow configuration and test procedure

The permeability test rig was designed to work like a wind tunnel. The test was carried with two different inert gases: argon and air. Both converging and diverging flow configurations were tested.

3.3.6.1. Converging flow

For the converging flow, the gas in the first place enters into the packed bed from the outer mesh side, and after passing through the mesh the particles will collect at the centre of the packing using the inner section, as illustrated in Figure 3.10.

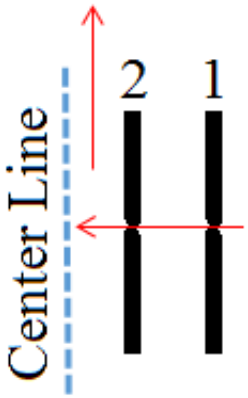

Figure 3.10. Converging flow pattern with centre line position. (1) Outer mesh. (2) Inner mesh.

Figure 3.11 shows that the gas enters the packed core located at the middle of the *3"* outside shell using the *¾"* line (Figure 3.11-right) connected to the outside shell, then the inert gas, after passing through the outer mesh and packed bed, was collected by the *¾"* line (Figure 3.11-left). The *¾"* tube at the outlet was connected

to the mesh which previously formed the tube (Figure 3.9-A). Figure 3.11-right shows that after gas collection at the middle, the gas was discharge into the atmosphere. The pressure and temperature were measured at the outside shell inlet, and then at the top flange.

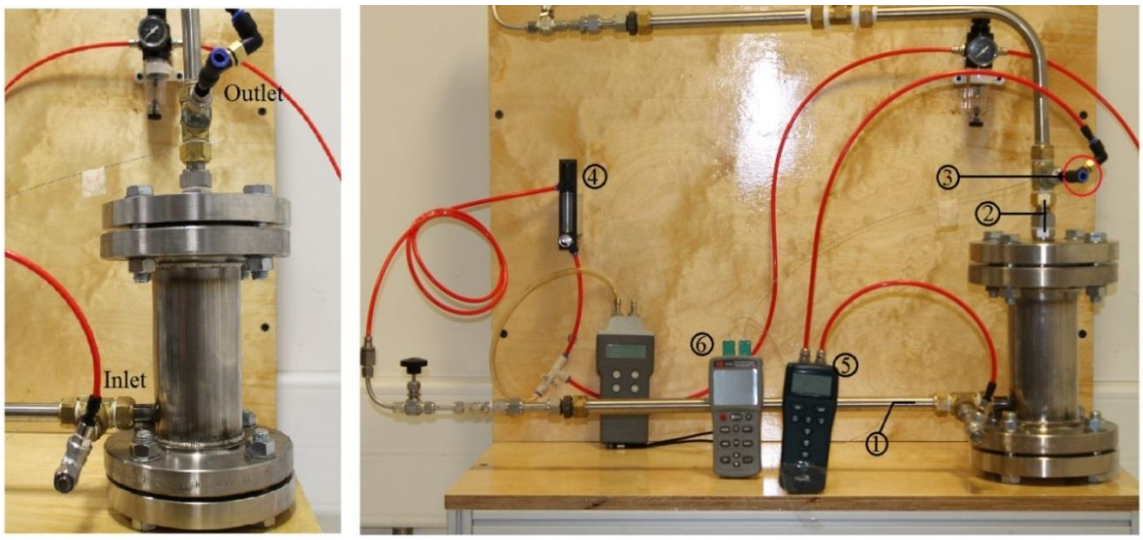

Figure 3.11. (Right) – Radial test rigs for converging flow arrangement. (Left) – (1) Supplier line (inlet) ¾" stainless steel tube, (2) collector line (outlet) ¾" stainless steel tube, (3) gas discharge manifold, (4) rotameter with flow control valve, (5) manometer, (6) digital thermometer.

3.3.6.2. Diverging flow

For diverging flow, the gas in the first place should enter the packed bed from the inner mesh side, and after passing through the particles will collect at the outside of the outer mesh, as illustrated in Figure 3.12.

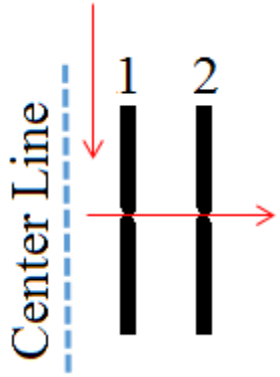

Figure 3.12. Diverging flow configuration with centre line position. (1) Outer mesh. (2) Inner mesh.

Figure 3.13 shows that the inert gas enters the packed core located at the middle of the *3"* outside shell by using the ¾" line (Figure 3.13-right). The inert gas, after passing through the packed bed, is collected by the *3"* outside shell and guided via

the ¾" line (Figure 3.13) to the shell. The gas was discharged into the atmosphere afterwards. The pressure and temperature were measured at the top flange inlet and then at the outside shell.

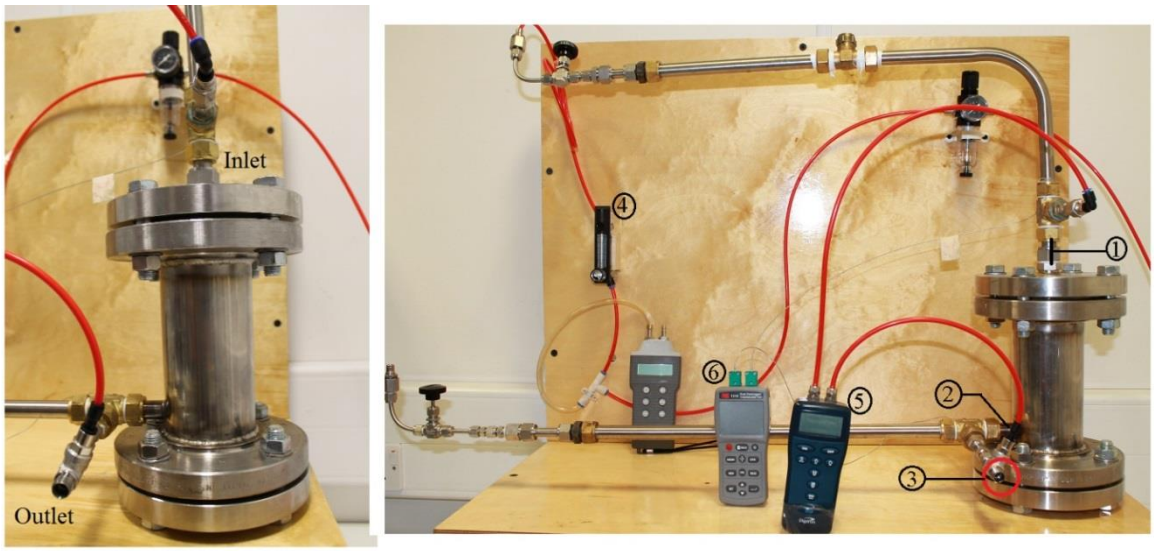

Figure 3.13. (Right) – radial test rigs for diverging flow arrangement. (Left) – (1) Supplier line (inlet) with ¾" stainless-steel tube, (2) collector line (outlet) ¾" stainless-steel tube, (3) gas discharge manifold, (4) rotameter with flow control valve, (5) manometer, (6) digital thermometer.

3.4. Experimental results and analysis

In order to measure the packed bed fluid flow parameters, 'K_p' (permeability) and 'β' (shape factor), gas flow rates were changed from *0.25 LPM* to *4.25 LPM*, and afterwards the pressure drop across the packed bed was measured. Prior to the main data collection, a preliminary test was carried out with an empty bed to establish the effect of the mesh and the whole rig on pressure drop. The pressure drop was marginal: therefore the effect of the mesh and rig itself was neglected.

Figures 3.14 and 3.15 show the pressure drop profile across the packed bed for densities *508 kg.m*$^{-3}$ and *575.8 kg.m*$^{-3}$: regardless of inert gas or flow pattern, the profiles are identical.

Figures 3.16 and 3.17 illustrates the linear regression based on Equation 3.18, to find the values of K (permeability) and β (shape factor) for the *508 kg.m*$^{-3}$ and *575.8 kg.m*$^{-3}$ densities. The values of W and X were calculated regarding their definition for each flow pattern at Table 3.1. All obtained parameters from the linear regression (Equation 3.18) are summarized in Table 3.3.

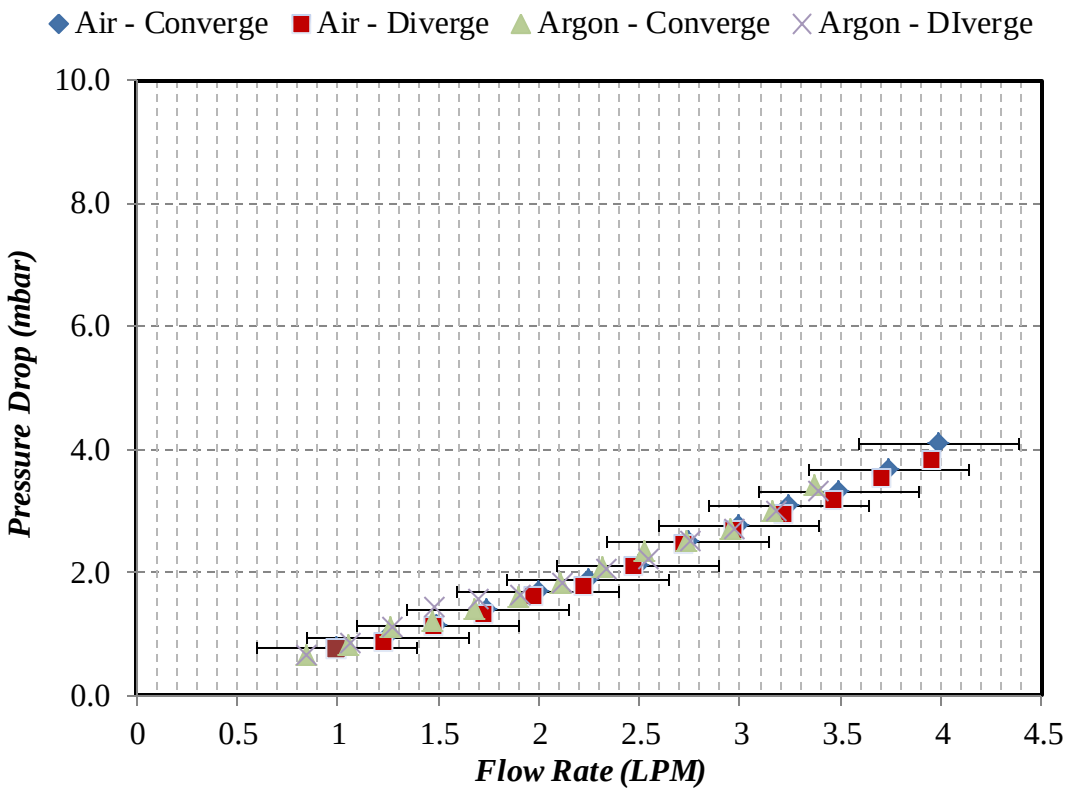

Figure 3.14. Pressure drop vs flow rate - density *508 kg.m*$^{-3}$.

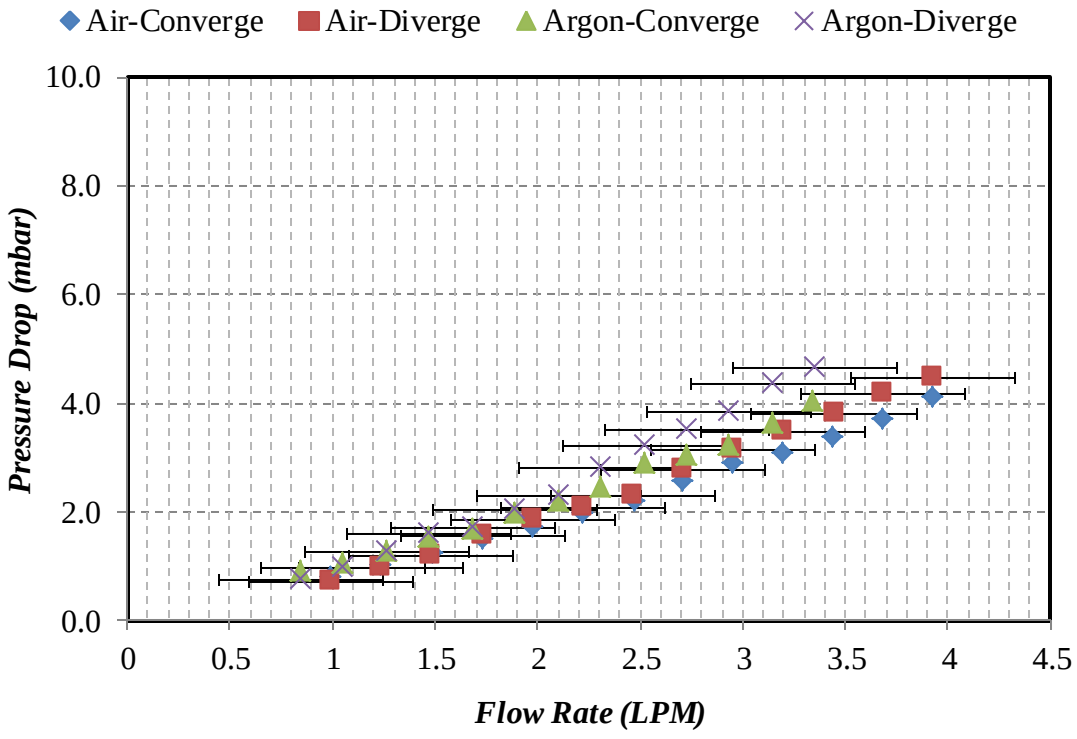

Figure 3.15. Pressure drop vs flow rate - density *575.8 kg.m*$^{-3}$.

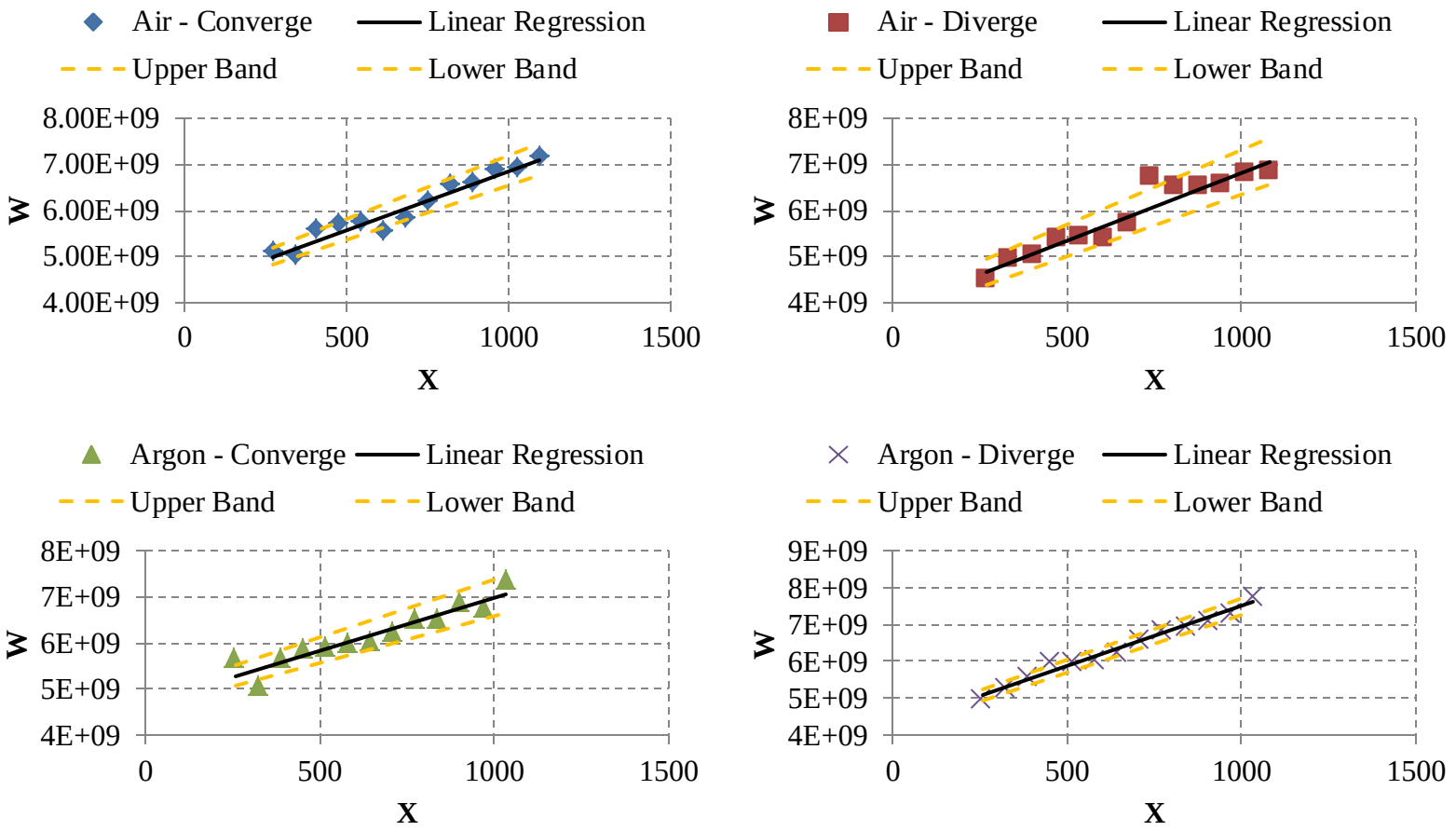

Figure 3.16. *W* vs *X* with linear regression and upper and lower bands - density *508 kg.m*$^{-3}$.

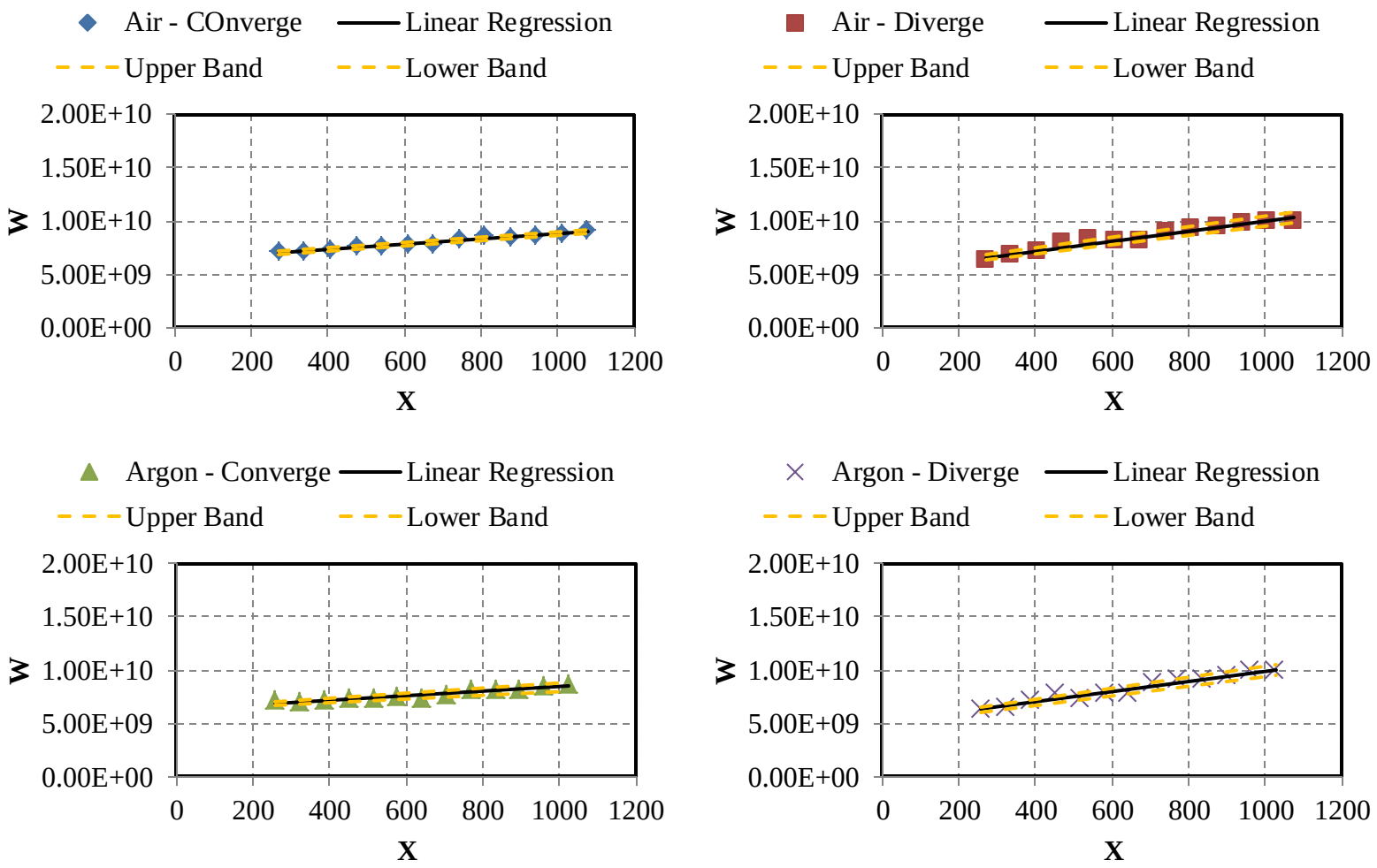

Figure 3.17. *W* vs *X* with linear regression and upper and lower bands - density *575.8* $kg.m^{-3}$.

By increasing the density, the open area between the packed grains was decreased. Therefore, by decreasing the open area when the gas flow passes through the packed bed, it faced more obstacles than at lower densities. Figures 3.15, 3.16 and 3.17 illustrate that by increasing the density by *11%* (from *589 kg.m^{-3}* to *655 kg.m^{-3}*), the pressure drop at the higher flow rate is three time higher than the pressure drop for the lower density (pressure drop changes from *12 mbar* to *36 mbar*).

Figures 3.18 and 3.19, showing pressure drop versus flow rate for the third and fourth densities (*589.5 kg.m^{-3}* and *625.7 kg.m^{-3}*), show that deviation starts between the air and argon pressure drops at the same flow rate; while the pressure drops for the first two densities are almost identical.

Figure 3.20 shows that for the higher density (*655 kg.m^{-3}*), deviation started from *1.5 LPM*. Figure 3.20 illustrates that for flow rates higher than *2 LPM*, the argon pressure drop test shows a *25%* increase, in comparison to air, while passing through the packed bed. Hence, it can be concluded that the argon gas, with *22%* higher viscosity (Table 3.3) than air, demonstrates a higher pressure drop due to the increase in viscous-inertial effect.

Density $kg.m^{-3}$	Flow Pattern	Air							Argon						
		Tg	$\mu \times 10^{-6}$	A $\times 10^{10}$	B $\times 10^{7}$	$\pm B_{accuracy} \times 10^{7}$	$K_p \times 10^{-10}$	$\pm K_{p\text{-}accuray} \times 10^{-10}$	Tg	$\mu \times 10^{-6}$	A $\times 10^{10}$	B $\times 10^{7}$	$\pm B_{accuracy} \times 10^{7}$	$K_p \times 10^{-10}$	$\pm K_{p\text{-}accuray} \times 10^{-10}$
		^{o}C	Pa s	m^{-2}	m^{-1}	m^{-1}	m^{2}	m^{2}	^{o}C	Pa s	m^{-2}	m^{-1}	m^{-1}	m^{2}	m^{2}
508.016	Converge	19.63	18.00	0.430	0.256	0.019	2.323	0.075	22.19	22.32	0.470	0.229	0.024	2.129	0.074
	Diverge	21.58	18.10	0.386	0.296	0.029	2.592	0.139	21.34	22.27	0.425	0.322	0.014	2.508	0.052
575.805	Converge	21.67	18.10	0.638	0.234	0.013	1.567	0.023	22.86	22.36	0.634	0.195	0.021	1.577	0.037
	Diverge	22.52	18.15	0.541	0.443	0.028	1.849	0.071	22.27	22.32	0.508	0.472	0.028	1.970	0.076
589.551	Converge	20.57	18.05	2.242	0.272	0.052	0.446	0.008	21.93	22.31	2.172	0.248	0.066	0.490	0.010
	Diverge	21.52	18.10	2.270	0.368	0.046	0.441	0.007	21.79	22.30	2.093	0.496	0.046	0.478	0.008
625.704	Converge	21.88	18.11	2.568	0.205	0.071	0.389	0.008	22.08	22.31	2.429	0.308	0.070	0.412	0.008
	Diverge	22.89	18.16	2.286	0.489	0.064	0.437	0.009	22.80	22.35	2.187	0.497	0.051	0.457	0.008
655.776	Converge	22.09	18.12	4.705	1.996	0.188	0.213	0.004	23.10	22.37	4.755	1.942	0.111	0.210	0.003
	Diverge	22.02	18.12	5.103	2.019	0.102	0.196	0.003	23.96	22.42	5.131	2.006	0.095	0.195	0.003

Table 3.3. Final results for permeability radial test. Table units: average gas temperature: Tg (^{o}C), gas viscosity: μ (Pa.s), slope of fitted line to the *W* vs *X*: A (m^{-2}), intercept of fitted line to *W* vs *X* which is called shape factor: *B* (m^{-1}), permeability: K_p (m^{2}).

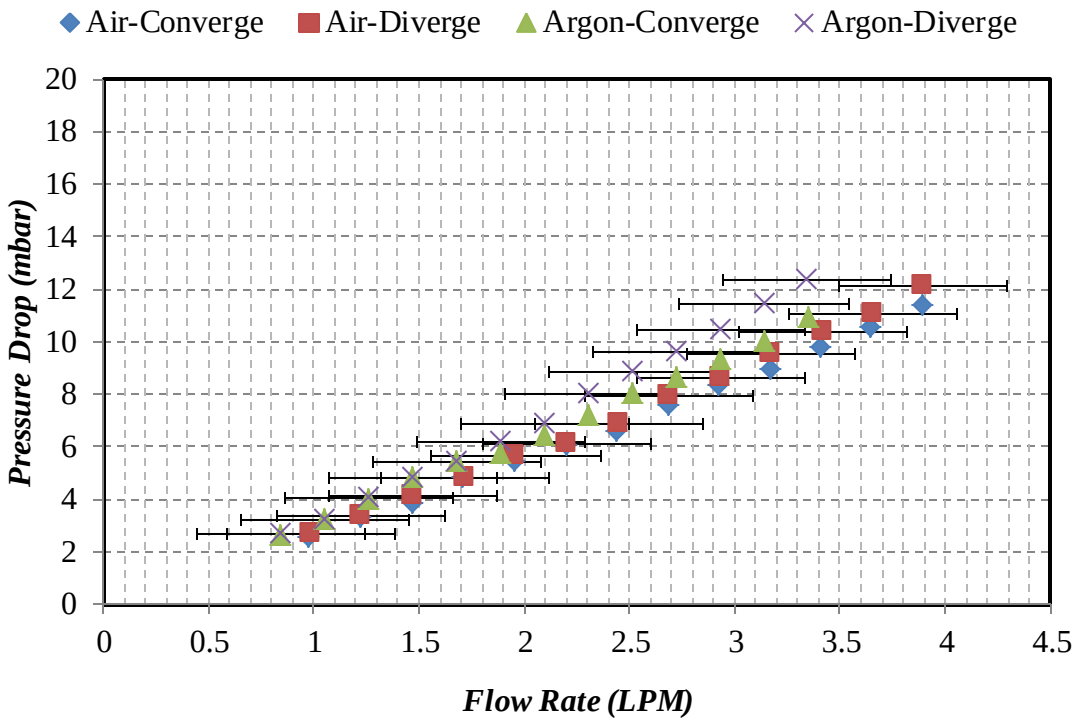

Figure 3.18. Pressure drop vs flow date for density of *589 kg.m^{-3}*.

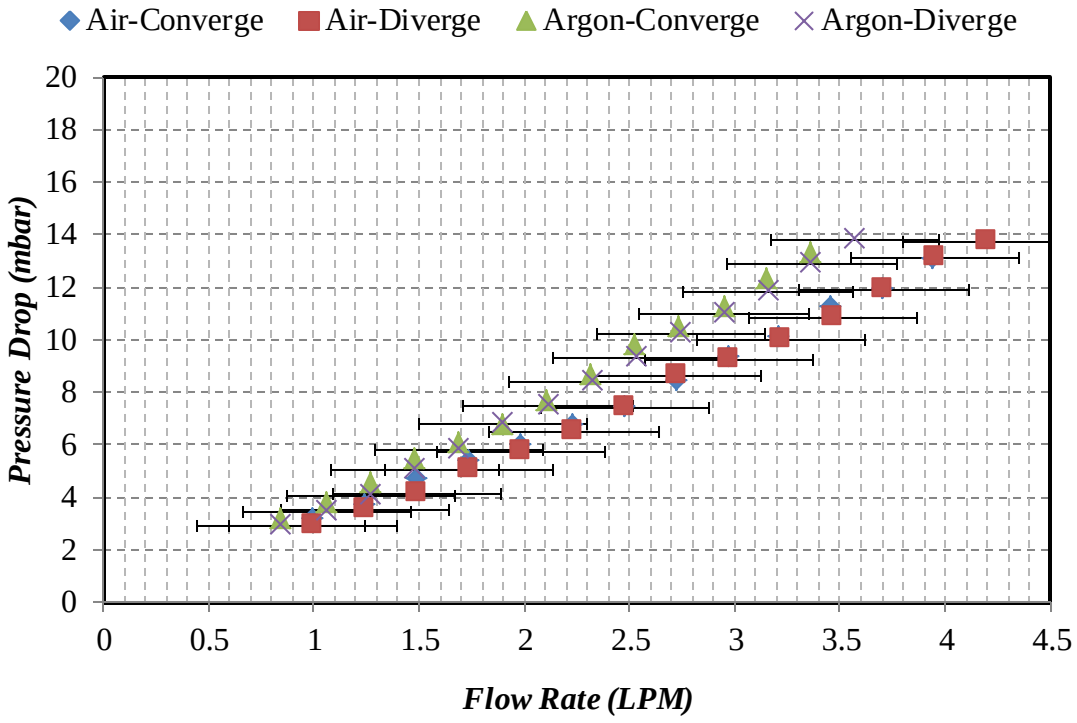

Figure 3.19 Pressure drop vs flow rate for density of *625 kg.m^{-3}*.

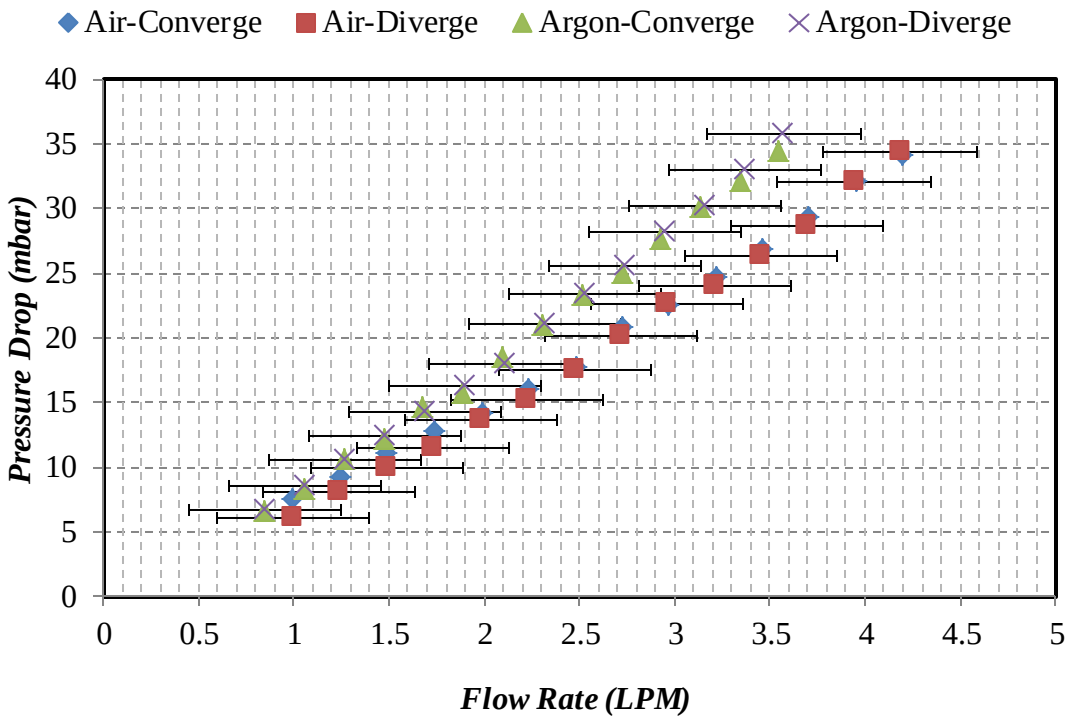

Figure 3.20. Pressure drop vs flow rate for density of *655 kg.m*$^{-3}$.

The permeability of the packed bed is a physical property; therefore the permeability value, regardless of gas or flow pattern, is identical for any specific density. By using the average values of the four tests which were performed (Table 3.3) for each flow pattern, regardless of packed bed density, the permeability value was determined. Figure 3.21 shows the average permeability deviation from the four tests conducted (air converging and diverging, argon converging and diverging) for the higher packed density (*655 kg.m*$^{-3}$). The results show that the maximum absolute difference is *4.4%*. Table 3.4 shows the summary of the deviation between average permeability and the four tests conducted for the other densities.

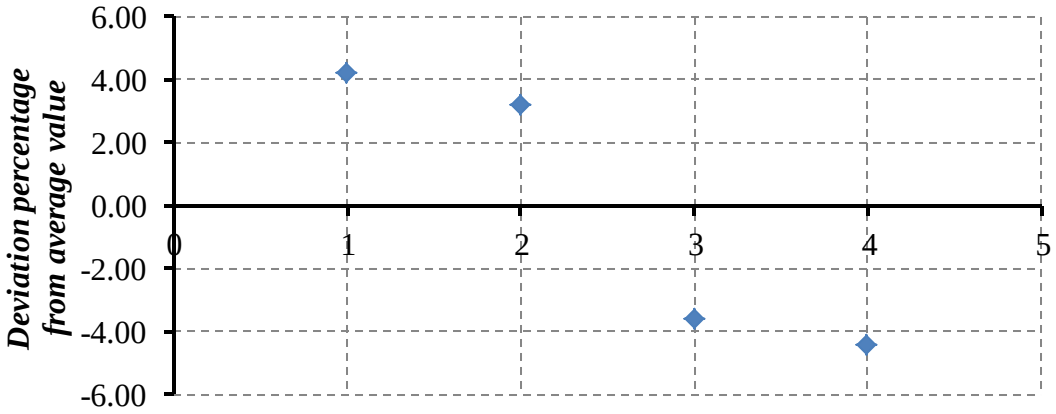

Figure 3.21. Permeability deviation percentage from average for the density of *655 kg.m*$^{-3}$.

		Packed Density ($kg.m^{-3}$)				
Flow Pattern	Gas	508.02	575.81	589.55	625.70	655.78
Converge	Air	-2.78	-11.08	-3.90	-8.88	4.24
	Argon	-12.18	-10.39	5.35	-2.98	3.21
Diverge	Air	7.86	5.83	-5.22	3.09	-3.61
	Argon	4.79	11.66	2.98	7.29	-4.44
Average '$K_p \times 10^{-10}$' (m^2)		2.388	1.741	0.464	0.424	0.204
Standard Deviation (STDV$\times 10^{-10}$)		0.206	0.201	0.024	0.030	0.009

Table 3.4. Deviation percentages of permeability result for each test in comparison with total average values, regardless of inert gas type and flow pattern for each density.

At lower densities, due to poor consolidation as a result of lower packing force, while the flow passes through the bed, the grains will start to move and vibrate in their place. This movement causes errors in the pressure drop measurement with a maximum of *12%* deviation from the average permeability values (Table 3.4).

Table 3.5 shows that for the same flow pattern (converging or diverging), the effect of gas type (gas properties) on shape factor is a maximum of *2.2%* at a packed bed density of *655 $kg.m^{-3}$*. Therefore, the value of shape factor was considered as an average value of air and argon tests together for each flow pattern. While the gas properties did not have a significant effect on shape factor, the flow configurations in terms of convergence and divergence patterns had a minimum difference of *14%* and a maximum of *52%*. Table 3.5 shows the shape factor for diverging pattern always remains higher than the converging pattern. The higher shape factor means a higher pressure drop across the packed bed. In fact, the higher the bed compaction is, the smaller the flow path cross-section will be.

Based on Bernoulli's theory, the pressure drop coefficient in a pipeline for expansion flow is higher than for contraction. In Table 3.5 is it noticeable that the diverging pattern, which is considered as an expansion flow, has a higher shape factor than the converging flow pattern (considered as a contraction flow). The higher shape factor, based on Equations 3.9 and 3.10, leads to an increased pressure drop cross the packed bed.

Density $kg.m^{-3}$	Flow Pattern	Air	Argon	Deviation percentage for same flow pattern	Average for each flow Pattern
		$\beta \times 10^7 m^{-1}$	$\beta \times 10^7 m^{-1}$		$\beta \times 10^7 m^{-1}$
508.016	Converge	0.256	0.249	2.86	0.252
	Diverge	0.296	0.312	4.96	0.304
Deviation percentage for different flow pattern		13.69	20.25		17.06
575.805	Converge	0.234	0.225	4.01	0.230
	Diverge	0.443	0.472	6.12	0.458
Deviation percentage for different flow pattern		47.13	52.28		49.79
589.551	Converge	0.272	0.258	5.64	0.265
	Diverge	0.398	0.426	6.57	0.412
Deviation percentage for different flow pattern		31.58	39.49		35.67
625.704	Converge	0.279	0.298	6.38	0.287
	Diverge	0.489	0.497	1.53	0.493
Deviation percentage for different flow pattern		43.75	40.07		41.90
655.776	Converge	1.996	1.942	2.77	1.969
	Diverge	2.019	2.006	0.66	2.012
Deviation percentage for different flow pattern		1.15	3.18		2.16

Table 3.5. Shape factor for different densities with effect of flow pattern and gas type.

3.5. Permeability exploitation

After reviewing all the experimental results, the next aim is to establish a correlation between the density of the granular packed bed, packing permeability and shape factor.

Figure 3.22 shows the permeability of the packed bed from Table 3.4, versus packed bed density. The linear regression method was applied to the experimental data. Table 3.6 shows the parameters of the polynomial regression based on Equation 3.23.

$$1/K_p = a\,\rho_{packed}{}^2 + b\,\rho_{packed} + c \qquad (3.23)$$

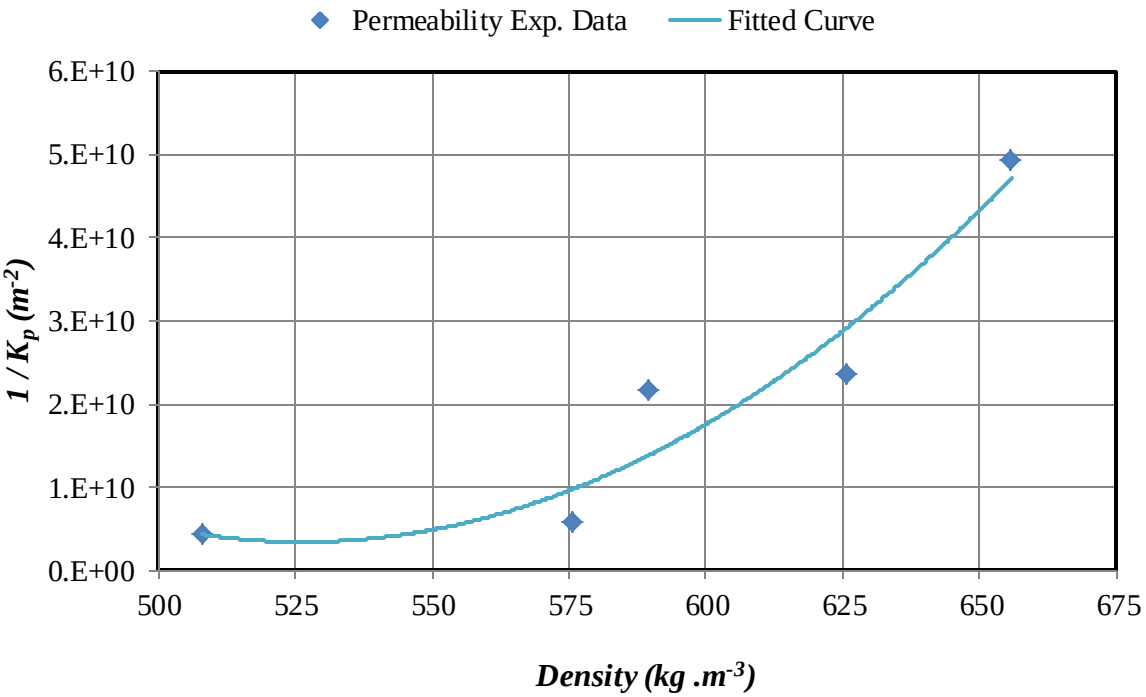

Figure 3.22. Permeability (m^2) vs density ($kg.m^{-3}$) of packed bed with polynomial regression

Regression Model	Parameters		
Polynomial	a × 10^6	b × 10^9	c × 10^{11}
	2.608	- 2.745	7.26

Table 3.6. Polynomial regression parameters to find the permeability based on density for the granular carbon packed bed.

Figure 3.23 shows the shape factor from Table 3.4 versus packed bed density. The polynomial regression was adopted to the experimental data for both converging and

diverging flow patterns. Table 3.7 shows the parameters of the polynomial regression based on Equation 3.24.

$$1/\beta = a\,\rho_{packed}{}^{2} + b\,\rho_{packed} + c \qquad (3.24)$$

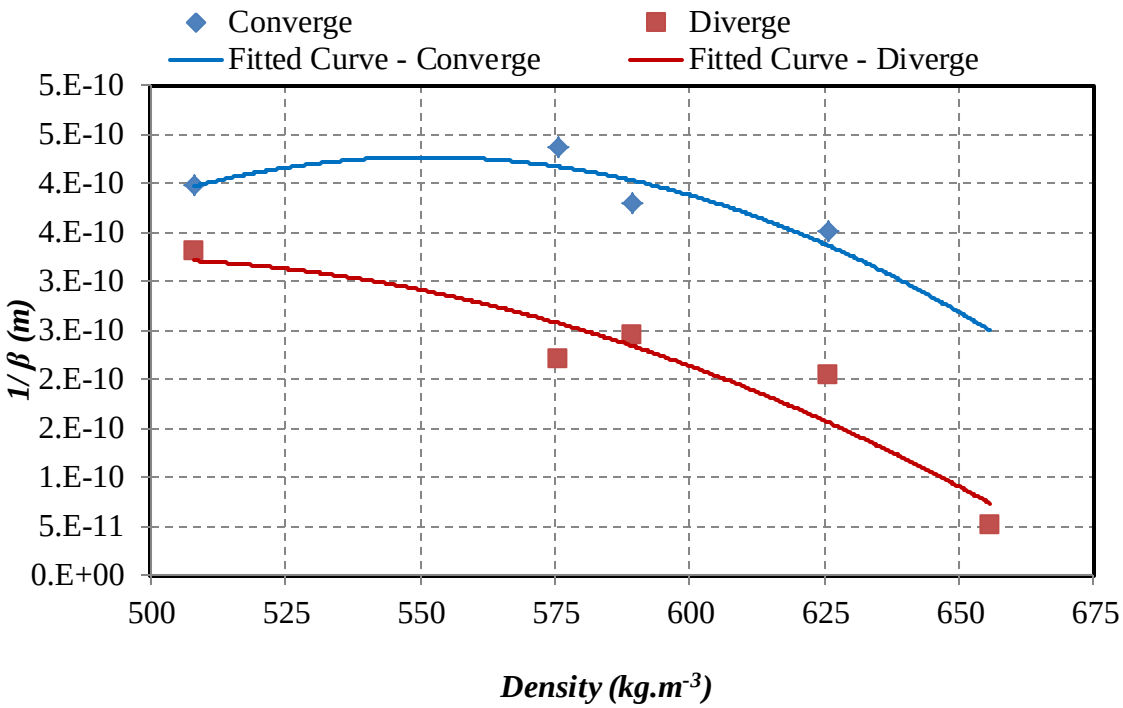

Figure 3.23. Shape factor (m^{-1}) vs density ($kg.m^{-3}$) of packed bed with polynomial regression for converging and diverging flow patterns

Regression Model	Flow Pattern	Parameters		
		a × 10^{-12}	b × 10^{-9}	c × 10^{-6}
Polynomial	Converge	- 16.156	- 17.804	- 4.478
	Diverge	- 9.151	8.973	-1.776

Table 3.7. Polynomial regression parameters to find the shape factor based on density for the granular carbon packed bed.

3.6. Conclusion

This chapter presents the experimental measurement of 'K_p' (permeability) and 'β' (shape factor) for the granular activated carbon packed bed. The density of the packed bed varied from *508 kg.m^{-3}* to *655.7 kg.m^{-3}*. Air and argon gases were used in order to obtain the physical properties of the packing.

Analysis of the results shows that the permeability of the packed bed is identical for each tested density, regardless of inert gas type or flow pattern. The permeability

determined from these experimental results shows a variation of $0.2\times 10^{-10}m^2$ to $2.4\times 10^{-10}m^2$. The results show the polynomial behaviour between packed bed density, permeability and shape factor. It was also concluded that 'β' (shape factor) for the same flow pattern is independent of gas type. Therefore, the shape factor was averaged for air and argon tests for both flow patterns investigated within this study. The results of the permeability tests show that the average shape factor for diverging flow is *30%* higher than for converging flow.

3.7. References

[1]. H. Darcy, 1856, Les Fontaines Publiques de la Ville de Dijon. Dalmont, Paris. 647 p. & atlas. ("The Public Fountains of the City of Dijon" is a lengthy work.")

[2]. M. Kiavany, Principles of Heat Transfer in Porous Media, 2nd ed., ISBN 0-387-94550-4, Springer-Verlag, New York, 1995.

[3]. Donald A. Nield, Adrian Bejan, Convection in Porous Media, 3nd ed., Springer Science+Business Media, Inc., ISBN 978-0-387-33431-8, New York, 2006.

[4]. P. Forchheimer, 1901, WasserbewegungdurchBoden. Zeitschrift des Vereines Deutscher Ingenieuer, 45 edition.

[5]. Z. Tamainot-Telto, R.E. Critoph, Thermo-physical properties of monolithic carbon, International Journal of Heat and Mass Transfer, 2000; 43(11): 2053-2058.

[6]. Z. Tamainot-Telto, R.E. Critoph, Monolithic carbon for sorption refrigeration and heat pump applications, Applied Thermal Engineering, 2001; 21(1): 37-52.

Chapter 4

Thermal conductivity of granular activated carbon

4.1. Introduction

In this chapter, the heat transfer characteristics of granular activated carbon (GAC) with different bed densities in the presence of air and R723 refrigerant are measured and analysed. The study provides a correlation which shows the effect of packing density on the heat transfer coefficients of the contact wall/packed carbon (h) and intrinsic thermal conductivity (λ). The measurement techniques were based on steady state and transient methods. A guarded thermal flow meter, in terms of steady state and time-response transient methods, was used for the air and GAC packed pair. The transient method was used for the GAC packed bed and refrigerant pair.

The chapter investigates the experimental and theoretical methods via a bilateral view on the heat transfer behaviour of the thermal generator for an adsorption refrigeration system and with regards to GAC packed bed density behaviour. It also proposes a measurement and analysis procedure which overcomes the complexity of the actual thermal behaviour of packed GAC in a thermal generator in the presence of refrigerant gas. The advantage of this model is in bringing the gas's dynamic behaviour in the desorption process in to account, instead of using the stagnant gas behaviour.

4.2. Literature review

Examples of the adsorbent used in the generator of adsorption refrigeration systems include activated carbon, silica gel and zeolite. Many researchers have studied their adsorbent thermal conductivity in the presence of a refrigerant; for instance, Critoph and Turner [1] verified the Zehner-Bauer model through experiments with various levels of adsorption with helium, neon and argon. The expanded model, when subjected to adsorption of ammonia, yielded a thermal conductivity of *0.165 W.m*$^{-}$

$^{1}.K^{-1}$, and showed very little variation with concentration. Tamainot-Telto and Critoph [2, 3] measured the thermal conductivity of monolithic carbon with a guarded-hot plate, using a steady state method. Tamainot-Telto and Critoph [4] also measured the thermal conductivity of the carbon-ammonia pair for adsorption refrigeration using a transient method. Wang et al. [5] measured the thermal conductivity of consolidated expanded natural graphite treated with sulphuric acid in the presence of air at atmospheric pressure, with a guarded heat flow meter, using a steady state method. Wang et. al [6] obtained the thermal conductivity of the consolidated bed, made of a combination of expanded natural graphite and granular activated carbon in the presence of air, within atmospheric pressure. Eun et al. [7, 8] studied the thermal conductivity of silica gel in various shapes, such as grain and a mixed shape, with graphite composite. Yanahi and Ino [9] studied the thermal properties of consolidated silica gel/water using the same method as Eun [7,8]. Guilleminot [10] studied the thermal conductivity of zeolite at different shapes.

In general, thermal conductivity has been measured using either steady state or unsteady (transient) methods. The steady state method generates a static temperature field inside the specimen and measures the thermal conductivity directly, while in the transient method the dynamic temperature field is generated inside the specimen and measures the thermal conductivity indirectly via thermal diffusivity.

The heat transfer phenomenon is complex, in both the thermal generator and packed bed. Figure 4.1 and Figure 4.2 illustrate some of the heat transfer mechanisms suggested by Argo and Smith [11], Yagi and Kunni [12], Calderbank and Progorski [13], and Flamant et al. [14], for packed and fluidized beds.

Table 4.1 provides a summary of heat transfer mechanisms, which reflect the complexity of heat transfer in a packed bed. This complexity shows the necessity of finding an experimental and analysis procedure able to reflect packed bed heat transfer behaviour in a thermal generator for an engineering application, without including all the complexity of the model.

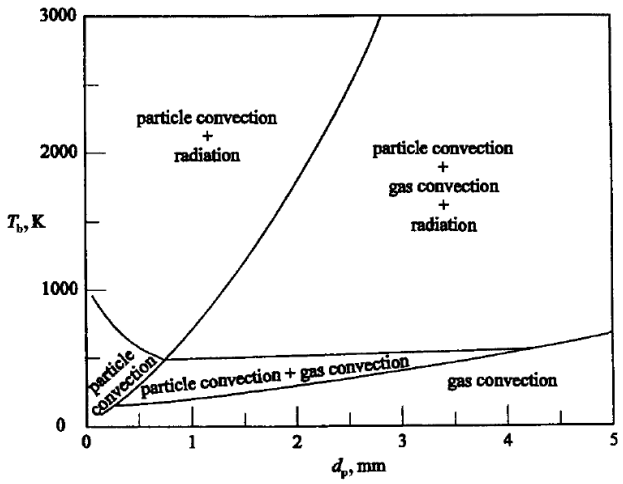

Figure 4.1. Heat transfer diagram for various governing modes of gas-solid fluidized beds by Flamant et al. [14].

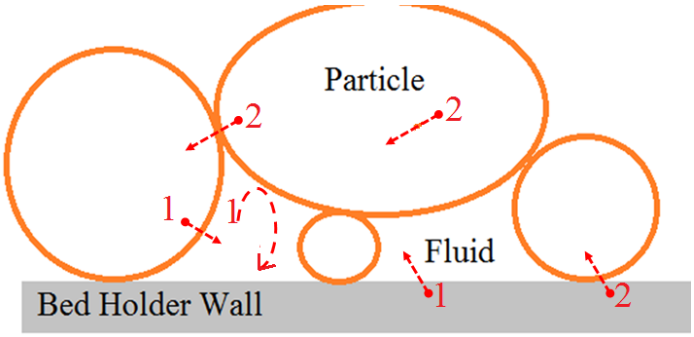

Figure 4.2. Heat transfer phenomena in the packed bed.

Heat Transfer Mechanism	***Governing Modes***
1- Convection	a. Particle – fluid
	b. Wall – fluid
	c. Fluid – fluid (fluid mixing)
2- Conduction	a. Through the particle
	b. Particle – particle
	c. Gas layer around the particle – particle
	d. Stagnant gas (gas – particle)
	e. Wall – particle
3- Radiation	a. Grain surface – grain surface
	b. Neighbouring voids (void – void)

Table 4.1. Heat transfer mechanisms in the thermal generator and packed bed.

These studies have explored the heat transfer mechanisms in a GAC packed bed. One of the heat transfer mechanisms which has dominated contributions to heat transfer through the granular bed in a high vacuum and at high temperatures is radiation [15]. The convection effect between particle and wall increases through the

desorption process, while it is possible to neglect the convective heat flow according to pore size [15]. The temperature gradient in the thermal generator, due to the desorption process, will cause system pressure to increase. Therefore, by increasing system pressure, the overall heat transfer effect will increase. The two conduction heat transfer mechanisms, particle-particle and particle surrounded gas layer-particle, act in parallel in the granular packed bed. The particle-particle and particle surrounded gas layer-particle mechanisms act in series with conduction through the particles. Therefore, both mechanisms can be observed in conduction through the particle mechanism [16]. The other two reaming conduction mechanisms, gas-particle and wall-particle, have only a small effect on heat transfer through the granular packed bed. Therefore it is possible to remove them from heat transfer modelling [17].

4.3. Steady state method

In the steady state method, the temperature filed is static, since the specimen should be kept in a steady situation for a long time; this method normally involves lengthy measurement times. The carbon sample is placed in between the flat plates and the heat flux used in the measurements travels through the sample.

In general, the steady state method could be divided into absolute and comparative methods. In absolute methods, the thermal properties can be calculated from the experimental results without any additional information; while in comparative methods, another probe should be set up in parallel with the packed bed during the experimental process [17]. A guarded-hot plate based on ASTM C177 or BS 874 standards [2, 3] is an absolute method to determine the thermal conductivity of the material from experimental results, without any additional information. A guarded heat flow meter based on ASTM E1530 or ASTM C518 standards [5, 6] is a comparative method, and supplies the ratio between the unknown thermal conductivity of the packed bed and the known reference calorimeter.

4.3.1. Theory and measurement method

To measure the thermal properties of a GAC packed bed, this study used a guarded thermal flow meter based on a comparative method. There are numerous manufacturers of guarded thermal flow meters; the Anter Instrument Corporation is an example, with its Anter Quickline-10 machine.

The steady state method, in comparative mode, uses the Fourier law of conduction [18] to define heat conduction through the packed bed or the solid material.

$$Q = -A\lambda \frac{\partial T}{\partial l} \tag{4.1}$$

where Q is the heat transfer rate, A is the cross-sectional area of the sample in the direction of heat flow (m^2), λ is thermal conductivity $(W.m^{-1}.K^{-1})$, T is the temperature (K) and δl is the conduction length in the direction of heat flow (m). The minus sign is to satisfy the second law of thermodynamics, in which heat flows from a higher temperature to a lower temperature reservoir [18]. Supposing that the conduction is one-dimensional, and uses the heat flux in a guarded thermal flow meter, the Fourier law could be rewritten as follows:

$$\dot{q} = -\lambda \frac{\partial T}{\partial l} \tag{4.2}$$

Using the analogy between the heat transfer and electrical resistance:

$$R_{Totalresistance} = \frac{\delta T / \delta l}{\dot{q}} \tag{4.3}$$

where $R_{Total\ Conduction}$ is total thermal resistance, which is a combination of contact (internal) resistance, reference resistance and sample resistance $(m^2.K.W^{-1})$, T is the temperature (K), δl is the conduction length in the direction of heat flow (m) and $\dot{q}$ is heat flux $(W.m^{-2})$. The reference and interfacial (contact) thermal resistances are obtained from the calibration process with a Quickline-10 machine, providing the material with known thermal conductivity.

Figure 4.3 shows the principle of the Anter Quickline-10 machine (the details of each section's materials are given in Appendix B-2). The instrument includes a heater, upper plate, lower plate, reference calorimeter and heat sink. The sample was placed between the upper and lower plates. The temperatures of the upper plate, lower plate and heat sink were measured by thermostats [6]. In the Anter Quickline-10TM machine, by a combination of Fourier with electrical resistance, thermal conductivity of the sample was estimated, which comes out as follows:

$$\lambda = \frac{d}{R_{Sample}} \tag{4.4}$$

where λ is thermal conductivity $(W.m^{-1}.K^{-1})$, d is sample thickness (m) and R_{Sample} is the thermal resistance of the sample $(m^2.K.W^{-1})$.

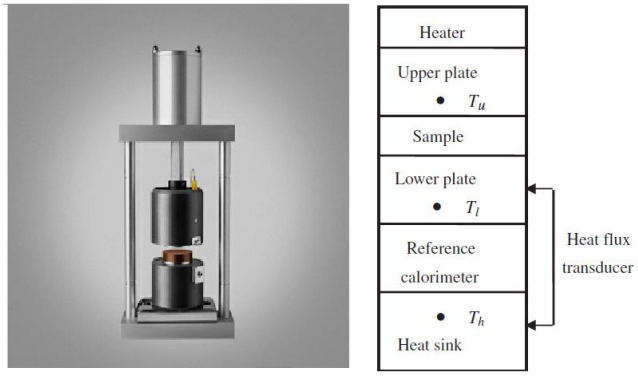

Figure 4.3. Schematic of Anter Quickline-10 machine, used to measure thermal conductivity using the steady state method.

$$R_{Sample} = \frac{d}{\lambda} = F \times \frac{(T_U - T_1)}{(T_1 - T_h)} - R_{internal} \tag{4.5}$$

where T_U, T_1 and T_h are the temperatures of the upper plate, lower plate and heat sink, respectively. F is reference thermal resistance $(m^2.K.W^{-1})$ and $R_{internal}$ is interfacial thermal resistance $(m^2.K.W^{-1})$. To determine reliable values for $R_{internal}$ and F in Equation 4.5, the aperture must be calibrated with three samples of known thermal conductivity.

The manufacturer estimates that the measurement accuracy of the Anter Quickline-10 machine varies between ± *3%* and *8%*. In order to obtain accurate thermal resistance readings using error propagation rules, it must be taken into account that the Anter Quickline-10TM machine software converts the voltage measured by the three thermistors in the upper plate, the lower plate and the heat sink to temperature at a constant rate of *7.045°C/V*. The resolution of the voltage meter is 1 *mV*, so the temperature resolution is *0.007°C*. The accuracy improves when the ratio between $R_{internal}$ and R_{Sample} is small. During the test the upper plate was set at *50°C* and the lower temperature at *10°C*. Due to the measurement accuracy effect, the upper, lower and heat sink temperatures were measured as *43.75°C*, *17.35°C* and *11.80°C*, respectively. By using the temperature resolution, measured temperatures, Equation 4.5 and error propagation rules for quotient and difference, it is possible to calculate the thermal resistance reading error as *0.2 %*.

$$T_u - T_l = (43.75 - 17.35) \pm \sqrt{0.007^2 + 0.007^2} = 26.40 \pm 0.01°C$$

$$T_l - T_h = (17.35 - 11.8) \pm \sqrt{0.007^2 + 0.007^2} = 5.55 \pm 0.01°C$$

$$\frac{T_u - T_l}{T_l - T_h} = \left(\frac{26.40}{5.55}\right) \pm \left(\frac{26.40}{5.55}\right)\sqrt{\left(\frac{0.01}{26.40}\right)^2 + \left(\frac{0.01}{5.55}\right)^2} = 4.76 \pm 0.008°C$$

4.3.2. Experimental set-up and procedure

To obtain the thermal conductivity and surface thermal resistance of the granular carbon packed bed with the Anter Quickline-10, the following steps were followed:

1. Generation of the calibration line and finding the values of F (reference thermal resistance ($m^2.K.W^{-1}$)) and $R_{internal}$ (interfacial thermal resistance ($m^2.K.W^{-1}$)), using the different thicknesses of the Vespel samples provided by the Anter Company.
2. Evaluation of thermal conductivity and resistance of blocks of Circular Square shapes from PEEK material with *5.10 mm* thickness and 10 sheets of paper. The values used were the F and $R_{internal}$ found by the Vespel calibration process at step one.
3. Generation of the calibration line and finding the values of F and $R_{internal}$ for different paper sheet numbers and blocks of circular & square shape, from PEEK material with different thicknesses.
4. Finding the thermal conductivity and thermal resistance of the circular carbon packed bed using the values of F and $R_{internal}$ obtained from the calibration process for a circular block shape of the PEEK material.
5. Finding the thermal conductivity and thermal resistance of the square carbon packed bed using the values of F and $R_{internal}$ obtained from the calibration process of a square block shape of the PEEK material.

4.4. Transient method

The temperature field is dynamic inside the specimen. At the starting point of the transient experiment, the specimen temperature must be uniform, and then a small disturbance in the form of a step-wise function is applied to the specimen. This disturbance could be in the heat flux or the temperature jump at the boundary. One

thermometer was placed at the heat source and the other was placed inside the sample, separate from the heat source, to measure the temperature change or response at the located position.

Once again, in general, transient methods can be divided into absolute and comparative methods. Many different methods have been established based on the transient method, such as the Gustafsson Probe, hot wire, hot disc and immersed body methods.

The absolute transient technique illustrated in Figure 4.4 is called the hot wire or transient line source method, and was used by Swift [19] and later improved by Okazaki et al. [20] and Shulman et al. [21]. This method uses the experimental data directly to find medium thermal conductivity instead of thermal diffusivity. The sample is contained in a stainless steel cylindrical holder, *2"* long and *0.075"* in diameter. A *0.025"* OD hypodermic tube is soldered along the cylinder axis; this tube contains a *36* gauge constantan wire heater and two *40* gauge iron-constantan thermocouples. Two reference thermocouples are attached to the cell exterior. The heating wire is powered by a DC supply. The resistance of the heating wire is measured independently using a bridge, while the current during the experiment is determined from the voltage drop across a *3 ohm* precision resistor in series with the heating wire. The cell is enclosed in a furnace which is capable of maintaining a temperature of 300^oC. Finally, the thermal conductivity is obtained from the line temperature:

$$T_2 - T_1 = (q4\pi\lambda)\ln\frac{t_2-t_0}{t_1-t_0} \qquad (4.6)$$

where T_1 (K) is line temperature at time t_1, T_2 (K) is line temperature at time t_2, q is heat input, λ is thermal conductivity, t is time, t_0 is zero-time correlation, the approximate value is $\delta^2/4\alpha$ where δ is heating wire radiuses and α is the thermal diffusivity of the sample. Figure 4.5 illustrates another transient technique, entitled the Gustafsson Probe, invented by Gustafsson [22]. The Gustafsson Probe is a combination of the hot wire and hot disc methods.

The Swift [19] and Gustafsson [22] methods are called contact transient methods (CTM). Much attention has been paid to developing those methods. Table 4.2 is a summary of the most frequently-applied contact transient methods by Tye et al. [23].

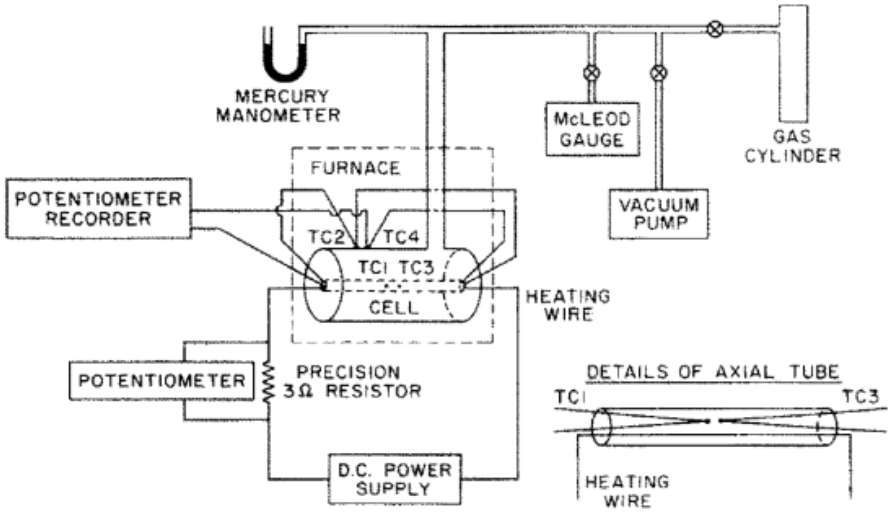

Figure 4.4. Hot-wire method arrangement to measure the packed bed thermal conductivity with Swift [19].

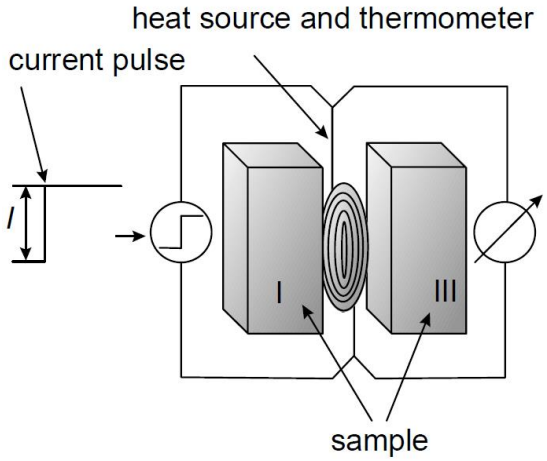

Figure 4.5. Gustafsson Probe for transient method with circular probe shape [22].

All contact transient methods have limitations with regards to study of the effects of liquid, moisture and inert gases on consolidated granular material. To overcome these limitations, Smoluchowski [24] suggested an experimental method, later improved by Schumann and Voss [25]. The method is based on an absolute radial transient. Figure 4.6 shows how the bed is located in a glass cylinder in order to measure the thermal conductivity of the material. The probe is put in a bath of boiling water and the temperature-time function in the middle of the axis is measured by means of a thermometer. A pressure tap enables adjustment of the vacuum or pressure levels in the packed bed. In order to use one-dimensional conduction in the cylinder, the length of the cylinder is ten times more than its inside diameter.

Method	*Heat source geometry*	*Method of heat production*	*Heat source/temperature sensor configuration*	*Measured and/or derived Parameter* [a]
Hot-wire/probe/ strip	Line, strip	Step-wise	United[b] separated[c]	λ, a (c and E in some experimental forms)
Pulse Transient	Plane	Pulse	Separated	a, c, λ
Step-wise transient	Plane	Step-wise	Separated	a, c, λ
Hot-Plate Transient	Plane	Step-wise	United	E
Hot-disc transient	Disc	Step-wise	United	a, c, λ
Gustafsson probe	Concentric Circles	Step-wise	United	a, c, λ

[a] λ = thermal conductivity, a = thermal diffusivity, E = thermal effusivity, c = specific heat. [b] one sensor. [c] two sensors.

Table 4.2. Summary of Basic Forms of Contact Transient Methods (CTMs), [23].

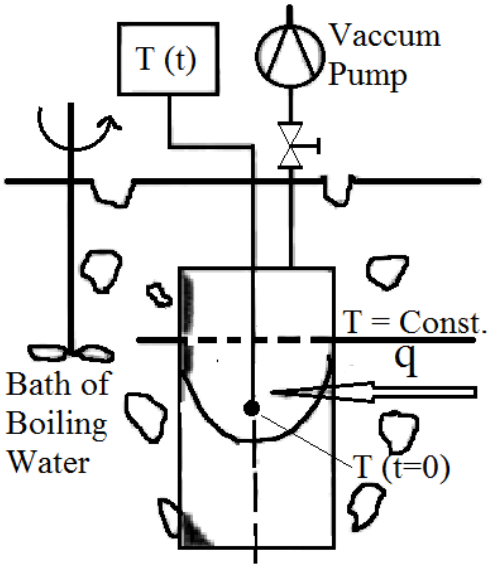

Figure 4.6. Experimental arrangements used by Smoluchowski [24], Schumann and Voss [25]. The thermometer, which is located at the middle and the axis of the cylinder, records the temperature curve after the specimen is plunged in to a bath of boiling water at constant temperature.

The advantages of Smoluchowski's [24] experimental method for studying porous media in real conditions have made it a popular choice for the food industry [26, 27, 28], and in civil engineering, measuring the thermal properties of sand, concrete and soil [29]. In the food industry, porous media contains moisture, fat and vitamins, and thus a method is required to find the thermal properties of food as a porous media in the presence of those substances.

4.4.1. Theory and concept

The measurement and analysis methods in this study are combinations of Smoluchowski's [24] test rig and procedure for measuring the sections, and the one-dimensional transient numerical method. The one-dimensional transient numerical method for a granular packed bed was used for analysis and obtaining the heat transfer coefficients of the contact wall/packed carbon (h) and intrinsic thermal conductivity (λ).

As shown in Figure 4.7, the idea is to investigate the thermal properties of the packed GAC in a real thermal generator condition. The granular material was therefore placed within a cylindrical stainless steel sample holder with a thin wall. The cylinder height was kept as long as possible in comparison to its diameter, in order to satisfy the one-directional radial heat conduction through the packed bed. Two thermocouples were located at the centre and outside of the sample wall, to monitor temperature changes in the packed GAC in case of sudden changes in temperature imposed into the wall of the sample reactor.

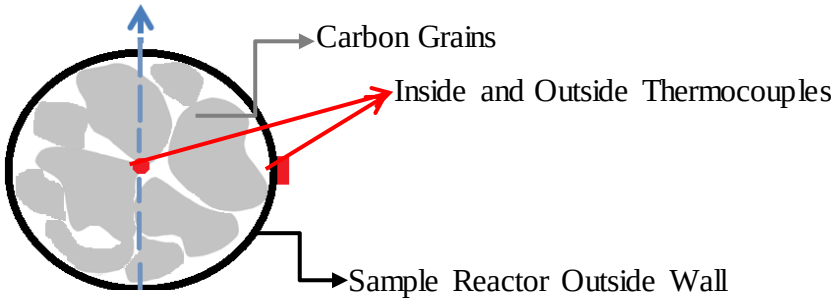

Figure 4.7. Concept for a granular holder with stainless steel wall and thermocouple allocation.

Based on the main concept, the sample holder was made from stainless steel with an outside diameter of *25.4 mm*, *0.71 mm* wall thickness and *200 mm* length, to satisfy the one-dimensional conditions. Figure 4.8 shows that the granular material was held in place by welding two caps on the top and bottom of the cylinder. Another stainless-steel tube, which is called the inside thermocouple tube, with *3.175 mm* OD, was welded to the top cap. This tube will be used to measure the packed temperature at the centre of the sample. The tube helps to locate the thermocouple at an exact position at the centre of the sample holder cylinder. The second thermocouple was attached to the cylinder wall from the outside at the same height as the internal thermocouple. The outside thermocouple measures the temperature at the outside boundary when the sample is exposed to heat waves.

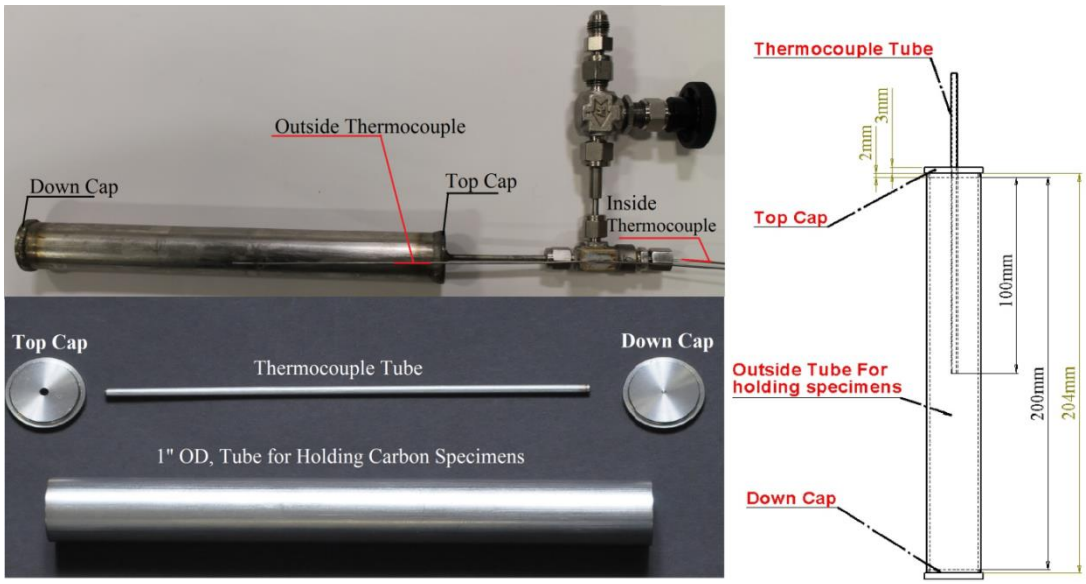

Figure 4.8. Packed GAC sample holder for transient model in present of adsorbate.

After recording the temperature profile changes by time at the centre node, by disturbing the temperature profile at the boundary of the cylindrical sample holder, the one-dimensional transient numerical method was used. Figure 4.9 shows the domain discretization and location of the nodes in the sample holder.

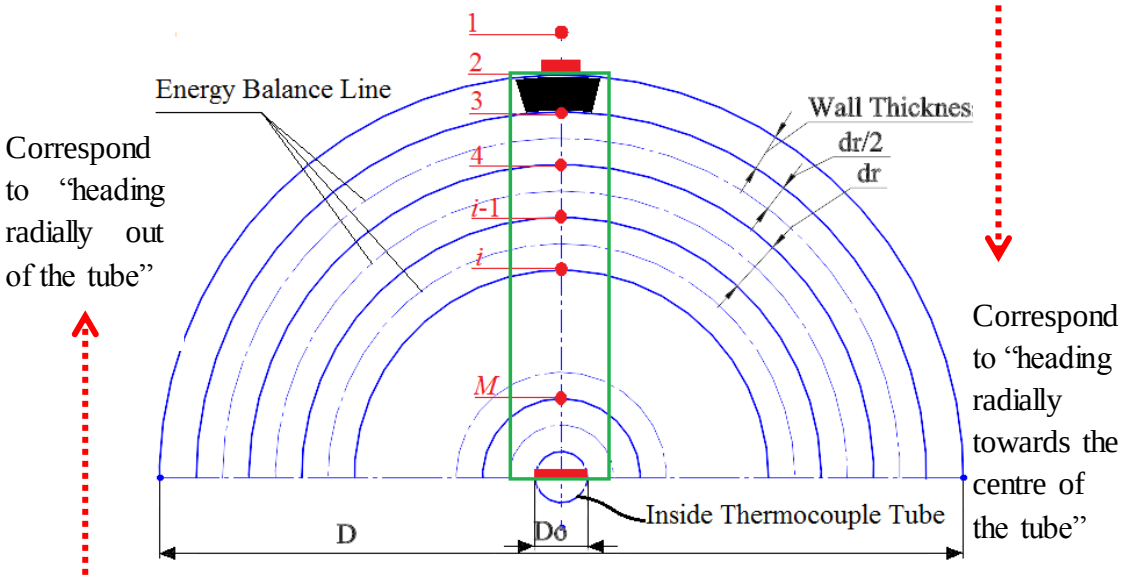

Figure 4.9. Illustration (half cross-section) of domain discretization for energy balance at the packed carbon in a one-dimensional cylindrical configuration.

The domain in Figure 4.9 shows that the heat is flowing into the packed bed from the top into the bottom, which is represented by the symmetry line in the sample. Node *1* is allocated to the heating area and node *2* is assumed to be attached to the outside wall of the cylindrical holder. The outside thermocouple displays the temperature at

node *2*. To simplify the modelling process, we assume that the temperatures at nodes *1* and *2* are identical.

Equation 4.7 shows the one-dimensional domain discretization for the energy balance over the specific volume, which is illustrated in Figure 4.9, at the carbon packed bed. The temperature changes over a specific volume at a specified time step, which is connected to the temperature and thermal resistance of the nodes towards the inner (west) and outer (east) of cylinder, for the same time step.

$$UAdT = M_{Carbon}\left[C_{P,Carbon} + xC_{P,R723\ Liquid}\right]\frac{dT}{dt} - H\frac{dm_{R723}}{dt} \qquad (4.7)$$

In Equation 4.7, UA is overall heat transfer coefficient. Figure 4.9 shows that the overall heat transfer coefficient for each energy balance line is divided across the two sections. The thermal resistance which the heat flow faces when travelling from the upper (west) to the lower (east) boundary and vice versa is called west ($UAwest$) and east ($UAeast$) overall heat transfer coefficients, respectively. The value dT is temperature change over the represented cell of carbon between the two nodes. M_{Carbon} is the mass of the carbon for each representing cell. Therefore, it could also be written as the following discretized energy balance equation:

$$UAdT = UAwest[T_{i-1}^{t} - T_{i}^{t}] + UAeast[T_{i+1}^{t} - T_{i}^{t}] \qquad (4.8)$$

The values of *UAwest* and *UAeast*at in Equation 4.8 are divided into three regions. The first region is a node on the carbon surface in the vicinity of the sample holder wall from the inside, the second region involves the inner nodes and the final is the centre node.

Figure 4.10 shows the first region or outer boundary node. The node (i = *3*) in Figure 4.10 is located on the carbon surface, which is in contact with the steel body of the cylindrical holder from the inside. Therefore, heat transfer from the steel wall to that node is a combination of conduction through the steel wall and conduction through the voids between the steel wall and the first layer of packed carbon, which is called contact resistance. Equations 4.9 and 4.10 are the overall heat transfer coefficient which the heat flow faces while travelling through the energy balance lines to the cell boundaries in Figure 4.10.

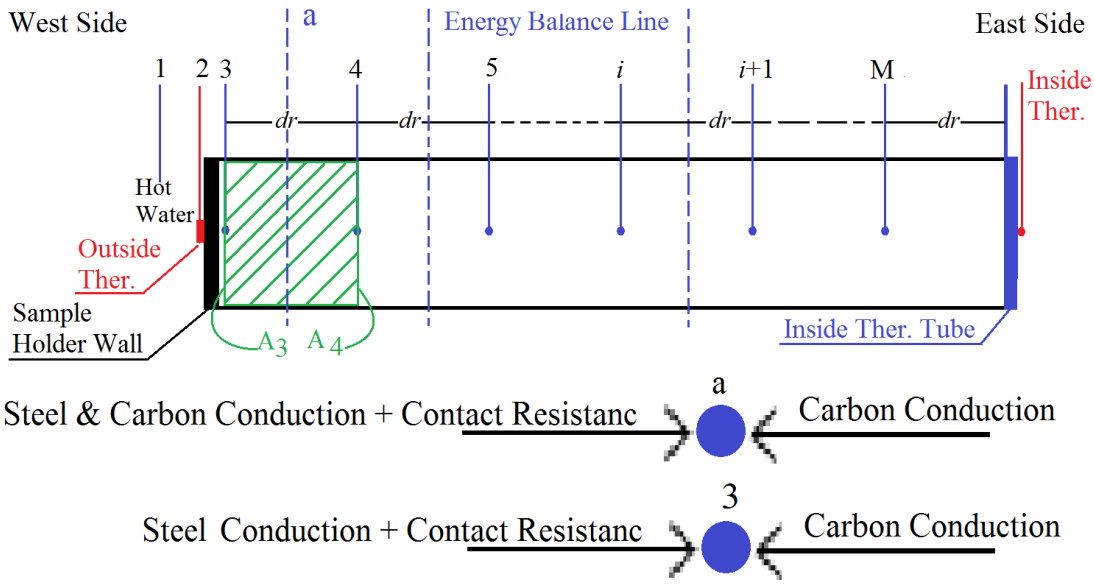

Figure 4.10. Domain discretization for energy balance at the carbon packed outer boundary. Heat transfer mechanism into the boundary node and energy balance line with delimiting of the control volume (A_3, A_2); dr is a radial increment.

$$\begin{matrix} Steel\ Conduction \\ Convection \\ Carbon\ Conduction \end{matrix} \rightarrow UAwest = \frac{A_3}{\frac{t_w}{\lambda_{Steel}} + \frac{2}{h_{internal}} + \frac{dr/_2}{\lambda_{Carbon}}} \tag{4.9}$$

$$Carbon\ Conduction \rightarrow\ UAeast = \frac{A_4}{dr/_{\lambda_{Carbon}}} \tag{4.10}$$

$$A_3 = 2\pi r_3 L_C \quad r_3 = \frac{ID}{2} \tag{4.11}$$

$$A_4 = 2\pi r_4 L_C \quad r_4 = \frac{ID}{2} - dr \tag{4.12}$$

Mass of carbon for repressing cell is:

$$M_{3-Carbon} = \pi(r_3^2 - r_4^2) \times \rho_{Carbon} \times L_C \tag{4.13}$$

Figure 4.11 shows the second regions or internal nodes. Equations 4.14 and 4.15 show that the only resistance which the heat flow is confronted with while travelling towards the energy base lines over the specific control volume is the carbon packed conduction resistance. Therefore, the overall heat transfer from the west and east boundaries for the internal nodes is just heat conduction through the carbon packed bed.

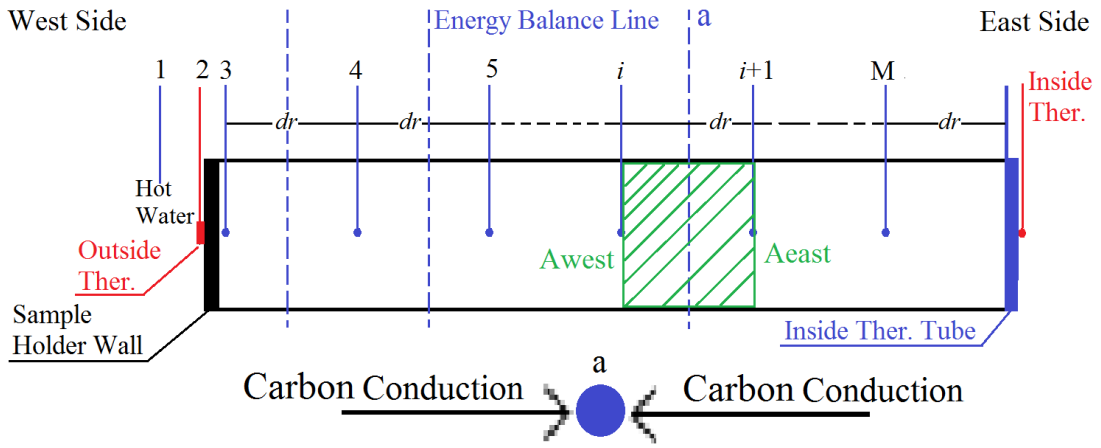

Figure 4.11. Domain discretization for energy balance at the carbon packed bed for the inner nodes. Heat transfer mechanism to the boundary node and energy balance line with delimiting of the control volume (A_i); dr is a radial increment.

$$Carbon\ Conduction \rightarrow UAwest = \frac{A_i}{dr/\lambda_{Carbon}} \tag{4.14}$$

$$Carbon\ Conduction \rightarrow\ UAeast = \frac{A_{i-1}}{dr/\lambda_{Carbon}} \tag{4.15}$$

$$A_i = 2\pi r_i L_C \quad r_i = \frac{ID}{2} - (i-3)dr \tag{4.16}$$

The mass of the carbon for the representing cells is:

$$M_{i-Carbon} = \pi(r_i^2 - r_{i+1}^2) \times \rho_{Carbon} \times L_C \tag{4.17}$$

Figure 4.12 shows the third region or centre node. The centre node is allocated in the middle of the sample reactor, where the internal thermocouple was located. Because of the symmetry condition in the sample cylinder, Equation 4.18 shows that the heat flow through the centre cell is from the west boundary, and that it is purely heat conduction through the carbon packed bed. Equation 4.19 shows no heat transfer from the east boundary because of the assumption of an adiabatic condition.

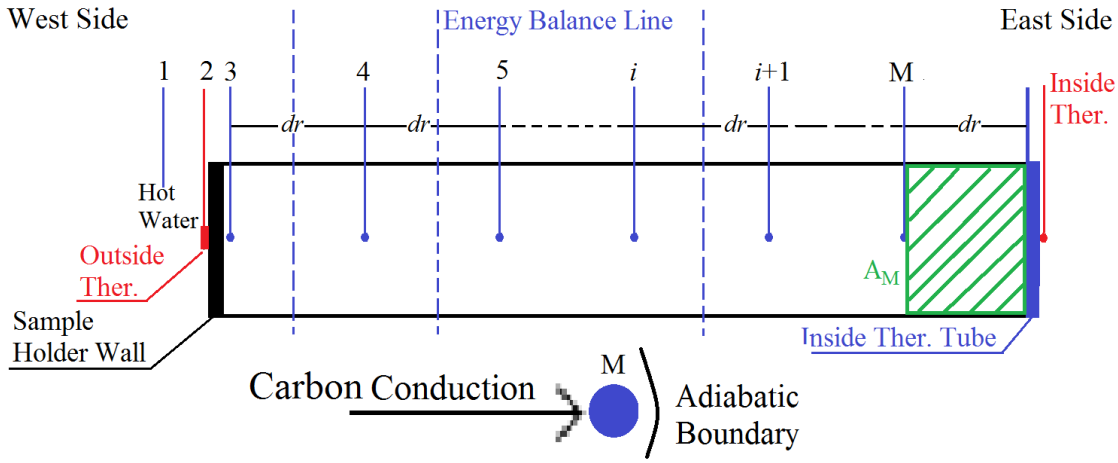

Figure 4.12. Domain discretization for energy balance at the carbon packed bed for the centre node. Heat transfer mechanism to the centre node and energy balance line with delimiting of the control volume (A_M); *dr* is radial increment.

$$Carbon\ Conduction \rightarrow UAwest = \frac{A_M}{dr/\lambda_{Carbon}} \tag{4.18}$$

$$Adiabatic\ Boundary \rightarrow\ UAeast = 0 \tag{4.19}$$

$$A_M = 2\pi r_M L_C \quad r_M = dr \tag{4.20}$$

Mass of carbon for representing cell is:

$$M_{M-Carbon} = \pi\left(r_M^2 - D_o^2/4\right) \times \rho_{Carbon} \times L_C \tag{4.21}$$

The effective specific heat of the sample with adsorbed *R723* was calculated from the following expression:

$$CP = C_{P-Carbon} + xC_{P-R723\ Liquid} \tag{4.22}$$

where $C_{p\text{-}Carbon}$ and $C_{p\text{-}R723Liquid}$ are the specific heat of the GAC and liquid *R723*, respectively. To simplify the modelling, both specific heats are assumed to be constant: $C_{p\text{-}Carbon}$ = *1125* $J.kg^{-1}.K^{-1}$ and $C_{p\text{-}R723Liquid}$ = *4500* $J.kg^{-1}.K^{-1}$ in the temperature range of the thermal conductivity test. The value $xC_{p\text{-}R723Liquid}$ is the *R723* adsorbed phase contribution with the concentration *x*, calculated from Dubinin-Astakhov (D-A) [4]:

$$x = x_0\ exp\left[-K\left(\frac{T}{T_{sat}} - 1\right)^n\right] \tag{4.23}$$

where T is the sample temperature (K), T_{sat} (K) is the saturation temperature corresponding to the gas pressure P, x_0 is the concentration of R723 under saturation conditions corresponding to the maximum concentration ($0.354\ kg.kg^{-1}$), K is 3.7342 and n is 1.187 [30].

$H\frac{dm_{R723}}{dt}$ is a heat generation term in the represented cells in Equation 4.7. H is the heat of the sorption and is given by:

$$H = RA\frac{T}{T_{sat}} \tag{4.24}$$

where R is gas constant ($364.2\ J.kg^{-1}.K^{-1}$), T is the sample temperature (K), T_{sat} (K) is the saturation temperature corresponding to the gas pressure P and finally A corresponds to the slope of the saturation curve on a plot of $ln(P)$ vs. $-1/T_{sat}$ ($A = 2621.3$).

The phrase dm_{R723}/dt in Equation 4.7 corresponds to the changing of the adsorbed refrigerant mass in the carbon for the represented cells over the time. The mass of the adsorbed refrigerant gas, the gas which is condensed in the activated carbon pores, per mass of carbon, is called concentration x (*kg of adsorbate / kg of adsorbent*):

$$x = \frac{m_{R723}}{M_{Carbon}} \rightarrow m_{R723} = xM_{Carbon} \rightarrow \frac{dm_{R723}}{dt} = \frac{dx}{dt}M_{Carbon} \tag{4.25}$$

Equation 4.25 shows the relevancy of mass of adsorbed refrigerant with mass of adsorbent (GAC) and concentration. Then it is possible to rewrite Equation 4.25:

$$\frac{dm_{R723}}{dt} = M_{Carbon}\frac{dx}{dt} \tag{4.26}$$

Regarding D-A Equation 4.23, the concentration depends on sample temperature and pressure. Therefore, in Equation 4.26 the differentiation of concentration changes by time based on partial deferential rules, and this is rewritten as:

$$\frac{dx}{dt} = \frac{dx}{dT}\frac{dT}{dt} + \frac{dx}{dP}\frac{dP}{dt} \tag{4.27}$$

In the D-A equation the pressure is represented by T_{sat} ($dP\ \alpha\ dT_{sat}$), therefore Equation 4.27 turns into:

$$\frac{dx}{dt} = \frac{dx}{dT}\frac{dT}{dt} + \frac{dx}{dT_{sat}}\frac{dT_{sat}}{dt} \tag{4.28}$$

Equation 4.29 shows the differentiation of Equation 4.23 (D-A Equation) with respect to the sample temperature and saturated temperature:

$$\frac{dx}{dT} = -\frac{Knx}{T_{sat}}\left(\frac{T}{T_{sat}} - 1\right)^{n-1} \quad \frac{dx}{dT_{sat}} = Knx\frac{T}{{T_{sat}}^2}\left(\frac{T}{T_{sat}} - 1\right)^{n-1} \tag{4.29}$$

Finally, substituting Equation 4.29 into Equation 4.28, it could be written as follows:

$$\frac{dx}{dt} = \left[-\frac{Knx}{T_{sat}}\left(\frac{T}{T_{sat}} - 1\right)^{n-1}\right]\frac{dT}{dt} + \left[Knx\frac{T}{{T_{sat}}^2}\left(\frac{T}{T_{sat}} - 1\right)^{n-1}\right]\frac{dT_{sat}}{dt} \tag{4.30}$$

In Equations 4.7 and 4.30, dT/dt and dT_{sat}/dt change with temperature and saturation temperature (or pressure) for the represented cells over the time. Therefore, the discretized models are:

$$\frac{dT}{dt} = \frac{T_i^{t+1} - T_i^t}{dt} \quad and \quad \frac{dT_{sat}}{dt} = \frac{T_{sat}^{t+1} - T_{sat}^t}{dt} \tag{4.31}$$

This would be the result of substituting all those equations which have been mentioned above with Equation 4.7, and rearranging it for discretized domain and time:

$$UAdT = M_{Carbon}(CP)\frac{dT}{dt} - M_{Carbon}\left(RA\frac{T}{T_{sat}}\right)\left[-\frac{Knx}{T_{sat}}\left(\frac{T}{T_{sat}} - 1\right)^{n-1}\right]\frac{dT}{dt} - M_{Carbon}\left(RA\frac{T}{T_{sat}}\right)\left[Knx\frac{T}{{T_{sat}}^2}\left(\frac{T}{T_{sat}} - 1\right)^{n-1}\right]\frac{dT_{sat}}{dt} \tag{4.32}$$

$$\rightarrow \frac{UAdT}{M_{Carbon}} + \left(RA\frac{T}{T_{sat}}\right)\left[Knx\frac{T}{{T_{sat}}^2}\left(\frac{T}{T_{sat}} - 1\right)^{n-1}\right]\left(\frac{T_i^{t+1} - T_i^t}{dt}\right) = \left[(CP) - \left(RA\frac{T}{T_{sat}}\right)\left[-\frac{Knx}{T_{sat}}\left(\frac{T}{T_{sat}} - 1\right)^{n-1}\right]\right]\left(\frac{T_{sat}^{t+1} - T_{sat}^t}{dt}\right) \tag{4.33}$$

$$\rightarrow \frac{\frac{UAdT}{M_{Carbon}}dt + \left(RA\frac{T}{T_{sat}}\right)\left[Knx\frac{T}{{T_{sat}}^2}\left(\frac{T}{T_{sat}} - 1\right)^{n-1}\right](T_{sat}^{t+1} - T_{sat}^t)}{(CP) - \left(RA\frac{T}{T_{sat}}\right)\left[-\frac{Knx}{T_{sat}}\left(\frac{T}{T_{sat}} - 1\right)^{n-1}\right]} = T_i^{t+1} - T_i^t \tag{4.34}$$

$$\rightarrow \frac{\frac{UAdT}{M_{Carbon}}dt + \left(RA\frac{T_i^t}{T_{sat}^t}\right)\left[Knx_i^t\frac{T_i^t}{{T_{sat}^t}^2}\left(\frac{T_i^t}{T_{sat}^t} - 1\right)^{n-1}\right](T_{sat}^{t+1} - T_{sat}^t)}{(CP) - \left(RA\frac{T_i^t}{T_{sat}^t}\right)\left[-\frac{Knx_i^t}{T_{sat}^t}\left(\frac{T_i^t}{T_{sat}^t} - 1\right)^{n-1}\right]} + T_i^t = T_i^{t+1} \tag{4.35}$$

4.4.2. Sample preparation and experimental set-up

208-C granular activated carbon from the Chemviron Company with *13×30 US* sieve mesh size (*1.5 mm × 0.6 mm*, Appendix E), previously used in the permeability test, was used to make five packed beds with different densities for thermal measuring purposes. The packed densities of the five test-samples were *546.7 kg.m^{-3}*, *661.9 kg.m^{-3}*, *707.7 kg.m^{-3}*, *749.8 kg.m^{-3}* and *768.1 kg.m^{-3}*.

Figure 4.8 shows the cylindrical sample holder, made from a stainless-steel seamless tube with *25.4 mm OD*, *204 mm* total length and *0.71 mm* wall thickness. Two *5 mm* stainless steel caps were welded to the top and bottom. The filled height after welding the caps was *200 mm*. To pass the inside thermocouple into the centre sample holder, another seamless stainless steel tube (the thermocouple tube) with *3.175 mm OD* and *2.1 mm ID* was welded to the top cap. The thermocouple tube was located at the middle of sample holder with *105 mm* distance from the top cap surface. To avoid blocking the thermocouple tube during the process of packing with carbon particles, the steel wire passes through the tube. Later the steel wire was replaced by the thermocouple after finishing the packing process. To fabricate each reactor, the following stages were considered:

1. The themocouple tube was welded to the top cap.
2. The top cap was welded to the main sample holder body.
3. The carbon was packed at the desired density, via a special process, into the sample reactor. Figure 4.13 shows the carbon was packed to a height of *200 mm*. The bottom cap was secured into place to prevent any damage to the carbon pack.
4. The sample reactor was sent for a second welding run and the bottom cap was fixed at the desired position.
5. The protecting wire was replaced with the thermocouple and the specific connection for the leak test was assembled.
6. Each individual sample was tested for sign of any leak up to *25 bar* (twice working pressure) with compressed air.

The first sample reactor was filled with granular active carbon in particle form by vibration process only. The sample holder was filled with carbon up to the desired

adsorbent length while being kept on the vibration desk, which is shown in Figures 4.8 and 4.13.

In order to make the other packed density, the same procedure as in the permeability test was followed. A special plunger (Figure 4.14, left) and structural support (Figure 4.14, right) were designed and fabricated. A preliminary test was conducted in order to understand the granular carbon particle behaviour during the packing process. The following points were established:

- The height occupation of *10 gm*, *5 gm* and *2 gm* of granular carbon in the sample reactor with vibration process.
- The minimum height that could be achieved by the packing process and applying the force to the particles for *10 gm*, *5 m* and *2 gm* of granular carbon.
- The maximum packing force that can be applied to the sample holder and support without damaging the sample holder tube or the integrity of the holder.
- The amount of "spring back" after the packing process. After removing the packing force the packed carbon column was shown to have increased the most. Therefore, to accommodate an accurate packing density, the "spring back" effect of the packed carbon column was assisted.

This information was used to understand the packing force, the packing time for each density, and the length of the plunger, extension tube and support pipe.

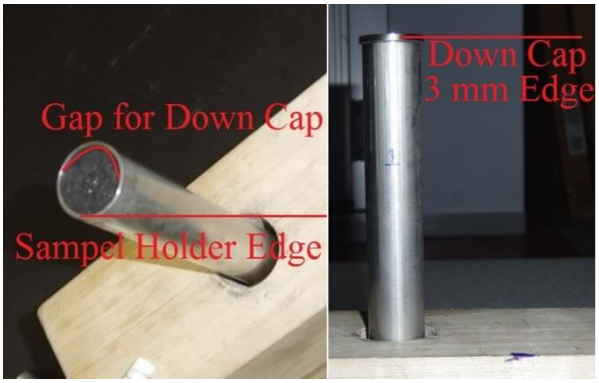

Figure 4.13. The *2 mm* gap between packed carbon surface and sample holder edge (left). Down cap in desired place before second-time welding process; the *3 mm* edge was designed to ensure the success of the welding procedure (right).

The structure of the sample holders was monitored by measuring the height and outside diameter, in order to spot any inconsistencies during the packing and sample fabrication. The outside diameter was measured at three specific points before and after the packing process. The average of those points was used as the outside diameter of the sample in general modelling. The heights were measured three times during the fabrication:

- After welding the top cap and the thermocouple tube.
- After the packing process.
- After welding the bottom cap.

Table 4.3 shows the summary of each sample holder in terms of outside diameter (OD), mass of packed carbon and number of packing courses. The packing course shows the number of fillings and plunging force applied to reach the desired density. The outside diameter of the sample holders during the packing process was expanded within a maximum amount of *2%*.

Density ***($kg.m^{-3}$)***	***Carbon weight*** ***(gm)***	***Average OD Before*** ***(mm)***	***Average OD After*** ***(mm)***	***Packing*** ***Course***
546.7	49.23	25.45	25.45	0
625.9	56.53	25.52	25.52	2
661.9	59.63	25.46	25.47	3
707.7	64.1	25.51	25.52	3
749.8	68.25	25.51	25.58	4
768.1	72.55	25.48	26.03	5

Table 4.3. Thermal conductivity sample information for transient test.

Figure 4.14 shows that the structural support was made from galvanised pipe with a *25.4 mm* inside diameter, with *5.6 mm* wall thickness. In order to prevent the sample holder from sticking to the structural support inside wall and for an easy disconnecting process, the galvanised pipe was split the two sections. During the packing process, two sections of the support pipe were attached to each other and held in place using four special clips from the outside.

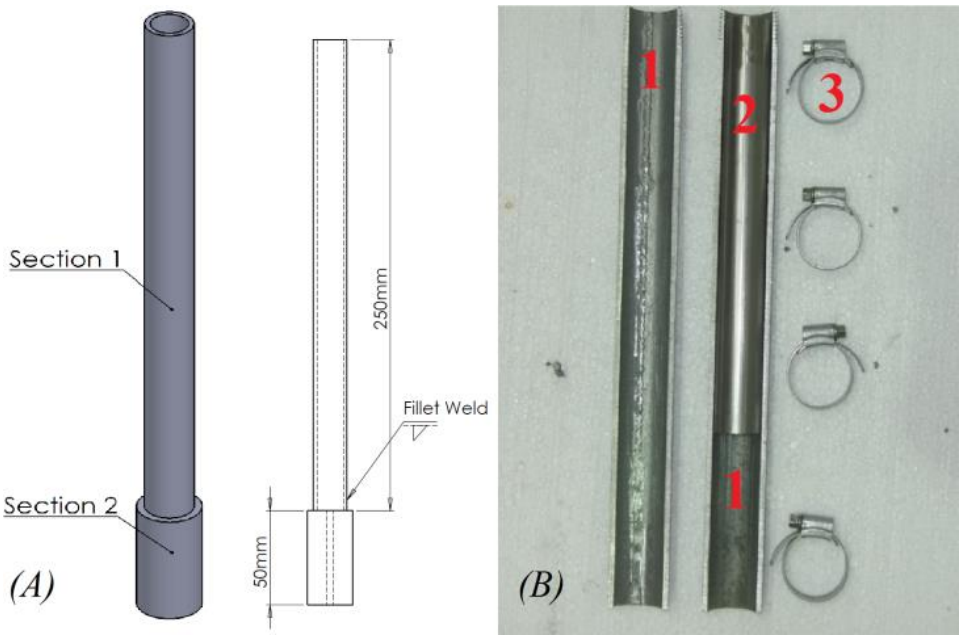

Figure 4.14. Left (A): Plunger: section 1 is a pipe with *4 mm* wall thickness and *12.7 mm* OD. Section 2 OD is *24± 0.15 mm* and has passage for a thermocouple tube with a *3.3 mm* OD. Right (B): Structural support: 1 is a split support pipe, 2 represents the sample holder wall and 3 shows the fastener clips.

The loose carbon height at some stages of the packing process was higher than the sample holder's total length. Therefore, the extension tube (Figure 4.15) was located in line at the top of the sample holder to guide the plunger into the main section of the sample holder and prevent any carbon being lost during the packing process. Figure 4.15 shows the wooden block provided to protect the thermocouple tube from bending and absorbing any sudden force during the packing process, and to prevent deformation of the sample holder. Finally, the granular particles were packed by press machine, as shown in Figure 4.15. The machine has the capability of controlling the displacement speed per second and force, which is transferred to the packed bed from the moveable load head.

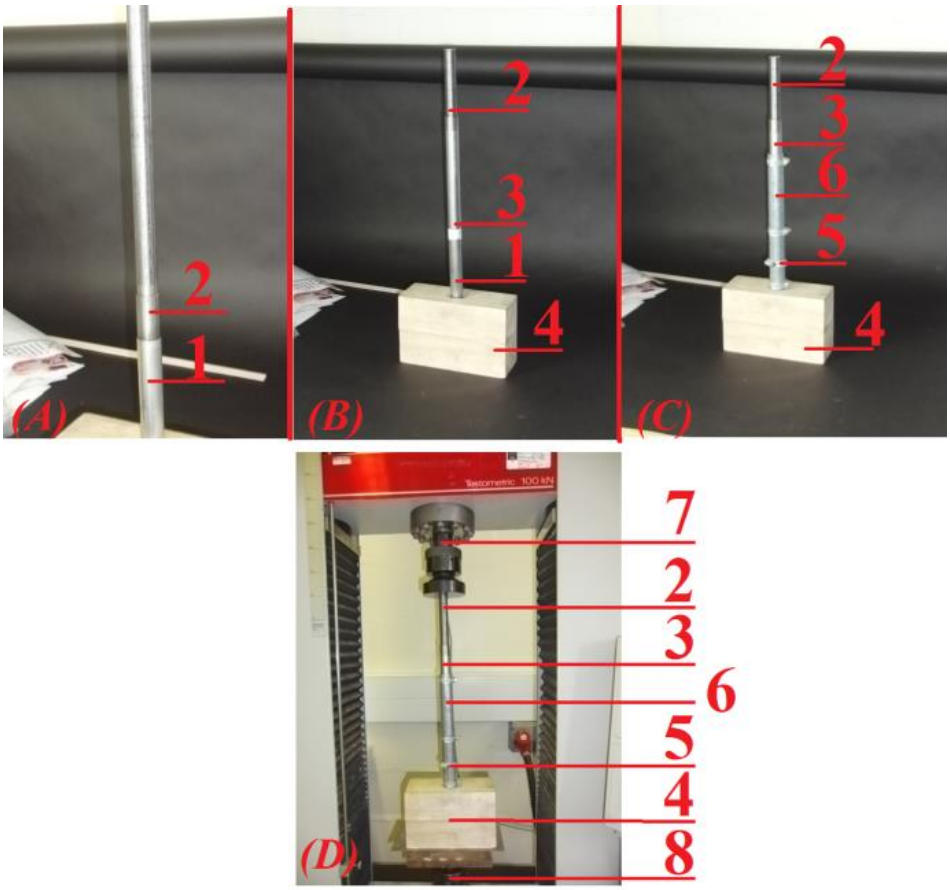

Figure 4.15. A: 1 is the sample holder, 2 is the plunger – B: 1 is the sample holder, 2 is the plunger, 3 is the extension tube, 4 is the wooden support – C: 2 is the plunger, 3 is the extension tube, 4 is the wooden support, 5 is the fastener clip, 6 is the split support pipe – D: 2 is the plunger, 3 is the extension tube, 4 is the wooden support, 5 is the fastener clip, 6 is the split support pipe, 7 is the press machine's moveable head and 8 is the press machine's fixed head.

4.4.3. Test procedure

Figure 4.16 shows the sample module, with the location of the two K-type thermocouples. One thermocouple was attached to the sample surface while another was passed into the centre of sample through the thermocouple tube. The sample module was isolated after vacuuming and charging with refrigerant using a swagelok *¼"* 316 stainless steel "M" series metering (needle) valve.

The experimental procedure for inter gas (air) consists of suddenly plunging the sample that was initially at ambient temperature into the hot water bath up to the neck of the female run tee. In the process of testing, the needle valve was fully open to maintain the atmospheric pressure while the sample was submersed. Figure 4.17 shows the hot water bath with the thermostat control. The bath temperature was set up at $85^{o}C$. Three thermocouples were located at different heights in the thermal bath

to monitor the water temperature uniformity at different levels. The Strawberry Tree Company, in association with the Workbench software, was used to record the data with a frequency of *0.015 (second)*.

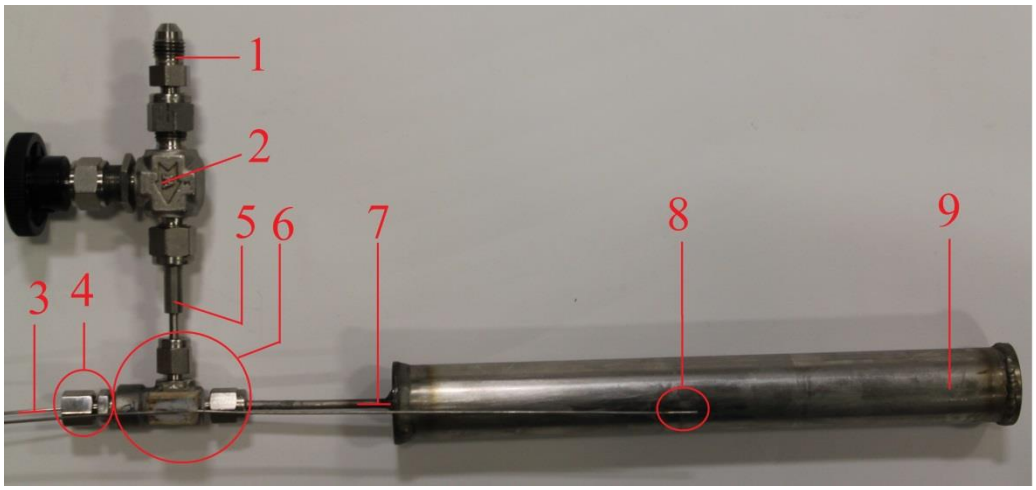

Figure 4.16. Sample holder general view with part details. 1: *¼"* filler to connect in to the vacuum and charging manifold hose, 2: Swagelok *¼"* 316 stainless steel "M" series metering (needle) valve for module isolation, 3: Inside thermocouple, 4: 316 stainless steel *1/8"* compression fitting to seal the thermocouple, 5: *1/8"* connection to *¼"*, 6: Swagelok 316 stainless *1/8"* female run tee, 7: Thermocouple tube with *1/8"* OD, 8: Outside thermocouple and attaching position, 9: Sample holder.

To perform the test with refrigerant the following steps were implemented:

- Drying the sample by heating it up to $200^{o}C$ under a vacuum for *24* hours.
- Charging the sample with refrigerant (R723).
- Letting the sample stabilise and reach ambient temperature for *12* hours.
- Conducting the thermal conductivity test.

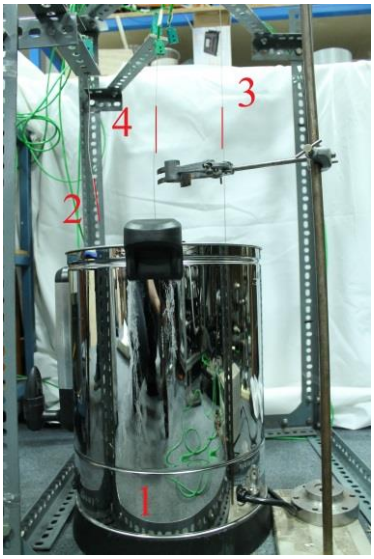

Figure 4.17. Hot water thermal bath with belt in thermostat and location of thermocouple inside the bath. 1: Thermal bath, 2: Bottom end thermocouple, 3: Middle thermocouple, 4: Top end thermocouple.

Granular activated carbon normally contains water moisture. Therefore, the pack of carbon contains both air and water moisture, which has an effect on the amount of adsorbed refrigerant. To prevent the effect of the water moisture and air, the carbon sample was heated to $200^{o}C$ while being kept under the vacuum for *24* hours. Figure 4.18 shows the tape heater with the control box, which was used to dry the carbon sample. The inside thermocouple was connected to the temperature control box to monitor the inside temperature and the heater power. The sample weight was measured before and after the drying process, in order to find out the actual amount of dried carbon in sample.

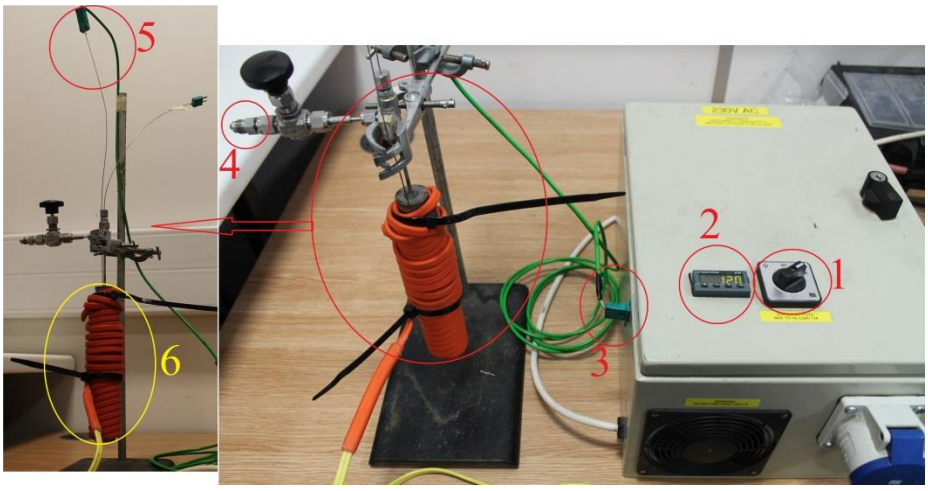

Figure 4.18. Tape heater arrangement with control box to heat the carbon packed bed up to $200^{o}C$ for the purpose of drying, 1: Isolation switch, 2: Temperature indicator with manual setting, 3: Thermocouple input plug in to the controller, 4: *¼"* filler connection to connect to the vacuum pump, 5: Sample inside thermocouple connection to the control box, 6: *180W* tape heater.

To charge the filled sample holder with refrigerant, a special vessel was used. Figure 4.19 shows the 316 stainless-steel vessel, which is connected to the three-way valves by the female run tee connection. The female side of the connection was connected to the compression fitting. A K-type thermocouple with a *500 mm* total length was passed through the compression fitting into the reservoir vessel, in order to measure the temperature of the liquid refrigerant. The vessel was charged with *61.3 gm* and *20%* extra from the refrigerant's main cylinder.

Figure 4.20 shows that the charged vessel with refrigerant was connected to the sample reactor with a *250 mm* stainless steel tube with *¼"* OD. The connection line and sample module were evacuated by vacuum pump for *30* minutes at room temperature. The main Swagelok *¼"* 316 stainless steel "M" series metering

(needle) valve for module isolation was opened and closed slowly during the vacuum process. At the end of the process, the isolation valve was fully closed. Afterwards, the vacuum line isolation valve (*1/8"* Swagelok "M" series metering (needle) valve) was closed and by using a *1/8"* on and off Swagelok three ways valve, the vacuum line was disconnected from the connection line and the vessel was connected to the connection line. At this stage, the refrigerant gas flowed into the connection line. Because the adsorption process causes heat generation in the sample reactor, to prevent any damage to the reactor or sudden overheating, the module *¼"* isolation valve was opened slowly while the pressure and temperature were monitored. At the end of the charging process, the module isolation valve was fully open, and the system pressure and temperature was allowed to stabilise within *12* hours. To prevent any condensation in the connection line or sample reactor (module) the charging vessel was kept in a water bath at 17.8^oC, which was colder than room temperature (21.3^oC).

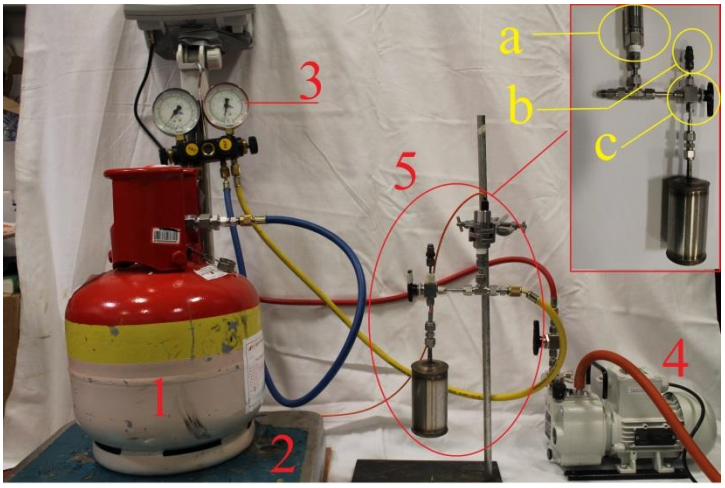

Figure 4.19. 1: R723 gas main cylinder, 2: Scale, 3: Charging manifold, 4: Vacuum pump, 5: Condensing & charging vessel, 5a: Druck pressure transducer, 5b: *1/8"* filler to connect to the vacuum and charging manifold hose, 5c: *1/8"* on & off Swagelok three ways valve.

After the sample reactor was stabilised, it was immersed into the hot water bath. Figure 4.21 shows the immersed sample reactor in the hot water while the module isolation valve was fully opened and the condensing vessel was kept in the cold water bath. Temperature was recorded inside and outside of the condensing vessel, the hot water bath at three different heights, the sample centre node and the sample outside wall. Pressure and temperature were recorded every *0.15 seconds* until the centre temperature reached to the outside temperature within $\pm 0.5^oC$ tolerances.

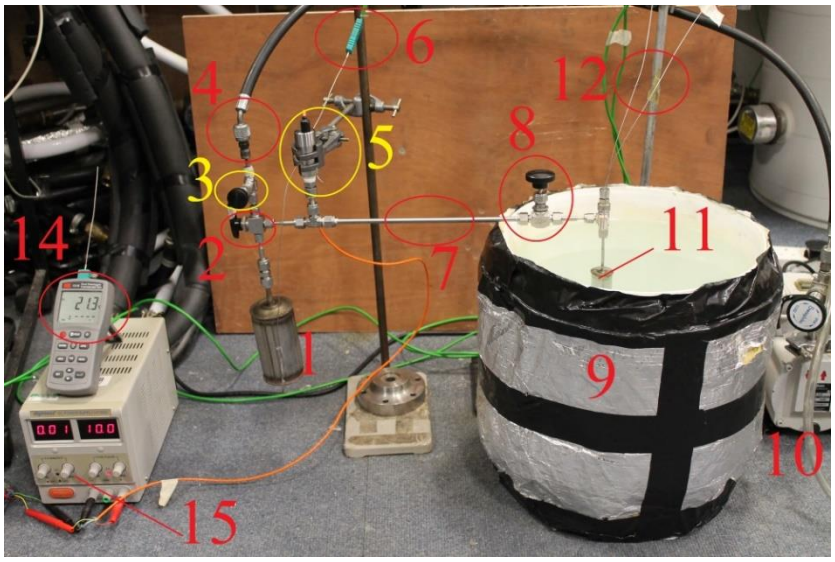

Figure 4.20. 1: Condenser & Charging vessel, 2: *1/8"* on & off Swagelok three ways valve, 3: Swagelok *1/8"* 316 stainless steel "M" series metering (needle) valve for vacuum line isolation, 4: *1/8"* filler to connect in to the vacuum and vacuum line, 5: Druck pressure transducer, 6: Condenser & Charging vessel outside thermocouple, 7: *¼"* connection tube, 8: Swagelok *¼"* 316 stainless steel "M" series metering (needle) valve for module isolation, 9: Cold water bath for reactor cooling during charging process , 10: Rotary vacuum pump, 11: Sample reactor, 12: Inside & outside thermocouples of sample reactor, 14: RS 656 digital temperature indicator for room temperature, 15: Precision adjustable power supply.

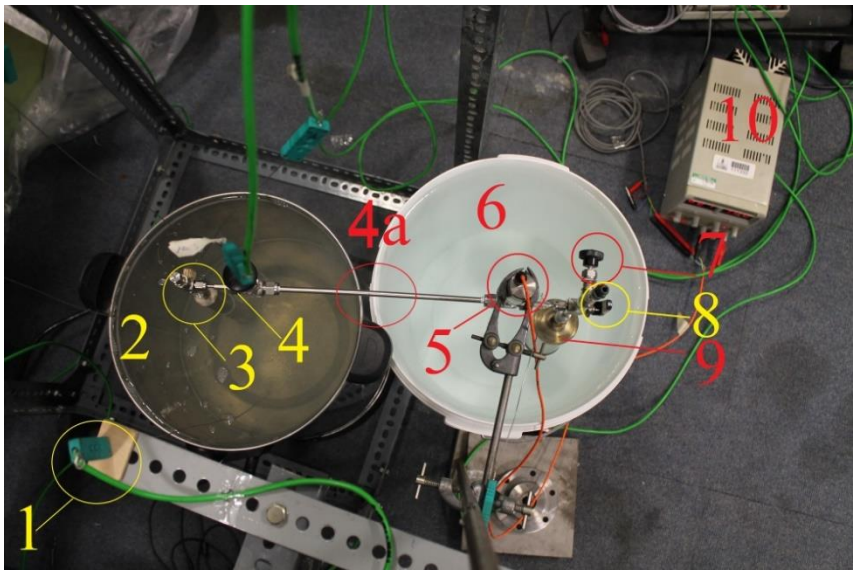

Figure 4.21. 1: Thermal bath K type thermocouple, 2: Hot water thermal bath with build in thermostat, 3: Sample module with inside & outside thermocouples, 4: Swagelok *¼"* 316 stainless steel "M" series metering (needle) valve for module isolation, 4a: *¼"* connection tube, 5: Druck pressure transducer, 6: Water bath to keep condensing vessel at steady temperature situation, 7: Swagelok *1/8"* 316 stainless steel "M" series metering (needle) valve for vacuum line isolation, 8: *1/8"* on & off Swagelok three ways valve and *1/8"* filler to connect to the vacuum and vacuum line, 9: Condenser & charging vessel, 10: Precision adjustable power supply.

4.5. Experimental results and discussion

4.5.1. Steady state test

In order to find the thermal conductivity of any material using the Anter Quickline-10 machine, the obtained thermal resistance of the unknown sample must be fall within the corresponding calibration range of a known sample. The unknown sample's thermal resistance is calculated by obtaining the values of upper, lower and heat sink temperatures. Finally, by using the reference and interfacial thermal resistances from the calibration process, the thermal resistance of the unknown sample can be calculated. To measure and analyse the steady state data, five steps, mentioned before in section 4.2.2, were followed:

Step 1:

The calibration line was established with a known material in order to find the reference values of thermal resistance ($m^2.K.W^{-1}$) and interfacial thermal resistance ($W.m^{-1}.K^{-1}$) in Equation 4.5. The calibration samples with known thermal conductivity and thickness (*3.175 mm*, *6.35 mm* and *9.525 mm*), made from Vespel material, were provided by the Anter Quickline-10 Company. The different thicknesses of the same material lead to different thermal resistance while the thermal conductivity is constant. Figure 4.22 shows the thermal resistance of deferent thicknesses of the same material vs *ΔT sample / ΔT reference*, measured by the Anter Quickline-10 machine. Fitting a curve to the experimental data allows us to calculate both the reference and interfacial thermal resistances.

$$Vespel\ thermal\ Resistance\ coefficients \rightarrow \begin{cases} F = 2.2902e-3 \\ R_{internal} = 2.9686e-3 \end{cases} \quad (4.36)$$

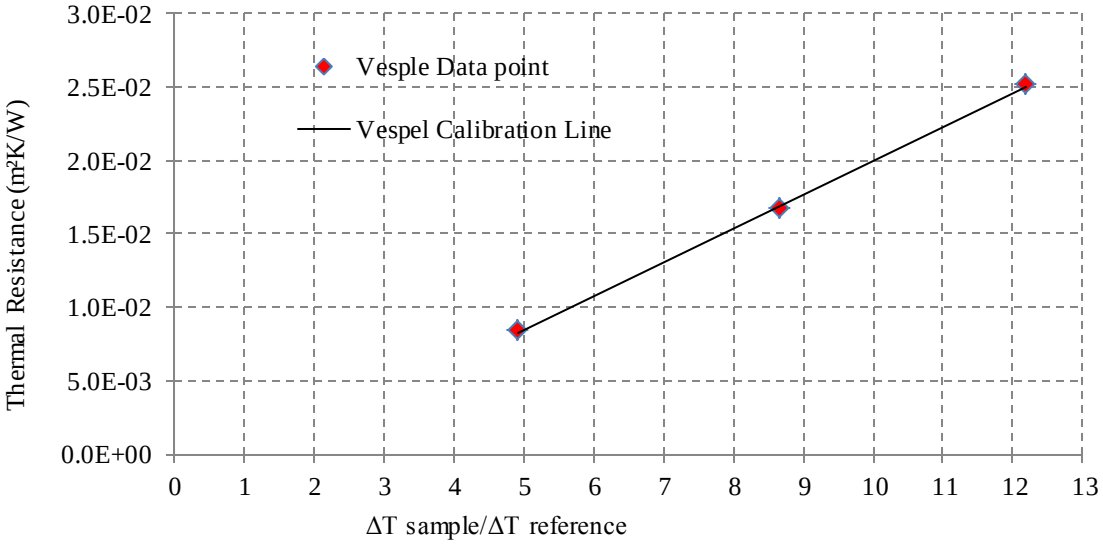

Figure 4.22. Vespel experimental and calibration line to find thermal resistance coefficients.

Step 2:

In this step, the thermal conductivity of circular and square block shapes of the PEEK material and 10 sheets of paper was obtained using the Vespel thermal resistance coefficients for Equation 4.5. The obtained values of thermal conductivity will be used in the third step to generate the calibration line, in order to find the thermal resistance coefficients for Equation 4.5 with different thicknesses of the material, and later to find the thermal conductivity of the granular carbon packed bed.

The paper samples were cut into a circular shape with a *2"* diameter. The circular sample block of PEEK material was also provided with a *2"* diameter. The square sample block of PEEK material was fabricated with two equal *2"* sides. Because the hot and cold headers of the Anter machine were made in a circular shape within a *2"* diameter, to locate the square shape block, two aluminium plates with *10 mm* thickness were attached to the top and bottom surfaces of the square shape block during the tests. The circular shape sample blocks were used directly in contact with the machine's hot and cold headers.

Table 4.4 and Figure 4.23 show that the thermal conductivity and resistance of the square and circular shape sample blocks made from PEEK material are identical. Therefore it can be concluded the effects of the aluminium plates are negligible in measuring the thermal conductivity of any material which is packed amongst two aluminium plates.

Material	*ΔT sample/ΔT reference*	*Thermal Resistance* $m^2.K.W^{-1}$	*Thermal Conductivity* $W.m^{-1}.K^{-1}$
10 Paper sheets	5.65	0.11	$9.98\ e^{-3}$
Circular PEEK	5.10	0.29	$8.72\ e^{-3}$
Square PEEK with Aluminium palates	5.10	0.29	$8.72\ e^{-3}$

Table 4.4. Thermal conductivity and resistance using the Vespel thermal resistance coefficients.

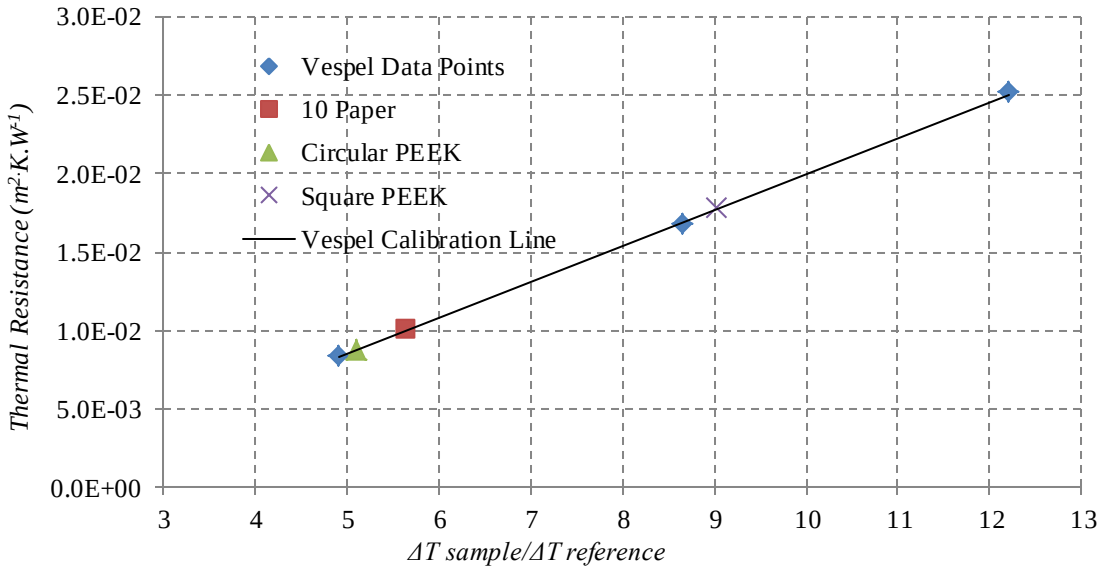

Figure 4.23. PEEK and paper thermal conductivity using the Vespel thermal resistance coefficients.

Step 3:

By using the thermal conductivity of each material, mentioned in Table 4.4, in this step tests were conducted with circular and square shape sample blocks of PEEK material and paper sheets with different thicknesses.

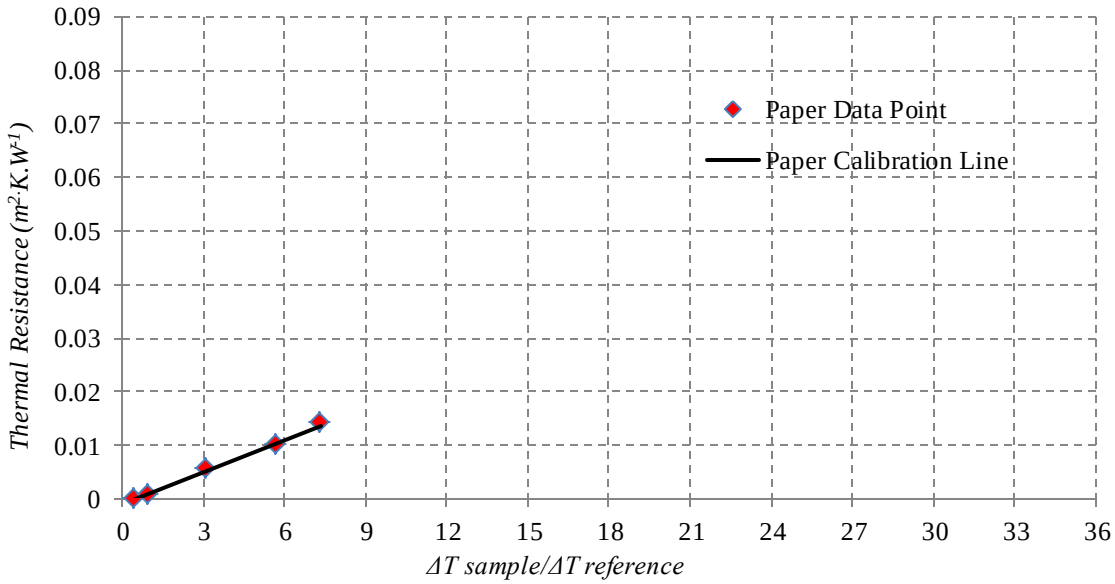

Figure 4.24. Paper experimental and calibration line with different number of sheets, in order to find thermal resistance coefficients

Table 4.5 shows the summary of each material thickness and the obtained thermal resistance coefficients for Equation 4.5, used in each experimental test.

Material	***Thickness***	***Thermal Resistance Coefficients***		***Relevant Figure***
		F	***R internal***	
Paper	1 sheet 2 sheets 5 sheets 10 sheets 20 sheets	$2.011e^{-3}$	$9.310\ e^{-4}$	Figure 4.24
Circular PEEK	2.51 mm 4.9 mm 7.51 mm 9.81 mm 19.95 mm 24.85 mm	$2.823\ e^{-3}$	$8.210\ e^{-3}$	Figure 4.25
Square PEEK	2.6 mm 5.19 mm 10.21 mm 20.05 mm	$2.790\ e^{-3}$	$5.816\ e^{-3}$	Figure 4.26

Table 4.5. Circular and square PEEK and paper sheet thickness and relevant thermal resistance coefficients.

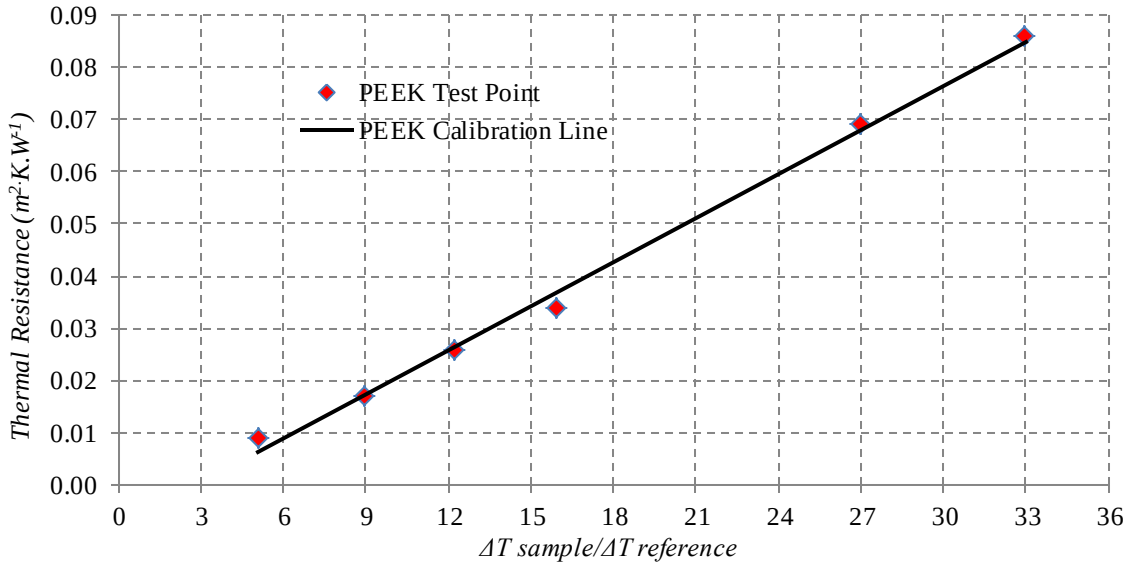

Figure 4.25. Circular PEEK experimental and calibration line with different thicknesses, in order to find thermal resistance coefficients.

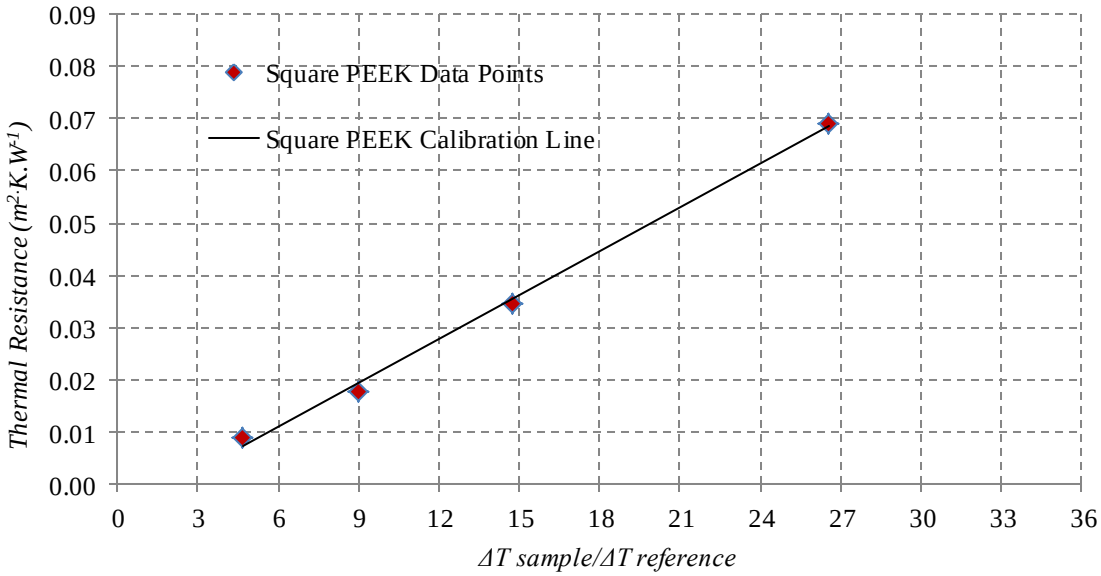

Figure 4.26. Square PEEK experimental and calibration line with different thicknesses, in order to find thermal resistance coefficients.

Step 4:

Figure 4.27 shows the circular sample holder, locating the pack of granular carbon between the hot and cold headers of the Anter machine. The sample holder section was made from PTFE material with a *2"* outside diameter and *3 mm* wall thickness. The end plate was located at the bottom of the sample holder, and to eliminate the effect of this on thermal concavity, was chosen from low thermal resistance material with a thickness of *2 mm*.

Afterwards, using the paper calibration line and thermal resistance coefficients from Table 4.5, the end plate thermal resistance was found and subtracted from the general packed thermal resistance. Figure 4.28 and Table 4.6 show the *ΔT sample / ΔT reference* for the end plate with the paper calibration line, which is provided with different sheet numbers of paper.

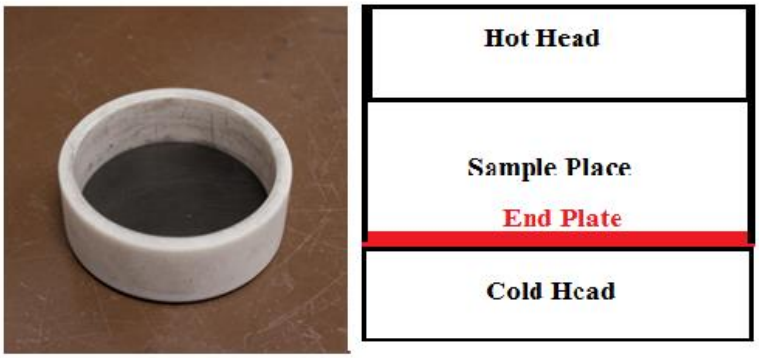

Figure 4.27. The place of the end plate at the packed GAC and circular sample holder.

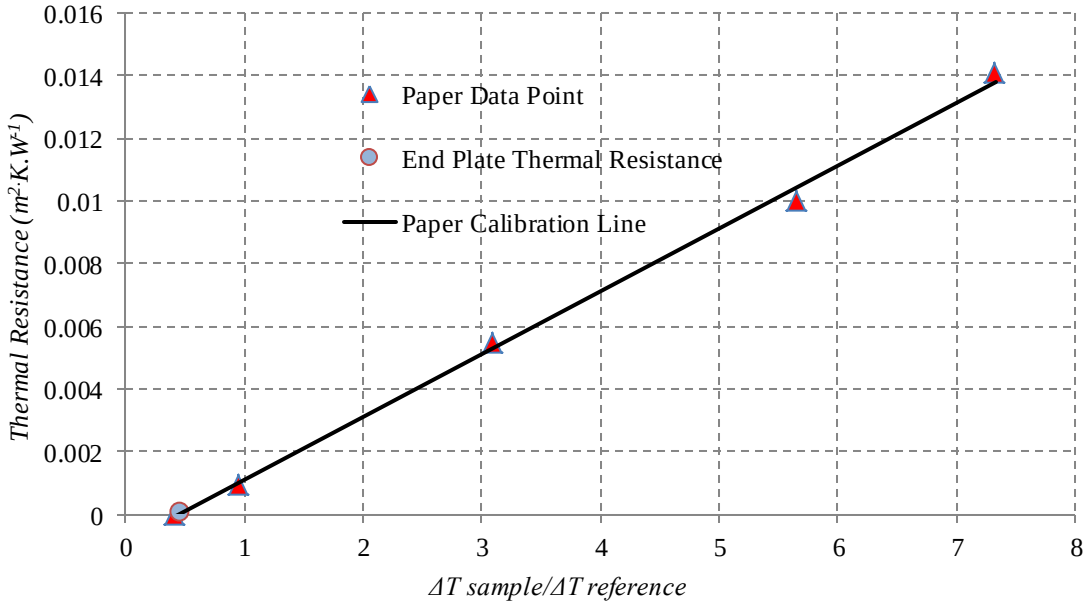

Figure 4.28. Thermal resistance of the end plates with paper calibration line.

Material	***ΔT sample/ΔT reference***	***Thermal Resistance*** $m^2.K.W^{-1}$	***Thermal Conductivity*** $W.m^{-1}.K^{-1}$
10 Paper sheets	5.65	0.11	9.98e-3

Table 4.6. Thermal conductivity and resistance of end plate using the paper calibration line.

The granular activated carbon, with a mesh size of *20 × 40* (*0.85 mm × 0.425 mm*), and with different thicknesses and densities, was packed between the end plate and hot head of the Anter machine, and measured *ΔT sample / ΔT reference*.

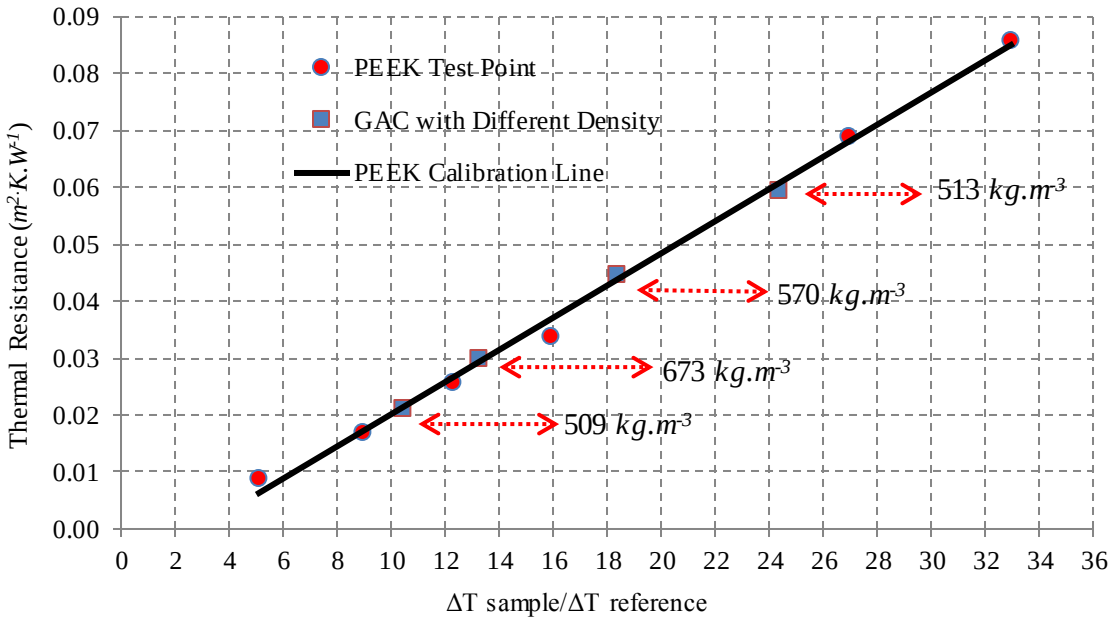

Figure 4.29. Circular GAC (208C - mesh size of 20 × 40) thermal resistance with circular PEEK calibration line.

Afterwards, by using the thermal resistance coefficient for the circular sample block shape made of PEEK material, mentioned in Table 4.5, and the calibration fitted line from Figure 4.29, the packed thermal resistance and conductivity were calculated. Table 4.7 provides a summary of the results.

Test No.	***Density kg.m^{-3}***	***Thickness cm***	***ΔTsample/ΔT reference***	***Thermal Resistance m^{2}.K.W^{-1}***	***Thermal Conductivity W.m^{-1}.K^{-1}***
1	509	0.388	10.422	0.021	0.185
2	513.6	1.247	24.419	0.061	0.210
3	672.8	0.44	13.245	0.029	0.147
4	570	0.728	18.4	0.044	0.163

Table 4.7. Thermal conductivity and resistance of packed granular size (20 × 40) with calibration line from circular sample block made of PEEK material.

The following are some disadvantages which cause inaccuracy in measuring thermal conductivity with the circular sample holder:

- The interfacial thermal resistance $R_{internal}$ introduces surface roughness of the sample at the contact places with the hot and cold surfaces of the Anter machine. The interfacial thermal resistance obtained from the calibration process of the circular sample block made of PEEK material is in reality less than the interfacial thermal resistance of the packed GAC.

- To find the $R_{internal}$ (interfacial thermal resistance) on thermal conductivity, we need to pack the carbon with the same density but different thicknesses. It is rarely possible to achieve this goal with this kind of sample holder.
- Because of weak clamping force between the hot and cold plates, it is not possible to achieve higher densities of GAC packing.

Step 5:

The issues with the circular sample holder led us to improve it by using two aluminium square blocks with *2"* sides. Figure 4.30 shows the two aluminium blocks connected to each other, with a gap between them, using rectangular PVC material with high thermal resistance. The high thermal resistance of the PVC material prevents the thermal bridge effect between the two aluminium blocks. To provide different gap thicknesses, simply change the heights of the rectangular PVC in the sample holder stack.

The advantage of this sample holder is that it allows for packed GAC with the same density but different thickness. Regarding the third step, it is now possible to calculate the $R_{internal}$ (interfacial thermal resistance) for each specific density and substrates from the packed GAC's thermal resistance.

Figure 4.30. Rectangular sample holder stack with aluminium blocks and different PVC spacer.

In this step, the granular activated carbon, with mesh sizes of *20 × 40 (0.85 mm × 0.425 mm)*, 30×70 *(0.6 mm × 0.212 mm)* and 50×100 *(0.3 mm × 0.15 mm)* was packed between aluminium plates and located between the hot and cold heads of the Anter machine and the *ΔT sample / ΔT reference* was measured. Afterwards, by using the thermal resistance coefficient for the square shape block made of PEEK

material as in Table 4.5, and using the calibration line in Figure 4.31, we calculated the packed thermal resistance and conductivity. All results are summarised in Table 4.8. For the same density, we could say that the sample thermal resistance found in the square shape block of PEEK material has a connection with the interfacial thermal resistance, sample thickness and the sample's real thermal conductivity. If Equations 4.37 and 4.37a are solved simultaneously, the values of λ and $R_{internal}$ will be found for the same density.

$$R_1 = R_{Interface} + \frac{Thickness_1}{\lambda} \qquad (4.37) \qquad R_2 = R_{Interface} + \frac{Thickness_2}{\lambda} \qquad (4.37a)$$

Thickness mm	***Density kg.m^{-3}***	***ΔT sample / ΔT reference***	***Thermal Resistance m^2.K.W^{-1}***	***Thermal Conductivity W.m^{-1}.K^{-1}***	$R_{internal}$ ***m^2.K.W^{-1}***	λ ***W.m^{-1}.K^{-1}***
30×70 mesh size (0.6 mm × 0.212 mm)						
5.18	534.6	9.894	2.15 e^{-2}	0.24	2.489e^{-3}	0.292
9.65	539.5	17	4.22 e^{-2}	0.23		
20×40 mesh size (0.85 mm × 0.425 mm)						
5.18	546.4	10.793	2.42 e^{-2}	0.21	6.469e^{-3}	0.216
9.65	547.8	16.254	3.95 e^{-2}	0.24		
50×100 mesh size (0.3 mm × 0.15 mm)						
5.18	452.9	19.755	4.93 e^{-2}	0.2	2.728e^{-2}	0.235
9.65	483.2	26.574	6.83 e^{-2}	0.23		

Table 4.8. Thermal conductivity and resistance of 208C packed with square PEEK calibration line.

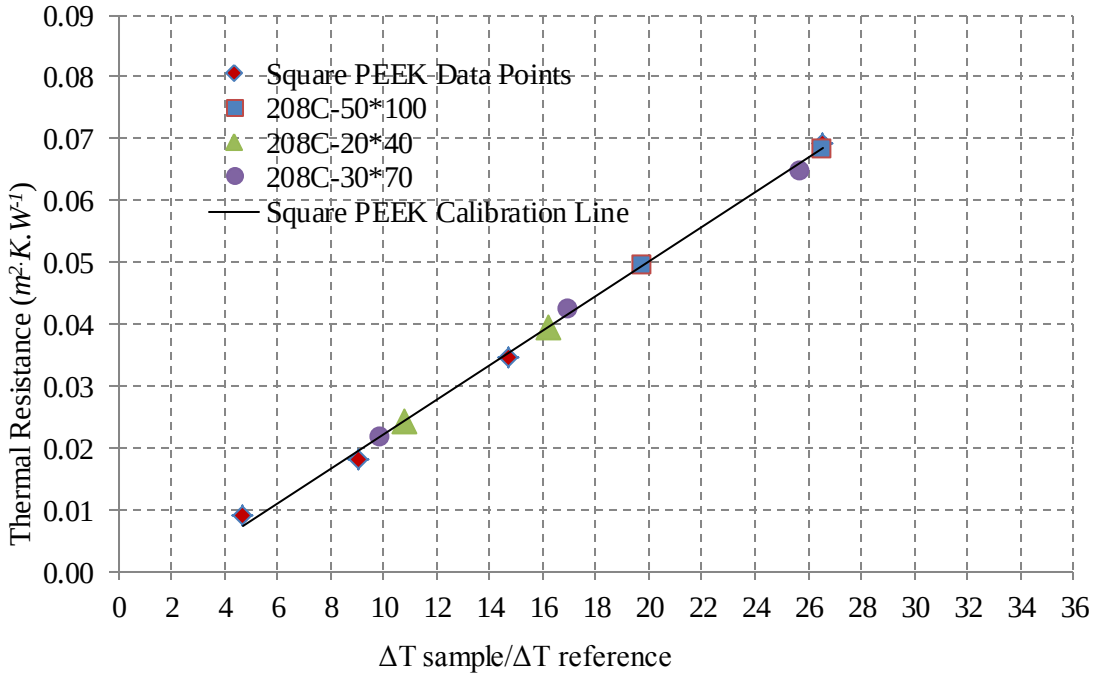

Figure 4.31. Square packed GAC thermal resistance with square PEEK calibration line.

4.5.2. Transient test

By setting up the time step or time increment (*dt*) and length step or length increment (*dr*) for tests with inert gas and refrigerant, the temperature of each node in Figure 4.9 was calculated using the heat transfer coefficients of the contact wall/packed carbon (*h*) and intrinsic thermal conductivity (λ) in Equation 4.35. Therefore, at the end of the numerical analysis for the specified *h* and λ values, the node temperature profile for the time period of the analysis was achieved.

Finally, to identify *h* and λ values for each density, the modelled temperature profile with in-house code in MATLAB R2012b for the centre node was compared with the experimental data for the same node through the optimization of the Mean Square Error (*MSE*) in Equation 4.38.

$$MSE = \frac{1}{n}\sum_{i=1}^{n}\left(T_{calculated\ i} - T_{\text{experimental } i}\right)^2 \quad (4.38)$$

4.5.2.1. Inert gas effect on thermal parameters

In order to conduct the iteration process, the time increment was set as *1 second* and the distance between the inside wall of the sample holder and the outside wall of the thermocouple tube was divided in to the *10* carbon layers. *10* layers represent the length step (*dr*) in the radial direction as a *0.882 mm*. In the model of the heat flow through the packed bed with inert gas, no adsorption effect was taken into account, thus the amounts of maximum concentration in Equation 4.23 and heat of the sorption in Equation 4.24 were assumed to be zero. The pressure of the system was assumed to be an atmospheric pressure.

Figure 4.32 and Figure 4.33 show the temperature profiles with minimum (*546.7* $kg.m^{-3}$) and maximum (*768.1* $kg.m^{-3}$) densities, respectively. The gap between both experimental data and model predictions of the temperature in the centre was well minimised. Figure 4.34 illustrates multiple values of *MSE* that were explored for the first sample (density *546.7* $kg.m^{-3}$) in a range of 0.*08* $W.m^{-1}.K^{-1} < \lambda < 0.2\ W.m^{-1}.K^{-1}$ with an increment of *0.01* $W.m^{-1}.K^{-1}$ and *90* $W.m^{-2}.K^{-1} < h < 200\ W.m^{-2}.K^{-1}$ with an increment of *1* $W.m^{-2}.k^{-1}$. For a particular density, the minimum *MSE* was obtained from the optimization process, as *0.2363*. All the samples were tested and the final results of the thermal conductivity (λ) and heat transfer coefficient of the contact wall/packed carbon (*h*) were identified; they are summed up in Table 4.9. Overall, a fairly good fit with a minimum *MSE* was obtained for each density.

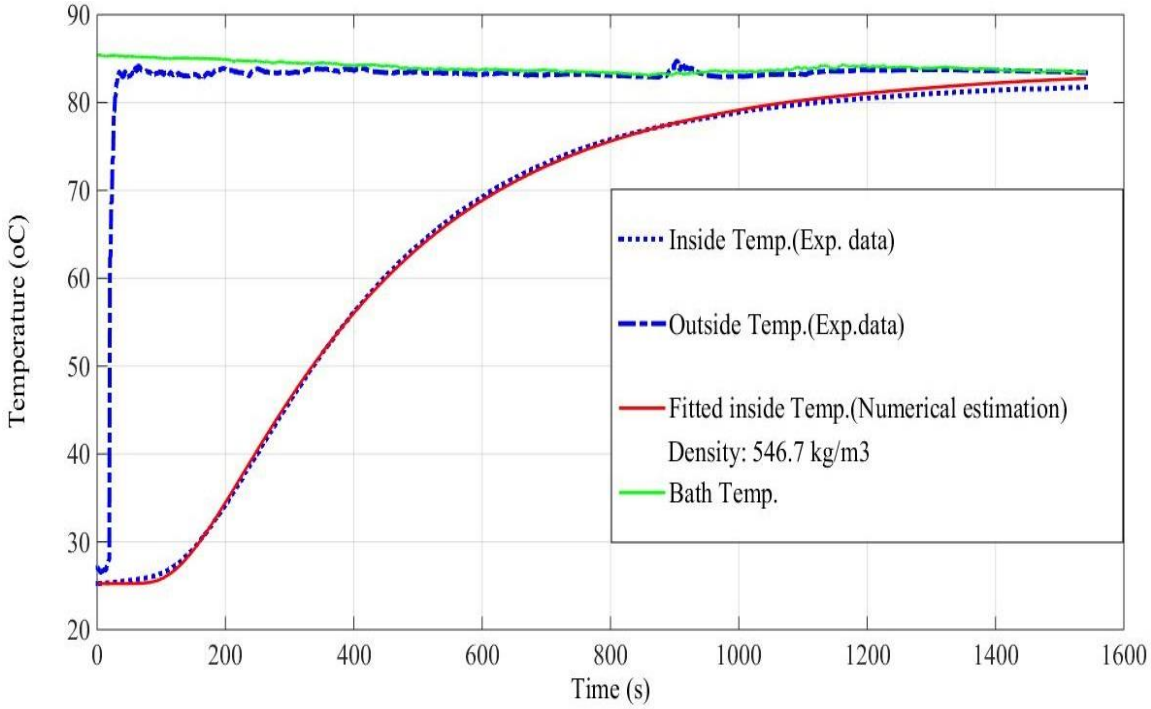

Figure 4.32. Temperature profiles with packed density of *546.7 kg.m^{-3}*, *λ = 0.2 W.m^{-1}.K^{-1}* and *h =149 W.m^{-2}.K^{-1}*.

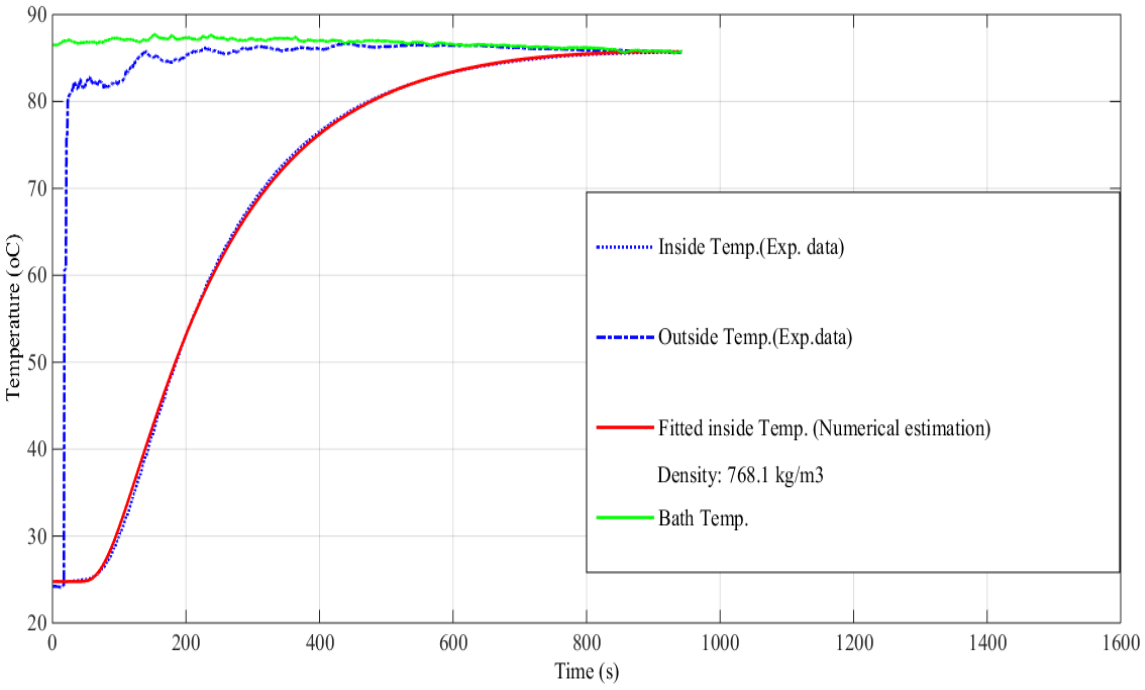

Figure 4.33. Temperature profiles with packed density of *768.1 kg.m^{-3}*, *λ = 0.48 W.m^{-1}.K^{-1}* and *h =1181 W.m^{-2}.K^{-1}*.

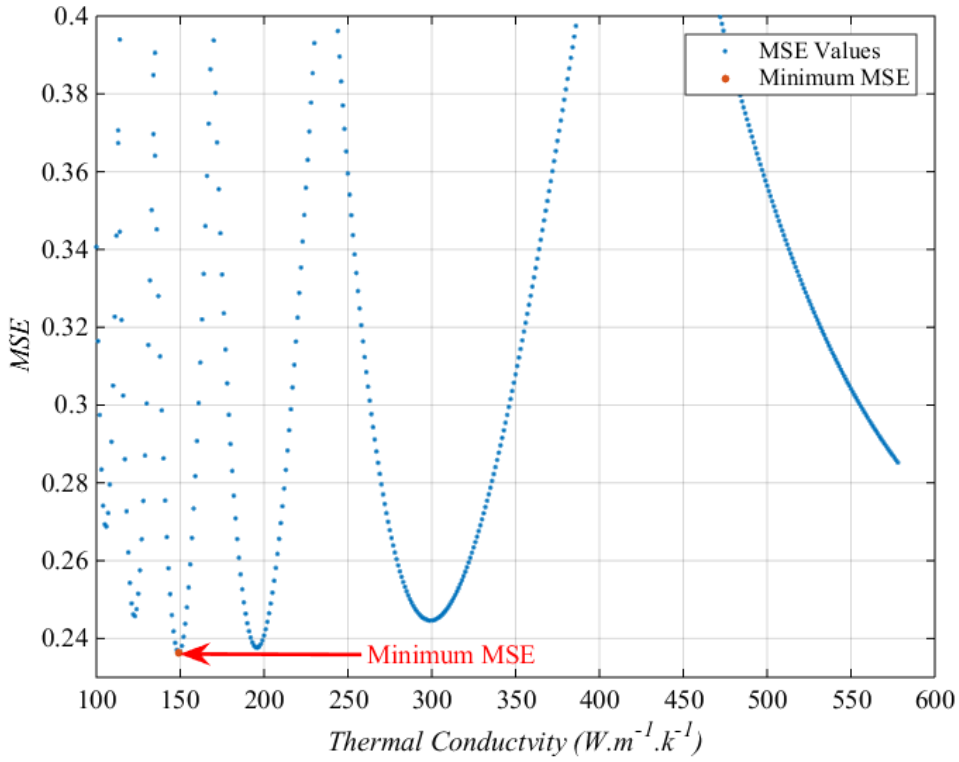

Figure 4.34. Thermal conductivity *MSE* values for carbon in ambient air; density is *546.7* $kg.m^{-3}$.

Density	***λ***	***h***	***MSE***
Kg.m^{-3}	***W.m^{-1}.K^{-1}***	***W.m^{-2}.K^{-1}***	
546.7	0.2	149	0.2363
625.9	0.31	302	0.1615
661.8	0.4	361	0.2274
707.7	0.42	519	0.2721
749.7	0.44	722	0.1508

Table 4.9. Summary of thermal properties for granular activated carbon packed in ambient air at different densities of packing.

Figures 4.35 and 4.36 show the thermal conductivity (λ) and heat transfer coefficient of the contact wall/packed carbon (h) function of the packed carbon density, respectively. As expected, both thermal conductivity (λ) and heat transfer coefficient (h) increase quasi-linearly with density. Table 4.10 shows a summary of the quasi-linear dependency of the thermal properties of granular activated carbon to the density of the packed bed.

Properties	***Estimation Equation***
For λ ($W.m^{-1}.K^{-1}$)	$\lambda = 0.0012\ \rho - 0.4555 \pm 0.02$
For h ($W.m^{-2}.K^{-1}$)	$h = 2.7292\ \rho - 1386.3 \pm 45$

Table 4.10. Fitted curve of the thermal properties vs packed density for an inert gas and carbon pair.

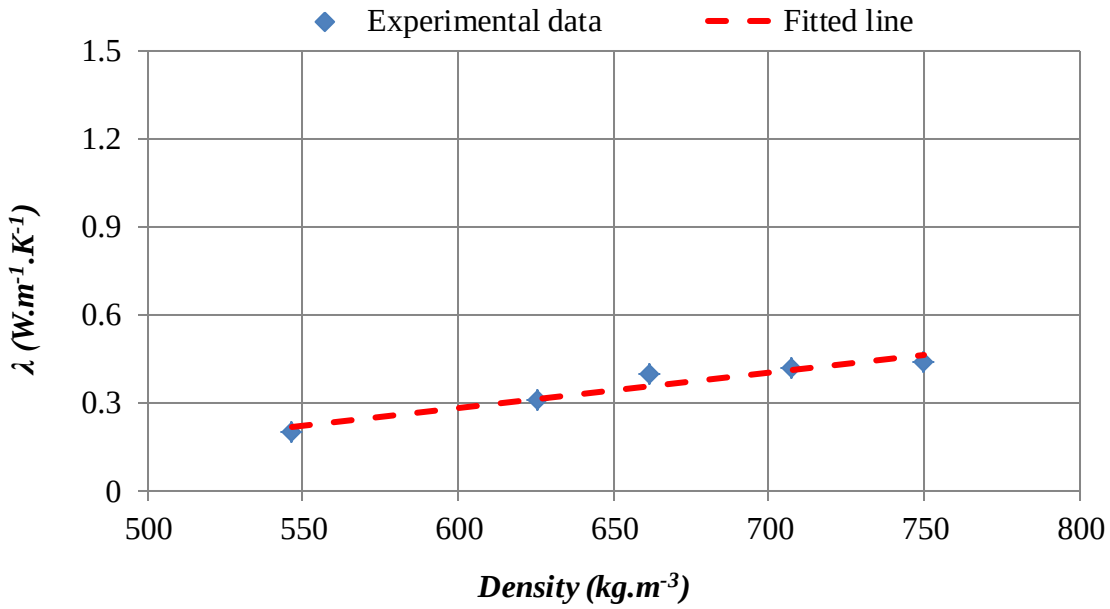

Figure 4.35. Thermal conductivity vs sample packed density experimental data in ambient air.

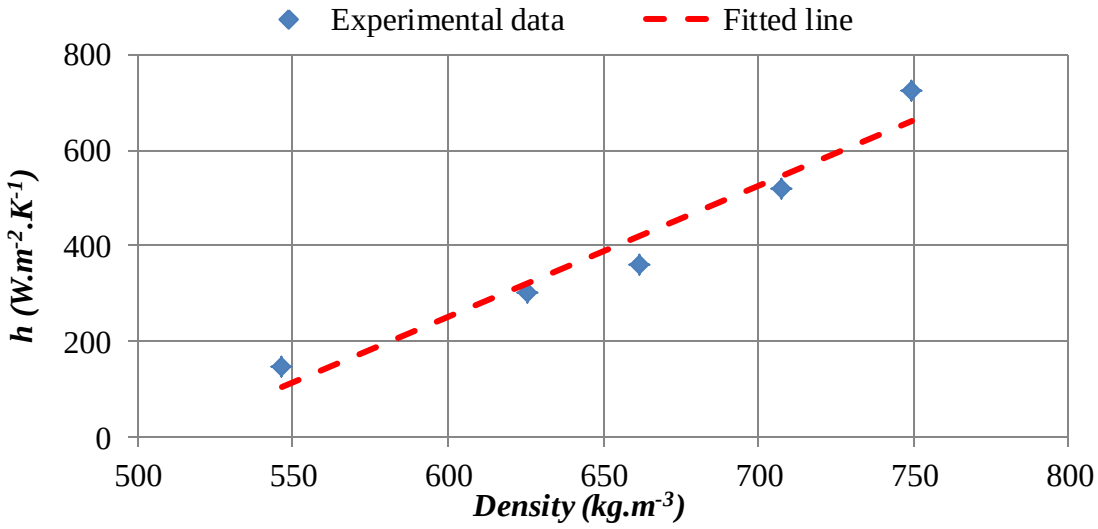

Figure 4.36. Heat transfer coefficient of the contact wall/packed carbon vs sample packed density experimental data in ambient air.

4.5.2.2. R723 refrigerant effect on thermal parameters

In order to conduct the iteration process, time and length increments were set up the same as the air-carbon pair test analysis, at *1 second* and 0.882 *mm* respectively.

Figure 4.37 and Figure 4.38 show the temperature profiles with minimum (*625.9 kg.m*$^{-3}$) and maximum (*749.7 kg.m*$^{-3}$) densities, respectively. The gap between experimental data and model predictions of the temperature at the centre was well minimised. Table 4.11 provides a summary of analysis results, allowing us to find the thermal properties of R723 and granular activated carbon pair with different packed bed densities.

Figures 4.37 and 4.38 show that all samples of the R723-GAC pair at the end of the experiment reach the same centre temperature (the same as the boiler set temperature, *90 ^{o}C*) and system pressure. Therefore, by increasing the packed density from 625.9 *kg.m^{-3}* to *749.7 kg.m^{-3}* the reaching time was changed from *900 seconds* to *750 seconds*.

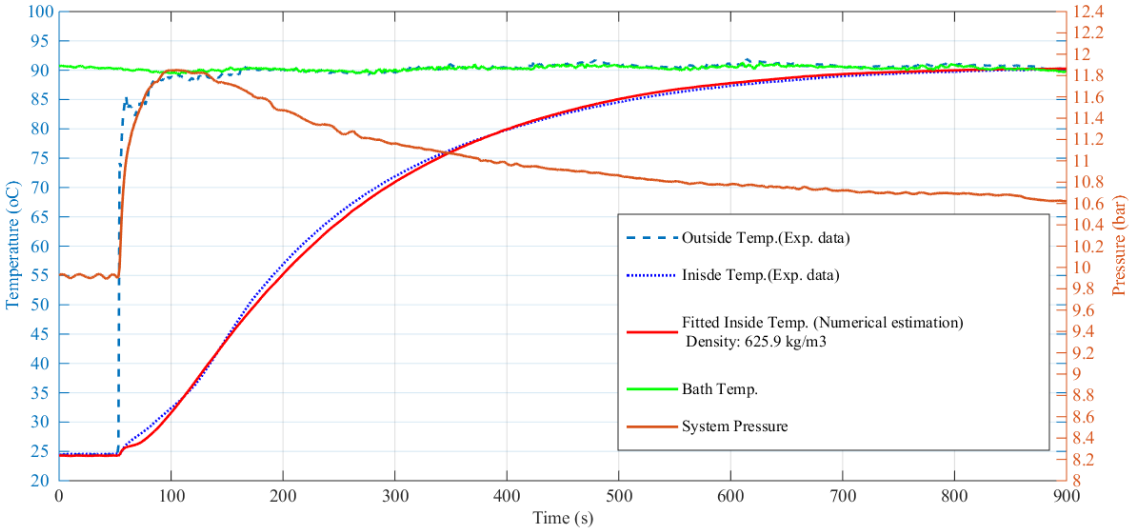

Figure 4.37. Temperature profiles for R723 and carbon pair with packed density of *625.9 kg.m^{-3}*, λ = *0.2 W.m^{-1}.K^{-1}* and *h =149 W.m^{-2}.K^{-1}*.

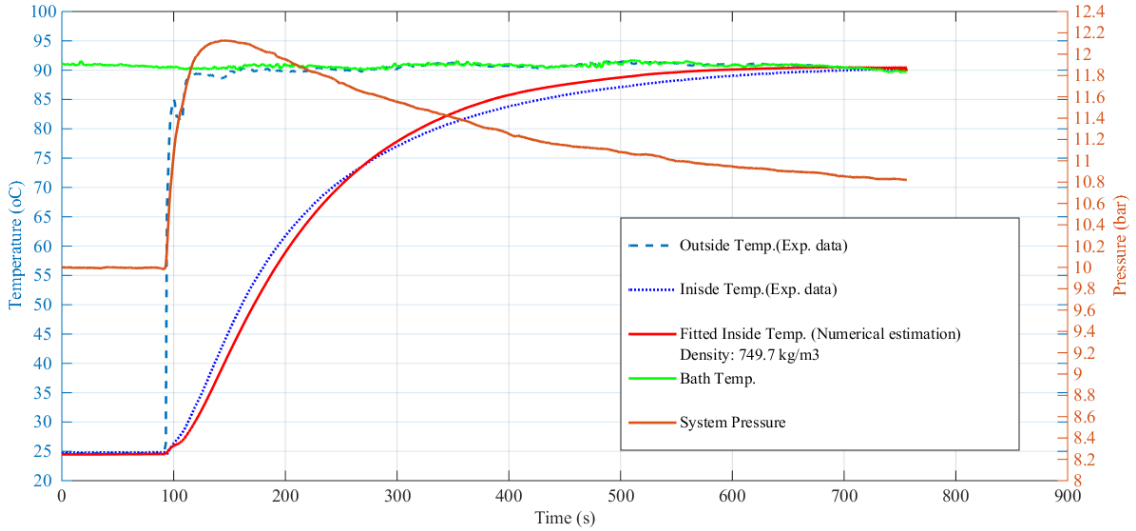

Figure 4.38. Temperature profiles for R723 and carbon pair with packed density of *749.7 kg.m^{-3}*, λ = *0.48 W.m^{-1}.K^{-1}* and *h =1181 W.m^{-2}.K^{-1}*.

Density	***λ***	***h***	***MSE***
Kg.m^{-3}	***W.m^{-1}.K^{-1}***	***W.m^{-2}.K^{-1}***	
625.9	0.77	390	0.3557
661.8	1.19	451	0.8498
707.7	1.26	536	0.7063
749.8	1.36	735	0.6982

Table 4.11. Summary of thermal properties of R723 and granular activated carbon packed pairs at different densities of packing.

Figures 4.39 and 4.40 show the thermal conductivity (λ) and heat transfer coefficient of the contact wall/packed carbon (h) function of the packed carbon density, respectively. As expected, both thermal conductivity (λ) and heat transfer coefficient (h) increase quasi-linearly with density.

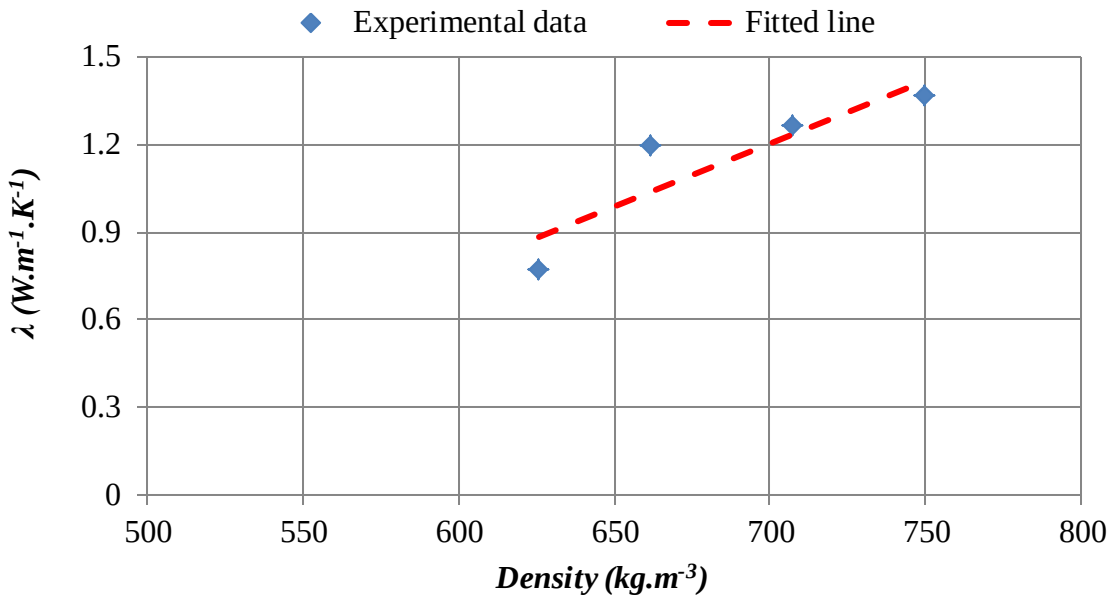

Figure 4.39. Thermal conductivity vs sample packed for R723 and carbon pair.

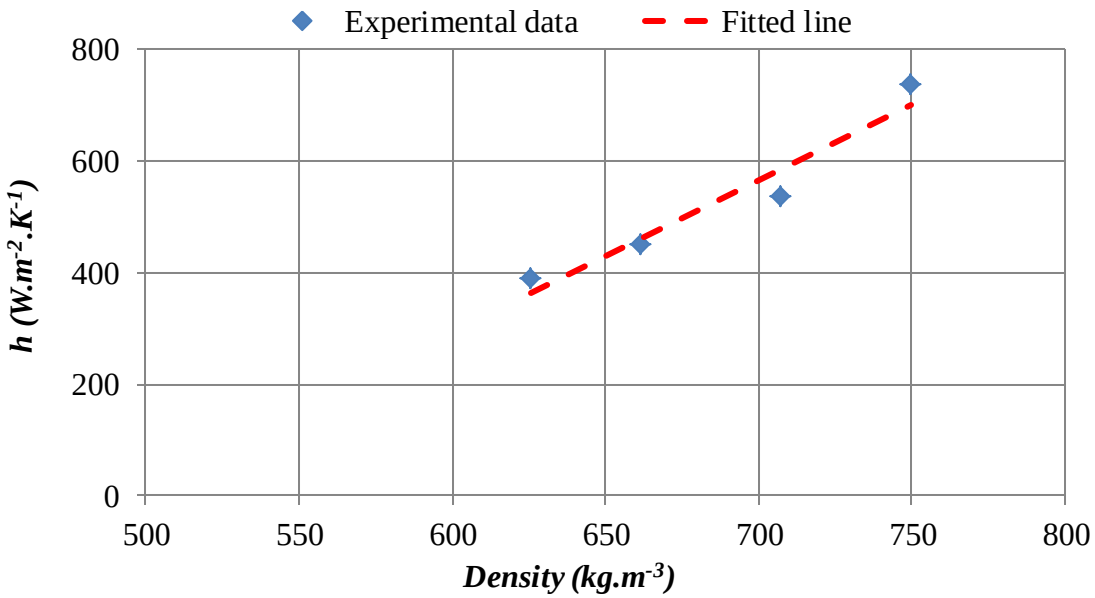

Figure 4.40. Heat transfer coefficient of the contact wall/packed carbon vs sample packed density for R723 and carbon pair.

Table 4.12 provides a summary of the quasi-linear dependency of the thermal properties of GAC in respect of R723 to the density of packed bed.

Properties	***Estimation Equation***
For λ ($W.m^{-1}.K^{-1}$)	$\lambda = 0.0043\ \rho - 1.8147 \pm 0.1$
For h ($W.m^{-2}.K^{-1}$)	$h = 2.6939\ \rho - 1320.8 \pm 33.6$

Table 4.12. Fitted curve of the thermal properties vs packed density for R723 and carbon pairs.

Figure 4.41 shows the average concentration of R723 in granular activated carbon. For all densities, the average concentration is fairly constant, as expected, because the operating conditions (pressure and temperature) are nearly the same for all modules. The maximum of *2%* difference of average concentration can be seen between the minimum (*625.9 kg.m*$^{-3}$) and maximum (*749.7 kg.m*$^{-3}$) densities.

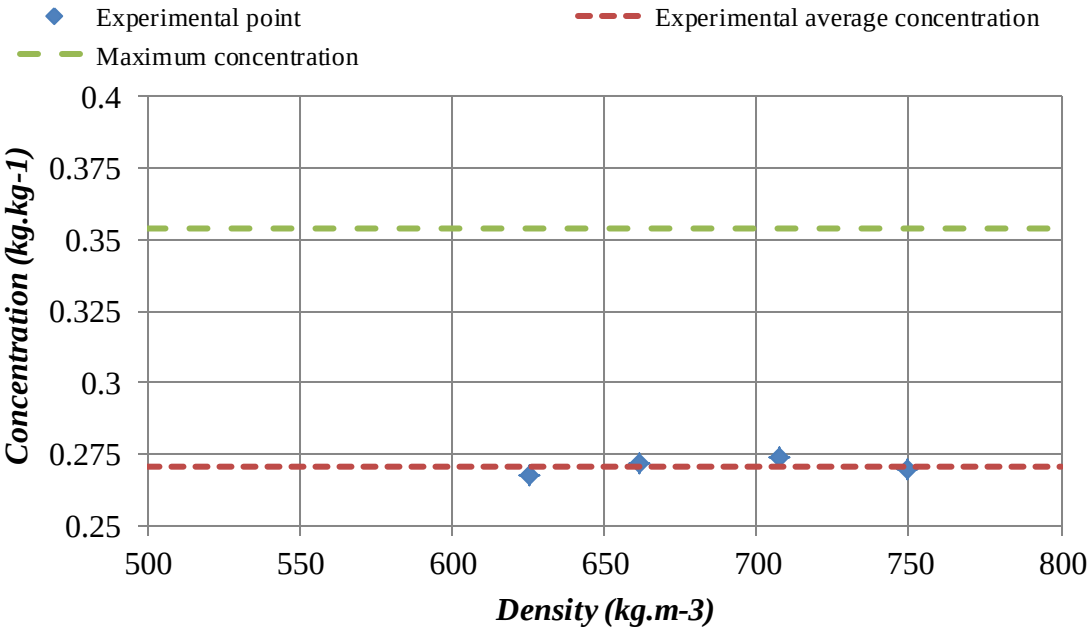

Figure 4.41. Average concentration of R723 in granular activated carbon.

Table 4.13 is a summary of Figures 4.42 and 4.43, which show the effect of concentration and density together on granular packed bed thermal properties. Figure 4.42 shows the predicted thermal conductivity 'λ' value based on linear regression versus density and concentration with experimental values. Therefore, packed density and concentration together have a linear effect on packed thermal conductivity prediction. Figure 4.43 shows the predicted heat transfer coefficients of the contact wall/packed carbon 'h' values based on linear regression versus density and concentration with experimental values. Therefore, packed density and concentration together have a linear effect on packed heat transfer coefficients of the contact wall/packed carbon prediction.

Properties	***Estimation Equation***
For λ ($W.m^{-1}.K^{-1}$)	$\lambda = 2.787\ x + 0.0026\ \rho - 1.4175 \pm 0.11$
For h ($W.m^{-2}.K^{-1}$)	$h = 192.5926\ x + 3.0562\ \rho - 1621.4058 \pm 19.16$

Table 4.13. Fitted curve of thermal properties vs packed density and R723 concentration.

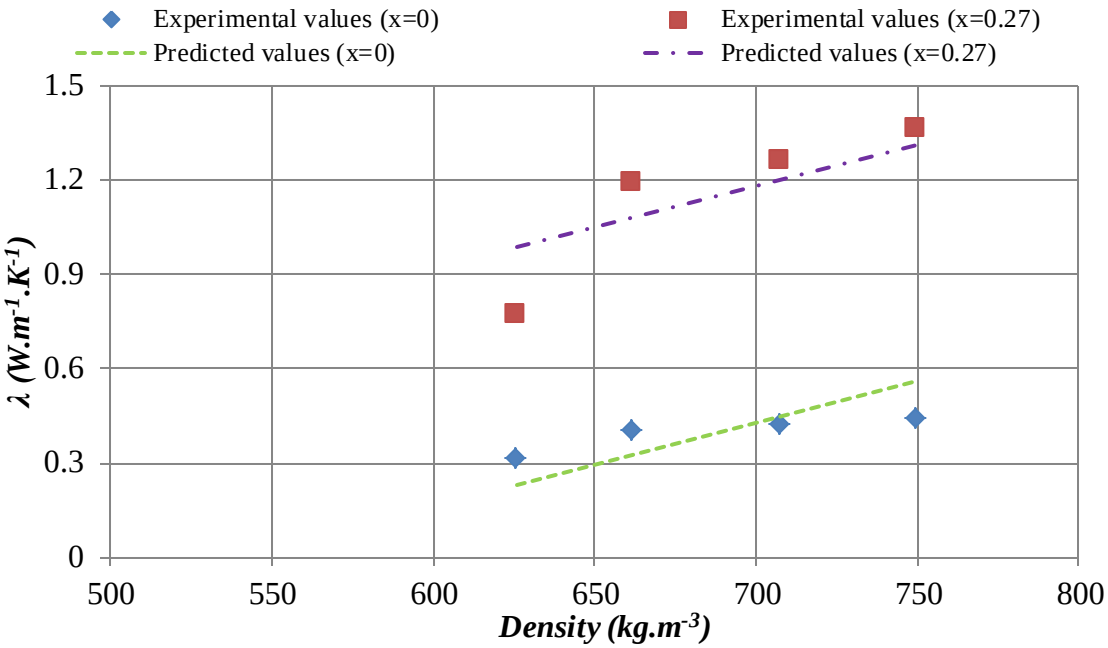

Figure 4.42. Experimental and linear regression predated values (Table 4.13) of thermal conductivity 'λ' vs density of packed bed and concentration of R723.

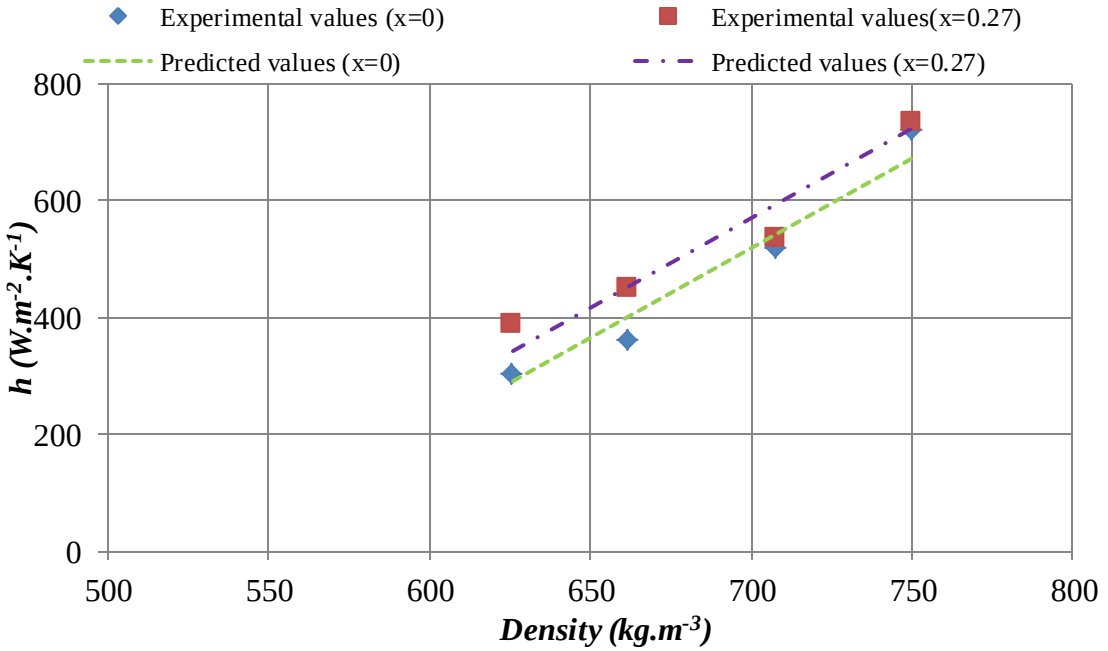

Figure 4.43. Experimental and linear regression predated values (Table 4.13) of heat transfer coefficients of the contact wall/packed carbon 'h' vs density of packed bed and concentration of R723.

4.6. Conclusions

In this chapter, measurement of '*h*' (heat transfer coefficient of the contact wall/packed carbon) and 'λ' (thermal conductivity) of a granular activated carbon packed bed was carried out at the density range of *625.9* $kg.m^{-3}$ to *749.7* $kg.m^{-3}$. In general, the air-GAC pair thermal conductivity changes from *0.31* $W.m^{-1}.K^{-1}$ to *0.44* $W.m^{-1}.K^{-1}$, while the thermal conductivity of the R723-GAC pair changes from 0.77 $W.m^{-1}.K^{-1}$ to 1.36 $W.m^{-1}.K^{-1}$, for packing with a density of 625.9 $kg.m^{-3}$ and *749.7* $kg.m^{-3}$, respectively. For the same densities, the heat transfer coefficients of the contact wall/packed carbon for the air-GAC pair changes from 302 $W.m^{-2}.K^{-1}$ to 722 $W.m^{-2}.K^{-1}$, while for the R723-GAC pair it changes from 390 $W.m^{-2}.K^{-1}$ to 735 $W.m^{-2}.K^{-1}$.

In comparison, the results obtained from the transient method show that the R723 refrigerant improved the thermal conductivity of the packed GAC and the heat transfer coefficient of the contact wall/packed carbon by an average of *180%* and *19%*, respectively. The thermal properties of packed GAC in the presence of air and R723 refrigerant in total increase by quasi-linear behaviour.

By reviewing the steady state method, we can see that it shows the difficulties of making samples with different densities, while keeping their height constant in circular shapes. The inconsistency in sample height prevents us from making comparisons and from finding the packed sample density effect on packed thermal properties. This problem led us to design a new sample holder (the square sample holder), gaining the advantages of packing the granular carbon at the same density with different heights. This advantage helped us to substrate the interfacial thermal resistance of the packed carbon from packed thermal resistance itself. Nevertheless, in the square shape sample holder it is not possible to measure the thermal properties of packed GAC in the presence of refrigerants. For the air-GAC packed pair, a comparison of the square shape sample holder results with the cylindrical sample holder results for the same density of *546* $kg.m^{-3}$ shows that we measured the thermal conductivity for the steady state method at *0.22* $W.m^{-1}.K^{-1}$, while in the transient method it was measured *0.2* $W.m^{-1}.K^{-1}$, which is *9%* less than in the steady state method. For the heat transfer coefficient of the contact wall/packed carbon, this shows that using the steady state method it is *154.5* $W.m^{-2}.K^{-1}$, while using the transient method for the cylindrical shape sample holder it is *149*$W.m^{-2}.K^{-1}$, which is

3.6% less than the steady state method with the square shape sample holder. Therefore, the steady state method with the square shape sample holder can be one of the recommended methods of measuring the thermal properties of a granular activated carbon packed bed in the presence of air.

A second method was suggested, based on transient heat transfer with reversed analysis in order to find the thermal parameters. The suggested method represents the thermal generator's physical appearance, and the credibility of measuring the thermal parameters in the presence of refrigerant gas; it is difficult to achieve both of these at the same time in the sample holder that was made previously. The tests with air and refrigerant show that an increase in packed density causes the time taken by the centre temperature to reach the boiler's set temperature to decrease. For minimum and maximum densities of the air-GAC packed pair, this time decreased by *50%*, and for R723-GAC packed pair the time decreased by *17%*.

Finding the thermal properties of a granular packed bed based on packing density and concentration allows us to use that information for finding the performance of the thermal generator. For a certain amount of density (*500 kg.m*$^{-3}$ to *800 kg.m*$^{-3}$) and refrigerant concentration, it is possible to find the thermal properties required using the correlations for different size and physical appearance of the generator, using an activated carbon-*R723* pair, in terms of performance of adsorption refrigeration, for air conditioning, ice making and heat pump applications.

References

[1]. R. E. Critoph, L. Turner, Heat transfer in granular activated carbon beds in the presence of adsorbable gases, International Journal of Heat and Mass Transfer, 1995; 38(9): 1577-1585.

[2]. Z. Tamainot-Telto, R.E. Critoph, Thermophysical properties of monolithic carbon, International Journal of Heat and Mass Transfer, 2000; 43(11): 2053-2058.

[3]. Z. Tamainot-Telto, R.E. Critoph, Monolithic carbon for sorption refrigeration and heat pump applications, Applied Thermal Engineering, 2001; 21(1): 37-52.

[4]. Z. Tamainot-Telto, R.E. Critoph, Adsorption refrigerator using monolithic carbon-ammonia pair, International Journal of Refrigeration, 1997; 20(2): 146-155.

[5]. L.W. Wang, S.J. Metcalf, R.E. Critoph, R. Thorpe, Z. Tamainot-Telto, Thermal conductivity and permeability of consolidated expanded natural graphite treated with sulphuric acid, Carbon, 2011; 49(14): 4812–4819.

[6]. L.W. Wang, S.J. Metcalf, R.E. Critoph, R. Thorpe, Z. Tamainot-Telto, Development of thermal conductive consolidated activated carbon for adsorption refrigeration, Carbon, 2012; 50(3): 977-986.

[7]. T. H. Eun, H. K. Song, J. H. Han, K. H. Lee, J. N. Kim, Enhancement of heat and mass transfer in silica-expanded graphite composite blocks for adsorption heat pumps: Part I. Characterization of the composite blocks, International Journal of Refrigeration, 2000; 23 (1): 64-73.

[8]. T. H. Eun, H. K. Song, J. H. Han, K. H. Lee, J. N. Kim, Enhancement of heat and mass transfer in silica-expanded graphite composite blocks for adsorption heat pumps. Part II. Cooling system using the composite blocks, International Journal of Refrigeration, 2000; 23 (1): 74-81.

[9]. H. Yanahi, N. Ino, Heat and mass transfer characteristics in consolidated silica gel/water adsorption –cooling system. ASME ASIA, 1997; 97-AA-33.

[10]. J.J. Guilleminot, A. Choisier, J.B. Chalfen, S. Nicolas, J.L. Reymoney, Heat transfer intensification in fixed bed adsorbers, Heat Recovery Systems and CHP, 1993; 13 (4): 297-300.

[11]. Argo, W. B., and J. M. Smith, "Heat Transfer in Packed Beds: Prediction of Radial Rate in Gas-Solid Beds," Chem. Eng. Prog., 1953; 49: 443-454.

[12]. S. Yagi, D. Kunni, Studies on effective thermal conductivities in packed beds, A.I.Ch.E. Journal, 1957; 3: 373-381.

[13]. Calderbank, P. H., and L. A. Pogorski, "Heat Transfer in Packed Beds," Trans. Instn. Chem. Engrs., 1957; 35: 195-202

[14]. G. Flamant, N. Fatah, Y. Flitris, Wall-to-bed heat transfer in gas—solid fluidized beds: Prediction of heat transfer regimes, Powder Technology, 1992; 69 (3): 223–230.

[15]. A.V. Luikov, A.G. Shashkov, L.L. Vasiliev, Yu.E. Fraiman, Thermal conductivity of porous systems, International Journal of Heat and Mass Transfer, 1968; 11(2): 117–140.

[16]. G.J. Cheng, A.B. Yu, P. Zulli, Evaluation of elective thermal conductivity from the structure of a packed bed, Chemical Engineering Science, 1999; 54(19): 4199–4209.

[17]. K. Ofuchi, D. Kunii, Heat transfer characteristics of packed beds with stagnant fluids, International Journal of Heat and Mass Transfer, 1965; 8(5): 749-757.

[18]. Holman, J.P. (1976). Heat Transfer. McGraw-Hill, Inc., 1-22.

[19]. D.L. Swift, The thermal conductivity of spherical metal powder including the effect of an oxide coating, International Journal of Heat and Mass Transfer, 1966; 9: 1061–1074.

[20]. M. Okazaki, T. Yamasaki, S. Gotoh, R. Toei, Effective thermal conductivity for granular beds of various binary mixtures, J. Chem. Eng. Jpn., 1981; 14:183–189.

[21]. Z.P. Shulman, L.N. Novichyonok, E.P. Belskaya, B.M. Khusid, V.V. Melnichenko, Thermal conductivity of metal-filled systems, International Journal of Heat and Mass Transfer, 1982; 25:643–651.

[22]. Silas E. Gustafsson, Transient plane source techniques for thermal conductivity and thermal diffusivity measurements of solid materials, Review of Scientific Instruments, 1991; 62(3): 797-804.

[23]. R. P. Tye, L. Kubicar, N. Lockmuller, The Development of a Standard for Contact Transient Methods of Measurement of Thermophysical Properties, International Journal of Thermophysics, 2005; 26(6): 1917-1938.

[24]. M. van Smoluchowski, Uber die Wiirmeleitung pulverfiirmiger Korpcr und ein hierauf gegrilndetes neues Warmeisolierungsverfahren, Bericht iiber den 2. Int. Kiiltekongrep, Vol. 2, Vienna, 1910.

[25]. T. E. W. Schumann and V. Voss, Heat flow through granulated material, Fuel, 1934; 13(8): 249-256.

[26]. S. Tavman, I. H. Tavman, S. Evcin, Measurement of thermal diffusivity of granular food materials, International Communications in Heat and Mass Transfer, 1997; 24(7): 945–953

[27]. A. Tansakul, R. Lumyong, Thermal properties of straw mushroom, Journal of Food Engineering, 2008; 87(1): 91–98.

[28]. A. Baïri, N. Laraqi, J.M. García de Maríab, Determination of thermal diffusivity of foods using 1D Fourier cylindrical solution, Journal of Food Engineering, 2007; 78(2): 669–675.

[29]. N. Ukrainczyk, Thermal diffusivity estimation using numerical inverse solution for 1D heat conduction, International Journal of Heat and Mass Transfer, 2009; 52(25-26): 5675–5681.

[30]. Z. Tamainot-Telto, Novel explanation of Dubinin-Astakhov theory in sorption reactors design for refrigeration and heat pump application, International sorption heat pump conference, ISHPC 2014, March 31 – April 2, 2014, Washington DC-USA; Paper No.84.

Chapter 5

Adsorption capacity of granular activated carbon

5.1. Introduction

This section deals with the adsorption capacity characteristics of activated carbon with R723 and its pure components R717 and RE170. Carbon characteristics such as pore volume and adsorption energy were measured. The adsorption capacity of activated carbon, which is the ability of activated carbon to adsorb a specific gas at different pressures and temperatures, was then investigated using the Dubinin-Astakhov adsorption model.

5.2. Activated carbon

Activated carbon is a solid and porous material which has properties more or less the same as graphite (see Figure 5.1). Graphite itself has a layer structure, formed from carbon atoms in a regular hexagonal layer, with each layer joining the other perpendicularly.

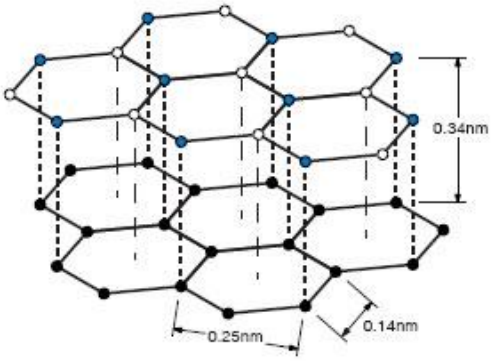

Figure 5.1. Structure of graphite (adopted from Nanosurf AG Ltd).

Activated carbon differs in structure from graphite, because it has a more random structure, as shown in Figure 5.2. The structure of activated carbon, which is often referred to as amorphous carbon, is an imperfect form of graphite, which causes a

high degree of adsorption capacity. Pores can form between plates or in visible cracks and fractures. Pores can be in a variety of sizes, and are classified according to pore diameter by the International Union of Pure and Applied Chemistry (IUPAC) [2, 3] as follows:

- Micropores $\leq 2\ nm$
- $2\ nm \leq$ mesopores $\leq 50\ nm$
- Macropores $\geq 50\ nm$

Macropores behave like pathways which help adsorbate molecules travel into the pores in range of mesopores and afterwards into the micropores level. Most gas adsorption takes place at the micropore level.

Any carbon source can be turned into activated carbon. The process of activated carbon formation is divided into activation and carbonization. The production of activated carbon can be according to either a physical or chemical model [4].

In the physical activation process the carbon skeleton itself is composed of a starting material such as coal or nutshells (e.g. coconut shells or walnut shells); non-carbon elements are removed in gaseous form at high temperatures (greater than 600^oC) in the presence of inert gases such as argon or nitrogen, leading to pyrolytic decomposition. The pores develop later on in the activation process. The activation process will continue in carbonised material in the presence of carbon dioxide, oxygen or steam at temperatures higher than 600^oC [5] .

Figure 5.2. A schematic representation of the structure of activated carbon [1].

Chemical activation, in comparison with the physical process, is a single-step method in which the carbonization and activation happen simultaneously at atmospheric temperatures in the range of 400^oC to 600^oC. Because of the lower temperature range used for the chemical activation process, the development of the porous structure is better compared to the physical activation method. The chemical agents used in chemical activation are normally alkali and alkaline earth metals containing substances such as potassium hydroxide (KOH), zinc chloride ($ZnCl_2$) and magnesium chloride ($MgCl_2$) [4].

This project used 208-C granular activated carbon based on coconut shells and the physical activation process, obtained from the Chemviron Company [6]. The particle size was in the range of $1.7mm$ to $0.595\ mm$, corresponding to a $12 \times 30\ US$ mesh sieve size.

5.3. Principal of physical adsorption

When the activated carbon comes into contact with a gas, the gas molecules strike the surface and some remain trapped. Brunauer [7] called this behaviour adsorption, "when the gas or vapour is brought in contact with an evacuated solid and takes up a part of it. The molecule disappears from the gas phase and either enters the inside of the solid or remains on the outside, attached to its surface." In this situation, the solid which takes the gas or vapour is called an adsorbent, and the gas which is attached to the solid surface or trapped inside is called the adsorbate.

Adsorption can take place in the form of physical adsorption (physisorption) or chemical adsorption (chemisorption). In physical adsorption, the driven force causing adsorption in the activated carbon is called Van er Waals force. When gas or vapour molecules are close enough to the surface, the Van der Waals force acts between the molecules of the adsorbate and the adsorbent surfaces. In chemical adsorption, the electron energy transference is significant and equivalent to the chemical bond between two substances, while in physical adsorption this interaction force is relatively weak. Table 5.1 shows in brief the differences between physical and chemical adsorption [8].

Chemical Adsorption	*Physical Adsorption*
Low heat of adsorption (<2 or 3 times latent heat of evaporation)	High heat of adsorption (>2 or 3 times latent heat of evaporation)
Mono-layer or multi-layer	Mono-layer only
No dissociation of adsorbed species	May involve dissociation
Reversible	Irreversible
No electron transfer, although polarisation of adsorbate may occur	Electron transfers leading to bond formation between sorbate and surface

Table 5.1. Chemical and physical adsorptions comparison [8].

This work mainly focuses on the equation for physical adsorption between solid/gas systems. The solid part or adsorbent is 208-C granular activated carbon, and the adsorbates are ammonia (R717), dimethyl ether (RE170) and R723 as an azeotropic mixture of ammonia and DME.

5.3.1. Adsorption equilibrium and isotherm

The amount of adsorbate that is adsorbed into an adsorbent is a function of pressure and temperature, and properties of both adsorbate and adsorbent. In conditions of equilibrium, the amount of adsorbate in mass, mole or volume which is adsorbed per unit mass of adsorbent at a constant temperature against the relative pressure (P/P_o) is called the adsorption isotherm. The adsorption isotherm, shown in Figure 5.3 for physical adsorption, is divided in general into six types [3, 9]. A Type I isotherm is typical adsorption for material with micropores (less than *2 nm*); the Langmuir model is commonly used to describe this isotherm [10]. Types II and III isotherms are typically used for non-porous materials with strong (Type II) or weak (Type III) fluid-wall interaction forces [10]. A Type IV isotherm is usually observed for mesoporous solids (pore size larger than *2 nm* and smaller than *50 nm*) where capillary condensation occurs, with strong gas-wall or fluid-wall forces, similar to Type II. In a Type IV isotherm a kind of hysteresis loop appears; this means that in the desorption process the amount of adsorbate is always higher than the adsorption process for a given relative pressure. A Type V isotherm is observed for mesoporous substances in which the gas-wall or fluid-wall force is weak, similar to Type III. In Type V isotherms the same hysteresis loop appears in the desorption process. A Type VI isotherm is observed in materials with very strong interaction forces which

causes multilayer formation, usually when the temperature is near the melting point of the adsorbed gas [10].

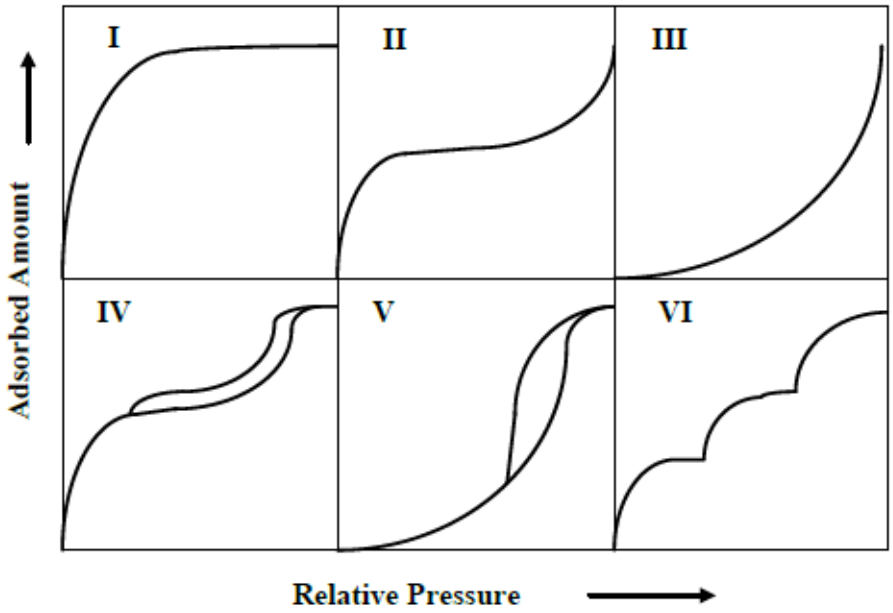

Figure 5.3. The six types of adsorption isotherms [3, 9, 10].

5.3.2. Theoretical modelling of adsorption isotherm

Different models have been proposed to describe the adsorption isotherm model. The first model was proposed by Freundlich [11] for monolayer and multilayer adsorption, and gives the amount of adsorbate per unit mass of adsorbent, while the Langmuir [12, 13] model assumes the adsorption on a solid is monolayer (Figure 5.4). The monolayer adsorption shown in Figure 5.4 (Type I isotherm) illustrates that the entire solid surface of the adsorbent is covered with one layer of adsorbate molecules, and the adsorbate molecules are stacked with another layer of adsorbate molecules. Therefore the Langmuir model gives the surface coverage of the adsorbent by adsorbate molecules. The Langmuir model could be used for chemisorption, while the Freundlich is not suitable for this use.

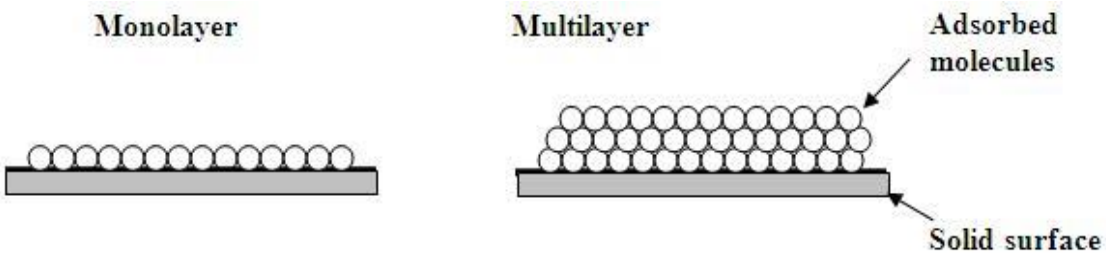

Figure 5.4. Comparison between monolayer and multilayer adsorption (adopted from NPTEL University – adsorption lecture notes [14]).

Brunauer and his colleagues [15] later improved the Langmuir model by incorporating the concept of multilayer adsorption. They assumed that the energy, which in the previous model was used to bind the layer of adsorbate to the surface of the adsorbent, has an influence on the adsorbate molecules up to a certain distance from the adsorbent surface. This force will cause monolayer adsorption on a solid surface.

The other model, which was proposed around 1914 by Polanyi [16, 17], assumes the existence of a potential field around the adsorbent. Figure 5.5 shows that the potential field can penetrate up to a certain level from the solid surface. The adsorbate exists in a compressed state and its density is varied from maximum to minimum, from a solid surface to $\varepsilon_3 = 0$. The adsorption potential ε is expressed by the following equation:

$$\varepsilon_i = R\ T\ ln\frac{P_2}{P_1} \tag{5.1}$$

where R (8.314×10^{-3} $kJ.mol^{-1}{\cdot}K^{-1}$) is the universal gas constant, T (K) is the absolute temperature, P_1 is the pressure of the adsorbate in its gaseous state (bar) and P_2 is the pressure of the compressed adsorbate on an equipotential surface (bar).

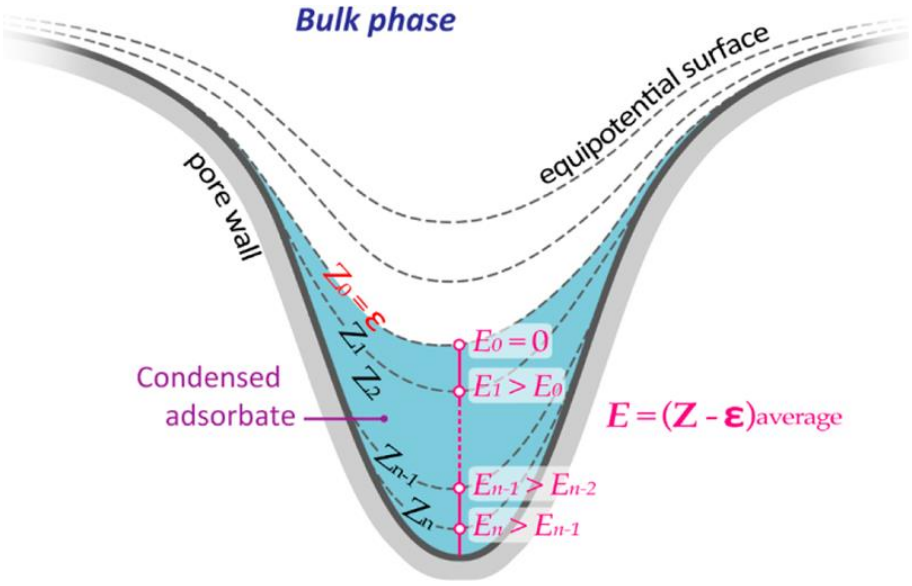

Figure 5.5. Representation of adsorption potential fields in activated carbon, characteristic energy (E), which reflects the average excess energy of an adsorbate at the adsorbed state as compared to that at the reference state. The dashed lines indicate equipotential surfaces [17].

Dubinin and Radushkevich [19] later utilized the Polanyi [18] and Berenyi [20] explanations and employed pore size Gaussian distribution, and proposed a

correlation (Equation 5.2) to explain equilibrium isotherm adsorption [21]. Dubinin's equations have several advantages, including:

1. Adsorbent property parameters;
2. Vapour property (adsorbate) parameters;
3. Adsorbent temperature.

The Dubinin-Radushkevich (*D-R*) correlation is as follows:

$$V = V_0 exp[-k(\varepsilon_i)^2] \tag{5.2}$$

where V ($m^3.kg^{-1}$) is the volume filled at an equipotential surface (volumetric adsorption uptake), V_0 ($m^3.kg^{-1}$) is the limiting volume (maximum volumetric uptake) for adsorption and k is a constant.

Replacing Equation 5.1 into Equation 5.2 gives:

$$V = V_0 exp\left[-k\left(R\,T\,ln\frac{P_2}{P_1}\right)^2\right] \tag{5.3}$$

Equation 5.3 can be improved by substituting the definition of k [19]:

$$V = V_0 exp\left[-\left(\frac{R}{E}\right)^2\left(T\,ln\frac{P_2}{P_1}\right)^2\right] \tag{2.4}$$

where V ($m^3.kg^{-1}$) is the specific volume adsorbed at pressure P *(bar)*, V_0 ($m^3.kg^{-1}$) is the micropore limiting specific volume, R ($J.mol^{-1}.K^{-1}$) is a universal gas constant, T *(K)* is the carbon sample temperature and E ($kJ.mol^{-1}$) is characteristic adsorption energy of the adsorbate. $E = E_0\beta$ where E_0 ($kJ.mol^{-1}$) is characteristic adsorption energy for the reference adsorbate. Benzene is often taken as the reference adsorbate. β is called adsorbate 'affinity coefficients' or 'similarity coefficients', which is *1* for reference vapour. An affinity coefficient for the adsorbate is completely dependent on the molecular structure and physico-chemical properties.

Now, P_2 is the saturation pressure corresponding to the adsorbed phase within the micro-pores; henceforth written as *Psat* (*bar*), while system pressure P_1 will be written as P (*bar*) [22, 23].

$$V = V_0 exp\left[-\left(\frac{R}{E}\right)^2\left(T\,ln\frac{P_{sat}}{P}\right)^2\right] \tag{5.5}$$

where V ($m^3.kg^{-1}$) is the specific volume, V_0 ($m^3.kg^{-1}$) is the micropore limiting specific volume, R ($J.mol^{-1}.K^{-1}$) is a universal gas constant, T is the carbon sample temperature (K), E ($kJ.mol^{-1}$) is characteristic adsorption energy of the adsorbate, $Psat$ (bar) is the saturation pressure corresponding to the adsorbed phase within the micropores and P (bar) is the system pressure.

Critoph and Turner [24] show via error analysis of experimental data that the adsorption capacity of activated carbon is well presenting with changing from adsorbed volume of adsorbate per unit mass of adsorbent, V, ($cm^3.g^{-1}$) to the adsorbed mass of adsorbate per unit mass of adsorbent, x ($g.\ g^{-1}$).

$$x = x_0 exp\left[-\left(\frac{R}{E}\right)^2 \left(T\ ln\frac{P_{sat}}{P}\right)^2\right] \tag{5.6}$$

where x is adsorbate mass concentration ($g.g^{-1}$) and x_o is the limiting adsorbate mass concentration ($g.g^{-1}$).

Furthermore, by using the Clapeyron diagram, a linear relationship links the saturation liquid temperature, T_{sat}, (K) and pressure, $Psat$ (bar) to each other:

$$\ln P_{sat} = B - \frac{A}{T_{sat}} \tag{5.7}$$

where A and B are constants.

By using Equation 5.7, Equation 5.6 will change into:

$$x = x_0 exp\left[-\left(\frac{AR}{E}\right)^2 \left(\frac{T}{T_{sat}} - 1\right)^2\right] \tag{5.8}$$

where x ($g.g^{-1}$) is adsorbate mass concentration, x_o ($g.\ m^1$) is the limiting adsorbate mass concentration, A is the slope of the saturated adsorbate line on a Clapeyron diagram, R ($J.mol^{-1}.K^{-1}$) is a universal gas constant, E ($kJ.mol^{-1}$) is characteristic adsorption energy of adsorbate, T is carbon sample temperature (K) and T_{sat} is the saturation temperature (K) corresponding to the gas pressure.

The D-R equations (Equations 5.5 and 5.8) however, fail to interpret some of the gas-solid pair; Dubinin-Ashtikov (D-A) [25] extended the D-R equation into a general form, by replacing the power *2* with power of *n*. Equations 5.5 and 5.8 turn into the general form:

$$V = V_0 exp\left[-\left(\frac{R}{E}\right)^{n1}\left(T\ ln\frac{P_{sat}}{P}\right)^{n1}\right] \quad (5.9\text{-a})$$

$$x = x_0 exp\left[-\left(\frac{AR}{E}\right)^{n}\left(\frac{T}{T_{sat}} - 1\right)^{n}\right] \quad (5.9\text{-b})$$

The values of *n* in the D-A equation lies within the range of *1* to *4*, and shows the deviation of the energy of the adsorption from the Gaussian distribution, which is assumed for the D-R correlation. The value of *n*, when it is close to *4*, shows that the adsorbent has narrow distributions of micropores, but when the values of *n* is small it shows that the sorbent has a wide range of pore sizes [25]. The amount of $(AR/E)^n$ in Equation 5.9-b will indicated by 'k'.

5.4. Adsorption capacity of granular activated carbon

The quantity of refrigerant adsorbed depends on the temperature of the adsorbent and the adsorbate pressure. Maximum adsorbed and desorbed amounts should be measured under equilibrium conditions, to assess how long it takes to reach this value. Volumetric [28] and gravimetric [29] methods are traditionally used to measure the adsorption rate.

In this study, the volumetric method, using Micrometric ASAP2020 [28], was used in order to obtain the maximum pore volume V_0 $(m^3.kg^{-1})$ of activated carbon. Magnetic suspension balances, based on the gravimetric method [28], were used to establish the parameters for the D-A equation, mentioned previously (Equations 5.9-a and 5.9-b). The results obtained from the volumetric and gravimetric methods were used to calculate the amount of E_0 $(kJ.mol^{-1})$ which is characteristic adsorption energy for the reference adsorbate. The obtained values of characteristic adsorption energy from two tests using the 208-C / ammonia and 208-C / DME pairs in theory should be identical. This comparison will show the validity of the conducted tests.

5.4.1. Volumetric method

The volumetric method contains two chambers, a gas storage chamber and an adsorption chamber. These two chambers are connected by a tube and a valve. Both chambers are placed in a thermostat and connected to the vacuum line. The pressure and temperature should be measured in both chambers; the line diagram of the volumetric method is shown in Figure 5.6. The adsorption quantity is calculated by using the pressure values during adsorption and desorption, and the value of the dead

volume of the adsorption equipment. For increasing the accuracy of measurement regarding the ASAP2020 manual recommendation, a sample tube holder was used with a *3/8"* outside diameter and with a glass filler rod. Regarding the manual recommendation for a material such as activated carbon with a high surface area *(> 100 $m^2.g^{-1}$)*, it is good to use a sample weighing less than *0.5 g*; therefore *0.2987 g* of activated carbon was used during the measurement.

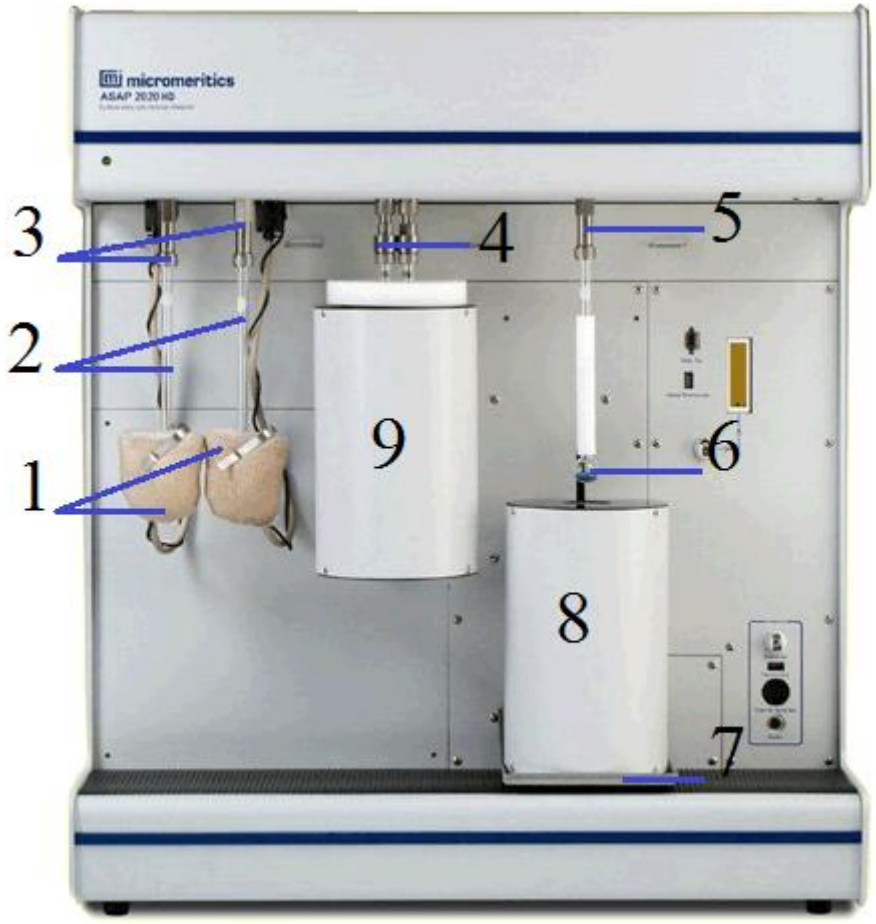

Figure 5.6. Micromeritics - ASAP2020 (adopted from Micromeritics Instrument Corporation). (1) electrical heating blanket with mounted thermocouple for sample degassing process, (2) sample holder glass, (3) degas port connected to the vacuum pump, (4) cold traps, (5) sample port and P_{sat} port behind that, (6) sample holder, (7) liquid nitrogen holder elevator, (8) analysis dewar full of liquid nitrogen, (9) cold trap dewar full of liquid nitrogen.

5.4.2. Gravimetric method

The basic concept behind the gravimetric method involves measuring the variation of adsorbent weight with regards to the adsorbent temperature and adsorbate pressure. This study used a magnetic suspension balance from Rubotherm [28]. A schematic diagram of the adsorption set-up and adsorbent location is given in Figure

5.7. The adsorbent sample is located in a container (a basket), which is suspended inside the stainless-steel chamber. Figure 5.8 shows the sample suspension mechanism and sample holder dimensions.

The mass measurement error represented by this system is $\pm 30\ \mu g$.

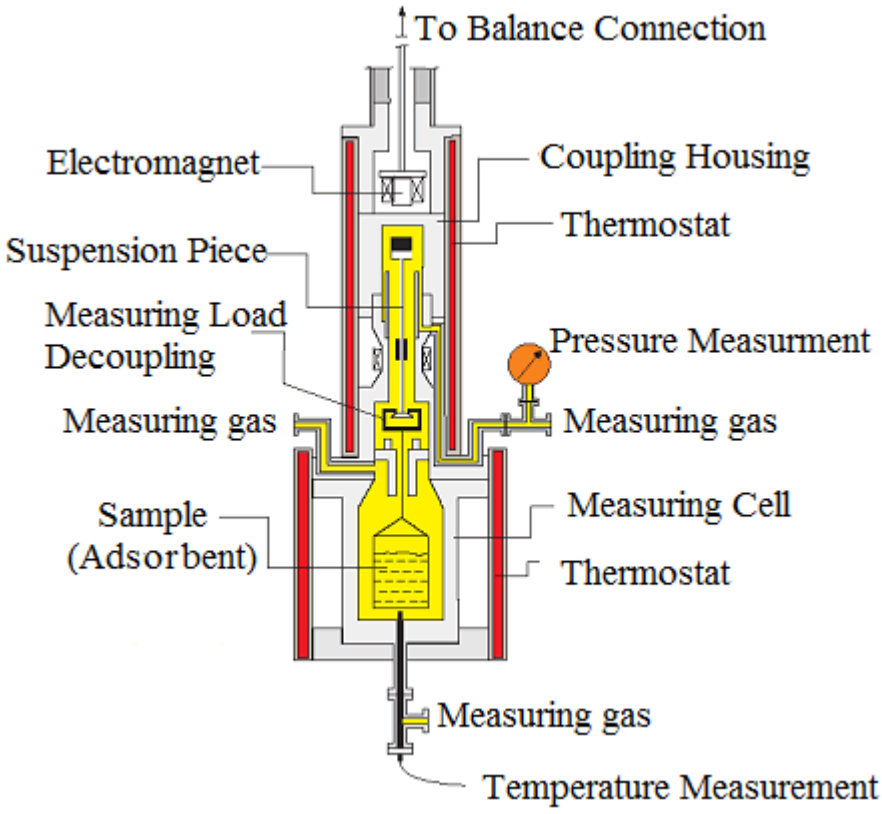

Figure 5.7. Rubotherm Magnetic suspension balance (adopted from Rubotherm GmbH).

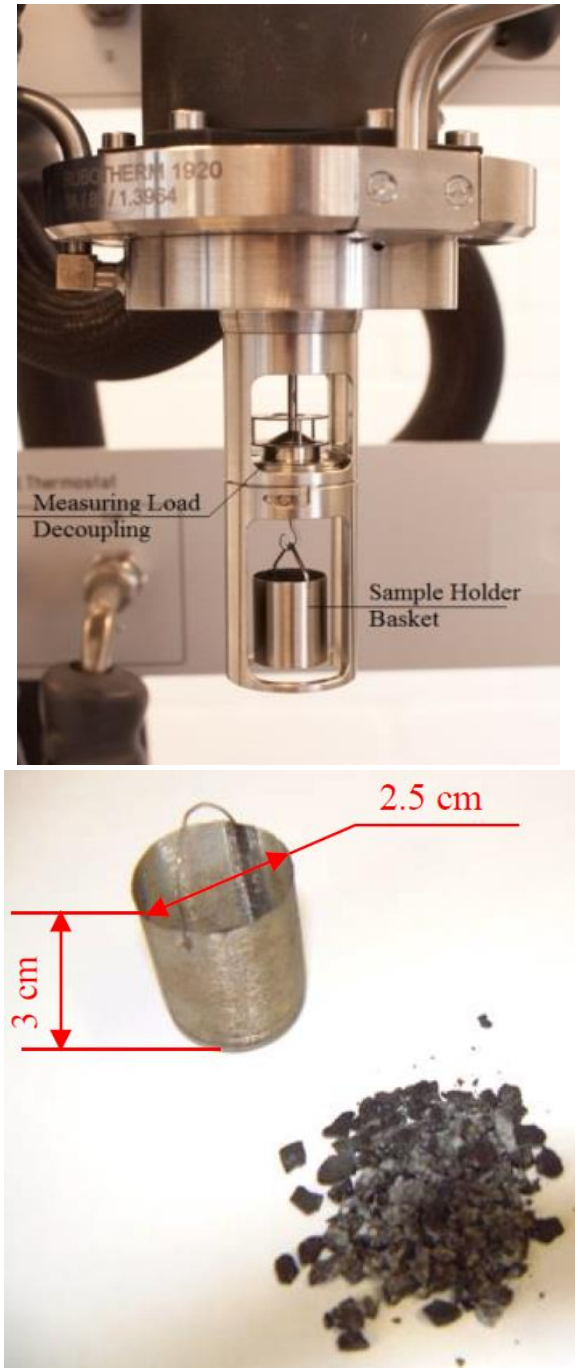

Figure 5.8. Top: sample holder and suspension mechanise [27]. Bottom: sample holder dimensions (adopted from Rubotherm GmbH).

5.5. Adsorption of single component refrigerant

The adsorption capacity test was first carried out for a refrigerant with pure components (ammonia and DME), and then the obtained parameters for the D-A equation (Equation 5.9) were compared to the theoretical values.

In the second step, mixture theory was used to establish the D-A equation parameters for adsorption of the mixed refrigerant (R723) over the activated carbon (208-C).

The validity of the D-A equation for mixture theory was compared with existing parameters from previous studies.

5.5.1. Ammonia and DME adsorption capacity test

The adsorption capacity tests for ammonia and DME were carried out using the Rubotherm magnetic suspension balance. The sample holder basket (Figure 5.8) was located at the middle of the stainless-steel vessel. The vessel's outside surface was covered with an electrical heater. The electrical heater maintained the heat coming into the steel chamber, which was subsequently transferred to the activated carbon sample.

For the DME and ammonia tests the activated carbon sample's temperature was set at 30^oC and 40^oC, going up to 180^oC in 20^oC increments. Figure 5.9 shows the sample holder chamber's pressure during the ammonia adsorption test while the carbon sample was held at specified temperatures. Figure 5.10 shows the ammonia pressure variation in the course of the adsorption and desertion loop on activated carbon at 60^oC. In order to provide different saturation pressures within the sample holder chambers, a refrigerant holding vessel was located in the thermal bath. The thermal bath's temperature varied between -10^oC up to 50^oC in 10^oC increments. The bath's temperature causes the pressure in the activated carbon holder chambers for the ammonia test to vary between *2.7 bar* and *19 bar*, while for the DME test it varies between *1.7 bar* and *11 bar*. The saturated refrigerant gas is then transferred thorough the stainless-steel tube into the sample holder chambers.

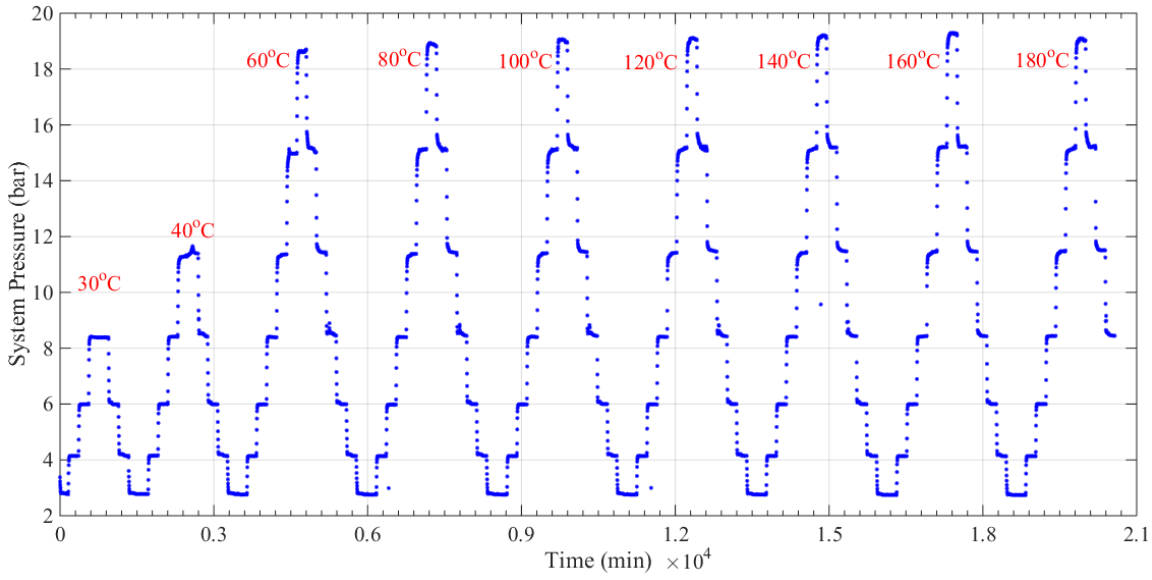

Figure 5.9 Sample holder chamber saturation pressure during the ammonia adsorption test.

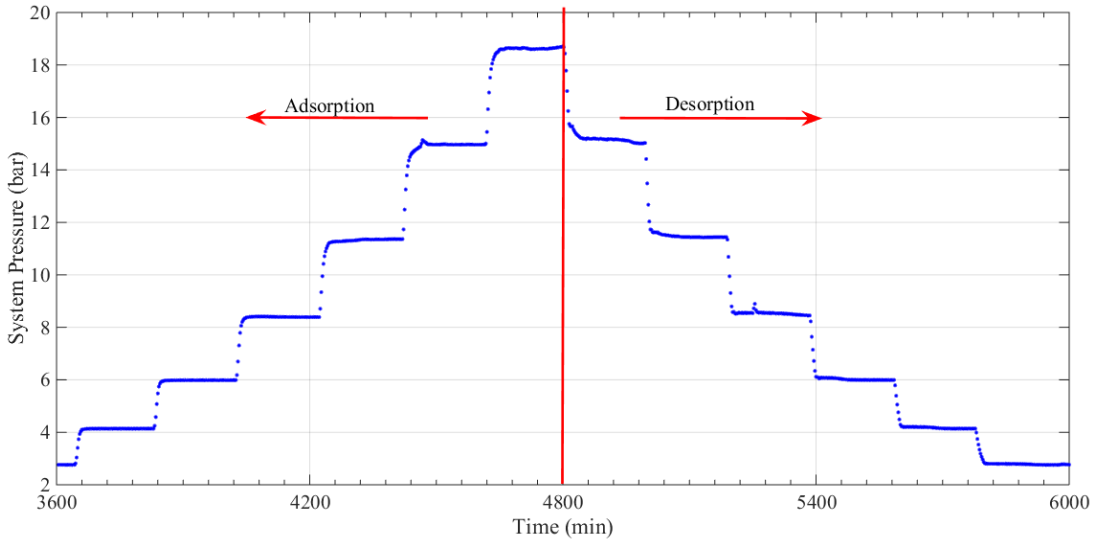

Figure 5.10. Sample holder chambers saturation pressure for carbon at $60\,^{o}C$, holding temperature of liquid ammonia vessel for equivalent saturation pressure.

The data are collected in both the DME and ammonia tests every *5 minutes* until equilibrium state is reached at each set point (specific carbon sample temperature and specific system pressure). The equilibrium state is the situation at which the adsorption and desorption process for each set point is completed. The completion of the adsorption and desorption processes is detectable by the stability of the sample holder chamber's pressure and temperature. Figure 5.11 shows the transition or non-equilibrium and equilibrium states over the course of the ammonia test for activated carbon at $60\,^{o}C$, while the refrigerant holder vessel was kept at $10^{o}C$ and $20^{o}C$. The preliminary test showed the ammonia and activated carbon pairs at each set point reached the equilibrium state in *50 minutes*, while the DME and activated carbon pair took *65 minutes*.

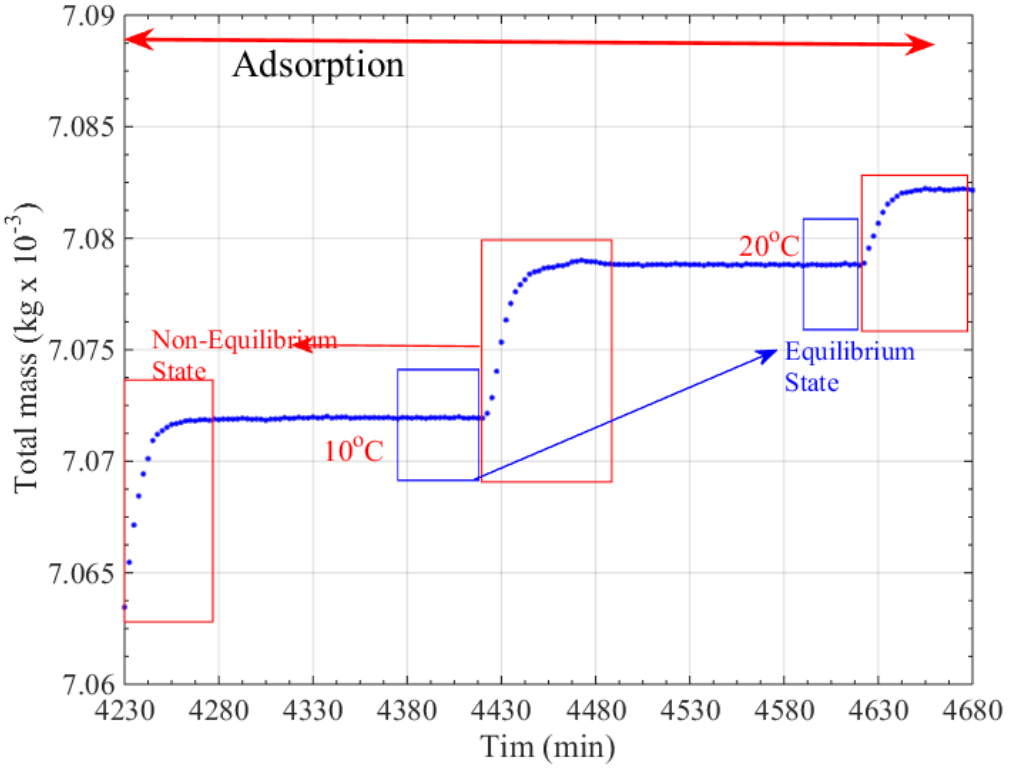

Figure 5.11. Non-equilibrium and equilibrium state over the course of the ammonia test for activated carbon at 60^oC. Refrigerant was kept at 10^oC and 20^oC.

In order to measure the weight of the adsorbed refrigerant the following procedure was followed:

- The sample holder chamber was heated to 180^oC while the whole system was vacuumed continually. The process was continued for *2* hours.
- The mass of empty sample holder basket was measured in its vacuumed situation state cooling down the system to the ambient temperature (m_h).
- The activated carbon sample was located in the holder basket and again the whole system was heated to 180^oC under vacuum conditions for *5* hours.
- The mass of the full sample holder basket with activated carbon was measured in a vacuum after cooling down the system to the ambient temperature (m_f).
- The mass of the adsorbent was found by subtracting the empty mass of the holder basket from the full mass:

$$m_c = m_f - m_h \tag{5.10}$$

- Variations in the adsorbent mass (full mass of basket) were monitored over the course of adsorption and desorption processes for each set point (m_t).

Figure 5.12 shows the variation of measured adsorbent mass (total mass) for each measured point based on constant time interval over the period of test for each adsorbent temperature. Figure 5.12 illustrates that the adsorbed mass of the adsorbate (ammonia) will decrease by increasing the adsorbent (208-C) temperature, while the refrigerant vessel temperature (representative of saturation pressure) is kept constant.

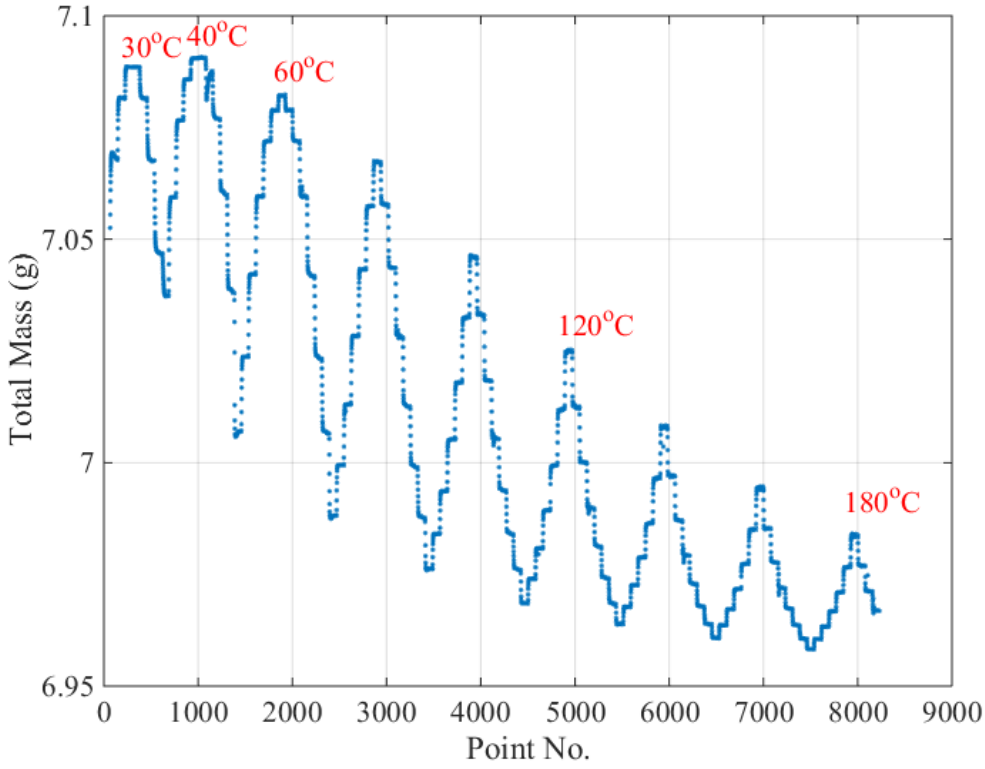

Figure 5.12. Total mass (m_t) variation over the ammonia adsorption and desorption tests.

Figure 5.13 shows the adsorbed mass of adsorbate on activated carbon at 120^oC over the course of adsorption and desorption for different system pressure ranges, so that each pressure represents the specific bath temperature for the refrigerant vessel. Figure 5.14 shows that for all adsorbent temperatures the adsorbed total mass of the refrigerant in the desorption course is higher than the adsorption course. The mass difference for the same condition over the adsorption and desorption courses varied between $0.5\ g$ up to a maximum of $1.21\ g$.

Regarding the $\pm 30\ \mu g$ balance error, the root source of this kind of mass difference in Figure 5.14 is called the desorption hysteresis effect, which was explained previously in Figure 5.3. Because of the hysteresis effect, the relative pressure for the same adsorbent temperature during the desorption course will be higher than in the adsorption course. Therefore, the refrigerant will be adsorbed more in the adsorbent.

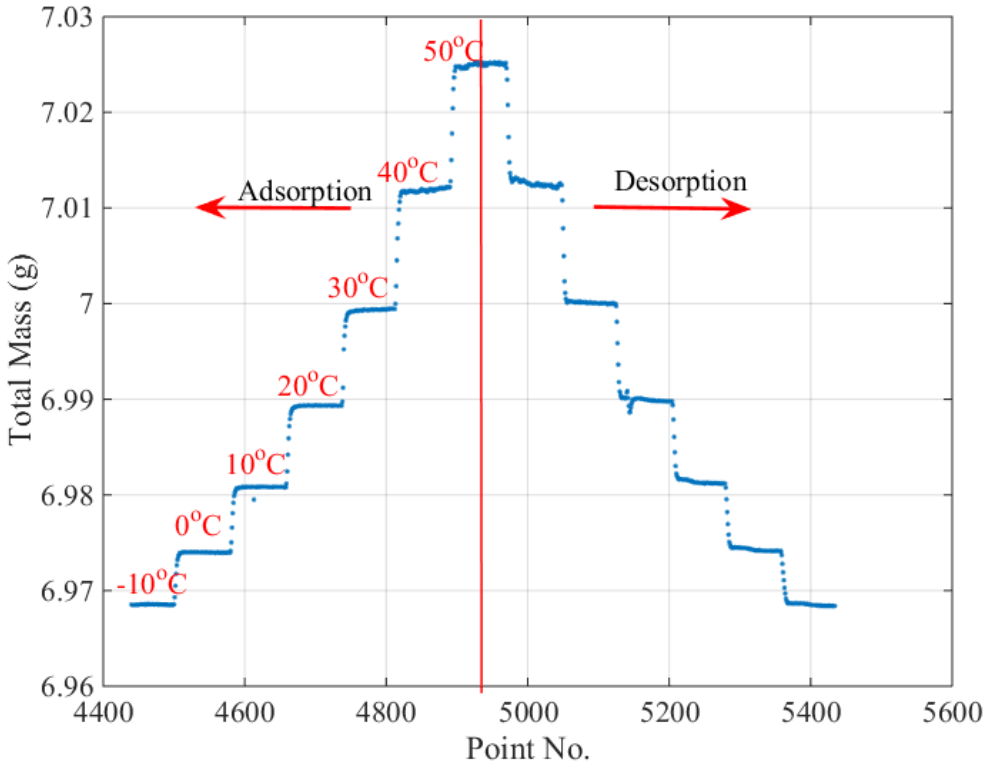

Figure 5.13. Total mass (m_t) variation over the ammonia adsorption and desorption test for activated carbon at $120\,^{o}C$ with saturation pressure (refrigerant vessel bath temperature).

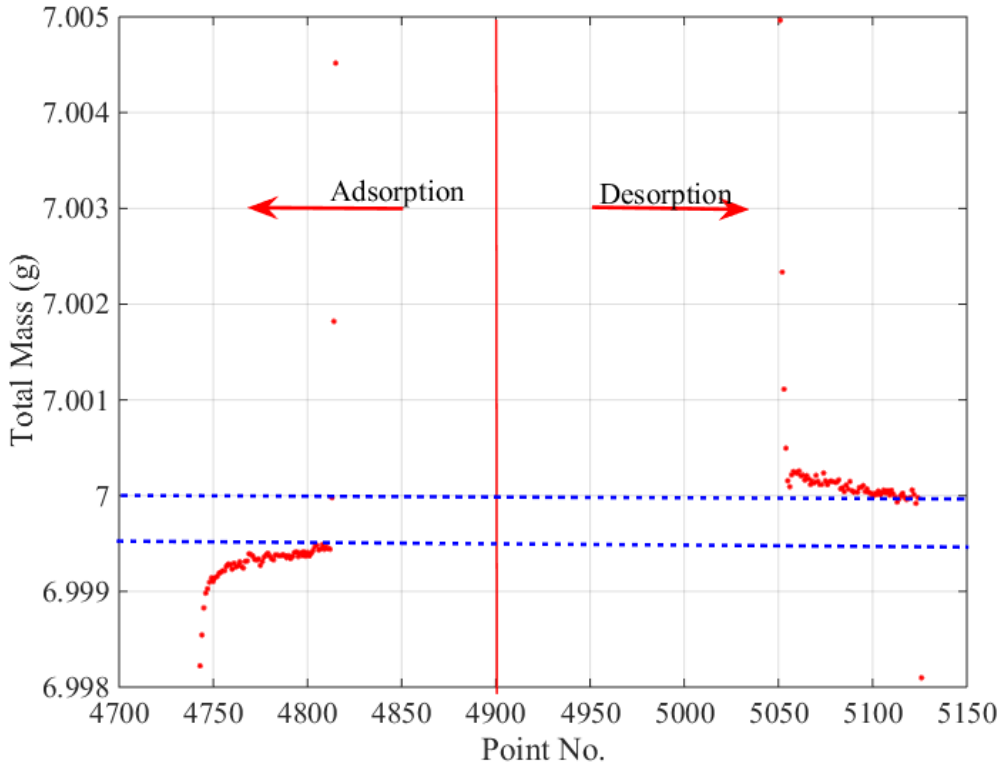

Figure 5.14. Hysteresis effect, which causes adsorbed mass increase in the desorption course in comparison with the adsorption course; adsorbate is ammonia at $30^{o}C$ and adsorbent is activated carbon at $120^{o}C$.

5.5.2. Buoyancy effect correction factor

Figures 5.7 and 5.8 show how the sample holder basket is suspended in the middle of the chamber by using a magnetic field force. The existing gas density (in the chamber at a certain pressure and temperature) affects the displacement of the sample holder basket with the adsorbent. Therefore, the adsorbed mass (apparent weight), which is read by the scaling instrument, will be lower due to the buoyancy effect. The adsorbed mass for calculating the concentration over the adsorbent mass in Equation 5.9-b was corrected due to the buoyancy effect.

$$m_{corrected} = m_t - m_b \tag{5.11}$$

$$m_b = m_h \frac{\rho_{gas}}{\rho_h} + m_c \frac{\rho_{gas}}{\rho_c} \tag{5.12}$$

$$\rho_h = 8000 \ kg.m^{-3} \ and \ \rho_c = 1000 \ kg.m^{-3}$$

where m_t is the mass measured by the instrument scale, m_b is mass correction due to the buoyancy effect on the steel sample holder and the adsorbent itself, m_h is the mass of the empty sample holder, m_c is the mass of the adsorbent (activated carbon), ρ_h is the density of the sample holder material (stainless steel) and ρ_c is the density of the dry activated carbon.

Figure 5.15 shows the mass differences between corrected mass and measured mass on the instrument scale for equilibrium data points, for the ammonia test.

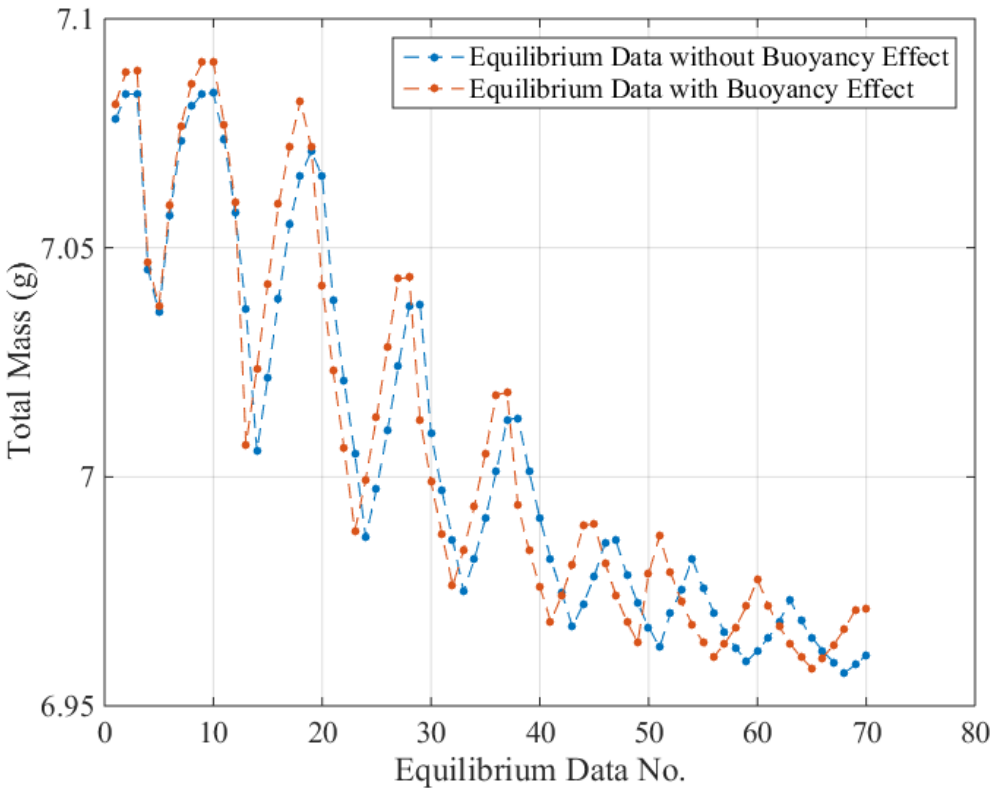

Figure 5.15. The effect of buoyancy mass correction on apparent mass or measured mass by instrument scale.

5.5.3. Evaluation of D-A equation parameters for pure refrigerant component

To evaluate the D-A equation and find the relative parameters for the pure refrigerant, the curve fitting process (see Appendix C-2) was applied to the adsorbate mass concentration (Equation 5.13) in comparison to $T/T_{sat} - 1$ for nominated equilibrium experimental data points. Figure 5.16 shows the equilibrium experimental data points for a temperature range of 35^oC and 40^oC up to 180^oC in 20^oC increments and a pressure range of *2.7 bar* up to *11.5 bar* for a pairing of granular activated carbon / R717 (208C & ammonia: see Appendix C). Figure 5.17 shows the equilibrium experimental data points for a temperature range of 30^oC and 40^oC up to 180^oC in 20^oC increments, and a pressure range of *1.7 bar* up to *10.8 bar* for a pairing of granular activated carbon / RE170 (208C & DME: Appendix C-1).

Table 5.2 shows the fitted curve based on the mass concentration of the D-A equation (Equation 5.9-b), on the experimental equilibrium data for DME and ammonia. The results of the fitted curve in relation to finding the adsorbed mass of

the adsorbate shows the standard estimated errors (SEE) were 6×10^{-4} and 11×10^{-4} ($kg.kg^{-1}$) for DME / 208-C and ammonia / 208-C pairs, respectively.

$$x = \frac{m_{corrected} - m_f}{m_c} \tag{5.13}$$

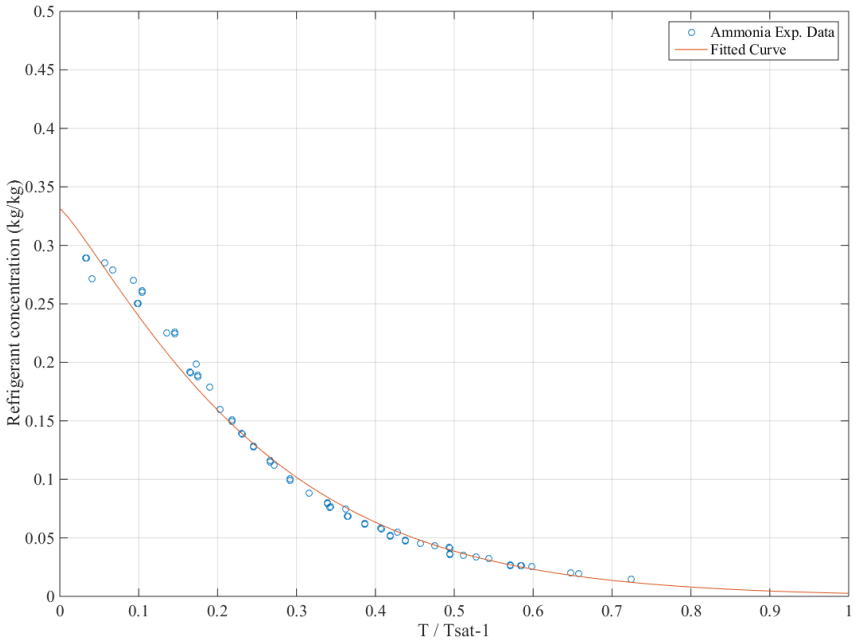

Figure 5.16. Ammonia mass concentration ($kg.kg^{-1}$) vs. $\frac{T}{T_{sat}} - 1$ to evaluate D-A parameters by curve fitting process.

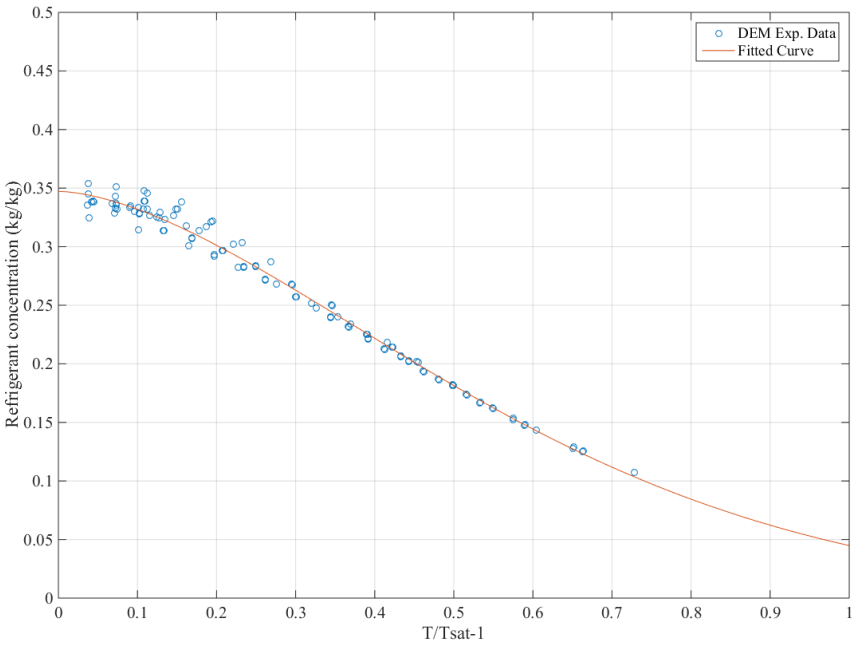

Figure 5.17. DME mass concentration ($kg.kg^{-1}$) vs. $\frac{T}{T_{sat}} - 1$to evaluate D-A parameters by curve fitting process.

$$SEE = \frac{\sqrt{\Sigma(x_{exprimental} - x_{calculated})^2}}{Number\ of equilibrium\ test\ data\ point} \quad (5.14)$$

Refrigerant	D-A Parameters			
	$x_0\ (kg.kg^{-1})$	k	n	$SEE\ (kg.kg^{-1})$
DME	0.3472	2.0464	1.6570	0.0006
Ammonia	0.3316	4.8434	1.1720	0.0011

Table 5.2. D-A equation parameters summary for ammonia and DME experimental equilibrium data points with fitted curve performances regarding standard estimated errors.

5.5.3.1. Theoretical and experimental comparison of D-A equation parameters

In the D-A equation (Equation 5.9-b), x_o [18], which is the maximum or limiting adsorbate mass concentration, is dependent on the specific micropore volume of the adsorbent structure and liquid density under normal pressure conditions or atmospheric pressure [33, 34].

$$x_0 = \rho_L . V_s \quad (5.15)$$

Table 5.3 shows that the textural properties of 208-C were determined with adsorption of N_2 at -196^oC over $0.2988\ g$ of activated carbon using the ASAP2020. The values were extracted from the test data using the machine's internal program.

Material	BET surface area	Specific volume (V_S)
	$m^2.g^{-1}$	$cm^3.g^{-1}$
208C	887.84	0.47

Table 5.3. Textural properties of 208-C obtained from adsorption and desorption of N_2 at -196^oC with ASAP2020 instrument.

Table 5.4 shows the deviation (Equation 5.16) of maximum mass concentration, obtained by the curve fitting process on the experimental data (Table 5.2) in comparison to the theoretical values obtained from Equation 5.15. The maximum deviation between theoretical and experimental values occurred in the ammonia / 208-C pair test.

$$Deviation = \left| \frac{x_{0-Exprimental} - x_{0-Theoretical}}{x_{0-Exprimental}} \right| \times 100 \quad (5.15)$$

Refrigerant	ρ_L	V_S	$x_{0\text{-}Theoretical}$	$x_{0\text{-}Exprimental}$	$Deviation$
	$kg.m^{-3}$	$cm^3.g^{-1}$	$kg.kg^{-1}$	$kg.kg^{-1}$	%
DME	734.70	0.47	0.3453	0.3472	0.55
Ammonia	682.12	0.47	0.3206	0.3316	3.32

Table 5.4. Comparison between theoretical and experimental values of maximum mass concentration.

By looking at the definition of the '*k'* parameter of the D-A equation (Equation 5.9-b), based on experimental data regardless of refrigerant type, the characteristic adsorption energy for the reference adsorbate (benzene) "E_0 ($kJ.mol^{-1}$) " on the same type of activated carbon (208-C) should be a constant value within the range of acceptable error. Therefore, the fitted curve into the experimental data based on D-A equation (Equation 5.9-b) lead to calculation the *k'* parameter of the D-A equation for each tested pair. Table 5.5 shows the summary of D-A equation parameters which obtained from exponential curve fitting. The two obtained values of E_0 ($kJ.mol^{-1}$) from fitted curve into DME / 208-C and ammonia / 208-C pairs experimental, show *1.5%* difference. Therefore, it is possible to use either both values or a single average value for E_0 ($kJ.mol^{-1}$) as characteristic adsorption energy for the reference adsorbate (benzene) on 208-C.

b

Refrigerant	R	A	B	n	k	E_0	$\bar{E}_0$
	$J.mol^{-1}$					$kJ.mol^{-1}$	$kJ.mol^{-1}$
DME	8.3144	2625.75	0.64 [35,36]	1.657	2.0464	22.14	21.98
Ammonia		2823.40	0.28 [34,37]	1.172	4.8434	21.82	

Table 5.5. The values of *E0* ($kJ.mol^{-1}$) characteristic adsorption energy obtained for the reference adsorbate (benzene) on 208-C activated carbon using the experimental data and fitted curve parameters (Table 5.2) from the DME an ammonia / 208-C pairs, based on the D-A equation (Equation 5.9-b).

Tables 5.4 and 5.5 show the reliability of the experimental data for adsorption of each pure refrigerant (ammonia and DME) as part of a gas mixture over the activated carbon (208-C). Table 5.4 shows that the maximum mass concentration obtained from the experiment is reliable compared to the theory. Table 5.5 shows the value of E_0 ($kJ.mol^{-1}$) characteristic adsorption energy obtained for the reference adsorbate (benzene) on 208-C is consistent and is not dependent on the tested refrigerant as expected.

5.6. Refrigerant mixture

Refrigerant mixtures have recently been receiving great attention as they are able to replace halogenated refrigerants in existing products; the latter involve

environmental hazards. The types of individual refrigerant that can be used in mixtures can be categorized into six groups as follows [31]:

1. Hydrocarbons (HC)
2. Hydrofluorocarbons (HFC)
3. HFC/HC
4. Hydrochlorofluorocarbons (HCFC)
5. Carbon dioxide (R744)
6. Ammonia (R717)

The molecular structure of refrigerant mixture in blended form is categorized as follows [32]:

1. Azeotropes
2. Near azeotropes
3. Zeotropes

The azeotropes mixture is a blend of two or more refrigerants (binary or ternary mixture), which act like a single component and cannot be separated into single components by a simple separation process. The new substance behaves independently, in terms of thermal properties, from each single component. It maintains its composition in either a liquid or vapour state.

The near azeotropes mixture could be a blend of two or more refrigerants (binary or ternary mixture). This type of mixture, similar to the azeotropes type, keeps the composition the same in the liquid and gas phases, but because of the different boiling temperature of the composition, the mixture has a temperature glide. In single components or pure refrigerants, the saturation vapour and saturation liquid temperature at a given pressure are constant and temperature glide is zero, while in the near azeotropes mixture those temperatures at a given pressure are slightly different.

The zeotropes mixture could be a blend of two or more refrigerants (binary or ternary mixture). This type of mixture, unlike the azeotropes and near azeotropes mixtures, shows different vapour and liquid compositions in equilibrium conditions at a given pressure. The temperatures glide of the zeotropes mixture is usually *90%* to *95%* higher than near azeotropes mixtures.

In early 2004, a new azeotropic refrigerant based on ammonia was introduced into the market. R723 is an azeotropic mixture made of *40%* ammonia and *60%* dimethyl ether.

The early research on a R723-activated carbon pair in a sorption generator showed the refrigerant's composition stability in the adsorption and desorption process [38]. Lychnos and Tamainot-Telto [39] showed that R723 keeps azeotrope features even at driving temperatures as high as 170^oC and a condensing temperature of 35^oC. After several adsorption and desorption cycles the refrigerant liquid temperature in receiver was measured. Then, the measured temperature was compared with the saturation temperature. The saturation temperature was calculated from the measured pressure in the receiver vessel. They concluded that with a temperature difference of less than 3K between the measured and calculated temperatures, the refrigerant was considered unchanged in the consistence of its composition.

5.6.1. Volumetric adsorption uptake for single component refrigerant

This section will establish the D-A equation for R723 based on mixture theory from a component adsorption capacity test and compare the results with existing equations from previous research.

Table 5.2, above, shows a summary of D-A parameters for Equation 5.9-b based on adsorption mass concentration. The volumetric adsorption uptake V ($m^3.kg^{-1}$) was found from an adsorption mass concentration test (Appendix C and Appendix C-1) via the following equations [41]:

$$V = x.v \tag{5.16}$$

where v is the specific volume ($kg.m^{-3}$) of the adsorbed phase [40];

$$v = v_b \exp[\Omega(T - T_b)] \tag{5.17}$$

where the v_b is specific volume ($kg.m^{-3}$) of the adsorbate at the normal boiling point of the refrigerant, Ω is the thermal expansion coefficient (K^{-1}) (Equation 5.18), T_b is the refrigerant's normal boiling temperature (K) and T is the adsorbent temperature (K).

$$\Omega = \frac{\ln\left(\frac{v_a}{v_b}\right)}{(T_c - T_b)} \quad where \ v_a = {}^{RT_c}/_{8P_c} \tag{5.18}$$

where υ_a is Van der Waals volume, R is universal gas constant, T_c is adsorbate critical temperature (K) and P_c (bar) is critical pressure.

Table 5.6 provides a summary of R723, R717 and RE170 properties.

Adsorbate	M_W	T_b	T_C	P_C	υ_a	υ_b	Ω
	$g.mol^{-1}$	K	K	bar	$kg.m^{-3}$	$kg.m^{-3}$	K^{-1}
R717	17.031	239.81	405.45	112.8	2.194×10^{-3}	1.466×10^{-3}	2.433×10^{-3}
RE170	46.068	249	400.3	53.702	1.686×10^{-3}	1.361×10^{-3}	1.409×10^{-3}
R723	22.772	241.15	404.15	110	1.677×10^{-3}	1.438×10^{-3}	1.107×10^{-3}

Table 5.6. Summary of the properties of R723, DME (RE170) and ammonia (R717).

Equation 5.19 is a linear mode of the D-A equation (Equation 5.9-a) for volumetric adsorption uptake:

$$\log(V) = \log(V_0) - K_1 \left(T \,.\, ln \frac{P_{sat}}{P} \right)^{n_1} \tag{5.19}$$

where V is volumetric adsorption uptake $(m^3.kg^{-1})$, V_0 is maximum volumetric adsorption uptake $(m^3.kg^{-1})$, $K_1 = (R/E)^{n_1}$ refers to adsorption parameters, T is adsorbent temperature (K), and P_s and P define the saturation and equilibrium pressure, respectively. To find the saturation pressure during the test, Equation 5.6 was used, using the parameters in Table 5.8.

Adsorbate	A	B
R717	2823.40	11.749
RE170	2625.75	10.582
R723	2689.60	11.300

Table 5.7. Summary of parameters for Equation 5.7 to find the P_s (bar) from adsorbent temperature (K)

Employing the data presented in Figures 5.18 and 5.19, the adsorption parameters of Equation 5.19 in terms of $log\ (V_0)$, K_1 and n for granular activated carbon / R717 (ammonia) and granular activated carbon / RE170 (DME) pairs are estimated and presented in Table 5.8.

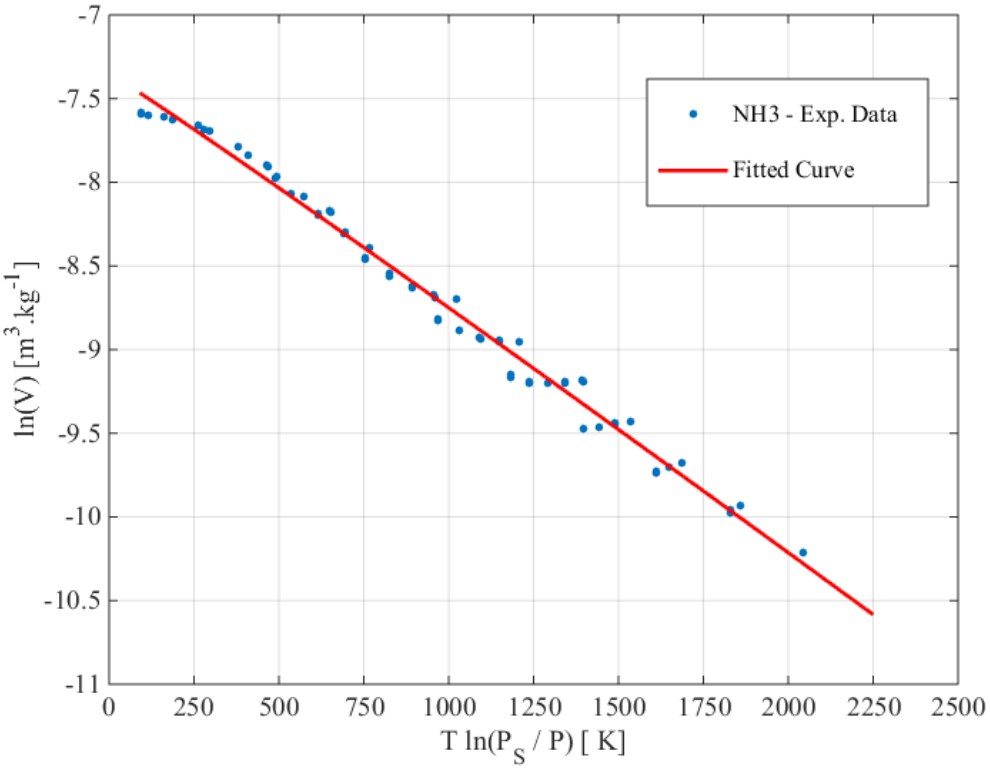

Figure 5.18. Linear fitting of D-A equation on activated carbon / ammonia (R717) pair – experimental data for ammonia (R717) volumetric adsorption uptake ($m^3.kg^{-1}$) vs. $T \ln {}^{P_{sat}}/_{P}$ (K^{-1}).

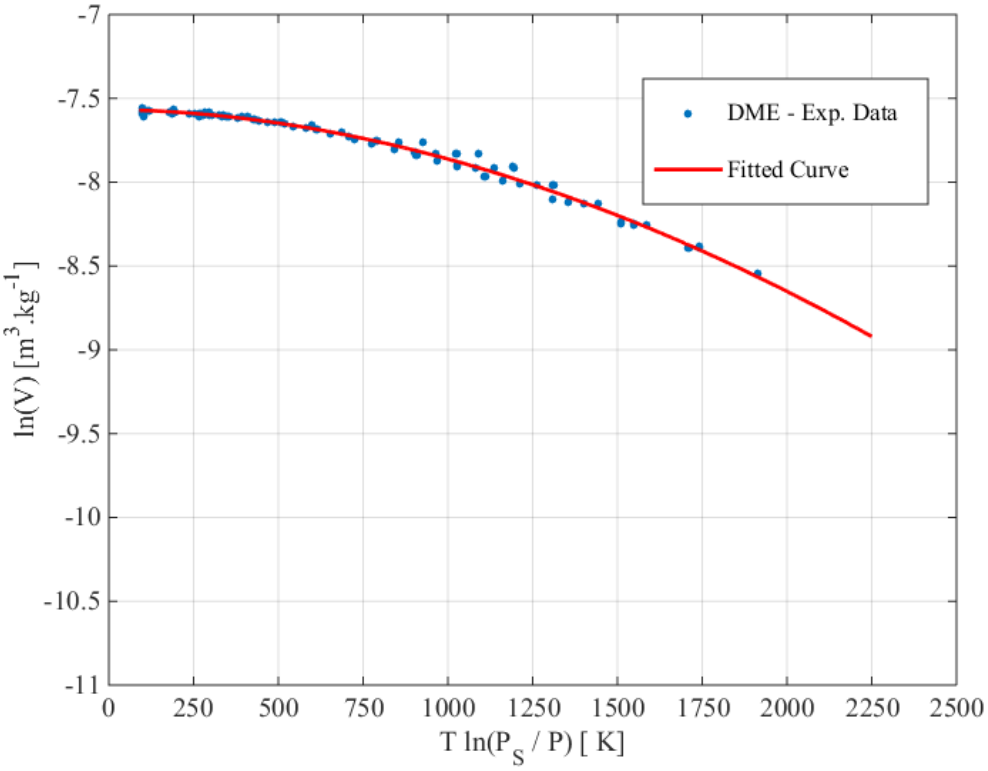

Figure 5.19. Linear fitting of D-A equation on activated carbon / DME (RE170) pair – experimental data for DME (RE170) volumetric adsorption uptake ($m^3.kg^{-1}$) vs. $T \ln {}^{P_{sat}}/_{P}$ (K^{-1}).

Adsorbate	$log(V_0)$	K_1	n_1	SEE
	$m^3.kg^{-1}$	K^{-1}		$m^3.kg^{-1}$
R717	-7.349	1.123×10^{-3}	1.032	0.385
RE170	-7.354	6.592×10^{-7}	1.883	0.060

Table 5.8. D-A parameters (Equation 5.19) based on least squares curve fitting method with standard estimated error (Equation 5.14) for activated carbon / R717 and activated carbon / RE170 pairs experimental data.

Table 5.8 shows the fitted curve parameters (see Appendix C-2) based on the least squares curve fitting method for volumetric adsorption uptake over the activated carbon. The maximum standard estimated errors (Equation 5.14) from the fitted curve on the experimental data were calculated *0.4* $m^3.kg^{-1}$ and *0.06* $m^3.kg^{-1}$ for ammonia (R717) / 208-C and DME (RE170) / 208-C, respectively.

5.6.2. Mixture theory for volumetric adsorption uptake of refrigerant mixture

Much research has been carried out on adsorption mixture theory. Lewis et al. [42], Bering et. al [43], Myers and Prausnitz's ideal adsorption solution theory (IAST) [44], and Doong and Yang's exclusion theory [45] propose methods of predicting gas mixture adsorption from pure component adsorption. An extensive summary of their methods is provided by Wood [46].

One of the earliest models was proposed by Lewis et al. [42] based on the Polanyi adsorption model [16]. Equation 5.20 is called the Lewis equation, where n_i^o is the reference adsorbed molar capacity of the pure components and n_i is the molar capacity of the component in the adsorbed mixture.

$$\sum \frac{n_i}{n_i^o} = 1 \tag{5.20}$$

Lavanchy and Stoeckli [47] combined the D-A adsorption model and the Lewis equation with Raoult's Law. Based on Raoult's Law the vapour pressure of the ideal solution (mixture) is dependent on the vapour pressure of each chemical component at the mole fraction of the component presented in the mixture [44].

$$P_i = P_i^* X_i \tag{5.21}$$

where P_i is the partial pressure of the component i in the mixture, P_i^* is the vapour pressure of the pure component i and X_i is the mole fraction of the component i in the mixture.

By using the known total pressure for the gas mixture, the volumetric adsorption uptake for the pure components was calculated based on the partial pressure of each pure component in the D-A equation in the absence of other parties. Afterwards, by using proportionality theory [46], the adsorbed amount of pure component in the presence of other parties was calculated. In terms of proportionality theory, the different components in the mixture do not interact except to prevent adsorption of the other components. Therefore, each component occupies a share of the total volume based on the mole fraction of each in the mixture. The total volume of the mixed gas adsorption with two components is as follows:

$$V_T = V_1 X_1 + V_2 X_2 \tag{5.22}$$

R723 is an azeotropic mixture of ammonia and DME with *60%* and *40%* mass fraction, respectively. By considering the mass fraction of each component and their molecular weight (Table 5.9), the molar fractions of each pure component are:

Adsorbate	Molar fraction
R717	0.8023
RE170	0.1977

Table 5.9. Mole fraction of each pure component at R723 as mixed refrigerants.

Based on a consideration of the mole fraction of each pure component in the mixed refrigerant, Equation 5.20, partial pressure effect (Equation 5.21) and Equation 5.22, Figure 5.20 shows the volumetric adsorption uptake of R723 on activated carbon (208-C) over the adsorbate pressure range of *3.5 bar* to *18 bar* while the adsorbent temperature varied between 45^oC to 200^oC.

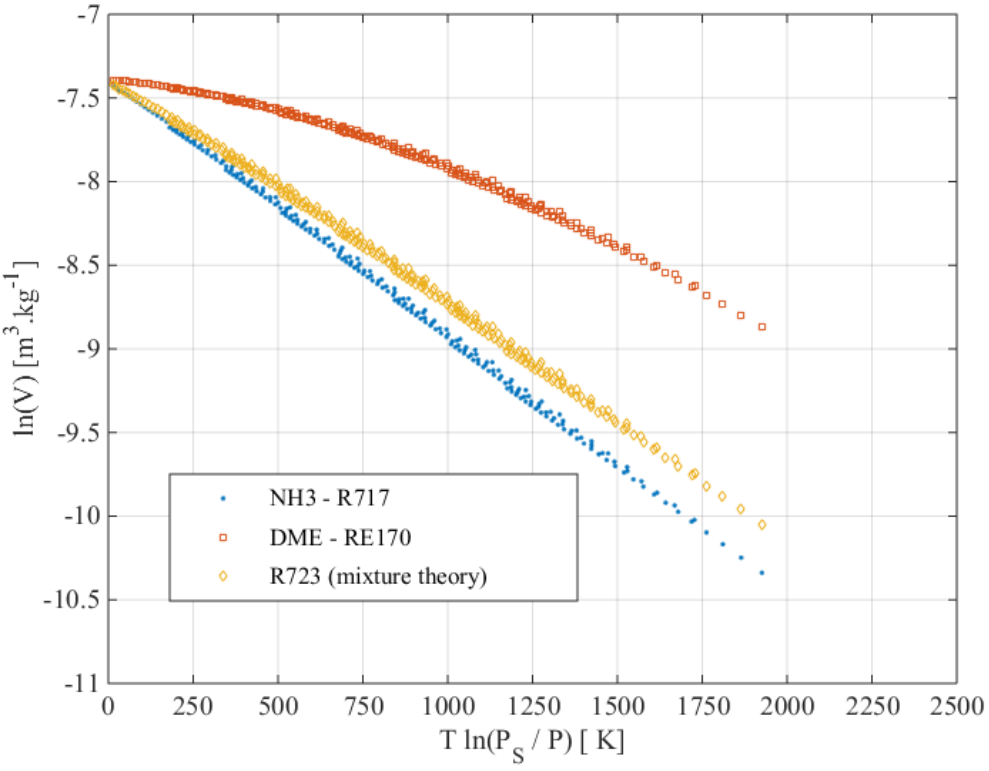

Figure 5.20. R723 volumetric adsorption uptake based on proportionality theory from pure component adsorption; D-A parameter for pure component from Table 2.8. Pressure range is *3.5 bar* to *18 bar* and temperature range is 45^oC to 200^oC.

The D-A equation's parameters (Equation 5.9a) for R723 volumetric adsorption uptake over the activated carbon (208-C) were obtained by applying the least squares curve fitting method (Appendix C-2) with standard estimated errors (Equation 5.14) over the data obtained from volumetric mixture theory (Figure 5.20). The D-A equation's parameters are summarised in Table 5.10. The standard estimated error (SEE) for the fitted curve over the data obtained from mixture theory was calculated to be $0.085\ m^3.kg^{-1}$.

Adsorbate	$log(V_0)$	K_1	n	SEE
	$m^3.kg^{-1}$	K^{-1}		$m^3.kg^{-1}$
R723 – Mixture Theory	-7.403	8.248×10^{-4}	1.068	0.085

Table 5.10. D-A parameters (Equation 5.19) based on least squares curve fitting method with standard estimated error (Equation 5.14) for GAC / R723 data from mixture theory (Figure 5.20).

To validate the mixture theory, the volumetric uptake adsorption data obtained from the theory for the R723 / 208-C pair was compared with data for the same pressure and temperature ranges from previous studies. Tamainot-Telto [33] suggested D-A equation parameters (Table 5.11) based on the mass concentration adsorption (Equation 5.9b) of an R723 / 208-C pair,

Refrigerant	D-A Parameters			
	x_0 $(kg.kg^{-1})$	k	n	SEE $(kg.kg^{-1})$
R723- Z. Tamainot-Telto [33]	0.3540	3.7342	1.187	0.0006

Table 5.11. D-A equation parameters (Equation 5.9b, mass concertation adsorption form) for R723 / 208-C, suggested by Z. Tamainot-Telto [33].

By using the parameters from Table 5.11 and the D-A equation in mass uptake form (Equation 5.9b), the adsorbed mass of R723 per mass of activated carbon was calculated. For calculating the mass uptake, the R723 pressure range was varied from *3.5 bar* to *18 bar*, while the activated carbon temperature varied between 45^oC to 200^oC; the same pressure and temperature range was used before in mixture theory. Afterwards, the calculated mass concentration was changed into the volumetric uptake adsorption per mass of activated carbon using Equations 5.16, 5.17 and 5.18.

Knowing the volumetric uptake adsorption, pressure and temperature, the least square curve fitting method was used to estimate the parameters of the linear form (Equation 5.19) of the D-A equation (Equation 5.9a). Table 5.12 shows the parameters of the D-A equation in volumetric uptake form (Equation 5.9a) which were extracted from the D-A equation in mass concentration form (Equation 5.9b and Table 5.11).

Adsorbate	$log(V_0)$	K_1	n	SEE
	$m^3.kg^{-1}$	K^{-1}		$m^3.kg^{-1}$
R723	-7.544	2.265×10^{-4}	1.225	0.000

Table 5.12. D-A equation parameters (Equation 5.9a, volumetric uptake adsorption form) for 208-C / R723, calculated from data obtained from Equation 5.9b with parameters suggested by Tamainot-Telto [33].

At the final stage of the comparative study, the volume of the adsorbed R723 per mass of activated carbon (V $(m^3.kg^{-1})$), shown before in Figure 5.20 using the mixture theory, over a pressure range of *3.5 bar* to *18 bar* and a temperature range of 45^oC to 200^oC, was compared to the calculated adsorbed R723 volume per mass of activated carbon (V $(m^3.kg^{-1})$) using the D-A equation in volumetric form (Equation 5.9a and Table 5.12). In Figure 5.21, the calculated adsorbed volume of R723 per mass of 208-C type activated carbon based on mixture theory is in the range of *±2%* $m^3.kg^{-1}$ calculated adsorbed volume of R723 over 208-C type activated carbon, using Equation 5.9a with the parameters illustrated in Table 5.12.

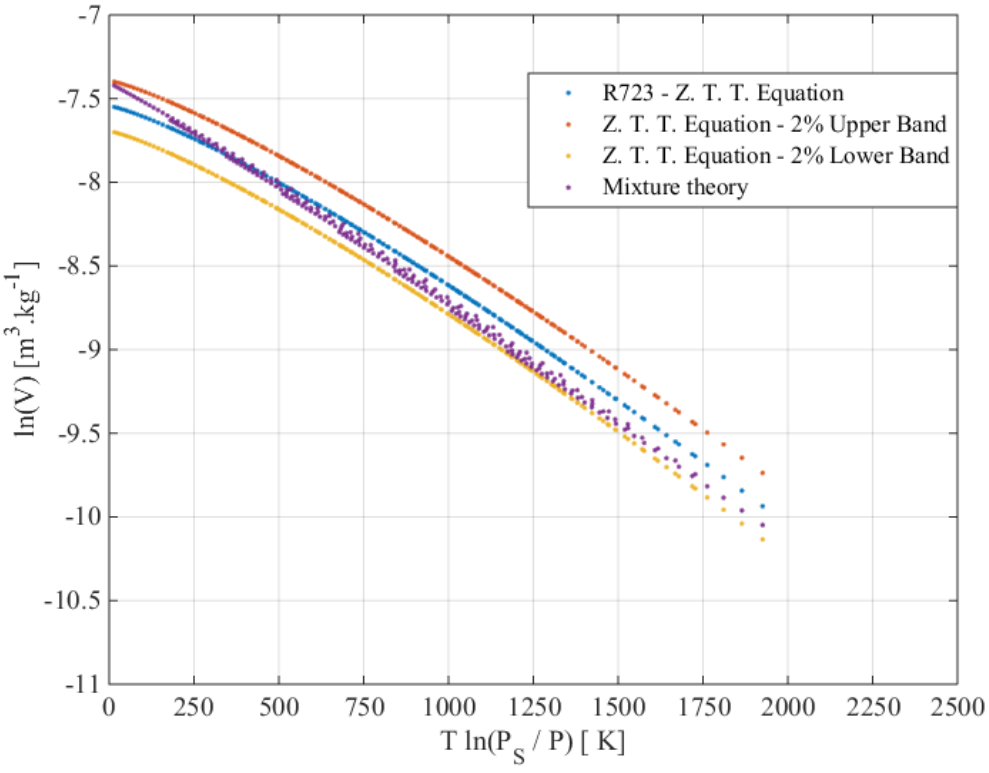

Figure 5.21. Comparison between volumetric uptakes of R723 over per mass of 208-C type activated carbon for mixture theory and Equation 5.9a with parameters mentioned in Table 5.12.

5.7. Conclusion

Dubinin-Astakhov's theory, in terms of volumetric uptake adsorption and mass concentration adsorption methods, has been outlined. In this chapter, the adsorption capacity of activated carbon (208-C) was evaluated using ammonia (R717) and dimethyl ether (RE170) refrigerants, via the gravimetric adsorption method. Afterwards the least square curve fitting method was applied to the experimental data to obtain the parameters of the D-A equation for both forms of volumetric uptake and mass uptake adsorption. The standard estimated error for the fitted curve on the experimental data for each form of the D-A equation were calculated as follows:

D-A equation in mass uptake form:

- 208-C / R717 pair calculated SEE is $0.0011\ kg.kg^{-1}$.
- 208-C / RE170 pair calculated SEE is $0.0006\ kg.kg^{-1}$.

D-A equation in volumetric uptake form:

- 208-C / R717 pair calculated SEE is $0.385\ m^3.kg^{-1}$.

- 208-C / RE170 pair calculated SEE is $0.06\ m^3.kg^{-1}$.

The adsorption theory of the refrigerant mixture (208-C / R723) was established using two individual refrigerant adsorptions (208-C / R717 and 208-C / RE170) in the form of volumetric uptake of the D-A equation. Afterwards the value of the adsorbed volume of refrigerant mixture (R723) per mass of activated carbon (208-C) over the adsorbate pressure range of $3.5\ bar$ to $18\ bar$ and adsorbent temperature range of 45^oC to 200^oC was compared with previous research. D-A equation parameters in mass uptake form in previous studies [33] were turned into D-A equation parameters in volume uptake form. Comparing the adsorbed volume of R723 per mass of activated carbon using mixture theory with previous research shows a difference in a range of $\pm 2\%\ m^3.kg^{-1}$. Therefore, because of good establishment of the values for D-A equation parameters in mass uptake format from previous research, the following values of $x_0 = 0.3540\ kg.kg^{-1}$, $n = 1.187$ and $k = 3.7342$ were considered for the modelling in Chapters 4 and 6.

References

[1]. F. Stoeckli, Microporous carbons and their characterization: the present state of art, Carbon, 1990; 28:1-6.

[2]. R. A. Perez, G. Mestres, Role of pore size and morphology in musculo-skeletal tissue regeneration, Materials Science and Engineering: C, 2016; 61 (1): 922- 939.

[3]. K. S. Sing, D. H. Everett, R. A. W. Haul, L. Moscou, R. A. Pierotti, J. Rouquerol, T. Siemienewska, Reporting physisorption data for gas/solid systems with special refernces to the determination of surface area and porosity, Pure and applied chemistry, 1985; 57:603- 619.

[4]. A. Ahmadpour, D.D. Do, The preparation of active carbons from coal by chemical and physical activation, Carbon, 1996; 34 (4): 471-479

[5]. R. Kandiyoti, J. I. Lazaridis, B. Dyrvold, C. R. Weerasinghe, Pyrolysis of a $ZnCI_2$-impregnated coal in an inert atmosphere, Fuel, 1984; 63 (11): 1583-1587.

[6]. http://www.chemvironcarbon.com/en/; 01/07/2012.

[7]. S. Brunauer, The Adsorption of Gases and Vapour, Vol. I - Physical Adsorption, Princeton University Press, 1974.

[8]. D. M. Ruthven, Principles of adsorption and adsorption processes, Jhone Wiley and Sons, 1984.

[9]. S. Brunauer, L.S. Deming, W. S. Deming, E. Teller, On a Theory of the van der Waals Adsorption of Gases. Journal of the American Chemical Society, 1940; 62: 1723- 1732.

[10]. P. B. Balbuena, K. E. Gubbins, Theoretical interpretation of adsorption behaviour of simple fluids in slit pores, Langmuir, 1993; 9: 1801- 1814.

[11]. H. M. Freundlich, Over the adsorption in solution,. Z Phys Chem, Stoechiom Verwandtschaftsl. 1906:385-471.

I. Langmuir, The constitution and fundamental properties of solid and liquids. Part I. solid. Journal of the American Chemical Society. 1916; 38(11):2221-95.

[12]. I. Langmuir, The adsorption of gases on plane surfaces of glass, mica and platinum.Journal of the American Chemical Society. 1918; 40(9):1361-403.

[13]. http://nptel.ac.in/courses/103103026/module1/lec2/3.html 20/05/2016

[14]. S. Brunauer, P. H. Emmett, E. Teller. Adsorption of Gases in Multimolecular Layers. Journal of the American Chemical Society. 1938; 60(2):309-19.

[15]. Polanyi M. Adsorption from the Point of View of the Third Law of Thermodynamics. Verhandlungen der Deutschen Physikalischen Gesellschaft. 1914;16:1012-6.

[16]. B. Pan, H. Zhang, Reconstruction of adsorption potential in Polanyi-Based Models and application to various adsorbents, Environmental Science & Technology, 2014; 48 (12): 6772- 6779.

[17]. Dubinin M. M. The Potential Theory of Adsorption of Gases and Vapors for Adsorbents with Energetically Nonuniform Surfaces. Chemical Reviews. 1960; 60 (2): 235-41.

[18]. Dubinin M. M., Zaverina E. D., Raduškevič L. V. Sorption and structure of active carbons. I. Adsorption of organic vapors. Ž Fiz Chim. 1947;21:1351–62.

[19]. Berenyi L. Examination of the Polanyi theory of adsorption. Z Physik Chem. 1920;94: 628–62.

[20]. Ruthven Douglas M. Principles of adsorption and adsorption processes. New York: John Wiley & Sons; 1984.

[21]. M. Smisak, S. Cerny, Active Carbon, Elsevier, New York 1970. pp118-119

[22]. R. E. Critoph, Performance Limitations of Adsorption Cycles for Solar Cooling, Solar Energy, 1988; 41 (1): 21-31.

[23]. R. E. Critoph, L. H Turner, Performance of Ammonia-Activated Carbon and Ammonia-Zeolite Heat Pump Adsorption Cycles, Proceedings of Conference. Pompe A Chaleur Chiminique De Haut Performance. Perpignan. (publ. Lavoisier) 1988, pp202-211.

[24]. M. M. Dubinin and V. A. Astakhov, Description of Adsorption Equilibria of Vapors on Zeolites over Wide Ranges of Temperature and Pressure In Molecular Sieve Zeolites-Ii, American Chemical Society: Washington, D C., 1974;102:69-85.

[25]. R. E. Critoph, Evaluation of alternative refrigeration – adsorbent pairs for refrigeration cycle, Applied Thermal Engineering, 1996;16(11):891-900.

[26]. Y. Zhong, R.E. Critoph, R.N. Thorpe, Z. Tamainot-Telto, Yu.I. Aristov, Isothermal sorption characteristics of the $BaCl_2$–NH_3 pair in a vermiculite host matrix, In: Applied Thermal Engineering, 2007; 27(14-15): 2455-2462.

[27]. ASAP2020, Micromeritics Instrument Corporation, 01/07/2012 http://www.micromeritics.com/Product-Showcase/ASAP-2020-Plus-Physisorption.aspx

[28]. Magnetic suspension balances, Rubotherm Company, 01/07/2012 http://www.rubotherm.de/magnet.php.

[29]. G. O. Wood, Affinity coefficients of the Polanyi/Dubinin adsorption isotherm equations: A review with compilations and correlations, Carbon. 2001; 39(3): 343-56.

[30]. M. Mohanraj, C. Muraleedharan, S. Jayaraj, A review on recent developments in new refrigerant mixtures for vapour compression-based refrigeration, air-conditioning and heat pump units, International Journal of Energy Research, 2011; 35: 647–669.

[31]. DA. Didion, DB. Bivens, Role of refrigerant mixtures as alternatives to CFCs, International Journal of Refrigeration 1990; 13:163–175.

[32]. Z. Tamainot-Telto, Novel exploitation of Dubinin-Astakhov theory in sorption reactor design for refrigeration and heat pumps applications. 2014 International Sorption Heat Pump Conference, Maryland, USA, 31 Mar -3 Apr 2014, Published in Proceedings of 2014 International Sorption Heat Pump Conference, pp. 1-4.

[33]. R.E. Critoph, Activated carbon adsorption cycles for refrigeration and heat pumping, Carbon, 1989, 27 (1): 63-70.

[34]. Ho Teng James C. McCandless and Jeffrey B. Schneyer. Thermochemical characteristics of dimethyl ether — an alternative fuel for compression-ignition engines. In: SAE 2001 World Congress (2001-01-0154); Detroit, Michigan March 5-8, 200. ISSN 0148-7191, Copyright 2001 Society of Automotive Engineers, Inc.

[35]. X. Ye, N. Qi, Y. Ding, M. D. LeVan, Prediction of adsorption equilibrium using a modified D–R equation: pure organic compounds on BPL carbon, Carbon, 2003, 41 (4): 681-686.

[36]. F Stoeckli, A Guillot, A.M Slasli, Specific and non-specific interactions between ammonia and activated carbons, Carbon, 2004, 42 (8): 1619-1624.

[37]. Z. Tamainot-Telto., S. J. Metcalf, R. E. Critoph, Investigation of activated carbon-R723 pair for sorption generator, International Heat Powered Cycles Conference, Berlin (Germany)-2009a.

[38]. G. Lychnos, Z. Tamainot-Telto, Experimental investigation of activated carbon : R723 pair for use in adsorption heat pump and refrigeration systems. 2014 International Sorption Heat Pump Conference, Maryland, USA, 31 Mar -3 Apr 2014, Published in Proceedings of 2014 International Sorption Heat Pump Conference, pp. 1-6.

[39]. B. B. Saha, I. I. El-Sharkawy, K. Habib, S. Koyama, K. Srinivasan, Adsorption of Equal Mass Fraction Near an Azeotropic Mixture of Pentafluoroethane and 1,1,1-Trifluoroethane on Activated Carbon. Journal of Chemical Engineering Data, 2008, 53 (8): 1827- 1876.

[40]. B. B. Saha, I. I. El-Sharkawy, R. Thorpe, R. E. Critoph, Accurate adsorption isotherms of R134a onto activated carbons for cooling and freezing applications. International Journal of Refrigeration, 2012, 35 (3): 499- 505.

[41]. W. K. Lewis, E. R. Gilliland, B. Chertow, W. P. Cadogan, Adsorption equilibria: hydrocarbon gas mixtures. Industrial & Engineering Chemistry, 1950, 42 (7): 1319- 1326

[42]. B. P. Bering, V. V. Serpinskii, S. I. Surinova, Adsorption of a gas mixture. Communication 7. Joint adsorption of a binary mixture of vapors on activated charcoal. Izv Akad Nauk SSSR Ser Khim 1965; 5:769–76, English translation.

[43]. A. L. Myers, J. M. Prausnitz, Thermodynamics of mixed-gas adsorption. American Institute of Chemical Engineers Journal, 1965, 11 (1): 121-127.

[44]. S. J. Doong, R. T. Yang, A simple potential-theory model for predicting mixed-gas adsorption, Industrial & Engineering Chemistry, 1988, 27 (4): 630-635.

[45]. G. O. Wood, Review and comparisons of D/R models of equilibrium adsorption of binary mixtures of organic vapors on activated carbons. Carbon, 2002, 40 (3): 1883-1890.

[46]. A. Lavanchy, F. Stoeckli, Dynamic adsorption of vapour mixtures in active carbon beds described by the Myers-Prausnitz and dubinin theories. Carbon, 1997, 35 (10-11): 1573-1579.

Chapter 6

Thermal generator modelling and performance optimization

6.1. Introduction

The object of this section is the modelling of a tubular generator with granular activated carbon (208-C) / R723 pair, with regard to different applications such as air conditioning, ice making and a heat pump. The model under consideration was developed by including the ideal desorption effect without heat and mass recovery, while imposing the ideal temperature jump for the boundary of the tubular generator. During the modelling procedure, information such as driving temperature (T_g), coefficient of performance (COP), and specific cooling and heating powers (SCP & SHP) were collected. Finally, the information collected was used to establish a correlation to estimate the optimum driving temperature, COP, SHP and SCP, based on different governing parameters such as granular activated carbon packed density, outside diameter (OD) and the length of the thermal generator. This information will provide an overall picture that will allow us to choose the right size of thermal generator with granular activated carbon (208-C) / R723 pair for a specific application based on optimum governing parameters, such as the range of heat source availability and the power requirement.

6.2. Adsorption tubular generator

Stainless steel and copper alloy (CuNi10) were used as body material for the generator. Table 6.1 shows the properties of these materials.

Material	***Cp***	***λ***	***ρ***
	$J.kg^{-1}.K^{-1}$	$W.m^{-1}.K^{-1}$	$kg.m^{-3}$
Stainless Steel	460	16.3	7818
CuNi90/10	385	42	8610

Table 6.1. Properties of thermal generator body materials, used in tubular generator modelling.

To produce comparable results, tubular generator length was kept constant in all applications; the length was set at *1 meter*. Table 6.2 shows the physical specifications of the tubular generator, such as outside diameter and wall thickness, for each specified generator body material.

The adsorption pair which was used in modelling the thermal generator was granular activated carbon 208-C / R723. The density of the activated carbon-packed bed in the generator varied from *550 kg.m^{-3}* to *750 kg.m^{-3}*, by *50 kg.m^{-3}* increments. The 208-C granular activated carbon and liquid R723 specific heat were considered as *1125 J.kg^{-1}.K^{-1}* and *4500 J.kg^{-1}.K^{-1}*, respectively. The thermal conductivity (λ) and heat transfer coefficients of the contact wall / packed carbon (h) were obtained from Equation 6.1 and Equation 6.2, from *Chapter 4*:

Length	***Material***	***OD***		***Wall thickness***
m		***Inch***	***mm***	***mm***
1	Stainless Steel	$^1/_4$	6.38	0.15
		$^1/_2$	12.4	0.25
		$^3/_4$	19.05	0.56
		1	25.4	0.71
		$1\ ^1/_8$	28.58	0.91
	CuNi90/10	$^1/_4$	6.38	1
		$^1/_2$	12.4	
		$^3/_4$	19.05	
		1	25.4	
		$1\ ^1/_8$	28.58	

Table 6.2. Tubular thermal generator dimensions.

$$\lambda = 2.787\ x + 0.0026\ \rho - 1.4175 \quad (6.1)$$

$$h = 192.5926\ x + 3.0562\ \rho - 1621.4058 \quad (6.2)$$

where λ is thermal conductivity ($W.m^{-1}.K^{-1}$), h is the heat transfer coefficient of the contact wall/packed carbon ($W.m^{-2}.K^{-1}$), x is adsorption concentration ($kg.\ kg^{-1}$) and ρ is the density of the granular activated carbon packed-bed ($kg.m^{-3}$).

6.3. Application selection

The modelling was carried out for air conditioning, ice making and heat pump applications, at the range of *75^{o}C* to *250^{o}C* for driving temperature (T_g), in *25^{o}C*

temperature increments. Table 6.3 shows the evaporation and condensation conditions for each specified driving temperature (T_g).

Application	$T_{evaporation}$ ^oC	$P_{evaporation}$ bar	$T_{condensation}$ ^oC	$P_{condensation}$ bar	Evaporation Heat (LH) - $kJ.kg^{-1}$
Air Conditioning	10	6.8	35	14.5	747.3
Ice Making	-5	4.1	35	14.5	736.3
Heat Pump	5	5.8	40	16.6	725

Table 6.3. Evaporation and condensation pressures and temperatures for R723 where used in generator modelling.

6.4. Thermal generator modelling

The modelling program was divided into three sections. Figure 6.1 shows the first section of the program, in which initial information such as application, types of adsorbent / adsorbate pair (which lead to the extraction of thermal information), physical appearance of the generator and body material, were collected and passed into the modelling section.

Figure 6.2 shows the COP and SCP (or SHP), which were the output of the modelling section, as seen in the optimization program flow chart (Figure 6.1). The outputs of the modelling section were calculated with regard to the early-stage governing input parameters. The input parameters were used in the modelling section to obtain values for the cycle time (based on desorption cycle time), total heat input into the system, and cooling or heating power. In the later stages these values were used to calculate COP and SCP (or SHP) for comparison and optimisation purposes.

During the final stage, the optimization program (Figure 6.1) used the outputs of the modelling section, which are illustrated in Figure 6.2, to establish a meaningful correlation between COP and SCP (or SHP) versus driving temperature (T_g), activated carbon packed density, tubular generator wall thickness and outside diameter.

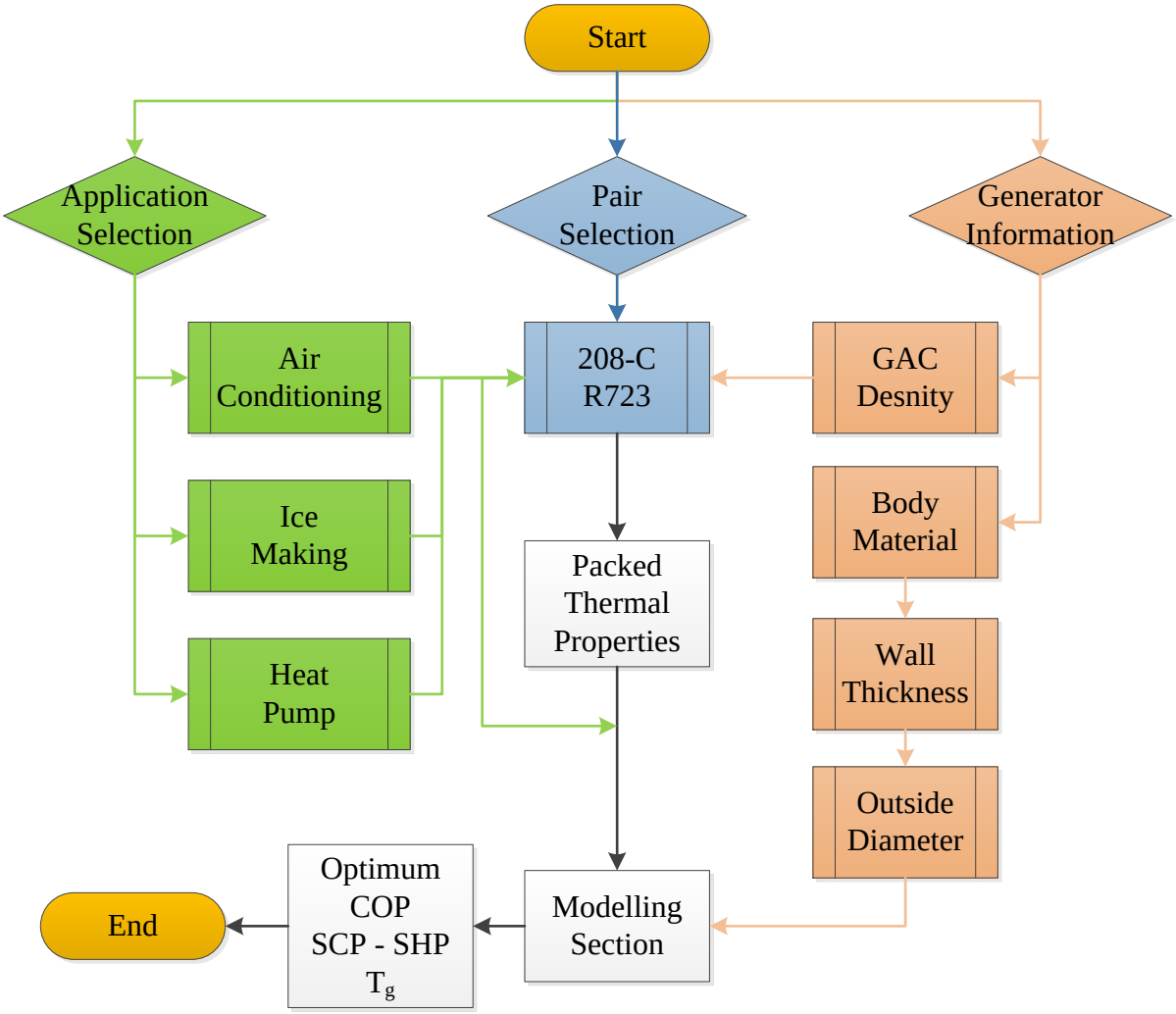

Figure 6.1. Three stages of the optimization and modelling program with input and output of each individual section.

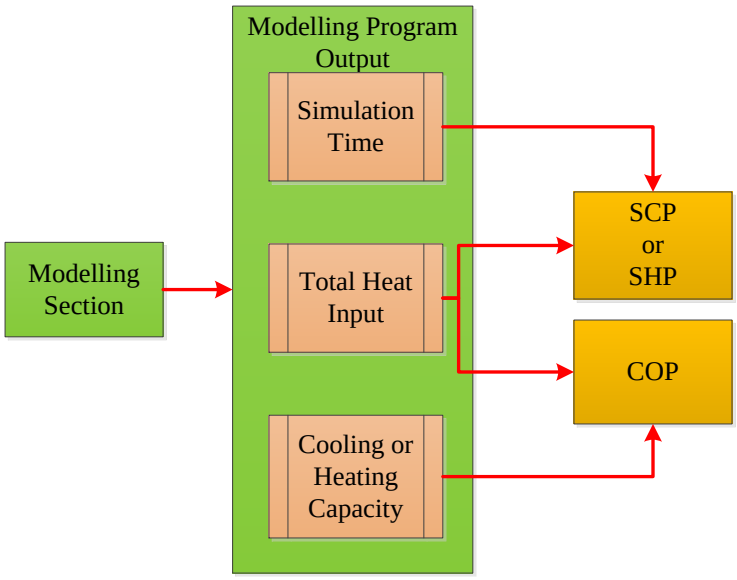

Figure 6.2. Internal breakdown and output of modelling section based on broad picture of the modelling program.

6.4.1. Heat and mass transfer modelling

In general, the mathematical modelling of the thermal generator is classified in three categories:

- Ideal adsorption model (steady state)
- Lumped model (transient)
- Numerical heat and mass transfer model (transient).

The ideal adsorption model normally uses thermodynamic equations to express the mathematical model for the steady state adsorption cycle [1, 2]. This model is widely used for comparative study to understand the effect of temperature or heat transfer parameters on the system's SCP or COP. The lump model, unlike the ideal model, considers the transient heat transfer through the thermal generator [3]. Figure 6.3 shows an example of thermal generator modelling using a transient model with ordinary differential equations (ODE). For the purposes of modelling, just three nodes were considered [4].

The third model, which is more complex than other two methods, is the numerical modelling of heat and mass transfer. This model, in comparison to the other two models, is more dynamic, and the equation can be expressed by finite difference [5], finite volume [6] or finite element [7] methods. More information could be found in the paper by Li Yong et al. [8].

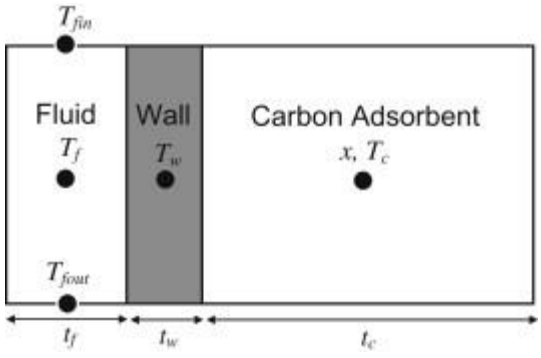

Figure 6.3. Schematic diagram of the modelled generator using the lumped model [4].

The simulation method used in the modelling of the thermal generator is a combination of a numerical method based on finite difference, with some assumptions from the ideal adsorption cycle. Since the length of the generator

compared to its diameter is long enough ($^{D}/_{L} < 0.03$), heat transfer through the cylindrical generator can be constructed as a one-dimensional model. The discretised domain for a half cross-section of the cylindrical generator for energy balance on a carbon and cylinder body is illustrated in Figure 6.8.

The generator temperature, including the generator body, carbon-packed bed and adsorbed gas, was initially assumed to be equivalent to the condensation temperature (*Tc*). The driving temperature was then imposed into the cylinder's outer surface, and afterwards the temperature of the internal node between the centre and the surface of generator and the centre node was calculated. Table 6.3 shows the initial temperature (condensation temperature – *Tc*) of the tubular generator; air conditioning and ice making applications were considered at $35^{o}C$, while the heat pump application was considered at $40^{o}C$.

After establishing the initial parameters, the second step in the numerical modelling of heat transfer through the tubular generator is to set up the boundary conditions. The boundary conditions were introduced at two sections:

- Figure 6.4 shows the adiabatic conditions at the centre node, which left the thermal conduction through the activated carbon as the only energy source.
- Figure 6.5 shows the constant temperature condition, which was introduced into the tubular generator's surface node.

During the modelling procedure the driving temperature (T_g) was changed from $75^{o}C$ to $250^{o}C$ in $25^{o}C$ increments.

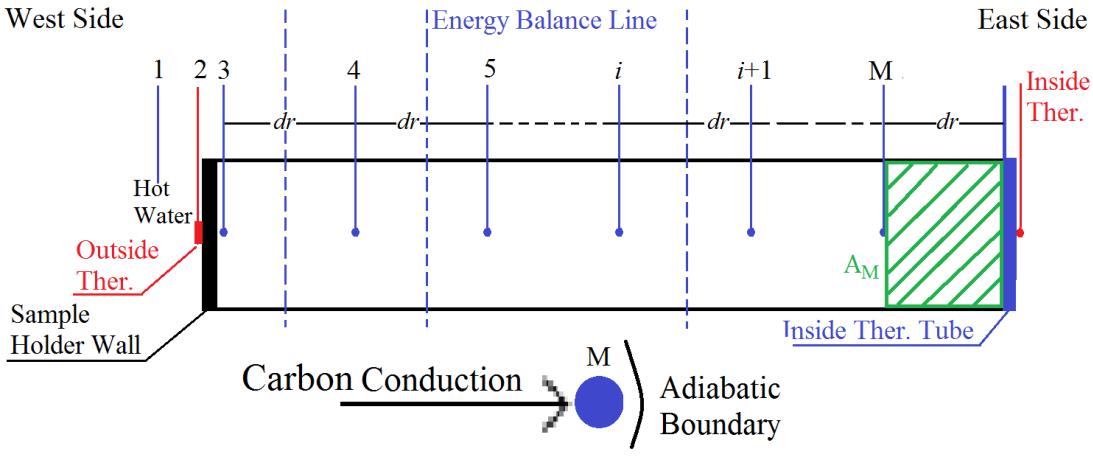

Figure 6.4, . Domain discretization for energy balance at the carbon-packed centre node. Heat transfer mechanism into the centre node and energy balance line with delimiting of the control volume (A_M).

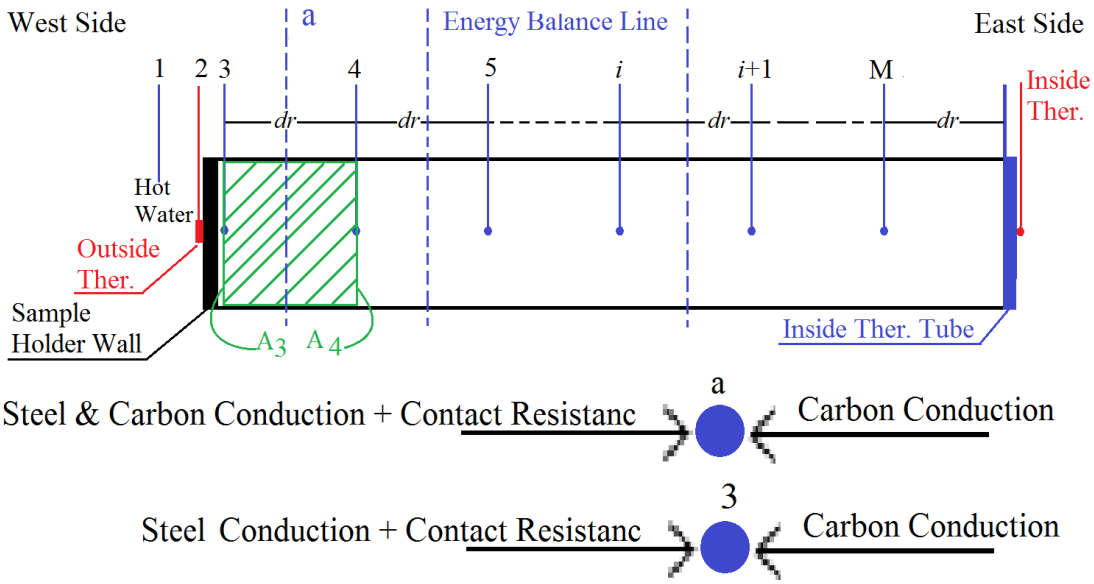

Figure 6.5. Domain discretization for energy balance at the carbon-packed outer boundary. Heat transfer mechanism into the boundary node and energy balance line with delimiting of the control volume (A_3, A_4).

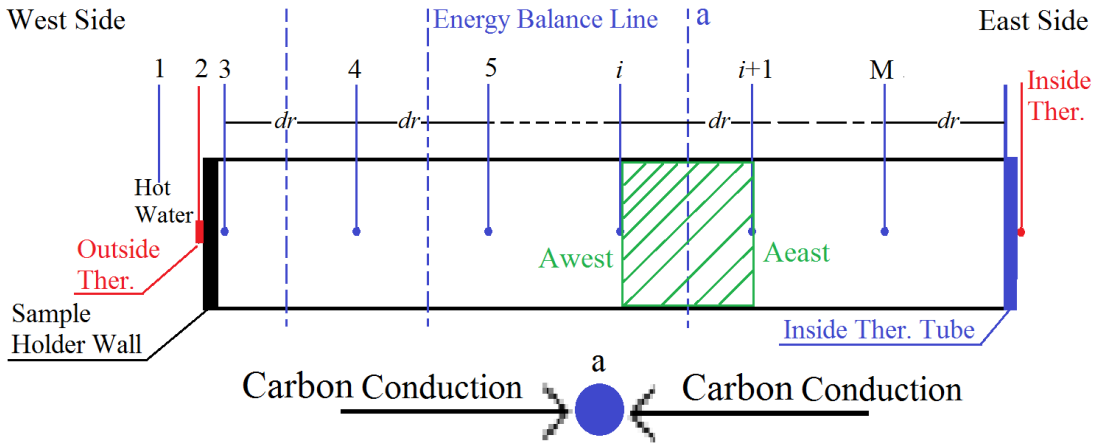

Figure 6.6. Domain discretization for energy balance at the carbon-packed inner nodes. Heat transfer mechanism into the boundary node and energy balance line with delimiting of the control volume (A_i).

The generator was assumed to be connected to a condenser during the desorption process, and pressure is uniform through the bed. Therefore, pressure at the initial set-up was considered to be evaporation pressure (Pe), and later on at the second step or at a new time field, suddenly jumped to condensation pressure (Pc). Figure 6.7 is an illustration of the generator surface temperature jump from the initial set-up, condensation temperature (T_C), to the driving generation temperature (T_g).

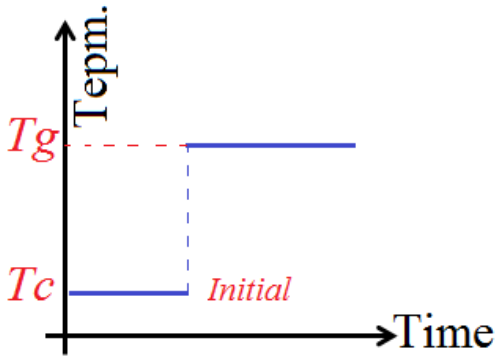

Figure 6.7. Step temperature at outer node on surface of tubular thermal generator model. The initial temperature is condensation temperature (*Tc*) which jumped to the driving temperature (*Tg*) at a new time field after the initial set-up.

To model heat and mass transfer through the tubular thermal generator, the same methodology and discrete numerical domain, as previously described in *Chapter 4*, were adopted. Figure 6.8 shows the discrete numerical model and the direction of the heat wave while travelling from the surface to the centre of the tubular generator.

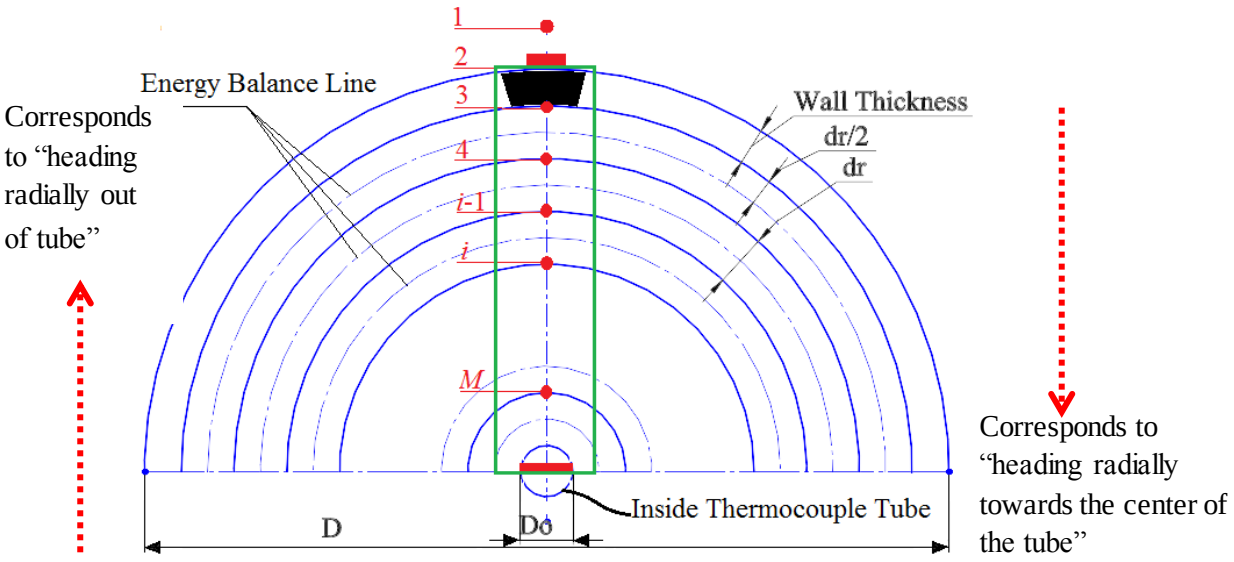

Figure 6.8. Illustration of a half cross-section of domain discretization for energy balance in the carbon-packed bed in a one-dimensional cylindrical configuration.

Equation 6.3 explains the energy balance over the specific volumes illustrated and highlighted in Figure 6.8.

$$UAdT = M_{Carbon}\left[C_{P,Carbon} + xC_{P,R723\ Liquid}\right]\frac{dT}{dt} - H\frac{dm_{R723}}{dt} \quad (6.3)$$

Finally, the discretised form of Equation 6.3 is Equation 6.4:

$$\frac{\frac{UAdT}{M_{Carbon}}dt+\left(RA\frac{T_i^t}{T_{sat}^t}\right)\left[Knx_i^t\frac{T_i^t}{{T_{sat}^t}^2}\left(\frac{T_i^t}{T_{sat}^t}-1\right)^{n-1}\right](T_{sat}^{t+1}-T_{sat}^t)}{(CP)-\left(RA\frac{T_i^t}{T_{sat}^t}\right)\left[-\frac{Knx_i^t}{T_{sat}^t}\left(\frac{T_i^t}{T_{sat}^t}-1\right)^{n-1}\right]}+T_i^t=T_i^{t+1} \quad (6.4)$$

In Equation 6.4, M_{Carbon} is the mass of the carbon that is allocated in the control volume. Equations 6.5 and 6.6 show the carbon mass at the centre node (Figure 6.4) and remainder of the control volume (Figure 6.5), respectively. R is the specific gas constant ($364.2\ J.kg^{-1}.K^{-1}$), A corresponds to the slope of the saturation curve on a plot of $ln(P)$ vs. $-1/T_{sat}$ ($A = 2621.3$) and T_{sat} is the saturation temperature (K) corresponding to the gas pressure P. The value x (*kg of adsorbate / kg of adsorbent*) is the concentration or mass of the adsorbed refrigerant per mass of carbon, which is calculated using the Dubinin-Astakhov (D-A) definition in Equation 6.7. The values k and n are constant values of the D-A equation. Equation 6.8 is the definition of total specific heat (CP).

$$M_{M-Carbon}=\pi\left(r_M^2-{D_o^2}/{4}\right)\times\rho_{Carbon}\times L_C \quad (6.5)$$

$$M_{i-Carbon}=\pi(r_i^2-r_{i+1}^2)\times\rho_{Carbon}\times L_C \quad (6.6)$$

$$x=0.354\ exp\left[-3.7342\left(\frac{T}{T_{sat}}-1\right)^{1.1817}\right] \quad (6.7)$$

$$CP=\ C_{P,Carbon}+xC_{P,R723\ Liquid} \quad (6.8)$$

Figure 6.8 shows the overall heat transfer coefficient, UA, which connects the west and east temperature nodes over the discrete domain.

$$UAdT=UA_{West}[T_{i-1}^t-T_i^t]+UA_{East}[T_{i+1}^t-T_i^t] \quad (6.9)$$

Table 6.4 shows the values of the top and bottom overall heat transfer coefficients regarding Figures 6.4, 6.5, 6.6 and 6.8, for boundary and internal nodes.

Node Location	UA_{West}	UA_{East}
Surface (outer boundary)	$\frac{2\pi r_3 L_C}{\frac{t_w}{\lambda_{Steel}} + \frac{2}{h_{internal}} + \frac{dr/2}{\lambda_{Carbon}}}$	$\frac{2\pi r_4 L_C}{\frac{dr}{\lambda_{Carbon}}}$
Internal node	$\frac{2\pi r_i L_C}{dr/\lambda_{Carbon}}$	$\frac{2\pi r_{i-1} L_C}{dr/\lambda_{Carbon}}$
Centre node (inner boundary)	$\frac{2\pi r_M L_C}{dr/\lambda_{Carbon}}$	0

Table 6.4. Discretised equations to calculate overall heat transfer coefficient regarding top and bottom of the nodes.

Equation 6.4, which is the discretised model of Equation 6.3, was used to calculate each internal node temperature at a specific time step. In Equation 6.4 the values of the time and length steps were kept constant for modelling the tubular generator with various physical dimensions and applications. The time step (*dt*) was set at *0.1 s* and the length step was set at *1.2 mm*.

In an ideal model, the numerical simulation would continue until the entire generator reaches the steady state situation, which means that the centre node temperature reaches the driving temperature at a certain amount of error, with an imposed temperature on the generator surface. In the proposed model, the cycle time was evaluated at the time when the centre node temperature reached the driving temperature, with a difference of 10^oC. When the temperature difference was satisfied, the simulation process was stopped. The final concentration, cycle time and bed temperature distribution were obtained from the modelling procedure.

6.4.2. COP calculation

The coefficient of performance (COP) was obtained in order to evaluate the performance of the adsorption system for air conditioning, ice making and heat pump applications. The COP is defined as the ratio between useful heat output and the total heat input into the system [1]. The expression of COP for the refrigeration cycle which was used in ice making and air conditioning applications is defined by Equation 6.10.

$$COP_{Refrigeration} = \frac{Refrigeration\ Effect}{Total\ Heat\ Input} \tag{6.10}$$

The refrigeration effect is heat which is absorbed by the evaporator and the latent heat of vaporisation, multiplied by the concentration at the initial and final stages, when the generator's centre node reaches the specified criteria.

$$Refrigeration\ Effect = LH \times \left(x_{Initial,\ Average} - x_{final,\ Average}\right) \tag{6.11}$$

Where "*LH*" is the latent heat of vaporisation ($kJ.kg^{-1}$), depending on the evaporation temperature. The latent heat of vaporisation for each application is specified in Table 6.3. The values $x_{\ Initial,\ Average}$ and $x_{\ Final,\ Average}$ are the average concentration ($kg.kg^{-1}$) for all discrete volumes that are estimated from the D-A equation (Equation 6.7), by considering the average temperature of the carbon-packed bed and the uniform pressure in the generator at the initial and end stages of the simulation.

$$Total\ Heat\ Input = \sum_{t=1}^{\substack{total\\ simulation\\ time}} \left[\left(\frac{\sum_{n=3}^{M} T_n^{t+dt}}{i} - \frac{\sum_{n=3}^{M} T_n^{t}}{i}\right) \times \sum_{n=3}^{M} CP_n^{t+dt}\right] \tag{6.11}$$

The total heat of the desorption ($kJ.kg^{-1}$) is obtained by the sum of the product of the temperature increase between a time *t* and time *t+dt*, with the *CP*, which is the overall specific heat ($kJ.kg^{-1}.K^{-1}$) of the carbon and adsorbed R723 over the discrete volume. The overall specific heat was obtained from Equation 6.8 and it is an average for all discrete volumes in the generator at a specific time step.

The nature of the heat pump is a reverse of the refrigeration effect; therefore useful heat was defined as the amount of rejected heat by the system over the total input heat rate. The performance of the adsorption heat pump was measured by the parameter defined as the heat pump's coefficient of performance ($COP_{\ Heat\ Pump}$), illustrated by Equations 6.13 and 6.14.

$$COP_{Heat\ Pump} = \frac{Rejected\ Heat\ by\ the\ System\ (Useful\ Heat)}{Total\ Heat\ Input} \tag{6.13}$$

$$COP_{Heat\ Pump} = COP_{Refrigeration} + 1 \tag{6.14}$$

6.4.3. SCP & SHP calculation

Specific cooling power (SCP) and specific heating power (SHP) are two parameters which can explain thermal generator performance and can help with the optimal selection of technology, design and adsorbent / adsorbate pair. The temperature

conditions of evaporation, condensation and driving temperature also have an effect on the SHP and SCP. For that reason, the SCP and SHP are essentially the useful power output per *kg* of the allocated adsorbent in the thermal generator ($kW.kg^{-1}$).

$$SCP = \frac{Refrigeration\ Effect}{Cycle\ Time} \tag{6.15}$$

$$SHP = \frac{Useful\ Heat}{Cycle\ Time\ \times Total\ Carbon\ Mass} \tag{6.16}$$

6.5. Optimum performance

Equations 6.10 (or 6.14) and 6.15 (or 6.16) show that the COP increases with an increase in cycle time. However, the SCP (or SHP) will decrease. Therefore, increasing the cycle time is a trade-off between COP and SCP.

Table 6.5 illustrates the results obtained from the simulation of a stainless-steel cylindrical thermal generator with a *6.38 mm* outside diameter (OD) and *0.15 mm* wall thickness. The granular activated carbon (GAC) packed density was fixed at *600* $kg.m^{-3}$. The table shows that by increasing the driving temperature, the cycle time was increased. Figure 6.9 shows that by increasing the driving temperature, which was imposed into the wall of the thermal generator, the SCP will increase while the COP decreases. The COP is a comparative value without any unit, but the SCP is a useful heat output per *kg* of adsorbent. As previously noted, the cycle time causes a trade-off between COP and SCP. Therefore, in order to achieve the optimum point, beyond which point any increase in one parameter causes a reduction in another, normalised values of COP and SCP (or SHP) were introduced. The normalisation process brings the COP and SCP (SHP) into the range of *0* to *1*, which gives us the capability to connect the driving temperature with dimensionless parameters.

Equations 6.17 and 6.18 define the normalised value in the range of *0* to *1* by using the maximum and minimum values of COP and SCP (or SHP), obtained from Table 6.5, for the specific range of driving temperature.

$$COP_{Normalized\ Value} = \frac{COP_{Main Vlue} - COP_{min}}{COP_{max} - COP_{min}} \tag{6.17}$$

$$SCP_{Normalized\ Value} = \frac{SCP_{Main Vlue} - SCP_{min}}{SCP_{max} - SCP_{min}} \quad (6.18)$$

Figure 6.9 shows the normalised values of COP and SCP regarding Equations 6.17 and 6.18, for the thermal generator, with the same configuration and density as Table 5.5. In Figure 6.9 the intercept of the $COP_{normalised}$ and $SCP_{normalised}$ trends is clearly recognisable in terms of driving temperature.

T_g	Cycle Time (s)	COP	SCP	λ	h	Collected liquid mass	$\bar{x}$	Normalised SCP	Normalised COP
^oC			$kW.kg^{-1}$	$W.m^{-1}.K^{-1}$	$W.m^{-2}.K^{-1}$	gr	$gr.gr^{-1}$		
75	57.00	2.24	1.07	0.934	267	1.422	0.284	0.00	1.00
100	71.80	1.90	1.40	0.848	261	2.353	0.253	0.18	0.65
125	77.80	1.70	1.69	0.776	256	3.077	0.227	0.34	0.45
150	79.20	1.56	1.96	0.718	252	3.625	0.206	0.49	0.30
175	78.10	1.47	2.21	0.673	249	4.029	0.190	0.63	0.2
200	75.60	1.40	2.45	0.638	247	4.322	0.178	0.76	0.13
225	72.50	1.33	2.67	0.612	245	4.532	0.168	0.88	0.06
250	69.30	1.27	2.89	0.593	243	4.681	0.162	1.00	0.00

Table 6.5. Analysis summary for stainless-steel cylindrical thermal generator for an air conditioning application with *600* $kg.m^{-3}$ GAC packed density, *6.38 mm OD* and *0.15 mm* wall thickness (t_w).

The intercept in Figure 6.9 is an optimum point, which is illustrate in Table 6.6. $COP_{normalised}$ and $SCP_{normalised}$ were turn into real values using Equations 6.19 and 6.20.

$$COP_{Main Vlue} = COP_{Normalized\ Value} \times (COP_{max} - COP_{min}) + COP_{min} \quad (6.19)$$

$$SCP_{Main Vlue} = SCP_{Normalized\ Value} \times (SCP_{max} - SCP_{min}) + SCP_{min} \quad (6.20)$$

$COP_{optimum}$	$SCP_{optimum}$	$Tg_{optimum}$
1.413	0.469	133.8 ^{o}C

Table 6.6. Optimum values of SCP, COP and T_g for stainless-steel cylindrical thermal generator for an air conditioning application, with *600* $kg.m^{-3}$ GAC packed density, *6.38 mm OD* and *0.15 mm* wall thickness.

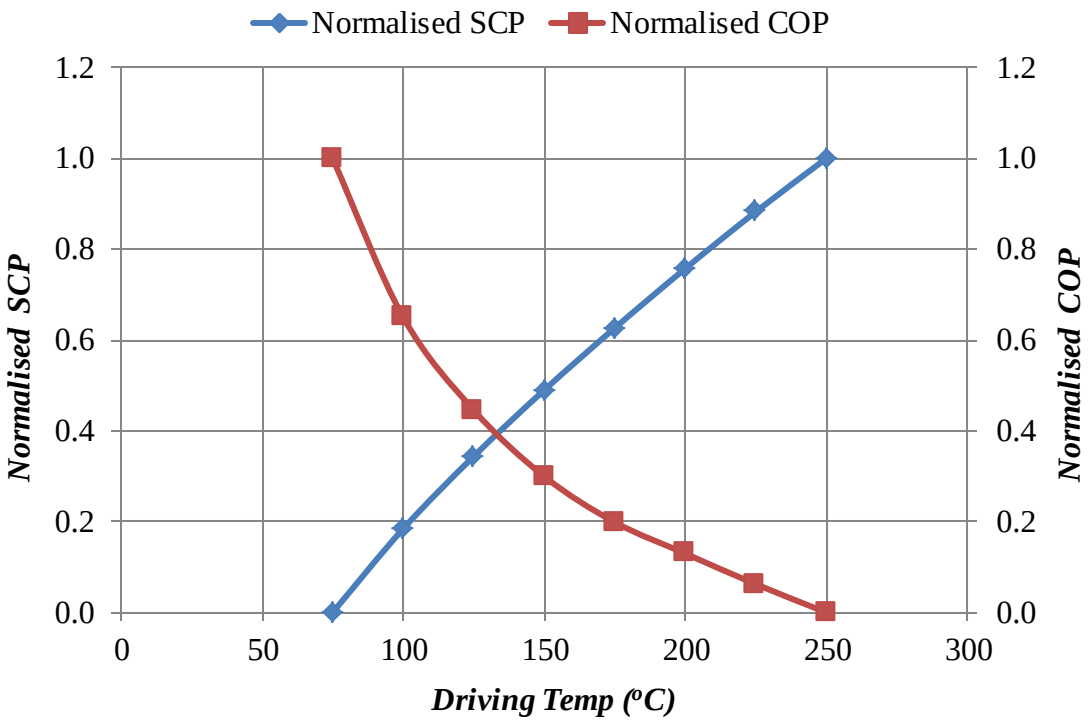

Figure 6.9. Normalised SCP and COP vs driving temperature for a stainless-steel cylindrical thermal generator for an air conditioning application. GAC packed density *600 kg.m^{-3}*, *6.38 mm OD* and *0.15 mm* wall thickness.

6.6. Results and analysis

The analysis was carried out for the following conditions:

- Two different body materials, stainless steel and copper alloy (Table 6.1).
- GAC packed density range of *550 kg.m^{-3}* to *750 kg.m^{-3}*, in increments of *50 kg.m^{-3}*.
- Driving temperature range of *75^{o}C* to *250^{o}C* in *25^{o}C* increments.

Figure 6.10 shows the temperature of the thermal generator's centre node for an air conditioning application, with *600 kg.m^{-3}* GAC packed density and body material of stainless steel.

Analysis of a stainless-steel body material with *600 kg.m^{-3}* GAC packed density for an air conditioning application is as follows:

- By increasing the outside diameter from *6.38 mm* to *28.58 mm* (*4.5* times higher), the cycle time for the higher T_g (*250^{o}C*) was increased from *69.3 s* to *494 s* (*7* times higher), while for the lower T_g (*75^{o}C*) the cycle time was increased from *57 s* to *389 s* (*6.9* times higher).

- By increasing the driving temperature from 75^oC to 250^oC (*3.3* times higher), the cycle time for a smaller diameter (*6.38 mm*) was increased by *22%*, while for a larger diameter (*28.58 mm*) it was increased by *27%*.

Analysis of a copper / nickel body material with *600* $kg.m^{-3}$ GAC packed density for an air conditioning application is as follows:

- By increasing the outside diameter from *6.38 mm* to *28.58 mm* (*4.5* times higher), the cycle time for the higher T_g (250^oC) was increased from *48 s* to *488 s* (*10* times higher), while for the lower T_g (75^oC) the cycle time was increased from *39.5 s* to *384 s* (*9* times higher).
- By increasing the driving temperature from 75^oC to 25^oC (*3.3* times higher), the cycle time for a smaller diameter (*6.38 mm*) was increased by *21.5%*, while for a larger diameter (*28.58 mm*) it was increased by *27%*.

Therefore, increments of outside diameter have a significant effect on the cycle time, compared to driving temperature increments for a thermal generator with similar GAC packed density.

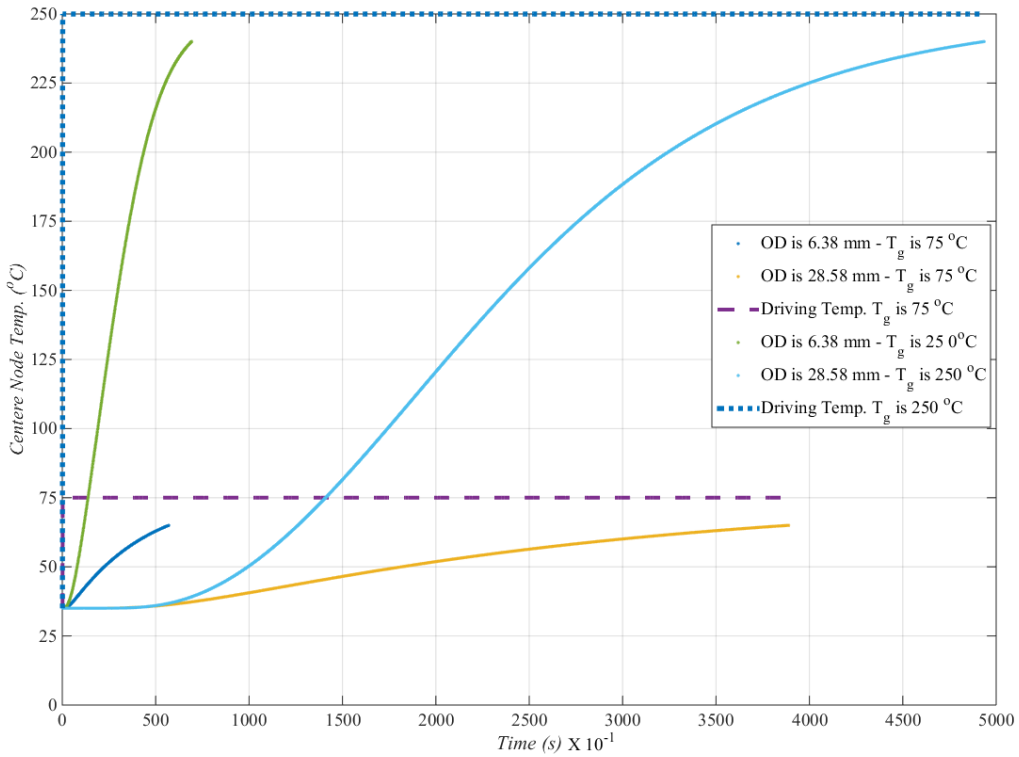

Figure 6.10. The effect of generator *OD* and T_g on trend of centre node temperature increments for a stainless-steel cylindrical thermal generator for an air conditioning application, with *600* $kg.m^{-3}$ GAC packed density.

6.6.1. Cycle time

Equations 6.15 and 6.16 illustrate the specific cooling / heating power (SCP / SHP) for adsorption refrigeration (ice making) and heat pump applications, respectively. The SCP and SHP evaluate the useful power output (kW) per kg of allocated granular activated carbon in the thermal generator ($kW.kg^{-1}$). These equations show that the cycle time has a significant effect: increasing the cycle time may gain some COP, but on the other side cause a reduction in SCP and SHP. In this section, the effect of different aspects of the thermal generator, such as driving temperature, GAC packed density and tubular generator outside diameter, are discussed individually with regards to cycle time. The (half) cycle is deemed to stop when the generator centre node temperature rise is at *90%* of driving temperature. For better comparison, this section considers the air conditioning case study for a thermal generator with a body material of stainless steel. Figures 6.11 shows that, regardless of GAC packed density, the T_g driving temperature effect on cycle time is an ascending trend. Figures 6.12 and 6.13 show that by increasing the GAC packed density, the trend of cycle time for both constant T_g driving temperature and tubular generator outside diameter is a descending one.

Figure 6.11 shows that for a thermal generator with a fixed outside diameter (*OD, 6.38mm*), by increasing the driving temperature from 75^oC to 250^oC at lower density ($550\ kg.m^{-3}$), the cycle time was increased by *38%*, while for a higher density ($750\ kg.m^{-3}$) the cycle time was only increased by *13%*. Figure 6.12 shows that for a thermal generator with a fixed outside diameter (*OD, 6.38mm*), by increasing the density from $550\ kg.m^{-3}$ to $750\ kg.m^{-3}$ at a lower driving temperature (75^oC), the cycle time was decreased *73%*, while for a higher driving temperature (250^oC) the cycle time was decrease by *78%*. Therefore, there is trade-off between the heat source and GAC packed density. To obtain the benefit of increasing the heat source temperature, the cycle time will increase, but it is possible to soften this effect by increasing the GAC packed density.

Figure 6.13 shows that by increasing the GAC packed density for a tubular generator with a specific outside diameter, the cycle time exhibits a descending trend. Table 6.7 shows the summary of Figure 6.13. The noticeable point about Table 6.7 is that by increasing the outside diameter (OD) of the tubular generator, the benefit of

increasing the GAC packed density with regards to reducing the cycle time declined by 18%.

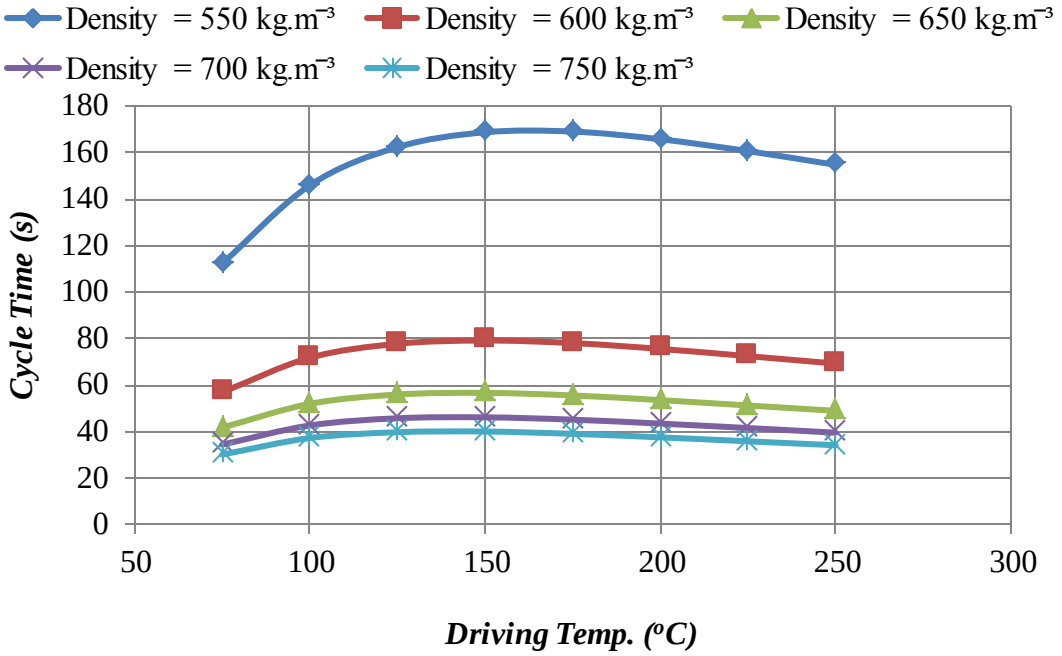

Figure 6.11. T_g effect on total cycle time for stainless-steel cylindrical thermal generator, for an air conditioning application with *6.38 mm* OD. Each line represents the generator's GAC packed density.

OD (mm)	6.38	12.4	19.05	25.4	28.58
Decreasing %	73.11	68.71	64.66	61.21	59.73

Table 6.7. Summary of Figure 6.14, which shows the density effect on reduction of cycle time at constant $T_g = 75^oC$ for a stainless-steel tubular thermal generator for an air conditioning application.

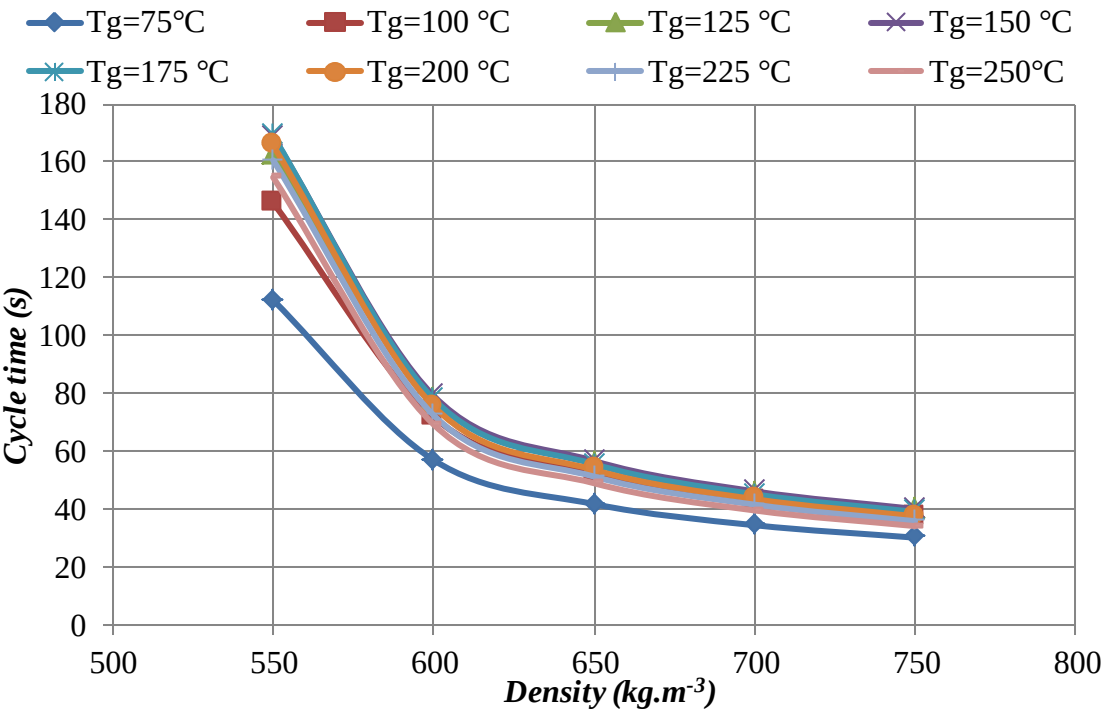

Figure 6.12. GAC density effect on total cycle time, for a stainless-steel cylindrical thermal generator for an air conditioning application with, *6.38 mm* OD. *0.15 mm* t_w. Each line represents the specific driving temperature.

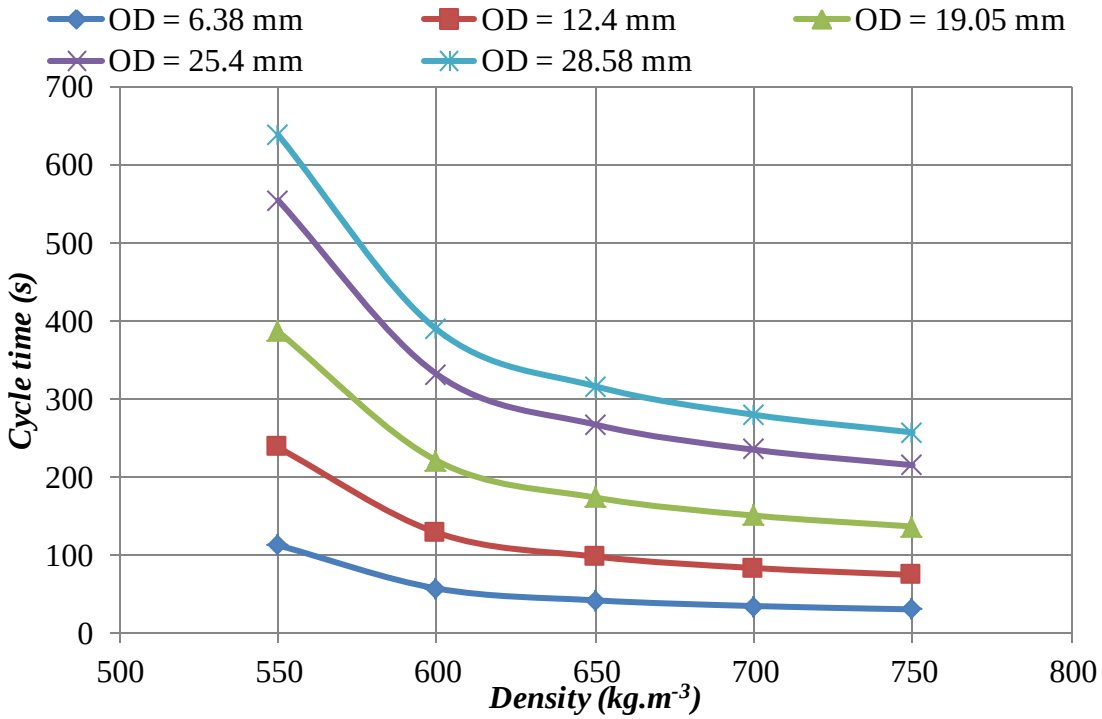

Figure 6.13. Generator GAC density effect on total cycle time at *75°C* T_g, for a stainless-steel cylindrical thermal generator for an air conditioning application. Each line represents the specific generator *OD*.

The other important parameter which has an effect on cycle time is the body material of the generator. The thermal conductivity of Cu-Ni 90/10 is *61%* higher than stainless steel. Therefore, the heat exchange for a generator that uses copper alloy was expected to be faster than one using stainless steel. Figure 6.14 shows, for a tubular generator made of copper alloy with a *6.38 mm* outside diameter (for an air conditioning application), that the cycle time at lower density (*550 kg.m*$^{-3}$) is *29%* and at higher density (*750 kg.m*$^{-3}$) is *32%* less than the cycle time for a tubular generator made of stainless steel.

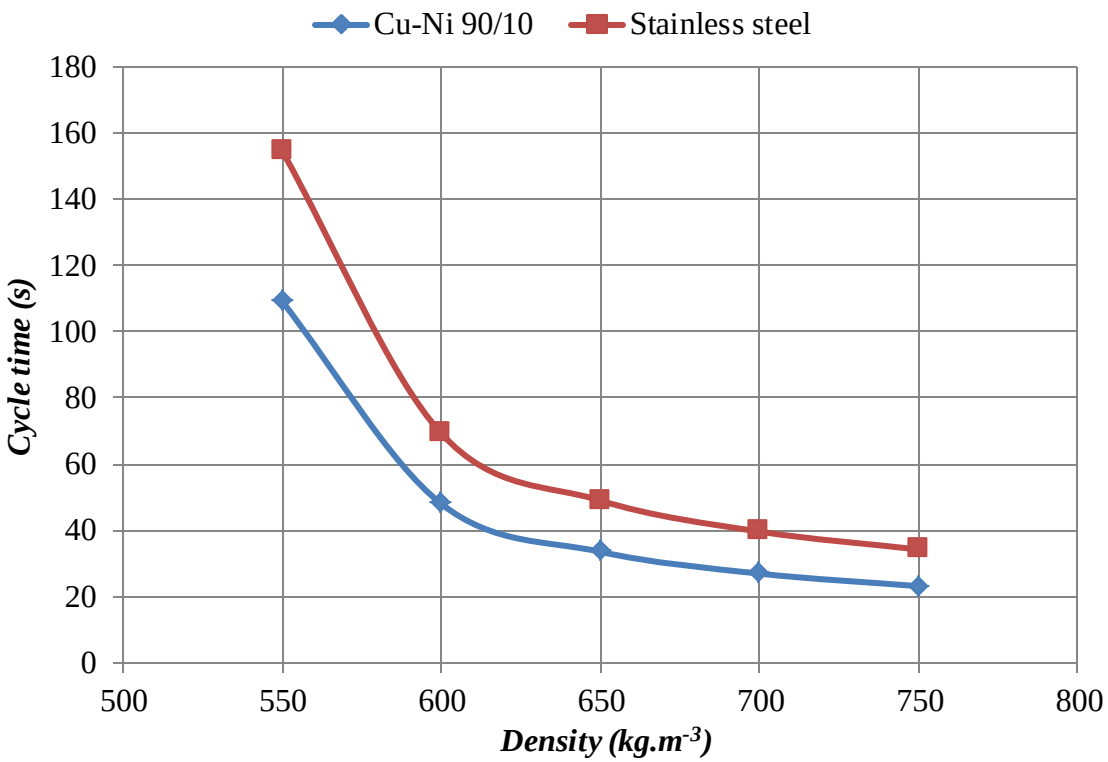

Figure 6.14. The effect of thermal generator body material and GAC packed density on cycle time. The tubular generator's outside diameter is *6.38 mm* and the application is set for air conditioning.

6.6.2. Summary of analysis

Tables 6.8 and 6.9 show the summary of the analysis of air conditioning, ice making and heat pump applications for an adsorption system with a thermal generator made of stainless steel and copper alloy (Cu-Ni 90/10). The summary includes the optimum driving temperature T_g, COP and SCP (or SHP).

Table 6.9 shows that for all types of applications, regardless of outside diameter, by increasing the GAC packed density in a tubular generator made of stainless steel, the COP has a descending trend while the SCP (SHP) has an ascending trend.

Table 6.10 shows the behaviour of COP when increasing the GAC packed density for a tubular generator made of copper alloy, for outside diameters from *12.4 mm* to *28.58 mm*: it exhibits a descending trend, while the SCP (SHP) has an ascending trend. However this trend is reversed for a copper alloy generator with a *6.38 mm* OD.

OD	t_w	GAC Density	Air Conditioning			Ice Making			Heat Pump		
			T_g	COP	SCP	T_g	COP	SCP	T_g	COP	SHP
mm	mm	$kg.m^{-3}$	^oC		$kW.kg^{-1}$	^oC		$kW.kg^{-1}$	^oC		$kW.kg^{-1}$
6.38	0.15	550	130	1.68	0.83	129.6	1.60	0.76	130.2	2.62	1.21
		600	132.3	1.65	1.77	131.5	1.57	1.64	131.2	2.58	2.63
		650	131.8	1.63	2.46	131.6	1.55	2.29	132.9	2.57	3.68
		700	131.7	1.62	3.01	132.6	1.54	2.83	132	2.56	4.49
		750	132.4	1.61	3.48	132.1	1.53	3.26	132.3	2.55	5.20
12.4	0.25	550	131.2	1.62	0.4	130.2	1.54	0.36	132	2.55	0.59
		600	133	1.52	0.80	132.4	1.43	0.73	134.7	2.45	1.23
		650	133.6	1.46	1.08	133.3	1.36	0.99	136.1	2.38	1.7
		700	134.6	1.41	1.29	133.4	1.33	1.19	136.4	2.34	2.0
		750	134.6	1.39	1.46	133.1	1.30	1.34	136.7	2.32	2.35
19.05	0.56	550	131.8	1.56	0.25	130.5	1.48	0.22	133	2.49	0.37
		600	133.8	1.41	0.47	132.4	1.32	0.42	136.2	2.34	0.75
		650	134.7	1.33	0.61	133.4	1.24	0.56	137.3	2.26	1.01
		700	135.3	1.28	0.72	134	1.2	0.66	138	2.21	1.21
		750	135.7	1.25	0.81	134.5	1.16	0.74	138.3	2.18	1.37
25.4	0.71	550	132.2	1.50	0.17	130.6	1.42	0.16	133.6	2.44	0.27
		600	134.2	1.33	0.31	132.5	1.24	0.28	137	2.25	0.51
		650	135.2	1.23	0.40	133.5	1.15	0.36	138.3	2.16	0.68
		700	135.7	1.16	0.46	134.2	1.10	0.42	139.1	2.11	0.81
		750	136.6	1.15	0.52	134.8	1.07	0.47	139.6	2.08	0.91
28.58	0.91	550	132.2	1.48	0.15	130.6	1.40	0.14	134	2.41	0.23
		600	134.2	1.30	0.27	132.5	1.21	0.24	137.2	2.22	0.44
		650	135.3	1.20	0.34	133.4	1.12	0.31	138.5	2.13	0.58
		700	136	1.15	0.39	134.4	1.07	0.35	139.4	2.08	0.69
		750	136.7	1.12	0.43	135	1.04	0.40	140	2.05	0.77

Table 6.8. Optimum results for driving temperature T_g, COP and SCP (or SHP) for a stainless-steel cylindrical thermal generator at different outside diameters (*OD*), wall thickness (t_w) and GAC packed density. Adsorbent / adsorbate pair is GAC / R723.

OD	t_w	GAC Density	Air Conditioning			Ice Making			Heat Pump		
			T_g	COP	SCP	T_g	COP	SCP	T_g	COP	SHP
mm	mm	$kg.m^{-3}$	^oC		$kW.kg^{-1}$	^oC		$kW.kg^{-1}$	^oC		$kW.kg^{-1}$
6.38	1	550	130.2	1.70	1.18	129.6	1.63	1.07	128.8	2.65	1.68
		600	131.2	1.71	2.53	130.6	1.63	2.34	129.3	2.66	3.62
		650	131.8	1.73	3.55	131.1	1.64	3.32	130.6	2.66	5.14
		700	131.9	1.73	4.36	131.4	1.65	4.08	130.3	2.69	6.29
		750	132	1.73	5.05	131.3	1.66	4.71	133.1	2.68	7.42
12.4	1	550	131	1.63	0.46	130.1	1.55	0.42	131.3	2.57	0.68
		600	133	1.55	0.94	131.8	1.47	0.86	133.8	2.48	1.43
		650	134	1.50	1.28	132.7	1.41	1.18	135.5	2.43	1.99
		700	134.2	1.47	1.54	133.2	1.38	1.42	135.1	2.40	2.40
		750	134	1.44	1.75	133.1	1.36	1.62	135.1	2.38	2.74
19.05	1	550	131.7	1.57	0.26	130.5	1.48	0.24	132.6	2.50	0.40
		600	133.8	1.42	0.50	132.5	1.34	0.46	136.01	2.35	0.80
		650	134.7	1.35	0.66	133.4	1.26	0.60	137.4	2.27	1.08
		700	135.3	1.30	0.78	134	1.21	0.71	138.1	2.22	1.29
		750	135.8	1.26	0.87	134.3	1.18	0.80	138.3	2.19	1.47
25.4	1	550	132	1.51	0.18	130.7	1.43	0.16	133.6	2.44	0.27
		600	134.3	1.33	0.33	132.5	1.25	0.29	137	2.26	0.53
		650	135	1.24	0.42	133.6	1.16	0.38	138	2.17	0.70
		700	135.8	1.19	0.48	134.0	1.11	0.44	139	2.12	0.84
		750	136.3	1.16	0.54	134.7	1.08	0.49	139.6	2.09	0.94
28.58	1	550	132.2	1.48	0.15	130.6	1.40	0.14	134	2.41	0.24
		600	134.4	1.30	0.27	132.4	1.21	0.24	137.3	2.22	0.45
		650	135.1	1.21	0.34	133.4	1.12	0.31	138.4	2.13	0.59
		700	136	1.15	0.40	134.3	1.07	0.36	139.3	2.08	0.70
		750	136.6	1.12	0.44	134.9	1.04	0.40	139.8	2.05	0.78

Table 6.9. Optimum results for driving temperature T_g, COP and SCP (or SHP) for a copper alloy cylindrical thermal generator at different outside diameters (*OD*), wall thickness (t_w) and GAC packed density. Adsorbent / adsorbate pair is GAC / R723.

6.6.3. Optimum Values

Figures 6.15 and 6.16 show the effect of GAC packed density and outside diameter on optimum driving temperatures, based on optimum point of COP and SCP, for an air conditioning application. The generator body material is stainless steel.

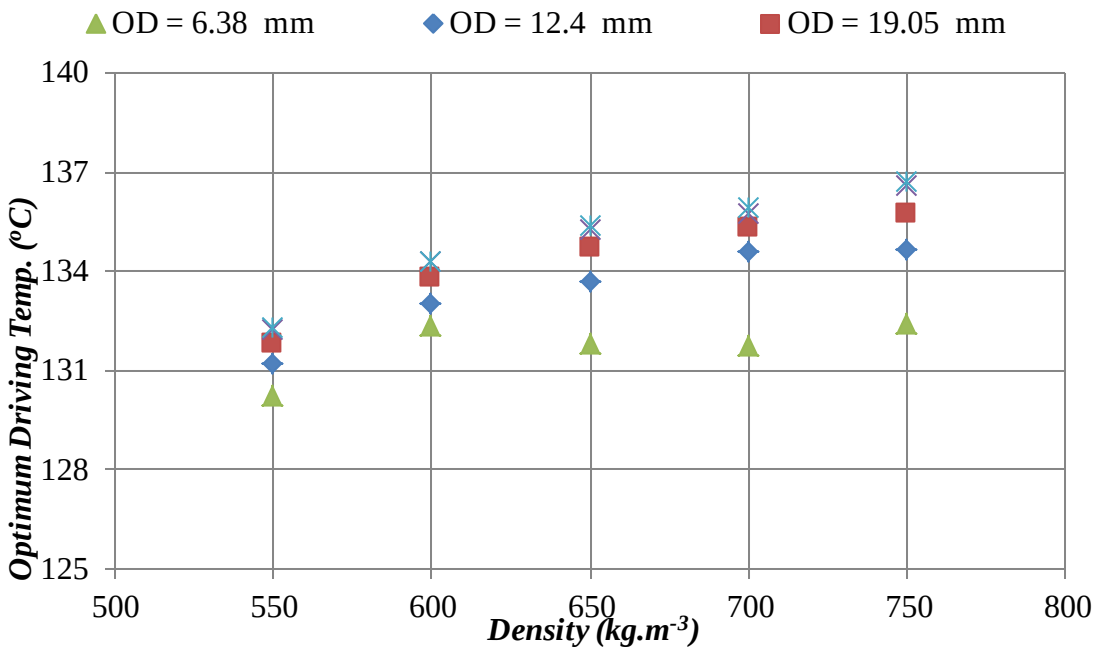

Figure 6.15. Effect of GAC packed density on optimum deriving temperature for a stainless-steel cylindrical thermal generator for an air conditioning application. Adsorbent / adsorbate pair is 208-C / R723.

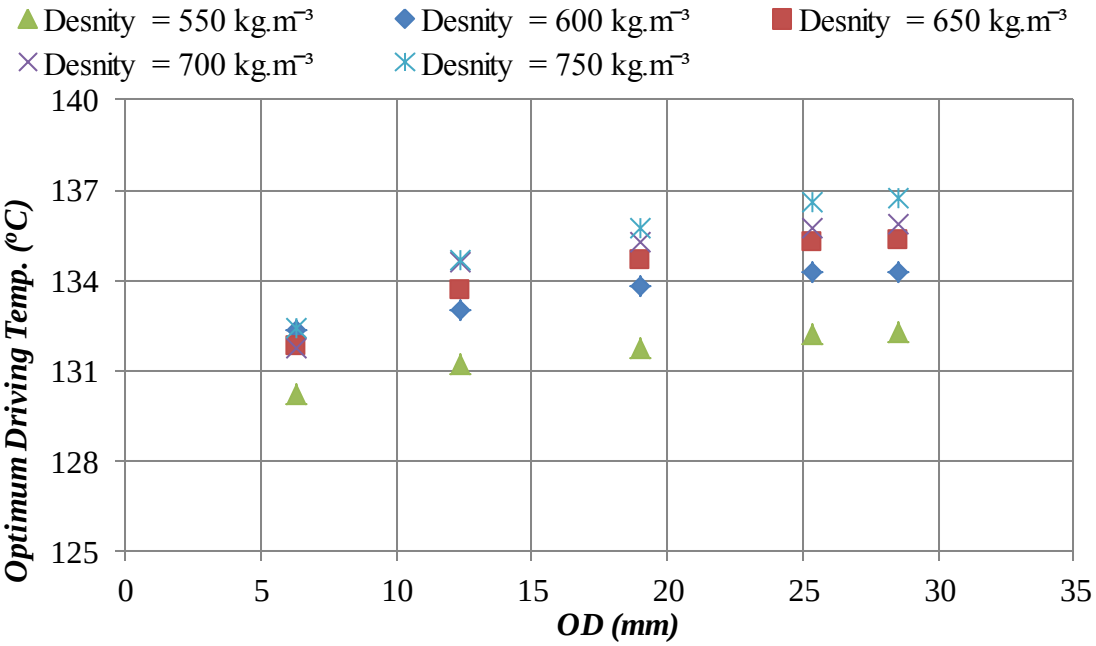

Figure 6.16. The effect of stainless-steel cylindrical thermal generator outside diameter on optimum deriving temperature for air conditioning application. Adsorbent / adsorbate pair is 208-C / R723.

Figures 6.16 and 6.17 show that driving temperature has a linear relationship with GAC packed density and generator outside diameter. Linear regression was therefore

applied to the results from Tables 6.8 and 6.9. Table 6.10 summarises the estimated parameters for Equation 6.21.

$$T_g = a_T \,.OD + b_T \,.\rho + c_T \tag{6.21}$$

Application	Body Material	a_T	b_T	c_T	Maximum Error %
Air Conditioning	Steel	0.1377	0.0169	120.2722	1.09
	Copper	0.1481	0.0168	120.051	1.19
Ice Making	Steel	0.0726	0.0174	119.9768	1.07
	Copper	0.0996	0.0164	119.9554	1.20
Heat Pump	Steel	0.2563	0.0229	116.1760	2.03
	Copper	0.2926	0.0213	116.177	2.4

Table 6.10. Parameters for Equation 6.21 based on linear regression for T_g as a function of thermal generator GAC packed density and outside diameter.

Table 6.11 shows that the maximum deviation between the values in Tables 6.8 and 6.9 and the predicted parameters is *2.4%*. The maximum deviation was observed for the heat pump application for a generator with a copper alloy body. Figure 6.17 shows the optimum driving temperature residual of the predicted values, from the values obtained from Tables 6.8 and 6.9, based on Equation 6.21.

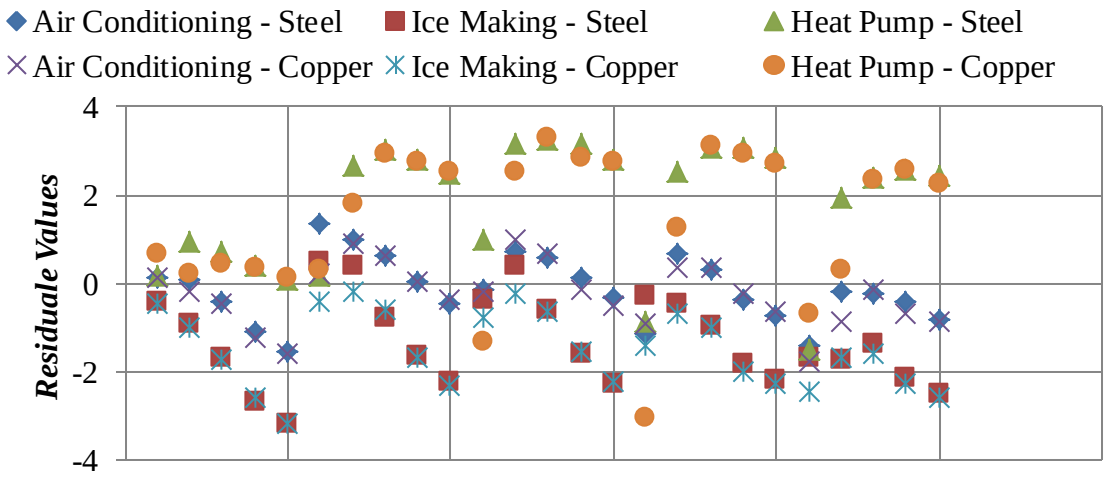

Figure 6.17. Residual of predicted values for optimum driving temperatures obtained from Table 6.8 and 6.9 based on the parameters of Equation 6.19, regardless of application and generator body material.

Figures 6.18 and 6.19 show the effect of GAC packed density and generator outside diameter on the optimum COP for a tubular generator made of stainless steel, for an air conditioning application. Figures 6.18 and 6.19 show that COP has a polynomial behaviour, with second order of GAC packed density and generator outside diameter, therefore an especial polynomial curve was applied to the results in Tables

6.8 and 6.9. In Table 6.11 the estimated parameters for Equation 6.22 are summarised for each application and generator body material.

$$COP = a_{COP} . OD^2 + b_{COP} . \rho^2 + c_{COP} . (\rho . OD) + d_{COP} \quad (6.22)$$

Application	Body Material	a_{COP} $\times 10^{-4}$	b_{COP} $\times 10^{-7}$	c_{COP} $\times 10^{-5}$	d_{COP}	Maximum Error %
Air Conditioning	Steel	5.3434	-1.9270	-5.5426	1.9310	4.96
	Copper	7.5808	1.6314	-7.3022	1.9269	5.17
Ice Making	Steel	5.4905	-1.7136	-5.6179	1.8413	5.46
	Copper	7.7899	1.9540	-4.4212	1.8355	5.71
Heat Pump	Steel	5.5547	-1.6042	-5.7112	2.8536	3.09
	Copper	8.056	2.3399	-7.6593	2.8516	3.47

Table 6.11. Parameters of Equation 6.22 based on polynomial curve applied to COP as a function of thermal generator GAC packed density and outside diameter.

Table 6.11 shows that the maximum deviation between the obtained values from Tables 6.8 and 6.9, and the values predicted by Equation 6.22, is 5.*71%*. This maximum deviation was observed for the ice making application for a copper alloy generator body material.

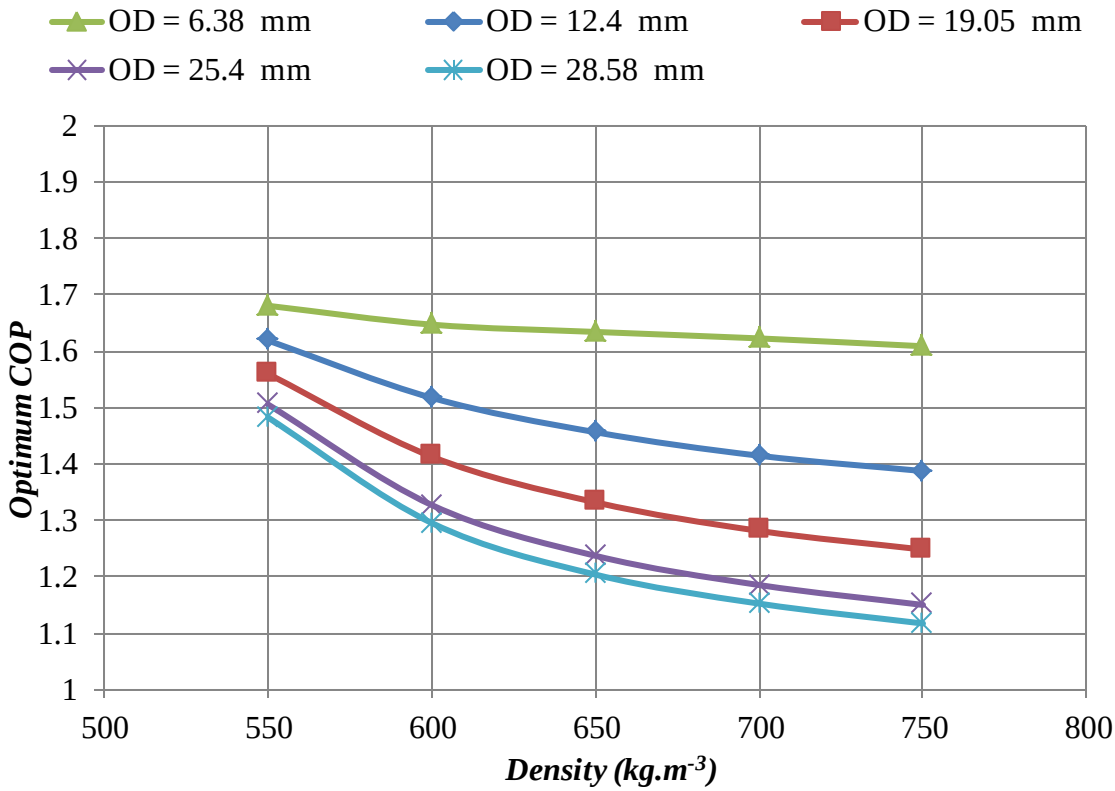

Figure 6.18. Effect of GAC packed density on optimum COP for a stainless-steel cylindrical thermal generator for an air conditioning application. Adsorbent / adsorbate pair is 208-C / R723.

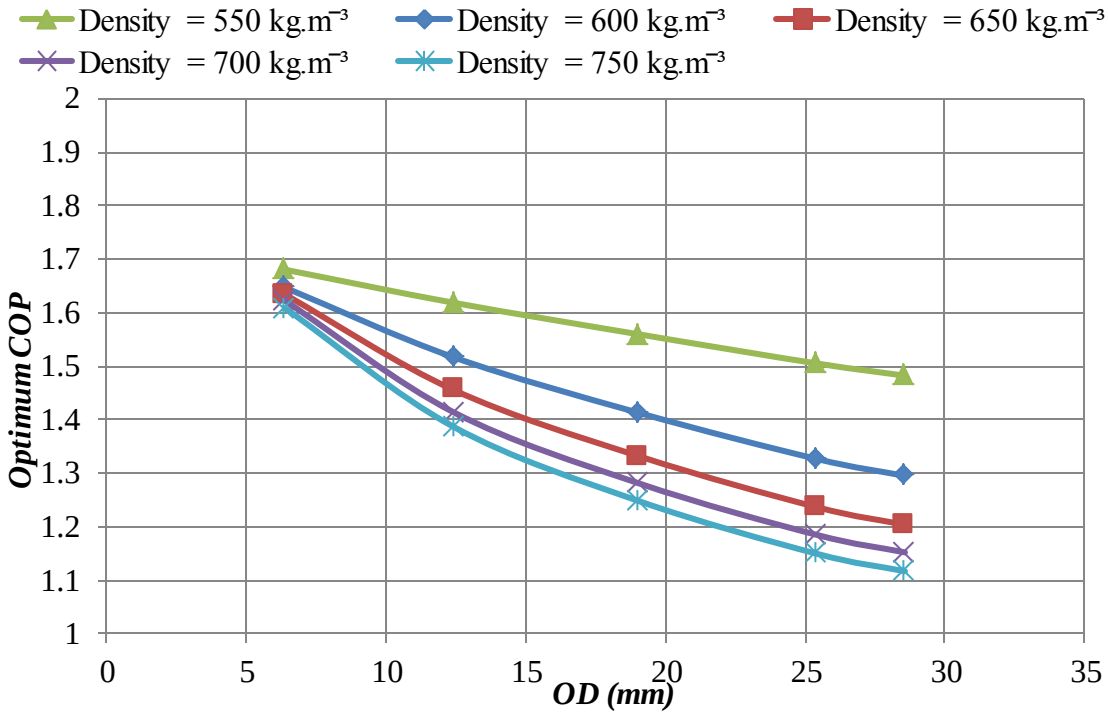

Figure 6.19. The effect of stainless-steel cylindrical thermal generator outside diameter on optimum COP for air conditioning application. Adsorbent / adsorbate pair is 208-C / R723.

Figure 6.20 shows the trend of optimum SCP while the GAC packed density was increased, with a constant tubular generator outside diameter for an air conditioning application. Figure 6.20 illustrates that, by increasing the outside diameter of a tubular generator, the slope of optimum SCP accretion for a generator with Cu/Ni body material is closer to a generator with body material of stainless steel. The slope of optimum SCP accretion for a generator with Cu/Ni body material and a *6.38 mm* outside diameter is *31%* higher than the generator with a body material of stainless steel with the same outside diameter. The slope of optimum SCP accretion for a Cu/Ni generator with a *28.58 mm* outside diameter is almost identical to the stainless-steel generator. This trend was also observed in ice making and heat pump applications.

Figures 6.21 to 6.24 estimate the optimum SCP for air conditioning and ice making applications for a stainless-steel cylindrical thermal generator. Figures 6.25 and 6.26 show estimates of optimum SHP for a heat pump application for a stainless-steel cylindrical thermal generator.

Figures 6.27 to 6.30 could be used to estimate the optimum SCP for air conditioning and ice making applications for a copper alloy cylindrical thermal generator. Figures 6.31 and 6.32 show the optimum SHP for a heat pump application for a copper alloy cylindrical thermal generator.

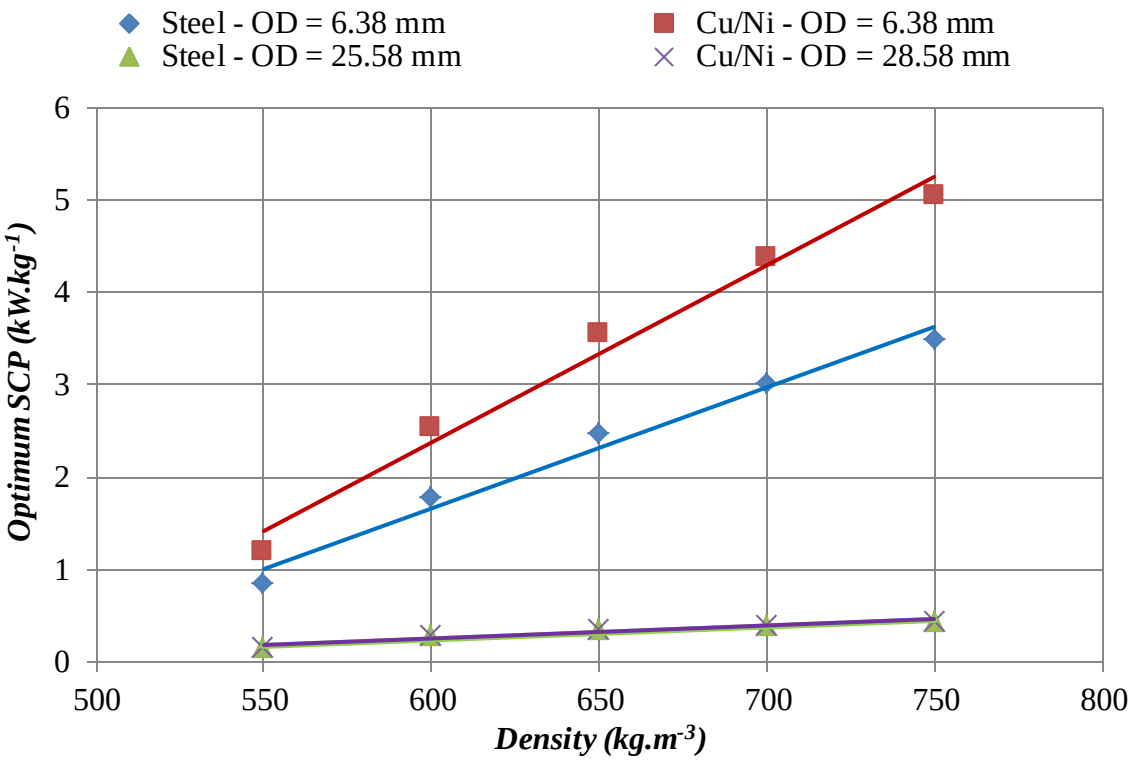

Figure 6.20. Comparison between the slopes of optimum SCP accretion for Cu/Ni and stainless-steel tubular generators with outside diameter of 6.28 mm and 28.58 mm, for an air conditioning application.

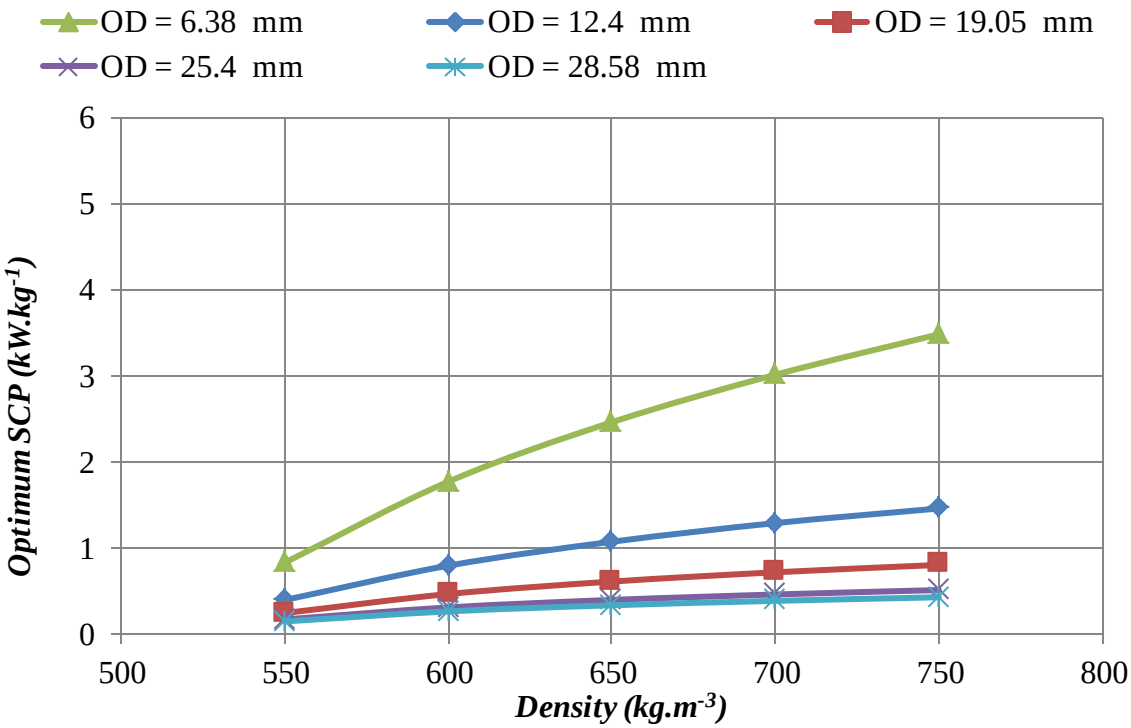

Figure 6.21. Effect of GAC packed density on optimum SCP for a stainless-steel cylindrical thermal generator for an air conditioning application. Adsorbent / adsorbate pair is 208-C / R723.

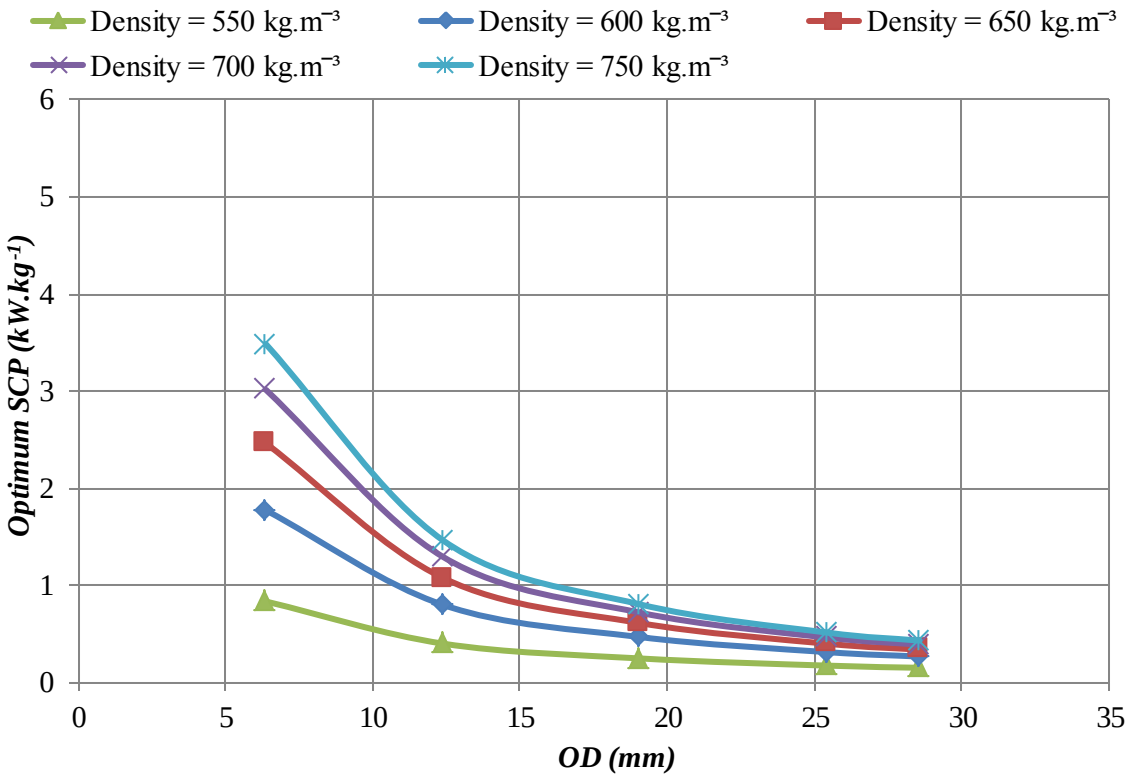

Figure 6.22. Effect of stainless-steel cylindrical thermal generator outside diameter on optimum SCP for an air conditioning application. Adsorbent / adsorbate pair is 208-C / R723.

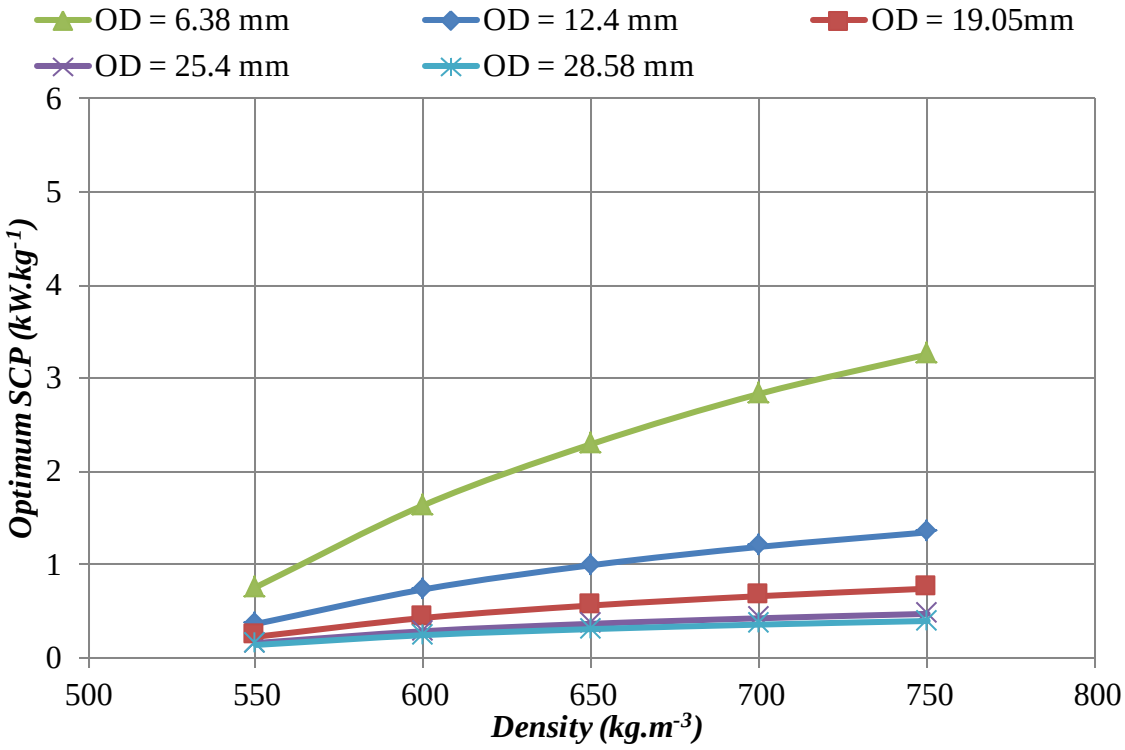

Figure 6.23. Effect of GAC packed density on optimum SCP for a stainless-steel cylindrical thermal generator for an ice making application. Adsorbent / adsorbate pair is 208-C / R723.

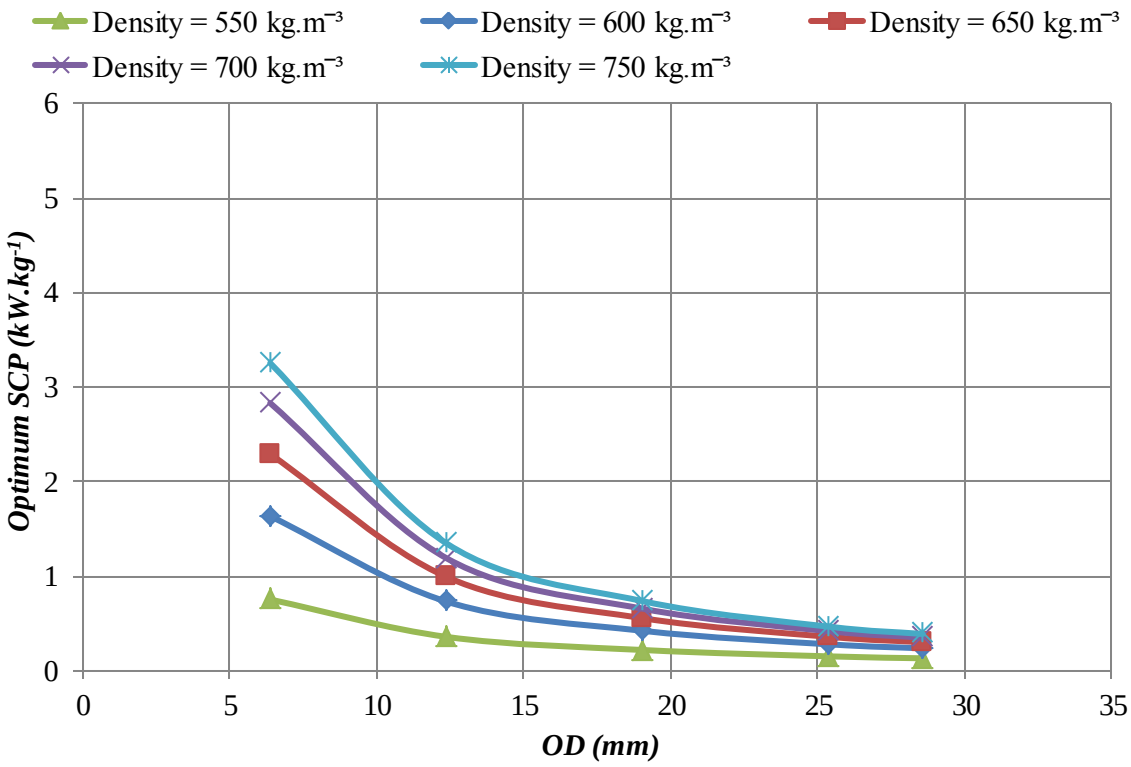

Figure 6.24. Effect of stainless-steel cylindrical thermal generator outside diameter on optimum SCP for an ice making application. Adsorbent / adsorbate pair is 208-C / R723.

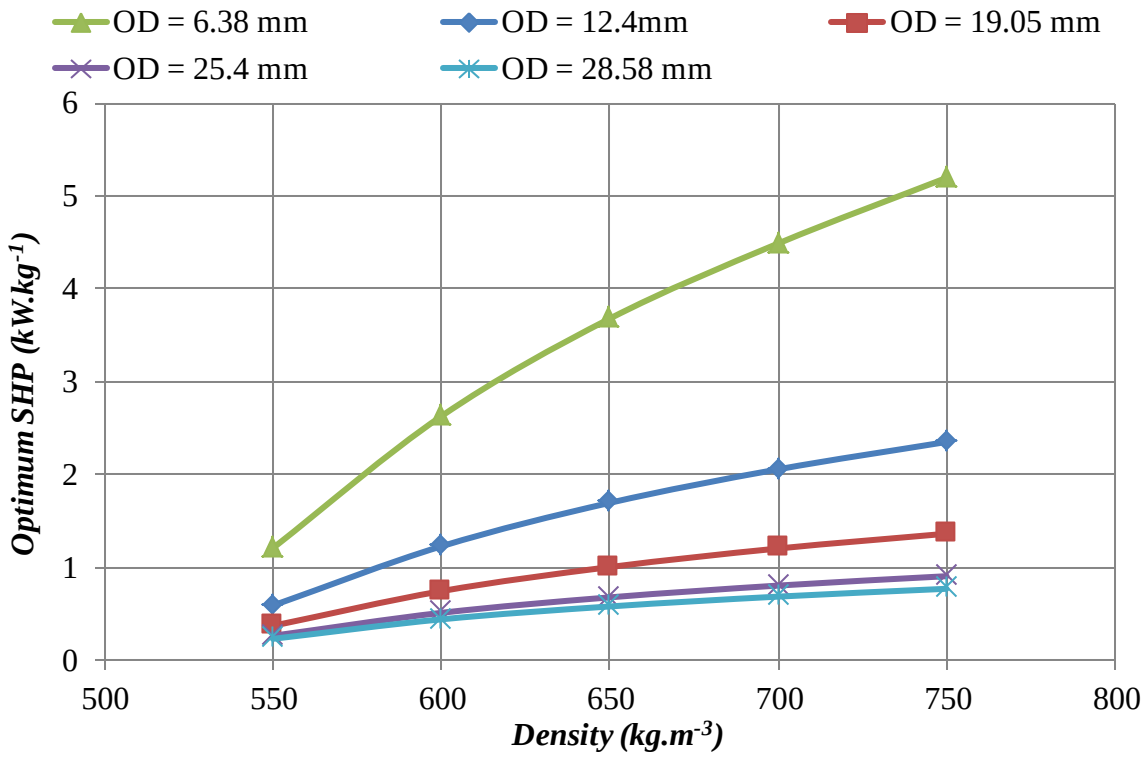

Figure 6.25. Effect of GAC packed density on optimum SCP for a stainless-steel cylindrical thermal generator for a heat pump application. Adsorbent / adsorbate pair is 208-C / R723.

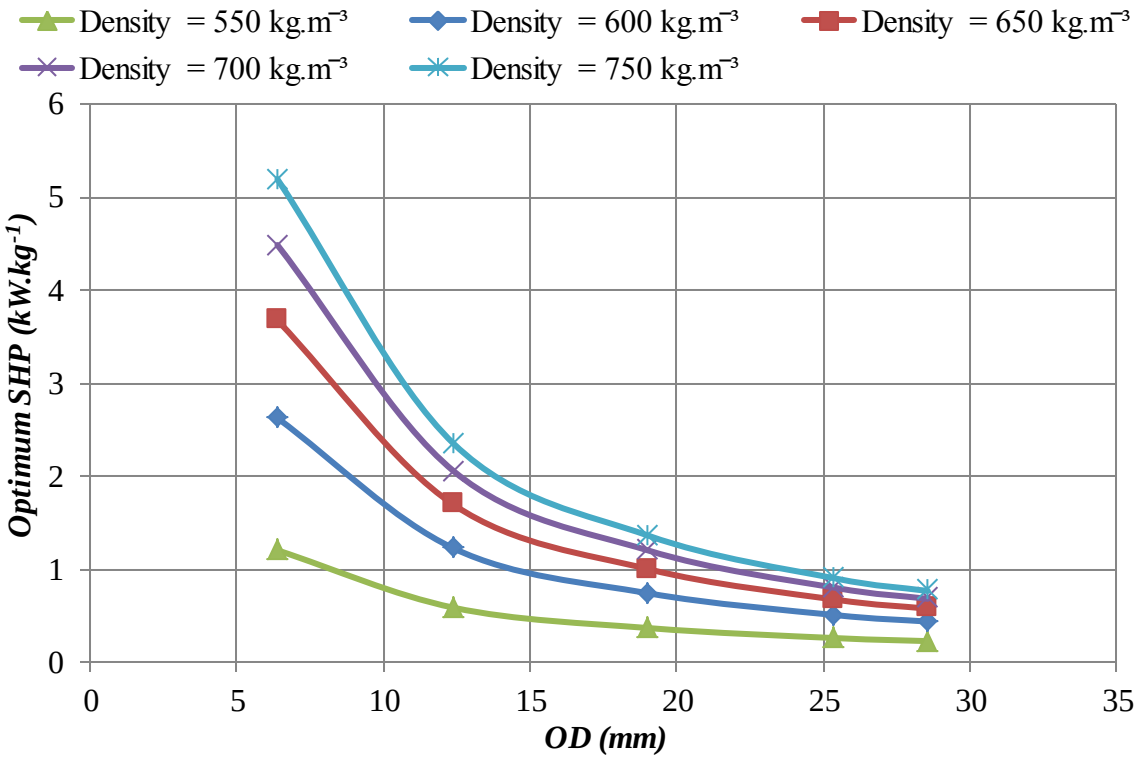

Figure 6.26. Effect of stainless-steel cylindrical thermal generator outside diameter on optimum SHP for a heat pump application. Adsorbent / adsorbate pair is 208-C / R723.

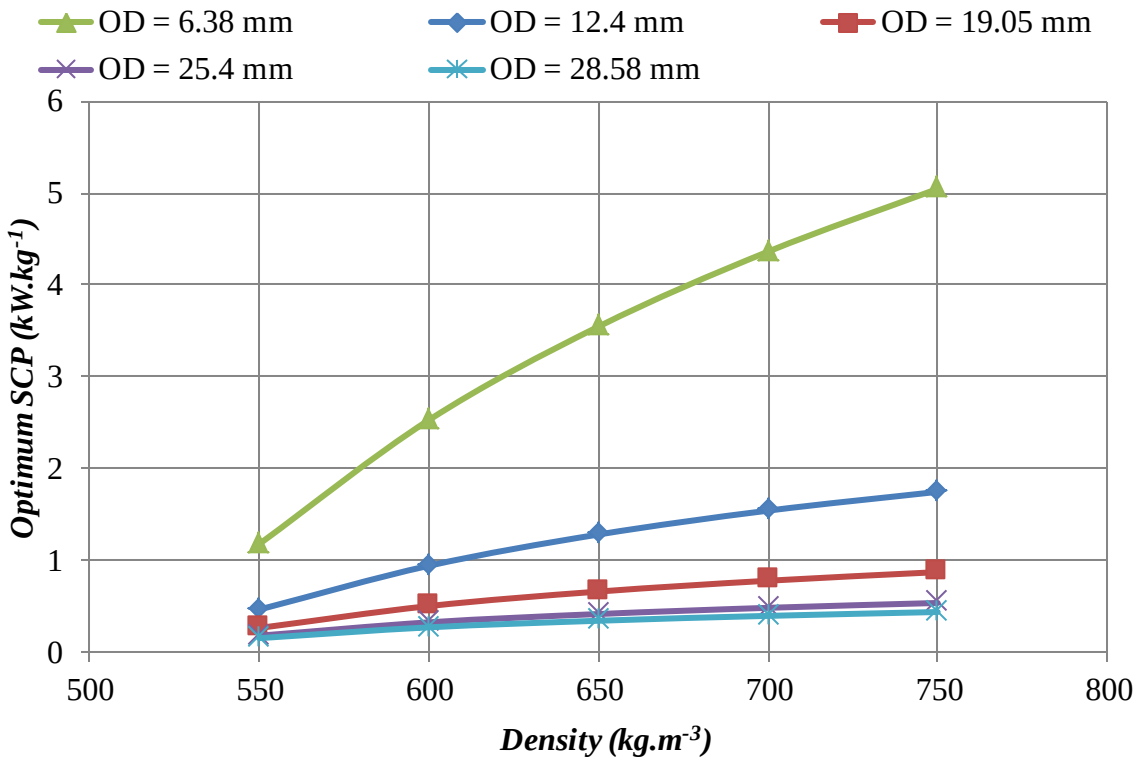

Figure 6.27. Effect of GAC packed density on optimum SCP for a copper alloy cylindrical thermal generator for an air conditioning application. Adsorbent / adsorbate pair is 208-C / R723.

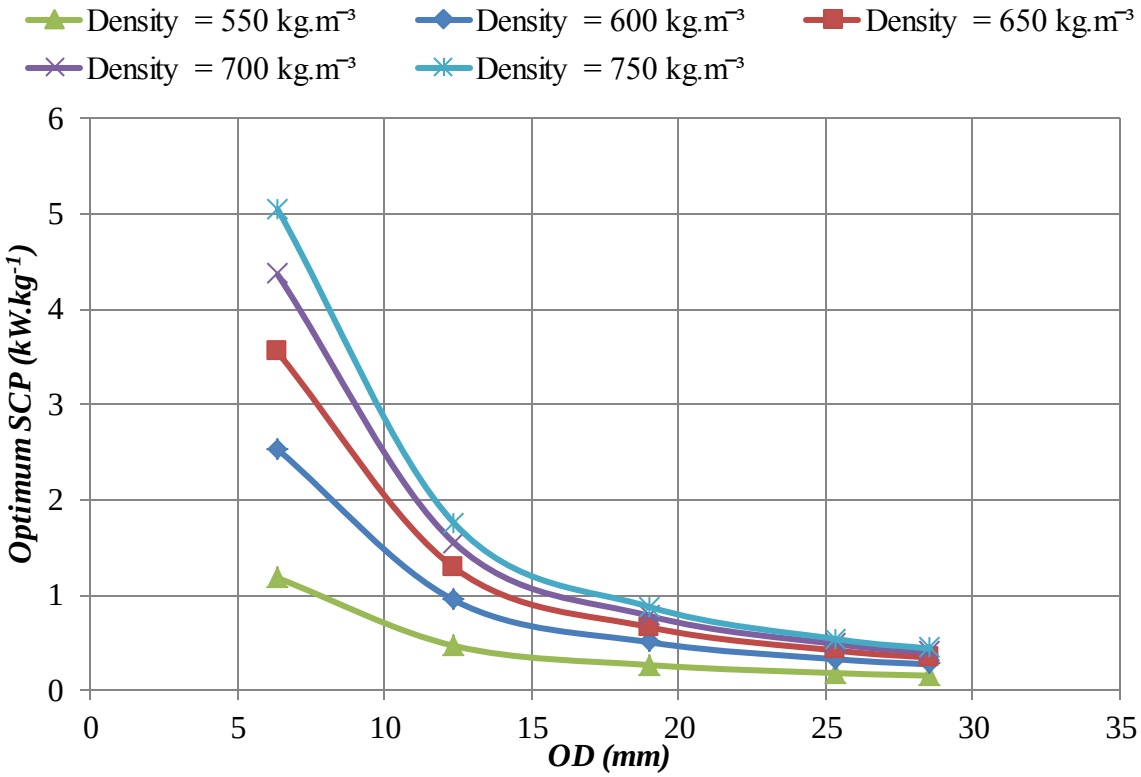

Figure 6.28. Effect of copper alloy cylindrical thermal generator outside diameter on optimum SCP for an air conditioning application. Adsorbent / adsorbate pair is 208-C / R723.

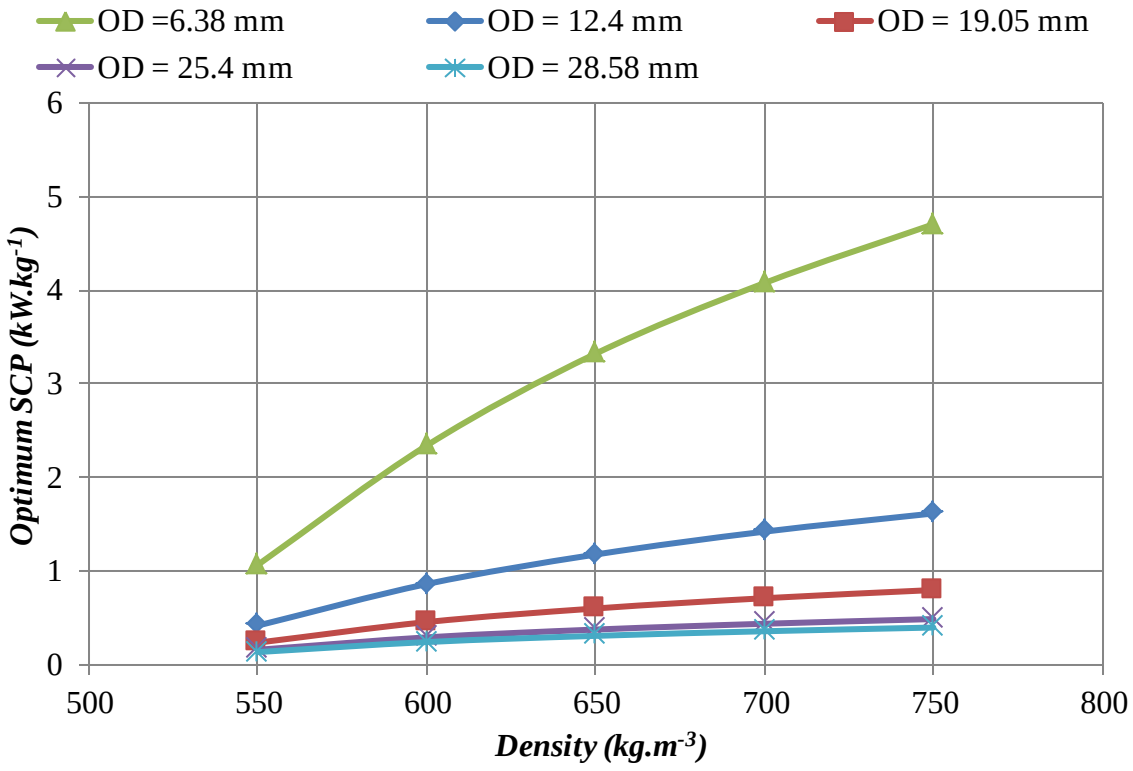

Figure 6.29. Effect of GAC packed density on optimum SCP for a copper alloy cylindrical thermal generator for an ice making application. Adsorbent / adsorbate pair is 208-C / R723.

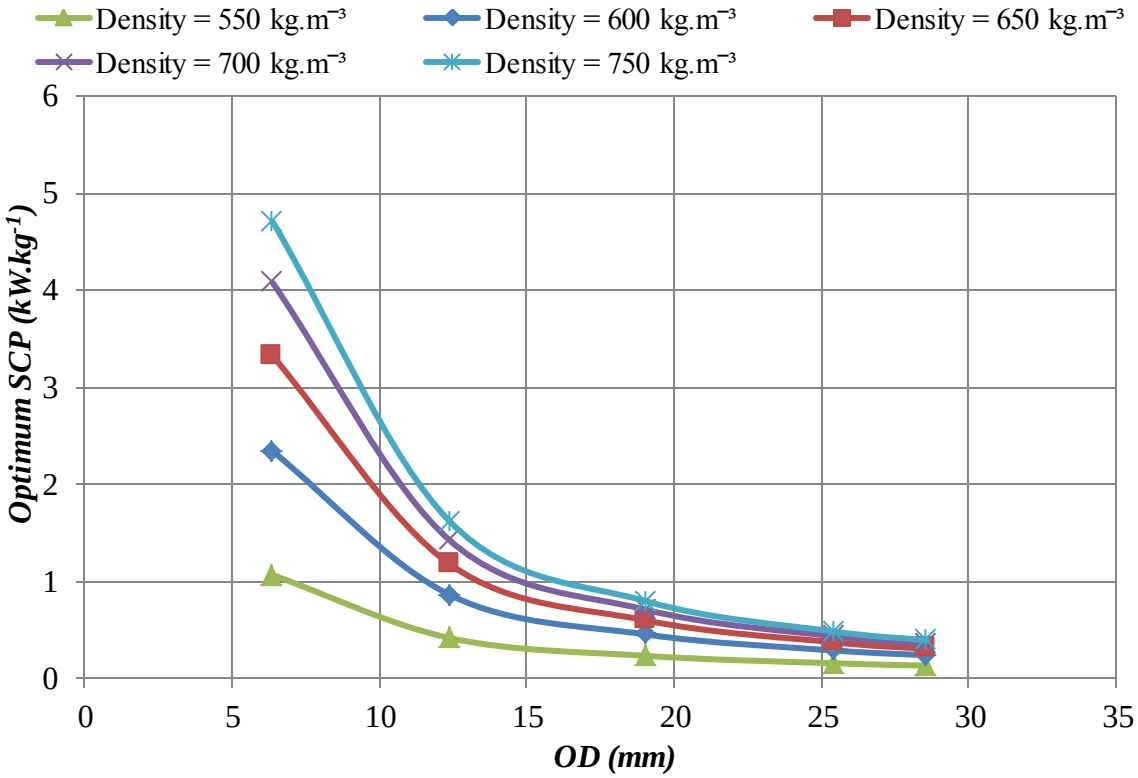

Figure 6.30. Effect of copper alloy cylindrical thermal generator outside diameter on optimum SCP for an ice making application. Adsorbent / adsorbate pair is 208-C / R723.

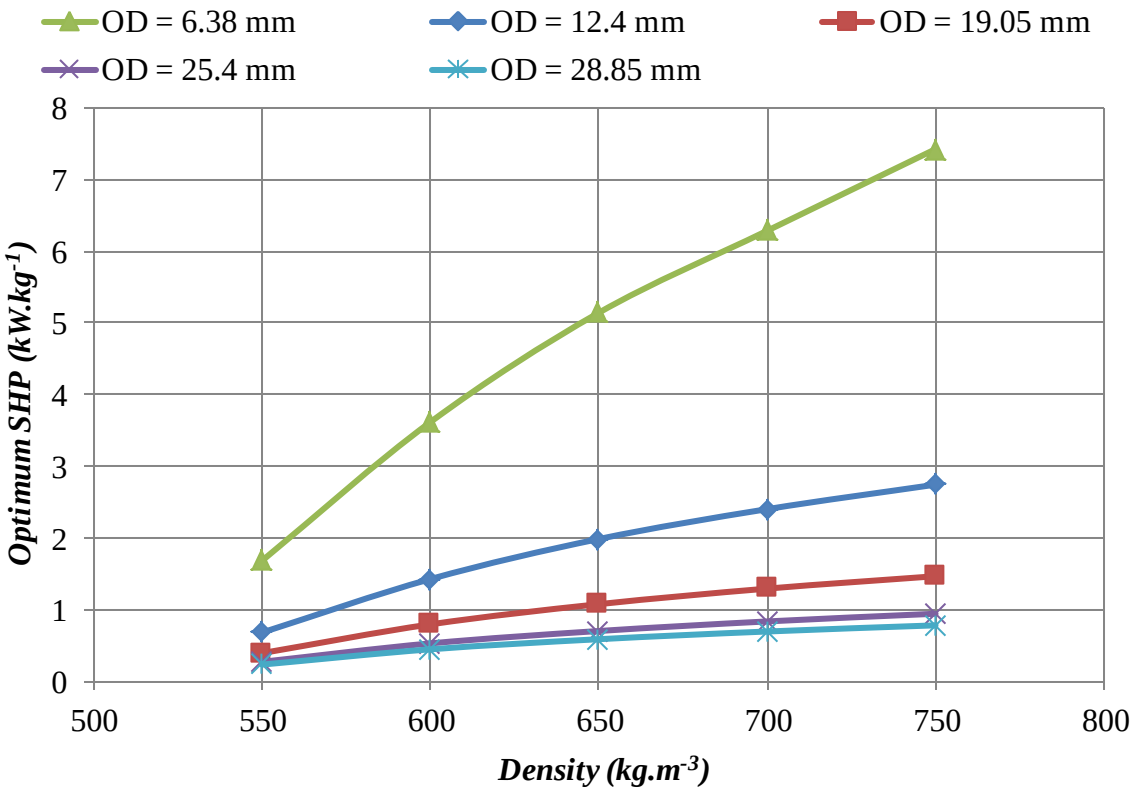

Figure 6.31. Effect of GAC packed density on optimum SCP for a copper alloy cylindrical thermal generator for a heat pump application. Adsorbent / adsorbate pair is 208-C / R723.

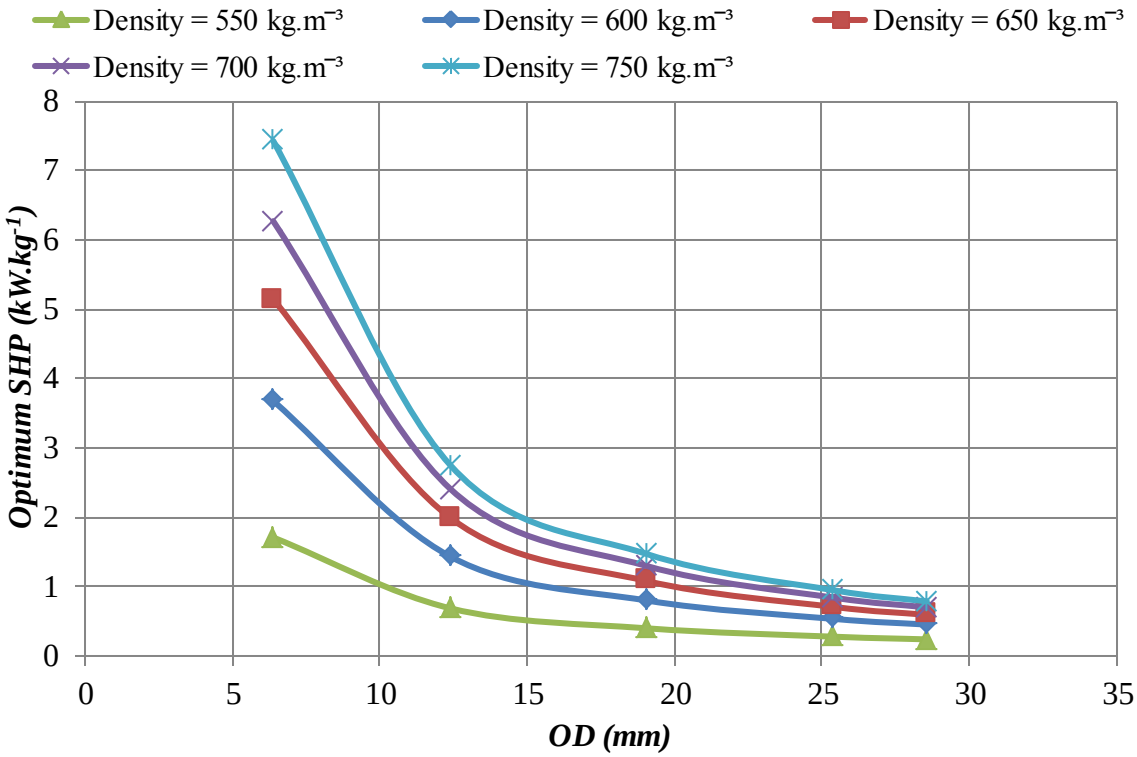

Figure 6.32. Effect of copper alloy cylindrical thermal generator outside diameter on optimum SCP for a heat pump application. Adsorbent / adsorbate pair is 208-C / R723.

6.7. Conclusions

The objective of this chapter was to find a map or correlation that would enable prediction of the optimum point of an adsorption system with a tubular generator in terms of driving temperature, COP and SCP (or SHP), for different adsorption applications. The optimization results in section 6.6 illustrate that it is possible to explain the optimum driving temperature as a linear function of GAC packed density and thermal generator outside diameter. A maximum deviation of *2.44%* was observed between the simulation values from Tables 6.8 and 6.9, and predicted values based on Equation 6.19 for a heat pump application for a generator with a copper alloy body.

This chapter also presents the correlation between COP and SCP (or SHP), in order to connect them to the physical appearance of the generator. The results in section 6.6.1 show a correlation between COP and the physical appearance of the thermal generator. The suggested correlation depends on the adsorption application area and the generator body material. A maximum deviation of *5.71%* was observed for an ice making application with a Cu/Ni generator body material. Another conclusion that was made during the analysis is that by increasing the generator's outside diameter,

the difference between the obtained COP for stainless steel and Cu/Ni body material was decreased: to the extent that the COP difference between the two generator body materials at 28.85 mm outside diameter was identical.

For SCP (or SHP) the suggested correlation failed to satisfy the deviation predicted from the obtained value of less than *7%*. Therefore, because of correlation complexity and high deviation (in some cases around *32%*), the author suggests using the provided charts to estimate the SCP (or SHP) of an adsorption system based on adsorption application, generator body material and generator physical appearance. Another conclusion that was made during the analysis is that, by increasing the generator's outside diameter, the difference between the obtained SCP (SHP) for stainless steel and Cu/Ni body materials was decreased. The differences between the obtained SCP (SHP) for stainless steel and Cu/Ni generator body materials was *30%* for an outside diameter of *6.38 mm*, but decreased to a maximum *1.4%* difference for an outside diameter of *28.58 mm*.

References

[1]. R. E. Critoph, Performance limitations of adsorption cycles for solar cooling. Solar Energy, 1988; 41 (1): 21-31.

[2]. G. Cacciola, G. Restuccia, Reversible adsorption heat pump: a thermodynamic model. International Journal of Refrigeration, 1995; 18 (2): 100-106.

[3]. R.E. Critoph, R. Thorpe, Momentum and heat transfer by forced convection in fixed beds of granular active carbon. Applied Thermal Engineering, 1996; 16 (5): 419-427.

[4]. S.J. Metcalf, R.E. Critoph, Z. Tamainot-Telto, Optimal cycle selection in carbon-ammonia adsorption cycles. International Journal of Refrigeration, 2012; 35 (3): 571-581.

[5]. J. J. Guilleminot, F. Meunier, J. Pakleza, Heat and mass transfer in a non-isothermal fixed bed solid adsorbent reactor: a uniform pressure non-uniform temperature case. International Journal of Heat and Mass Transfer, 1987; 30(8):1595–606.

[6]. A. Mhimid, Theoretical study of heat and mass transfer in a zeolite bed during water desorption: validity of local thermal equilibrium assumption. International Journal of Heat and Mass Transfer, 998; 41:2967–77.

[7]. E. F. Passos,J. F. Escobedo, F. Meunier, Simulation of an intermittent adsorptive solar cooling system. Solar Energy, 1989; 42(2):103–11.

[8]. L. Yong, K. Sumathy, Review of mathematical investigation on the closed adsorption heat pump and cooling systems. Renewable and Sustainable Energy Reviews. 2002; 6 (4): 305-338.

[9]. Z. Tamainot-Telto, R.E. Critoph, Advanced solid sorption air conditioning modules using monolithic carbon–ammonia pair. Applied Thermal Engineering, 2003; 23 (6): 650-674.

[10]. R.E. Critoph, S.J. Metcalf, Specific cooling power intensification limits in ammonia–carbon adsorption refrigeration systems. Applied Thermal Engineering, 2004; 24 (5): 661- 678.

[11]. Z. Tamainot-Telto, S.J. Metcalf, R.E. Critoph, Y. Zhong, R. Thorpe, Carbon–ammonia pairs for adsorption refrigeration applications: ice making, air conditioning and heat pumping. International Journal of Refrigeration, 2009; 32 (6): 1212- 1229.

Chapter 7

Conclusions and future work

7.1. Conclusions

This work has studied and evaluated a variety of areas in relation to a granular activated carbon / R723 pair for use in air conditioning, ice making and heat pump applications in a solid sorption machine.

In order to increase the heat transfer performance of granular activated carbon, a special packing method was suggested, to increase the mass of the adsorbent at a constant volume. The density of the granular activated carbon-packed bed varied from *508 ($kg.m^{-3}$)* to *656 ($kg.m^{-3}$)*. The effect of packing density on the efficiency of the packed bed was investigated by measuring the pressure drop of air and argon gases passing through the packed bed at different flow rates, in a range from *1 LPM* to *4 LPM*. A special rig for test purposes was designed in order to keep the flow pattern radially converging and diverting, respectively. Finally, by using the Darcy-Forchheimer model, permeability and shape factor as characteristics of packed bed density, in the form of second order correlations, were established.

The second step of this project involved studying the effect of increasing the adsorbent packed density on the thermal properties of granular activated carbon in a tubular generator. The study was carried out in two stages.

Stage one was a study the effect of packing density on the thermal parameters of granular activated carbon in the presence of air. The test results were analysed via the inverse method using the energy balance approach, in order to extract the thermal parameters. The results show that by increasing the packed density from *547 ($kg.m^{-3}$)* to *750 ($kg.m^{-3}$)* the thermal conductivity and heat transfer coefficient of the contact wall/packed carbon changed from *0.2* ($W.m^{-1}.K^{-1}$) to *0.44* ($W.m^{-1}.K^{-1}$) and *149* ($W.m^{-2}.K^{-1}$) to *722* ($W.m^{-2}.K^{-1}$), respectively. Therefore, increasing the packed density by *37%* brings *2.2* times improvement in thermal conductivity and *4.8* times improvement in heat transfer coefficient of the contact wall/packed carbon.

The second stage involved studying the effect of packed density and R723 on the thermal properties of granular activated carbon. The results show that by increasing the packed density from *626 ($kg.m^{-3}$)* to *750 ($kg.m^{-3}$)*, the thermal conductivity and heat transfer coefficient of the contact wall/packed carbon changed from *0.77* ($W.m^{-1}.K^{-1}$) to *1.36* ($W.m^{-1}.K^{-1}$) and *390* ($W.m^{-2}.K^{-1}$) to *735* ($W.m^{-2}.K^{-1}$), respectively. The R723 causes a threefold improvement on the thermal conductivity of granular activated carbon. The R723 causes an *27%* average increase in heat transfer coefficient of the contact wall/packed carbon at lower packed bed densities; as the packed density increases, the effect of R723 drops down to an average of *2%*. Finally, two correlations were used to calculate the thermal conductivity and heat transfer coefficient of the contact wall/packed carbon by using the concentration of R723.

A model of a tubular generator was constructed, with regard to air conditioning, ice making and heat pump applications. The physical appearance of the generator in terms of length was kept constant (*1 meter*), while the outside diameter and wall thickness were chosen from tube standards. Stainless steel and Cu-Ni 90/10 were used as the generator body material. The adsorption pair was granular activated carbon / R723. The model prediction performances, for each specific application, were conducted with a combination of generator outside diameter, wall thickness, adsorbent packed density and a range of driving temperatures. Here is a short summary of conclusions:

- The model of a tubular generator made from Cu-Ni 90/10 shows that the cycle time compared to stainless steel is less by an average of *30%*. Make example here from one of the modelling and let them know the second or min
- As a consequence of the shorter cycle time for a generator made from copper alloy, the SCP (SHP) was higher than the generator made from stainless steel. Put the percentage
- For the tubular generator with a stainless-steel body, increasing the GAC-packed density at the COP led to a descending trend, while the SCP (SHP) exhibited an ascending trend.
- For the tubular generator with a copper alloy body, the COP exhibited an ascending trend when the GAC packed density for outside diameter was

increased from *12.4 mm* to *28.58 mm*, while the SCP (SHP) had an ascending trend; but these trends are reversed for a copper alloy generator with *6.38 mm* outside diameter.

- By increasing the tubular generator outside diameter, the slope of optimum SCP accretion for a generator with a Cu/Ni body is closer to the generator with a stainless-steel body. The slope of optimum SCP accretion for a generator with a Cu/Ni body and *6.38 mm* outside diameter is *31%* higher than the generator with a stainless-steel body with the same outside diameter. The slope of optimum SCP accretion for a Cu/Ni generator with a *28.58 mm* outside diameter is almost identical to the stainless-steel generator. This trend was also observed in the ice making and heat pump applications.

7.2. Future work

More work is still needed in order to develop a full-scale model of an adsorption system with R723 and a generator made of Cu-Ni 90/10. The generator model will be the shell-and-tube type.

Future work would also need to include system cost analysis and manufacturing feasibility methods.

Appendixes

MATLAB Codes

Appendix A
Permeability converge flow

```
%  airprconv.m  (Convergence  of flow  to the centre)
%  This  program computes the radial permeability  Kr
%  function  of velosity  U and pressure  drop Dp
%  Date: 03/04/2013
   clear
%
*************************************************************************
%  Carbon packed sample  Spec
%
*************************************************************************
   D2=0.0522;          % Carbon packed outer Diameter  (m)
   D1=0.019274;        % Carbon packed inner  Diameter  (m)
   r1=D1/2;            % Carbon packed inner  radius  (m)
   r2=D2/2;            % Carbon packed outer radius  (m)
   Dz=0.042;           % Carbon packed Thickness  (m)
%
*************************************************************************
%   DATA  file
%
*************************************************************************
   name1=input('Input  data file  name for Air: ','s');
   eval(['load  ' name1 '.txt']);
   data1=eval(name1);
   qvread=data1(:,1);      % Flow  rate (l/min)
   Dp=data1(:,2)/1000;     % Pressure drop (bar)
   P1=data1(:,3)/1000;     % Outlet  pressure  (bar)
   Tg2=data1(:,4);         % Gas temperature  inlet  (^oC)
   Tg1=data1(:,5);         % Gas temperature  outlet  (^oC)
   Tg=(Tg1+Tg2)/2;         % Gas average  temperature  (^oC)
   P2=Dp+P1;               % Inlet  pressure  (bar)
   Pc=data1(:,7)/1000;     % Inlet  Pressure  for Rotameter  (bar)
   Pa=data1(:,8)/1000+P1;  % Outlet  Pressure  for Rotameter  (bar)
%
*************************************************************************
%   Correction  of gas flow  rate read
%
*************************************************************************
%  AIR Properties
   Roo=1.1774;     % Density  of air  at 20 C and 1 bar (kg/m3)
   R=287.1;        % Air  gas constant  (J.kg/K)
```

```
%  Air Density for Test (kg/m3)
   Ro1=1.e5.*(P1)./(R.*(Tg1+273.15));  % Density of air at Tg1 and P1 bar
   Ro2=1.e5.*(P2)./(R.*(Tg2+273.15));  % Density of air at Tg2 and P2 bar

%  Argon Density for Test
   Ro1=1.e5.*(P1)./(R.*(Tg1+273.15));  % Density of argon at Tg1 and P1 bar
   Ro2=1.e5.*(P2)./(R.*(Tg2+273.15));  % Density of argon at Tg2 and P2 bar

%  Working Fluid Corrected density with pressure befor rotameter (kg/m3)
   Roc=1.e5.*(Pc)./(R.*(Tg2+273.15));  % Density of air at Tg2 and Pc bar
%
**************************************************************************
%  Flow rate correction factor and flow rate
%
**************************************************************************
   F=(Roo./Ro2).^0.5;  % Correction Factor
   qv=F.*qvread;       % Air Flow Rate (l/min)
%
**************************************************************************
%  Working Fluid Viscosity Mu (Pa.s)
%
**************************************************************************
   Tgm=mean(Tg)                % Inlet&Outlet mean Temp. (^oC)

   Mu=1.e-5*(1.702+0.005*Tgm)     % Air Viscosity (Pa.s)

   Mu=(2.11+0.0055.*Tgm).*1.0e-5   % Argon Viscosity (Pa.s)
%
**************************************************************************
%  Working FLuid Velocity V (m/s) and mass flow rate (kg/s)
%
**************************************************************************
   V2=((1.e-3/60)/(2*pi*r2*Dz)).*qv;    % Inlet Velocity (m/s)
   V1=((r2.*Ro2)./(r1.*Ro1)).*V2;       % outlet Velocity (m/s)

   m2=(1.e-3/60).*Ro2.*qv;            % Inlet mass flow rate (kg/s)
   m1=(2*pi*r1*Dz).*Ro1.*V1;           % Outlet mass flow rate (kg/s)
   result=[V1,V2,m1,m2];
%
**************************************************************************
%  Permeability - Method by identification
%
**************************************************************************
   W=1.e10.*(P2.^2-P1.^2)./(Mu*R*(Tgm+273.15)*m1);
```

```
W1=pi*Dz*W/log(r2/r1);
X1=((1/r1-1/r2)/(2*pi*Dz*log(r2/r1)*Mu))*m1;
DATA=[X1,W1];
polyfit(X1,W1,1);
A=ans(1,2)
B=ans(1,1)
K=1/A
%
**************************************************************************
%  Plotting
%
**************************************************************************
figure(1)
clf
subplot(2,2,1)
plot(qv,Dp,'o')
xlabel('Flow  rate (l/min)')
ylabel('Pressure  drop (Bar)')
title('Air')
grid  on

subplot(2,2,2)
plot(1000.*m1,(P2-P1),'o')
xlabel('Mass  flow  rate (g/s)')
ylabel('Pressure  drop (Bar)')
grid  on
hold  on
plot(0,0)

subplot(2,2,3)
plot(1000.*m1,1.e10*(P2.^2-P1.^2)./m1,'o')
xlabel('Mass  flow  rate (g/s)')
ylabel('(P2^2-P1^2)/m1')
grid  on
hold  on
plot(0,0)

subplot(2,2,4)
plot(1000.*m1,1.e10*(P2.^2-P1.^2),'o')
xlabel('Mass  flow  rate (g/s)')
ylabel('(P2^2-P1^2)')
grid  on
hold  on
plot(0,0)
```

```
figure(2)
clf
plot(X1,W1,'o')
xlabel('((1/r1-1/r2)/(2*pi*Dz*log(r2/r1)*Mu))*m1')
ylabel('(P2.^2-P1.^2).*pi.*Dz./(Mu*R*(Tgm+273.15)*log(r2/r1)*m1)')
title('Carbon  packed sample')
grid  on
hold  on
plot(0,0)

Final  = [Tgm  Mu A B K]

AllFinal  = [ qvread qv F Ro1 Ro2 P1 P2 Dp V1 V2 m1  m2 W X1 W1];
```

Appendix A - 1
Permeability diverge flow

```
%  airprconv.m  (Divergence  of flow  to the centre)
%  This  program computes the radial permeability  Kr
%  function  of velosity  U and pressure  drop Dp
%  Date: 03/04/2013
   clear
%
*************************************************************************
%  Carbon packed sample  Spec
%
*************************************************************************
   D2=0.0522;          % Carbon packed outer  Diameter  (m)
   D1=0.019274;        % Carbon packed inner  Diameter  (m)
   r1=D1/2;            % Carbon packed inner  radius  (m)
   r2=D2/2;            % Carbon packed outer radius  (m)
   Dz=0.042;           % Carbon packed Thickness  (m)
%
*************************************************************************
%   DATA  file
%
*************************************************************************
   name1=input('Input  data file  name  for Air: ','s');
   eval(['load  ' name1  '.txt']);
   data1=eval(name1);

   qvread=data1(:,1);      % Flow  rate (l/min)
   Dp=data1(:,2)/1000;     % Pressure  drop (bar)
```

```
P2=data1(:,3)/1000;      % Outlet pressure (bar)
Tg2=data1(:,4);          % Gas temperature inlet (^oC)
Tg1=data1(:,5);          % Gas temperature outlet (^oC)
Tg=(Tg1+Tg2)/2;          % Gas average temperature (^oC)
P1=Dp+P2;                % Inlet pressure (bar)
Pc=data1(:,7)/1000;      % Inlet Pressure for Rotameter (bar)
Pa=data1(:,8)/1000+P1;   % Outlet Pressure for Rotameter (bar)
%
**************************************************************************
%   Correction of gas flow rate read
%
**************************************************************************
%  AIR Properties
Roo=1.1774;     % Density of air at 20 C and 1 bar (kg/m3)
R=287.1;        % Air gas constant (J.kg/K)

%  Air Density for Test (kg/m3)
Ro1=1.e5.*(P1)./(R.*(Tg1+273.15));  % Density of air at Tg1 and P1 bar
Ro2=1.e5.*(P2)./(R.*(Tg2+273.15));  % Density of air at Tg2 and P2 bar

%  Argon Density for Test
Ro1=1.e5.*(P1)./(R.*(Tg1+273.15));  % Density of argon at Tg1 and P1 bar
Ro2=1.e5.*(P2)./(R.*(Tg2+273.15));  % Density of argon at Tg2 and P2 bar

%  Working Fluid Corrected density with pressure befor rotameter (kg/m3)
Roc=1.e5.*(Pc)./(R.*(Tg2+273.15));  % Density of air at Tg2 and Pc bar
%
**************************************************************************
%  Flow rate correction factor and flow rate
%
**************************************************************************
F=(Roo./Ro2).^0.5;  % Correction Factor
qv=F.*qvread;       % Air Flow Rate (l/min)
%
**************************************************************************
%  Working Fluid Viscosity Mu (Pa.s)
%
**************************************************************************
Tgm=mean(Tg)                % Inlet&Outlet mean Temp. (^oC)

Mu=1.e-5*(1.702+0.005*Tgm)      % Air Viscosity (Pa.s)

Mu=(2.11+0.0055.*Tgm).*1.0e-5   % Argon Viscosity (Pa.s)
```

```
%
%************************************************************************
%  Working FLuid Velocity V (m/s) and mass flow rate (kg/s)
%
%************************************************************************
   V1=((1.e-3/60)/(2*pi*r1*Dz)).*qv;    % Inlet Velocity (m/s)
   V2=((r1.*Ro1)./(r2.*Ro2)).*V1;       % outlet Velocity (m/s)

   m1=(1.e-3/60).*Ro1.*qv;              % Inlet mass flow rate (kg/s)
   m2=(2*pi*r2*Dz).*Ro2.*V2;            % Outlet mass flow rate (kg/s)
   result=[V1,V2,m1,m2];
%
%************************************************************************
%  Permeability - Method by identification
%
%************************************************************************
   W=1.e10.*(P1.^2-P2.^2)./(Mu*R*(Tgm+273.15)*m1);
   W1=pi*Dz*W/log(r2/r1);
   X1=((1/r1-1/r2)/(2*pi*Dz*log(r2/r1)*Mu))*m1;
   DATA=[X1,W1];
   polyfit(X1,W1,1);
   A=ans(1,2)
   B=ans(1,1)
   K=1/A
%
%************************************************************************
%  Plotting
%
%************************************************************************
   figure(1)
   clf
   subplot(2,2,1)
   plot(qv,Dp,'o')
   xlabel('Flow rate (l/min)')
   ylabel('Pressure drop (Bar)')
   title('Air')
   grid on

   subplot(2,2,2)
   plot(1000.*m1,(P2-P1),'o')
   xlabel('Mass flow rate (g/s)')
   ylabel('Pressure drop (Bar)')
   grid on
   hold on
```

```
plot(0,0)

subplot(2,2,3)
plot(1000.*m1,1.e10*(P2.^2-P1.^2)./m1,'o')
xlabel('Mass  flow  rate (g/s)')
ylabel('(P2^2-P1^2)/m1')
grid  on
hold  on
plot(0,0)

subplot(2,2,4)
plot(1000.*m1,1.e10*(P2.^2-P1.^2),'o')
xlabel('Mass  flow  rate (g/s)')
ylabel('(P2^2-P1^2)')
grid  on
hold  on
plot(0,0)

figure(2)
clf
plot(X1,W1,'o')
xlabel('((1/r1-1/r2)/(2*pi*Dz*log(r2/r1)*Mu))*m1')
ylabel('(P2.^2-P1.^2).*pi.*Dz./(Mu*R*(Tgm+273.15)*log(r2/r1)*m1)')
title('Carbon  packed sample')
grid  on
hold  on
plot(0,0)

Final  = [Tgm  Mu A B K]

AllFinal  = [ qvread qv F Ro1 Ro2 P1 P2 Dp V1 V2 m1  m2 W X1 W1];
```

Appendix A - 2
Radial packed bed holder CAD

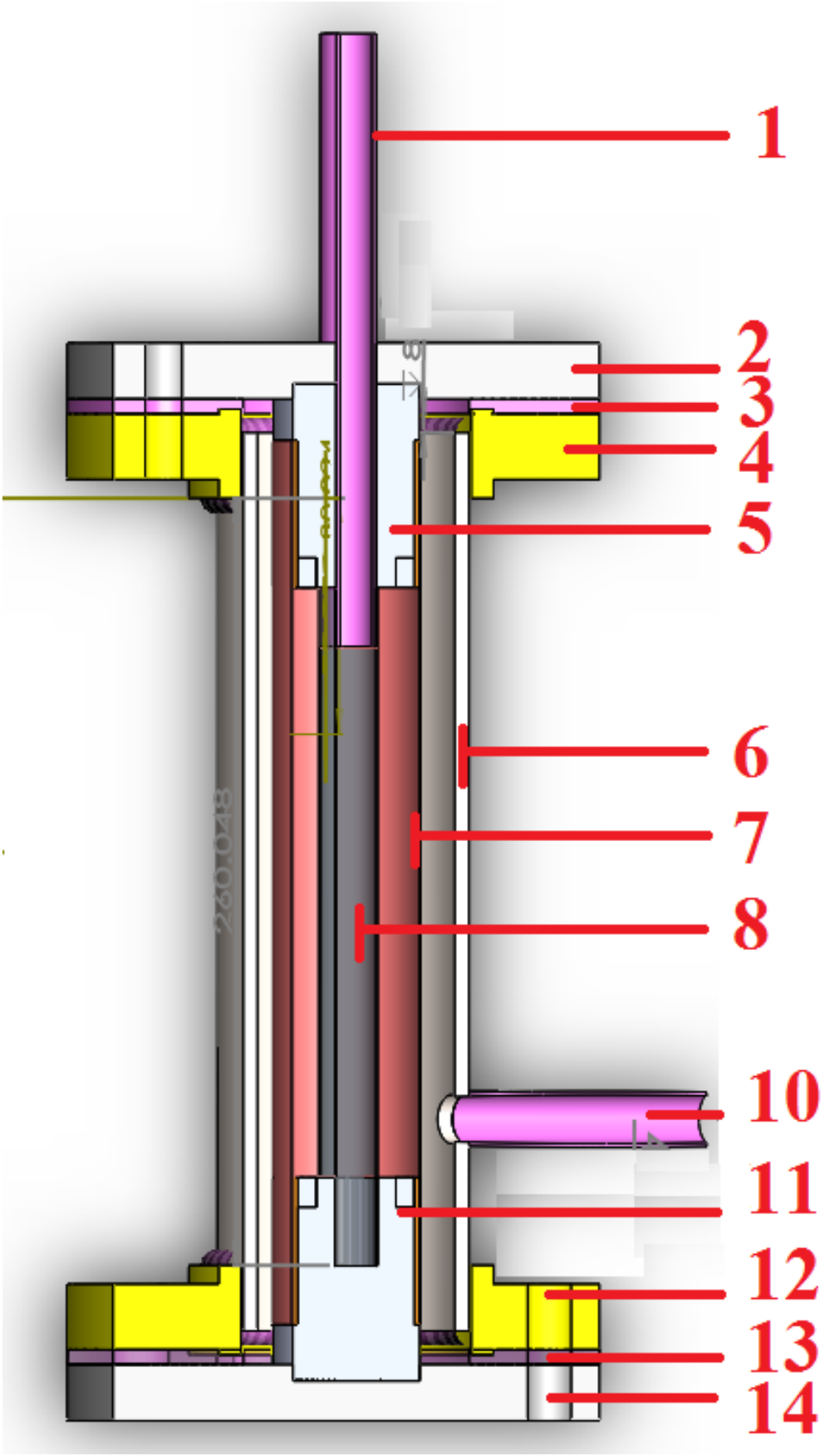

Section No.	Explanation
1	Supplier and collector ¾" stainless steel line for inner mesh
2	Gasket
3	Top raised faced modified ANSI B 16.5 Class 150 blank flange
4	Outside shell raised faced flanges ANSI B 16.5 Class 150 lap joint flanges
5	Top extender
6	3" stainless steel seam welded pipe with schedule10 for outside shell
7	Outer stainless steel mesh
8	Inner stainless steel mesh
10	Supplier and collector ¾" stainless steel line for outside shell
11	Bottom extender
12	Outside shell raised faced flanges ANSI B 16.5 Class 150 lap joint flanges
13	Gasket
14	Bottom raised faced modified ANSI B 16.5 Class 150 blank flange

Appendix B

Generating λ and h for numerical modelling and find the MSE minimum

```
% ver6.m
% This program: Identification of ? and h which pass to numeric model.
%
**********************************************************************
clear
% Counter for keep the number of h which examined
counter1=1;
index1=1;

% Maximum vakue of h which need to evalute
hint=149;
% Step of changing the h until reaches to maximum
dh=1;

while (index1 <150)
  hint=hint+dh
```

```
 x=clock;
 startime=[x(4)  x(5)  x(6)]

  index2=1;
  % Maximum  vakue  of ? which  need  to evalute
  kc=0.49;
  % Step  of changing  the ? until  reaches  to maximum
  dkc=0.01;

  while  (index2  <51)
     kc=kc+dkc;
     index2=index2+1;
     kc=kc;

    %This  subroutine  fin  the temperature  profile  at Centre node with  given
    %value  of h and ?, and compere the profile  with experimental  data and
    %calculate  the error based on MSE.
     programVer61;

     % Keep the  error amount  for specific  h and ?.
     midresult(index2,:)=[kc  hint  w R2];
  end

  eval(['result'  num2str(index1)  '= midresult;']);
  index1=index1+1;
  h=hint;
end
%
**************************************************************************
CC=result1;
for  i=2:1:(index1-1)

   eval([  'aaa' '=result'  ,num2str(i);]);
     CC=[CC;aaa];

end
%
**************************************************************************
k=0;
 for  j=1:1:length(CC)

    if  CC(j,3)> 0 & CC(j,3)<=10
       k=k+1;
       final(k,:)=CC(j,:);
```

```
    end

 end
%
**************************************************************************
% Find the minimum error (min of MSE) at error matrix
[W I]=min(final(:,3));

%find the related h and ? for the minimum value of MSE
 final(I,:)
```

Appendix B - 1
Calculate the temperature profile at centre node by given λ and h

```
%**************************************************************************
%       Find the carbon pack thermal conductivity
%       for different density by the transient method
%       version 61 (proramVer61)
%  MODELL 61 : It is complete program for modelling with desorption effect
%           Specific Heat of Carbon and Liquid Phase are Constant
%**************************************************************************
%**************************************************************************
%       Exp. Data Load
%**************************************************************************
  %data=load (uigetfile('*.txt'));
    data=load('1-1.ASC');
  % Tin:      inside temp. from exp. data (0C)
    Tin1=data(1:length(data),4);

  % Tou:      outside temp. from exp. data (0C)
    Tou1=data(1:length(data),5);

  % Treceive:  Receive Temp. from exp. data (0C)
    Treceive1=data(1:length(data),3);

  % P:      Pressure of system from exp. data (bar)
    P1=data(1:length(data),2);

  %Testtime1:      Test time from exp. data (each second)
    Testtime1=0:1:length(data)-1;
%**************************************************************************
%       Sample Information
%**************************************************************************
  % Ds:      sample density (kg /m3)
```

```
% Msc:       sample  carbon mass (kg)
% Vfree:     Sample  free volume  (m3)
% dz:        Sample  Length  (m)

% Sample  1 information

    Ds=546.721;
    Mc=49.23*10^-3;
    Vfree=4.0816E-05;
    dz=0.2;
%*************************************************************************
%          Refrigerant  Information
%*************************************************************************
% CpRL: Average Typical  value  of  R723 Liquid  phase specific  heat (J/kg.K)
   CpRL= 4.489757 * 1000;

% R: Gas Constant  (J/kg.K)
   R= 365.118;

% A: Is a Constant  correspinding  to the Slop of the Saturation  Curve on
%    Plot of ln(P)  Vs -1/Tsat
   A= 2690;
%*************************************************************************
%          Carbon Information
%*************************************************************************

% Typical  value  of carbon specific  heat (J/kg.K)
   Cpc=1000;

%*************************************************************************
%          Numerical  Calculation  General Information
%*************************************************************************
% dt:      Time  Step (Second)
   dt=0.3;

% n:       Number of deviation
   n1=16;

% np:      Number of points
   np=n1+1;

% Radius  for Node 1 on Carbon Surfaec
   r(1)=(25.45-2*0.7)*10^-3/2;
```

```
   % dr:      Length  Step (m)
      dr=r(1) / n1;
%*************************************************************************
%         Data Regeneration  Regarding  to Time  Step
%*************************************************************************
      Testtime  = 0: dt : Testtime1(length(Testtime1));
      Tin=interp1(Testtime1,Tin1,Testtime);
      Tou=interp1(Testtime1,Tou1,Testtime);
      Treceive=interp1(Testtime1,Treceive1,Testtime);
      P=interp1(Testtime1,P1,Testtime);
%*************************************************************************
%     Creation of Main Temp Matrix
%*************************************************************************
   % Main Temp. Matrix  Which  is Include  All  Nodes Temp.
      T=zeros(np,length(Tin));

   % Twmp.  Matrix  for Tube Wall
      Twall=zeros(1,length(Tin));

   % Finding  the Saturation  Temp.(OC) form  Pressure (bar)
   % Equation  is provided  by George
      Tsat  = 96.86 * P .^ 0.2098 - 134.3;
%*************************************************************************
%      Initial  Condition
%*************************************************************************
   % All  Nodes Temp.  at First  Time  Is Same as Each Other and is Equal  to
   % Inside  Termocouple  Temp.  at Staring  Time
      T(1:np,1)=Tin(1,1);

   % Tube wall  Temp.  Is Assume  Same as Outside  Termocouple  Temp.
      Twall=Tou;
%*************************************************************************
%      D-A Equation  Genral  Coefficient
%*************************************************************************
         X0 = 0.3540;
%           X0=0; % For evaluation  of activated  carbon with  air
         KK = 3.7342;
         nn  = 1.187;
%*************************************************************************
%          Main  Body
%*************************************************************************
        for n=1:1:length(Tin)-1

%=========================================================
```

```
%       Boundary Condition on the tube wall

%=========================================================
        % X value from D-A equation
          aa(1,n) = ((T(1,n)+273.15) ./ (Tsat(n)+273.15)) - 1;
          X(1,n) = ( X0 * exp(-KK * aa(1,n) .^ nn));

        % Left Cell Surface Area (m2)
          A1 = (2 * pi() * r(1)) * dz;

        % Right Cell Surface Area (m2)
          A2 = 2 * pi() * (r(1) - dr/2) * dz;

        % First Cell GeneralVvolume(m3)
          V(1) = pi() * (r(1).^2 - (r(1) - dr/2).^2) * dz;

        % First Cell Carbon Mass(kg)
          Mfirstcell = Ds * V(1);

      Z1(1,n)= real((X0 * exp(-KK * aa(1,n) .^ nn)) .* aa(1,n).^ (nn-1) .* (-KK * nn
./ (Tsat(n)+273.15)));

      Z11(1,n)= real((X0 * exp(-KK * aa(1,n) .^ nn)) .* aa(1,n).^ (nn-1) .* (KK * nn
* (T(1,n)+273.15)) ./ (Tsat(n)+273.15) .^2);

      Z2(1,n) = Mfirstcell * Cpc + Mfirstcell * X(1,n) * CpRL;

      Z3(1,n)= (R * A * (T(1,n)+273.15) ./ (Tsat(n)+273.15));

      Z4(1,n)= Z3(1,n) * Mfirstcell * Z1(1,n);

      Z5(1,n)= Z3(1,n) * Mfirstcell * Z11(1,n);

      E(1,n) =  Z2(1,n) - Z4(1,n);

          a1 = (dt * hint * A1)./ (E(1,n)) ;

          b1 = (dt * kc * A2)./ (E(1,n) * dr) ;

          c1 = Z5(1,n) ./ E(1,n);

       T(1,n+1)= T(1,n) + a1 * (Twall(1,n) - T(1,n)) + b1 * ( T(2,n) - T(1,n)) + c1 *
(Tsat(n+1) - Tsat(n));
```

```
%=============================================================
      %      For Internal  Nodes
%=============================================================
         for i=2:1:np-1
%=============================================================
         % X value  from  D-A equation
            aa(i,n)  = ((T(i,n)+273.15)  ./ (Tsat(n)+273.15))  - 1;
            X(i,n)  = (X0 * exp(-KK * aa(i,n)  .^ nn));

         % Radius  for specific  node
            r(i)  = (np-i)  * dr;

         % Left  Cell  Surface  Area (m2)
            A12= 2 * pi()  * (r(i)  + dr/2) * dz;

         % Right  Cell  Surface  Area (m2)
            A23= 2 * pi()  * (r(i)  - dr/2) * dz;

         % Each Internal  Cell  General  Volume(m3)
            V(i)  = pi()  * ((r(i)  + dr/2).^2 - (r(i)  - dr/2).^2) * dz;

         % Each Internal  Cell  Carbon Mass(kg)
            Mcell(i)  = Ds * V(i);


         Z1(i,n)=  (X0 * exp(-KK * aa(i,n)  .^ nn)) .* aa(i,n).^  (nn-1) .* (-KK * nn ./
(Tsat(n)+273.15));

         Z11(i,n)=  (X0 * exp(-KK * aa(i,n)  .^ nn)) .* aa(i,n).^  (nn-1) .* (KK * nn *
(T(i,n)+273.15))  ./ (Tsat(n)+273.15)  .^2;

         Z2(i,n)  = Mcell(i)  * Cpc + Mcell(i)  * X(i,n)  * CpRL;

         Z3(i,n)=  (R * A * (T(i,n)+273.15)  ./ (Tsat(n)+273.15));

         Z4(i,n)  = Z3(i,n)  * Mcell(i)  * Z1(i,n);

         Z5(i,n)=  Z3(i,n)  * Mcell(i)  * Z11(i,n);

         E(i,n)  =   Z2(i,n)  - Z4(i,n);

            a = (dt * kc * A12)./ (E(i,n)  * dr) ;
```

```
            b = (dt * kc * A23)./ (E(i,n)  * dr) ;

            c = Z5(i,n)  ./ E(i,n);


        T(i,n+1)=  T(i,n)  + a * (T(i-1,n)  - T(i,n))  + b * (T(i+1,n)  - T(i,n))  + c *
(Tsat(n+1)  - Tsat(n));

%==========================================================
      %       Boundary  Condition  at Tube  Middle  Node
%==========================================================
              T(np,n)=T(np-1,n);
          end

        end
%************************************************************************
%         Find  the answer  for modell  and MSE error
%************************************************************************
   Tanswer  = T(np,1:length(Tin)-1);

   NN=size(Tanswer);

% Calculate  the error value  (MSE)  between calculated  profile  and test data
   w = [sum((Tanswer-Tin(1:length(Tin)-1)).^2)]/NN(2);
```

Appendix B - 2
Anter QUICKLINE™ -10 Thermal conductivity meter catalogue

QUICKLINE™ -10 THERMAL CONDUCTIVITY METER

- Economical and easy to use
- Ambient temperature operation
- ASTM E1530 Guarded Heat Flow Meter Method
- Manual or computerized operation

This low cost, single temperature test instrument is used for quick determination of thermal conductivity of solid materials. Because of its simple operation, small sample size, and short cycle time, the QuickLine™-10 is ideally suited for quality control and screening of materials. Metals, ceramics, polymers, composites, glass, and rubber can be tested accurately. Thin samples like paper products and plastic films can also be tested. A manual and a computerized model is available.

QUICKLINE™-10 TEST METHOD

A test sample is held under a compressive load between two polished metal surfaces. The upper surface is temperature controlled. The lower surface is part of a calibrated heat flux transducer, which is attached to a liquid cooled heat sink. An axial temperature gradient is established through the stack as heat flows from the upper surface through the test sample to the heat sink.

After reaching thermal equilibrium, the temperature difference across the sample is measured along with the output from the heat flux transducer. These values and the sample thickness are then used to calculate thermal conductivity. The temperature drop through the sample is determined from temperature sensors in the metal surfaces on either side of the sample. The QuickLine™-10 is factory calibrated using samples of known thermal resistance spanning the range of the instrument. Calibration reference sets are available. The contact resistance is kept small by applying a reproducible, pneumatic load to the test stack.

The QuickLine™-10 test method is in accordance with specification **ASTM E1530** for measuring thermal conductivity. The manual unit is supplied with a utility software program for convenient data analysis using a PC. The user simply enters data from the QuickLine™-10 digital display via the computer keyboard and the thermal conductivity is automatically computed. If the measured thermal resistance value falls outside the range of the instrument, the program suggests testing a different sample thickness for obtaining more accurate test results. If a PC is not available, data analysis can also be carried out manually following instructions from the user's manual.

The new internally computerized QuickLine™-10(C) has the best of both worlds, the rapid testing of a manual device and the ease of operation of a fully computerized system, without the need for an external PC. Once a sample is loaded and a few keystrokes are performed, the thermal conductivity value is automatically measured and displayed in a predetermined length of time.

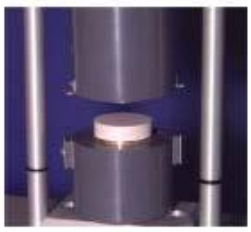

Samples are easy to load. Clamping pressures are adjustable with front panel regulator and pressure gage.

ANTER CORPORATION *an ISO 9001 Certified Company*
1700 Universal Road, Pittsburgh, Pennsylvania 15235-3998 USA
Phone: (412) 795-6410 Fax: (412) 795-8225 *sales@anter.com* *www.anter.com*

The QuickLine™-10(C) has been programmed with 8 reference materials covering an approximate thermal conductivity range of 1.0-220 W/mK. Two additional references may be added for user-specific materials. Sample thickness ranges of approximately 2.5" are programmed into the on-board computer based on the customer's typical sample size. Three test duration times (30, 45, or 60 minutes) are available.

Once the QuickLine™-10(C) has been properly installed and all heaters and electronics have been turned on, the first step is to calibrate the unit. This is only necessary when the instrument is shut off and turned back on, when a different test duration time is wanted, or when a material with a vastly different conductivity than the calibrated range is to be tested. By selecting the references that have a conductivity value closest to the material to be tested, adjusting the reference thickness to the proper value and selecting the test duration time, the system will automatically calibrate itself.

Loading an actual sample and adjusting to the sample thickness is all that is necessary to perform an actual test at this point with no additional interaction with the operator necessary until the test is complete. At the end of the test duration time, the calculated thermal conductivity and sample mean temperature will be displayed and will remain on the display until the next test is started.

Ease of use, versatility, reproducibility and accuracy are all traits of the new internally computerized QuickLine™-10(C), making it particularly ideal for those who perform continuous and repetitive tests on batches of the same material.

The instrument is completely self contained and requires no additional instrumentation for the measurement. When city water is used for cooling, the mean sample temperature may vary slightly as the water temperature changes with the seasons. If this variation is undesirable, an optional chiller providing coolant at a fixed temperature can be connected to the unit instead. The QuickLine™-10 is a simple, fast, accurate, and reasonably priced laboratory instrument.

For thermal conductivity testing over a wide temperature range, contact Anter Corporation and inquire about Unitherm™ Model 2022.

QUICKLINE™ –10 SPECIFICATIONS

Model Designation:	QuickLine™-10[**X**]-[**Y**]-[**Z**]
Test Method	ASTM E1530 Guarded Heat Flow Meter Method
Sample Temperature	Near ambient
Computerized Model	Change model designation to 10(C)
Thermal Conductivity Range	0.1 to 100 W/mK (Up to 20 W/mK for manual model)
Thermal Resistance Range	0.0002 to 0.1 m^2K/W
Sample Size Options [X]	
(1)	1" round, (25mm) (manual version only)
(2)	1" square, (25mm) (manual version only)
(3)	2" round, (50mm)
Sample Thickness	Maximum 1.25" (32mm) (2.5" (64mm) for computerized model) depending on thermal resistance. Thin films down to 0.0004" (0.1mm)
Environment	Ambient air
Accuracy	±3% to 8% depending on sample size and conductivity
Reproducibility	±2%
Cycle Time	Approx. 30 minutes per sample
Utilities	City water (0.1gpm)* Compressed air (40-80 psi)
Dimensions	12" (31cm) W x 14"(36cm) D x 24" (61cm) H
Weight	30 lbs (14 kg)
Power Options [Y]	
[A]	115VAC-60Hz-1kVA
[B]	230VAC-50Hz-1kVA
[C]	100VAC-50/60Hz-1kVA
Chiller Options [Z]	
[0]	Not provided
[1]	Provided

*City water not required when optional chiller is provided.

Appendix C
Ammonia – 208C equilibrium data points for D-A equation

Pressure	Temperature	Concentration		Pressure	Temperature	Concentration
bar	oC	$gr.gr^{-1}$		bar	oC	$gr.gr^{-1}$
5.986	36.69	0.270192		2.758	120.01	0.036231
8.387	36.96	0.284839		4.141	119.99	0.047559
8.388	36.91	0.294929		5.985	120.02	0.061735
2.772	35.50	0.198333		8.402	120.01	0.079389
2.774	40.00	0.178928		8.425	120.00	0.080321
4.153	40.00	0.224569		6.000	119.99	0.062531
5.999	40.00	0.260179		4.149	120.00	0.047901
8.408	40.00	0.279151		2.761	119.99	0.036015
11.299	40.00	0.288964		2.758	140.02	0.026660
11.393	40.00	0.299214		8.409	139.94	0.057615
5.989	40.00	0.260920		11.469	140.01	0.074622
4.144	40.00	0.225676		8.429	139.96	0.058426
2.761	60.00	0.116003		5.997	140.00	0.045221
4.139	59.99	0.150577		4.138	140.06	0.034759
5.984	60.00	0.188769		2.746	140.00	0.026528
8.390	59.99	0.224803		2.744	159.99	0.020161
11.361	60.00	0.250536		4.135	159.99	0.026140
18.667	60.00	0.271554		5.995	160.00	0.033570
11.437	60.00	0.250548		8.428	160.00	0.042970
5.991	60.00	0.188001		11.457	160.01	0.055127
4.139	59.99	0.149696		8.428	160.00	0.043291
2.759	60.00	0.114875		5.999	160.02	0.033773
2.757	80.01	0.076898		4.135	160.00	0.026082
4.133	80.00	0.100273		2.739	159.98	0.019769
5.980	80.01	0.128484		2.740	180.01	0.014940
8.393	80.00	0.160080		4.135	179.98	0.019660
11.380	80.00	0.191005		6.001	179.97	0.025484
11.419	80.00	0.191730		8.436	180.03	0.032628
5.999	80.00	0.127465		11.469	180.02	0.041427
4.146	80.00	0.099338		11.508	179.99	0.041808
2.762	80.00	0.075821				
2.760	100.00	0.052216				
4.138	99.99	0.068430				
5.985	99.99	0.088336				
8.396	100.00	0.112190				
11.399	100.01	0.138688				
11.449	100.00	0.139486				
6.001	100.00	0.088524				
4.148	100.00	0.068433				
2.762	100.00	0.051728				

Appendix C - 1
DME – 208C equilibrium data points for D-A equation

Pressure	Temperature	Concentration		Pressure	Temperature	Concentration
bar	oC	$gr.gr^{-1}$		bar	oC	$gr.gr^{-1}$
1.807	30.49	0.338288		5.585	60.02	0.325140
2.585	29.09	0.347436		5.979	60.01	0.326659
3.615	30.00	0.351019		6.966	60.03	0.329761
4.935	30.01	0.354092		8.340	60.04	0.332186
4.940	30.00	0.354079		8.529	60.02	0.328799
3.619	30.00	0.350917		10.946	60.00	0.324324
2.578	30.00	0.345895		8.517	60.02	0.328603
1.777	30.00	0.338044		6.631	60.02	0.328083
1.777	40.00	0.321325		5.162	60.02	0.323416
2.579	40.00	0.332053		3.654	60.02	0.313841
3.616	40.01	0.338828		2.597	60.01	0.302053
4.928	40.00	0.342858		1.786	60.00	0.286860
6.552	40.00	0.344792		1.785	80.01	0.250170
4.907	40.00	0.343070		2.591	80.00	0.268060
3.589	40.00	0.339147		3.643	80.00	0.283382
2.553	40.00	0.332379		4.966	80.01	0.296532
1.757	40.00	0.321608		6.613	80.04	0.307826
1.759	50.00	0.303538		8.652	80.04	0.313481
2.554	50.00	0.316907		10.958	80.05	0.314570
3.584	50.00	0.326308		8.679	79.98	0.313449
4.886	50.00	0.332321		6.656	80.03	0.307027
6.470	50.00	0.335776		4.992	80.01	0.296434
5.616	49.99	0.333165		3.640	80.00	0.282942
4.682	50.01	0.332220		2.584	80.00	0.267447
5.569	50.00	0.334967		1.776	80.00	0.249402
6.729	50.00	0.337154		1.777	100.00	0.214167
8.147	50.01	0.338750		2.583	100.01	0.233981
8.072	50.00	0.338330		4.977	100.03	0.267894
8.641	49.99	0.335150		6.653	100.06	0.282857
8.627	50.00	0.335395		8.666	100.16	0.293243
8.286	50.02	0.338547		10.891	100.05	0.300439
8.143	50.01	0.338587		8.674	100.20	0.291963
6.444	50.01	0.336522		6.661	100.03	0.282144
5.103	50.00	0.333636		4.987	100.02	0.267933
4.119	50.01	0.329688		3.635	100.02	0.251714
4.166	60.00	0.317444		2.580	100.00	0.234182
5.445	60.01	0.324320		1.773	100.00	0.214322
6.633	60.02	0.328649		1.772	119.98	0.181373
8.461	60.04	0.332687		2.576	120.02	0.202146
8.463	60.04	0.332658		3.631	120.01	0.221260

Appendix C - 2
Curve fitting program to find D-A equation parameters

```
%  dubcoef.m
%  This program computes D-R coefficients (xo, k, n)
%  Dr. Z. Tamainot-Telto
%  School of Engineering
%  University of Warwick
  clear
 %  REFRIGERANT GAS SELECTION
%
  Z1=input('REFRIGERANT SELECTION (1: AMMONIA (R717), 2:
DME(R170),  3: R723, 4: METHANOL :  ')

  % AMMONIA (R717)*************************************************
  if Z1==1;
     A=2823.4;  B=11.749;  % Tsat=A/(B-LogP)  or P=exp(B-A/Tsat)
                    % where Tsat(K) and P(bar)
  end

%  DME(R170)*****************************************************
  if Z1==2;
    A=2625.75;  B=10.58235;   % Tsat=A/(B-LogP)  or P=exp(B-A/Tsat)
  end

%  R723**********************************************************
  if Z1==3;
     A=2689.6;  B=11.3;   % Tsat=A/(B-LogP)  or P=exp(B-A/Tsat)
  end

%  METHANOL******************************************************
  if Z1==4;
     A=4594.4;  B=13.6;   % Tsat=A/(B-LogP)  or P=exp(B-A/Tsat)
  end

%  TEST PARAMETERS***********************************************
  Nmax=2000;      % Max. number value of n ranging from 0 to 2 explored
  DDmax=1000;     % i/DDmax corresponds to incrementation of n

%  EXPERIMENTAL DATA FILE****************************************
  load data.txt
  data1=data;
  s=size(data1);
```

```
P=data1(:,1);              % Gas Pressure (bar)
T=data1(:,2);              % Sample temperature(^oC)
xa=data1(:,3);             % Refrigerant concentration(kg/kg)
Tsat=A./(B-log(P))-273.15; % Refrigerant Saturating temperature (^oC)
t=(T+273.15)./(Tsat+273.15);

%**************************************************************************
for i=1:Nmax
   n(i)=i/DDmax;
   fit=polyfit((t-1).^n(i),log(xa),1);
   xo(i)=exp(fit(2));
   ko(i)=fit(1);
   xcal=xo(i).*exp(ko(i)*((t-1).^n(i)));
   see(i)=(sum((xa-xcal).^2));
end
%**************************************************************************
[Y,I]=min(see);
Xo=xo(I);
Ko=ko(I);
No=n(I);
err=see (I)^0.5/s(1);
RESULT=[Xo  Ko No err]
%**************************************************************************
u=[0:0.01:1];
Xcal=Xo.*exp(Ko.*u.^No);
%**************************************************************************
figure(1)
clf
plot(t-1,xa,'o')
hold on
plot(u,Xcal)
grid on
xlabel('T/Tsat-1')
ylabel('Refrigerant concentration (kg/kg)')
axis([0,1,0,0.50])
text(0.1,0.48,'X=Xo*exp (-K(T/Tsat-1)^n)'
```

Appendix D

Main program to model the tubular generator for different application

```
% This is a modified program from EU-SOCOOL Project(ZTT/REC)2003.
% MODIFIED VERSION COMPLETED ON 23/01/2015.
% Provided to Hasan by ZTT on the 06/02/2015
% Adopted By Hasan at 24/01/2016
% ZTT amendments on the 25/01/2016
% ZTT amendments on the 24/02/2016 Temperature step
% (approximation on instant change in pressure: only initial concentration
% with evaporating pressure and the rest follow from condensing pressure)
%*****************************************************************
clear
clc
global L M h delt x UAtop UAbot T xold p P Pold pold Mgas Mamm Tsatk Tmeant
global Tsatold Tsat Ml delm UAdTbym CP B Tsatoldk K x0 n Vvoid mass Told
Mamminit
global time Ntot N Texitdes Texitads Q A ksteel
global Cpl CpC dTsat Cpfintube coolJ Tadjust
global r2 w2 D

%*****************************************************************
% Tubular Generator Physical Appearance*********************************

D= 28.58 /1000;   % Tubular Generator Outer diameter OD (m)
tw= 0.91 /1000;   % Tubular Generator tube wall thickness (m)
ID=D-2*tw;        % Tubular Generator inner diameter ID (m)

lce=0.200*5;      % Receiver tube length (for void volume)(m)
lc=0.200*5;       % Carbon tube length (m)

Do=0;             % Thermocouple Tube outer diameter (m)
tc=ID/2-Do/2;     % Total carbon thickness (m)

%*****************************************************************
% Pakced Carbon Physical Appearance*************************************

rhoc=700;                          % Carbon Packed Density(kg/m3)
Dc=D-2*tw;                         % Carbon OD (m)
dc=Dc-2*tc;                        % Carbon ID (m)
mctot=pi*(Dc*Dc-dc*dc)/4*rhoc*lc;% Total carbon mass (kg)

%*****************************************************************
```

```
% Steel, Copper, Carbon and R723 thermo physical properties******************

CpC=1125;          % Cp of pure carbon (J/kg/K)

Cpl=4500;          % Adsorbate Cp (J/kg K) 27/01/2014 ZTT estimation

Cpsteel=460;       % Cp of steel (J/kg/K)
ksteel=16.3;       % Conductivity steel (W/mK)
rhosteel=7818;     % Density steel (kg/m3)

% Cpsteel=385;    % Cp of copper alloy (J/kg/K)
% ksteel=42;      % Conductivity copper alloy (W/mK)
% rhosteel=8610;  % Density copper alloy (kg/m3)

%*************************************************************************
% D-A Parameters ********************************************************

x0=0.354;K=3.7342;n=1.187;      % 208C/R723 (From ZTT model)

%*************************************************************************
% Length Step and Number of Carbon Layer*********************************
deltathickness = 1.2 / 1000;    %Thickness increment or Length step (m)

% Number of carbon layers for all different wall thickness
% at specific diameter
L1 = tc/deltathickness;         % Number of carbon layers

% Finding the exact value of number of carbon layers from
% constant Thickness increment
if ceil(L1)-L1 < 0.5            % Upper number
   L = ceil(L1);
else
   L = floor(L1);               % Lower number
end

M=L+2;                          % Number of rows
%*************************************************************************
% Simulation Time Step and Parameters************************************
delt=0.1;                       % time step (s)
tottime=7000;                   % total time for simulation (s)
steps=round(tottime/delt);      % number of timesteps in simulation
%*************************************************************************
% Application Selection**************************************************
```

```
Z1=input('Application selection(1:Ice Making, 2:AirCon, 3:Heat pump):')

% Ice Making
if Z1==1;
   Te=-5+273.15; Tc=35+273.15; T1=35+273.15;   % Temp. (K)
   Pevap=PsatR723(Te);                  % Pressure (bar), Temp. (K)
   Pcon=PsatR723(Tc);                   % Pressure (bar), Temp. (K)
   LH=(HGR723(Te-273.15)-HFR723(Tc-273.15))/1000;  %Evaporation heat(kJ/kg)
end

%  AirCon
if Z1==2;
   Te=10+273.15; Tc=35+273.15; T1=35+273.15;   % Temp. (K)
   Pevap=PsatR723(Te);                  % Pressure (bar), Temp. (K)
   Pcon=PsatR723(Tc);                   % Pressure (bar), Temp. (K)
   LH=(HGR723(Te-273.15)-HFR723(Tc-273.15))/1000;  %Evaporation heat(kJ/kg)
end

%Heat pump 1
if Z1==3;
   Te=5+273.15; Tc=40+273.15; T1=40+273.15;    % Temp. (K)
   Pevap=PsatR723(Te);                  % Pressure (bar), Temp. (K)
   Pcon=PsatR723(Tc);                   % Pressure (bar), Temp. (K)
   LH=(HGR723(Te-273.15)-HFR723(Tc-273.15))/1000;  %Evaporation heat(kJ/kg)
end

%*****************************************************************
% SIMULATION OPERATING CONDITIONS*****************************

pvt(1,1)=Pevap;              % Initial Pressure (bar)
pvt(1,1:1:steps+1)=Pcon;   % Final Pressure (bar)
Tvt(1,1)=Tc-273.15;          % Initial temperature (oC)

Tw=input('Generator wall temperature (oC): '); % Generation temperature(oC)

% Temp. Matix First Culumn Construction with Generation Temperature (oC)
Tvt(1,2:1:steps+1)=Tw;
%*****************************************************************
% PRELIMINARY CALCULATIONS & INITIAL CONDITIONS**************

Ttubein=Tvt(1,1);                % Initial temperature (C)
Ttubeink=Ttubein+273;          % Uniform tube initial temp (K)
pinit=Pevap;                     % Initial pressure (bar) ZTT24/02/2016
Tsatink=TsatR723(pinit);         % Initial saturation temperature(K)
```

```
Tsatin=Tsatink-273;              % Initial saturation temperature(C)
xinit=x0*exp(-K*(((Ttubeink)/(Tsatink)  -1).^n)); % Initial concentration
Vvoid=0;                         % Void volume (m3)
Mgasinit=pinit*1e5*Vvoid/rR723(pinit,Ttubein)/(Ttubeink);  % Charged gas mass
(kg)

%*****************************************************************
% The final temperature of centre node which used to stop the program (K)
TendK = (Tw-10) + 273;

% System final pressure is condensation pressure (bar)
Pend = Pcon;

% System final saturation Temp. based final pressure (K)
TsatendK = TsatR723(Pend);

% System final concentration based on final Temp. and saturation Temp.
xend = x0*exp(-K*(((TendK)/(TsatendK)  -1).^n));

% Average concentration based on initial and final concentration
XAVG = (xinit  + xend) ./ 2;

% Thermal Conductivity based on packed carbon density and average
% concentration (W/mK)
hint  = 192.5926 * XAVG + 3.0562 * rhoc  - 1621.4058;

% Internal wall heat transfer coeff. based on packed carbon density and
% average concentration (W/m2K)
kc  = 2.787 * XAVG + 0.0026 * rhoc  - 1.4175;

%*****************************************************************
% SET UP ARRAYS*****************************************************

A=zeros(1,M);                    % Vector of cell outer areas (m2/m length)
R=zeros(1,M);                    % Vector of cell outer radii
R(2)=D/2;                        % Outer radius
R(3:M)=[Dc/2:-tc/L:dc/2+tc/L];%  Radius from 3 node up to Centre node
A=2*pi*R*lc;                     % Control volume inn and out surface area
Atube=A(2);                      % Tube area (m2)
A(2)=A(2);
mcp=zeros(1,M);                  % m x Cp for all layers (J/K)
mass=zeros(1,M);                 % m for all layers (kg)
xold=zeros(1,M);                 % x for all layers
xold(3:M)=xinit*ones(1,M-2);     % Initial concentrations
```

```
x=zeros(1,M);                    % concentration for all layers
Tmeant=0;                        % Mean carbon temp (C)
p=0;                             % tube pressure (bar)
Tt=zeros(1,steps+1);             % Mean carbon temp - time array(C)
pt=zeros(1,steps+1);             % pressure - time array
Mlt=zeros(1,steps+1);            % Liquid mass - time array
Tt2=zeros(M,steps+1);            % All carbon temperatures - time array(C)
Tt2(:,1)=Ttubein*ones(M,1);      % Set initial temperatures
xt2=zeros(M,steps+1);            % All carbon concs - time array(C)
xt2(3:M,1)=xinit*ones(M-2,1);%  Set initial concentrations
mtube=pi*(R (2).*R(2)-R (3).*R(3))*rhosteel*lc  % Tube mass
mass(2)=mtube;                   % Mass matrix second index is tube mass
                                 % carbon mass at mass matrix from third index
                                 % up to one node before centre nod
mass(3:M-1)=pi*(R (3:M-1).*R(3:M-1)-R (4:M).*R(4:M))*rhoc*lc;
                                 % Carbon mass at mass matrix for centere node
mass(M)=pi*(R (M).*R(M)-dc*dc/4)*rhoc*lc;
                                 % Initial total R723 mass in tube(kg)
Mamminit=xinit*sum(mass(3:M)) + Mgasinit;

T=zeros(1,M);                    % New temps. (C)
Told=T;                          % Old temps
La=0;                            % Latent heat (J/kg)
delm=0;                          % R273 mass condensed in time step (kg)
Qgen=0;                          % Heat into generator in delt (J)
T=Ttubein*ones(1,M);             % Set initial temps to tube temp.
Mamm=Mamminit;                   % Total mass of R723 in tube.
Ml=0;                            % Mass of liquid R723 in receiver;
pold=pinit;                      % initial pressure (bar)
Pold=pold*1.e5;                  % initial pressure (Pa)
Mgas=Pold(1)*Vvoid/rR723(pold(1),Ttubein)/Ttubeink;  % Mass of gas in tube (kg)
xstart=x0*exp(-K*((Ttubeink/Tsatink -1).^n))         % Initial concentrations
Tsatold=Tsatin;
Tsatoldk=Tsatold+273;
Tt=Tvt;
pt=pvt;

%*****************************************************************
% Top overall heat transfer coefficient(W/K from cell 'above')*****************

% Matrix creation
UAtop=zeros(1,M);

% Thermal resistance for a node on carbon surface after tube wall
```

```
% thermal resistance = 1/2 carbon +steel + hint
UAtop(3)=A (3)/(tc/L/kc/2+tw/ksteel+2/hint);

% Thermal resistance of each node after nodes on tube body and carbon
% surface upto centere node
UAtop(4:M)=A (4:M)/tc*L*kc;

%*********************************************************************
% Bottom overall heat transfer coefficient(W/K from cell 'below')***************

% Matrix creation
UAbot=zeros(1,M);

% Matrix creation for Temp. differences over the control volume
% UA top & bottom x temp differences=heat conducted in per unit mass(W/kg)
UAdTbym=zeros(1,M);

UAbot(1:M-1)=UAtop(2: M);

%*********************************************************************
% Overall specific heat calculation*****************************************

% Matrix creation for overall specific heat of solid + adsorbate (J/kg K)
CP=zeros(1,M);

% The specific heat at second node is a Cp of tubular generator body
% material
CP(2)=Cpsteel;

% Group used to calculate Cp. Zero for tube,fin
B=zeros(1,M);

%*********************************************************************
% SIMULATIONS*********************************************************
for loop=1:steps
  timeold =(loop-1)*delt;
  timenew= delt*loop;
  Told(3:M)=T(3:M);              % Old temps. (C)
  Told(1)=Tt(loop+1);
  Told(2)=Tt(loop+1);
  H=2621.3*364.2;
                                 % Mean carbon temp. time t (C)
  Tmeant=sum (T (3:M).*mass(3:M))/sum(mass(3:M));
  Tmeantk=Tmeant+273;
```

```
  Mgas=Pold*Vvoid/rR723(pold,Tmeant)/Tmeantk;        % Mass of gas (kg)
  UAdTbym(3:M-1)=UAtop(3:M-1).*(Told(2:M-2)-Told(3:M-1))+UAbot(3:M-
1).*(Told(4:M)-Told(3:M-1));
  UAdTbym(M)=UAtop  (M) .*(Told(M-1)-Told(M))  ;
  UAdTbym(3:M)=UAdTbym  (3:M)./mass(3:M)  ;
                                                  %Changes  on 19/02/2014 by ZTT
  for a=3:M; if Tsatoldk>(T(a)+273);Tsatoldk;(T(a)+273);time;end;end
  xold(3:M)=x0*exp(-K*(((T(3:M)+273)./Tsatoldk-1).^n));
  CP(3:M)=xold(3:M)*Cpl  + CpC;
  T1=T(3:M)+273;
  Ts=Tsatoldk;
  B(3:M)=H*K  *n.*xold  (3:M).*T1/Ts/Ts.*((T1/Ts-1).^(n-1));
  g1=1e5*(pt(loop+1)-pt(loop));
  delp=findTxtest(g1,Pold,Mamminit);    % function  to find  T's and  x's
  Tt2(:,loop+1)=T';
  Tmean(loop+1)=sum  (T(3:M).*mass(3:M))/sum(mass(3:M));


%*********************************************************************
 %*********************************************************************
  % Breaking  critaria  which  the centre node reach to 10 degree less than
  % generating  Temp. (Tg)
  if  Tt2(M,loop+1)  >= (Tw-10)
      totalsimulationtime  = length  (Tmean)*delt;
      xt2(:,loop+1)=x';
      xmean(loop+1)=x0*exp(-K*(((Tmean(loop+1)+273)./Tsatoldk-1).^n));
      Bmean(loop+1)=H*K
*n*xmean(loop+1)*(Tmean(loop+1)+273)/Ts/Ts*(((Tmean(loop+1)+273)/Ts-1)^(n-
1));
      % Overall  specific  heat of Desorption  (J/kg.K)
      Cp(loop+1)=xmean(loop+1)*Cpl  + CpC+Bmean(loop+1);
      Mlt(loop+1)=Ml;
      break
  end

%*********************************************************************
%*********************************************************************
  xt2(:,loop+1)=x';
  xmean(loop+1)=x0*exp(-K*(((Tmean(loop+1)+273)./Tsatoldk-1).^n));
  Bmean(loop+1)=H*K
*n*xmean(loop+1)*(Tmean(loop+1)+273)/Ts/Ts*(((Tmean(loop+1)+273)/Ts-1)^(n-
1));
 % Overall  specific  heat of Desorption  (J/kg.K)
  Cp(loop+1)=xmean(loop+1)*Cpl  + CpC+Bmean(loop+1);
```

```
   Mlt(loop+1)=Ml;
end
massliquid=max(Mlt)
S=size(Tt2');
N=S(1);
NN=S(2);
Tcal=Tt2(NN,:)';
massliquid_kg=max(Mlt)

%**************************************************************************
%**************************************************************************
TT=Tmean(2:totalsimulationtime);
CCp=Cp(2:totalsimulationtime);
[TT' CCp'];
CCCp=Cp(2:totalsimulationtime-1);
Taverage=TT';

%**************************************************************************
% Ice Making
if Z1==1;
   total_desorption_heat_in_kJperkg=sum(diff(TT).*CCCp)/1000
%    cooling_in_kJperkg=LH*(xmean(2)-xmean(steps))
   cooling_in_kJperkg=LH*(xmean(2)-xmean(length (Tmean)))
%    SCP_in_kWperkg=cooling_in_kJperkg/tottime
   SCP_in_kWperkg=cooling_in_kJperkg/totalsimulationtime
   COP1=cooling_in_kJperkg/(total_desorption_heat_in_kJperkg)
end

%**************************************************************************
% AirCon
if Z1==2;
   total_desorption_heat_in_kJperkg=sum(diff(TT).*CCCp)/1000
%    cooling_in_kJperkg=LH*(xmean(2)-xmean(steps))
cooling_in_kJperkg=LH*(xmean(2)-xmean(length (Tmean)))
%    SCP_in_kWperkg=cooling_in_kJperkg/tottime
SCP_in_kWperkg=cooling_in_kJperkg/totalsimulationtime
   COP1=cooling_in_kJperkg/(total_desorption_heat_in_kJperkg)
end

%**************************************************************************
%Heat pump 1
if Z1==3;
   total_desorption_heat_in_kJperkg=sum(diff(TT).*CCCp)/1000
%    cooling_in_kJperkg=LH*(xmean(2)-xmean(steps));
```

```
    cooling_in_kJperkg=LH*(xmean(2)-xmean(length  (Tmean)));
    COP1c=cooling_in_kJperkg/(total_desorption_heat_in_kJperkg);
    COP1=COP1c+1
    heating_in_kJperkg=COP1*total_desorption_heat_in_kJperkg
%     SHP_in_kWperkg=heating_in_kJperkg/tottime
    SHP_in_kWperkg=heating_in_kJperkg/totalsimulationtime
end
disp('Total  corrected simulation  time  (Sec)')
totalsimulationtime  = length  (Tmean)*delt

%**************************************************************************
%**************************************************************************
% Final  results  for Ice Macking  and Aircon  application
FINALRESULTS  = [Tw totalsimulationtime  SCP_in_kWperkg  COP1 kc hint
massliquid  xstart  xend  XAVG];

%**************************************************************************
%**************************************************************************
% Final  results  for Heat Pump application
% FINALRESULTS  = [Tw  totalsimulationtime  SHP_in_kWperkg  COP1  kc  hint
massliquid  xstart  xend  XAVG];
```

Appendix D - 1
Subroutine: findTxtest

```
function  d=delpfind(g1,Pold,Mamminit)
% Previously  found  delp  assuming  error is linear  with  assumed  delp
%(Newton-Raphson)
% In tubetest,  delp  is specified
f1=masserrortubetest(g1)/Mamminit;
d=g1;
```

Appendix D - 2
Subroutine: HFR723

```
function  h=HFR723(t)
% returns  enthalpy  of sat R723 liquid  in J/kg (t in deg C)
%%temp  range(170,  390)K
     p1 =  3.601e-07 ;
     p2 =  2.887e-05  ;
     p3 =  0.0008902 ;
     p4 =  3.654  ;
     p5 =  201.7  ;
```

```
h= 1000*(p1*t^4 + p2*t^3 + p3*t^2 + p4*t + p5);
```

Appendix D - 3
Subroutine: HGR723

```
function  h=HGR723(t)
% returns  enthalpy  of sat R723 liquid  in J/kg (t in deg C)
%%temp  range(170,  390)K
      p1 =  -5.621e-09 ;
      p2 =  -3.233e-07  ;
      p3 =  2.487e-05 ;
      p4 =  -0.00498  ;
      p5 =  0.8288  ;
      p6 =  1073 ;

h=1000*( p1*t^5 + p2*t^4 + p3*t^3 + p4*t^2 + p5*t + p6);
```

Appendix D - 4
Subroutine: masserrortubetest

```
function  d=masserror3(dP)
% calculates  mass imbalance  based on guessed pressure  rise dp (Pa)
global  L M h Tairin  delt x UAtop  UAbot T xold  p P Pold pold Mgas  Mamm  Tsatk
Tmeant
global  Tsatold  Tsat  Ml delm  UAdTbym  CP B Tsatoldk  K x0  n Vvoid  mass  Told
Mamminit
global  time  Warning  dTsat  Cpl mce  Cpce sheat  mladjust  coolJ  Tadjust
% Find  all  new carbon temperatures
P=Pold+dP;
p=P/1.e5;
Tsatk=TsatR723(p);
dTsat=Tsatk-Tsatoldk;
T(1)=Told(1);
T(2)=T(1);
T(3:M)=Told(3:M)+(UAdTbym(3:M)*delt  +
B(3:M).*dTsat.*(Told(3:M)+273)/Tsatoldk)./(CP(3:M)+B(3:M));
x(3:M)=x0*exp(-K*(((T(3:M)+273)./Tsatk-1).^n));
T;
Told;
Tmeant=sum(T(3:M).*mass(3:M))/sum(mass(3:M));    % Mean carbon temp
Tmeantk=Tmeant+273;
Mgas=P*Vvoid/rR723(pold,Tmeant)/Tmeantk  ;          % Mass of gas  (kg)
```

```
Ml=Mamminit-Mgas-sum(x(3:M).*mass(3:M));          % Liquid mass in receiver
d=Ml;
```

Appendix D - 5
Subroutine: PsatR723

```
function  y=PsatR723(t)
%returns  T sat of vapour R723 in K for P in bar
 y = exp( 11.1811 - 2621.3 ./ t);
```

Appendix D - 6
Subroutine: rR723

```
function  y = rR723(p2,t)
%returns  gas constant for R723
%p in bar and T in oC
% J/kg.K  ZTT 06/023/2014 from REFPROP data processed
y=364.2;
```

Appendix D - 7
Subroutine: TsatR723

```
function  y=TsatR723(p)
%returns  T sat of vapour R723 in K for P in bar
if p<0; p,fail;end
 y = 2621.3./(11.1811-log(p));     % REFPROP Data - ZTT process 23/01/201
```

Appendix E

Corresponding particle size for US mesh sieve size

Particle Size mm	US Sieve Size
4.76	No. 4
4.00	No. 5
3.36	No. 6
2.83	No. 7
2.38	No. 8
2.00	No. 10
1.68	No. 12
1.41	No. 14
1.19	No. 16
1.00	No. 18
0.841	No. 20
0.707	No. 25
0.595	No. 30
0.500	No. 35
0.420	No. 40
0.354	No. 45
0.297	No. 50
0.250	No. 60
0.210	No. 70
0.177	No. 80
0.149	No. 100